



Quantifying the effect of chlorophyll on upper ocean processes and regional climate

A thesis submitted to the School of Environmental Science
of the University of East Anglia in partial fulfilment
of the requirements for the degree of Doctor of Philosophy

Jack Giddings

May 2021

© This copy of the thesis has been supplied on condition that anyone who consults it is understood to recognise that its copyright rests with the author and that use of any information derived there-from must be in accordance with current UK Copyright Law. In addition, any quotation or extract must include full attribution.

© Copyright 2021
Jack Giddings

Abstract

Through the absorption of solar radiation, chlorophyll influences mixed-layer radiative heating and sea surface temperatures and hence influences regional climate. Although the effect of chlorophyll on the El Niño-Southern Oscillation and the South Asian summer monsoon has been examined by previous studies, little is known about the effect of chlorophyll in the Bay of Bengal on the southwest monsoon. The absorption of solar radiation by chlorophyll is represented by varying the scale depth of blue light, h_2 , in ocean general circulation models. Here, a two-band solar absorption scheme is fitted to in-water photosynthetically active radiation profiles, measured from ocean gliders and profiling floats, to determine h_2 across the southern Bay of Bengal during the 2016 southwest monsoon. Values of h_2 are low (~ 14 m) in the Southwest Monsoon Current, Sri Lanka Dome and Bay of Bengal coastal regions when chlorophyll concentrations are high ($0.3-0.5 \text{ mg m}^{-3}$). A one-month surface-forced idealised simulation, using a one-dimensional K-profile parameterisation ocean mixed layer model, shows that a 0.3 mg m^{-3} increase in chlorophyll concentration increases sea surface temperature by 0.37°C in one month. Imposing seasonally and spatially varying h_2 in the Bay of Bengal in a coupled ocean-atmosphere model shows that the response of SST to chlorophyll is modulated by the depth of the mixed layer relative to the perturbed h_2 . The largest SST response to chlorophyll-induced warming occurs in the coastal regions where chlorophyll concentrations are high ($>1 \text{ mg m}^{-3}$), and when mixed layer depths shoal during the intermonsoon periods. Precipitation rates increase significantly by up to 3 mm day^{-1} across coastal Myanmar during the southwest monsoon onset and up to 3 mm day^{-1} over northeastern India and Bangladesh during the autumn intermonsoon period. The increase in precipitation rates improve model biases. Thus, imposing seasonally varying chlorophyll into models can improve intermonsoon rainfall amount and distribution. This thesis further investigates the effect of chlorophyll on radiant heating rates in the Sub-Antarctic Zone of the Southern Ocean during the austral spring and summer season of 2012/13. The chlorophyll concentration variability depends on the shoaling of the mixed layer depth, which is dependent on the strength of the wind-induced turbulent mixing. Although chlorophyll concentrations are high ($>1 \text{ mg m}^{-3}$) during summer, there is a negligible change in mixed layer temperature.

Access Condition and Agreement

Each deposit in UEA Digital Repository is protected by copyright and other intellectual property rights, and duplication or sale of all or part of any of the Data Collections is not permitted, except that material may be duplicated by you for your research use or for educational purposes in electronic or print form. You must obtain permission from the copyright holder, usually the author, for any other use. Exceptions only apply where a deposit may be explicitly provided under a stated licence, such as a Creative Commons licence or Open Government licence.

Electronic or print copies may not be offered, whether for sale or otherwise to anyone, unless explicitly stated under a Creative Commons or Open Government license. Unauthorised reproduction, editing or reformatting for resale purposes is explicitly prohibited (except where approved by the copyright holder themselves) and UEA reserves the right to take immediate 'take down' action on behalf of the copyright and/or rights holder if this Access condition of the UEA Digital Repository is breached. Any material in this database has been supplied on the understanding that it is copyright material and that no quotation from the material may be published without proper acknowledgement.

Acronyms

BoB	Bay of Bengal
GCM	General Circulation Model
MLD	Mixed Layer Depth
SAZ	Sub-Antarctic Zone
SLD	Sri Lanka Dome
SMC	Southwest Monsoon Current
SST	Sea Surface Temperature
PAR	Photosynthetically Active Radiation

Acknowledgements

I am hugely grateful for the supervision I have received these past four years. A special thanks goes to Karen Heywood, Adrian Matthews, Manoj Joshi and Ben Webber for their unrivalled enthusiasm, guidance and support throughout the project. Their honest opinion of my work may have resulted in a few iterations of certain drafts, but with their perseverance they have taught me to become a better writer, and with that, a better scientist.

I would like to thank Brian King and Alejandra Sanchez-Franks at the National Oceanographic Centre in Southampton for kindly providing the Argo float datasets and for their help on the data quality control process. I would like to thank Marcello Vichi who kindly provided the Southern Ocean glider data and supervised me during my three month stay at the University of Cape Town, as part of the Newton Fund PhD Exchange Program. I would also like to thank Nicholas Klingaman at the University of Reading for helping me set-up the modelling experiments and for the helpful discussions.

A special thanks has to go to my friends and colleagues in ENV department. This includes, but not limited to: Peter, Kirsty, Stephanie, Gillian and Marina. You have all made my time at UEA unforgettable, particularly for the incredibly loud lunches in the ENV social space. Thank you to all the housemates who I have lived with during my time in Norwich. It was notably the housemates in my final year who lifted my spirits and kept me sane during COVID-19 lockdown, and so deserve a special mention: Katherine, Gemma, Georgie, Ben, Rik, Austen, George and Perdeep. Finally, I would like to thank my wonderful mum, dad and sister for their continuous (and often emotional) support throughout the PhD.

This PhD project was funded by NERC and EnvEast DTP studentship (NE/L002582/1)

Part of the research in this thesis was carried out on the High Performance Computing Cluster supported by the Research and Specialist Computing Support service at the University of East Anglia.

Publications

Chapter 5 was in review for the Weather and Climate Dynamics journal prior to the submission of this thesis. Some changes to the submitted paper are listed below.

Chapter 5

Giddings, J., Matthews, A. J., Klingaman, N. P., Heywood, K. J., Joshi, M., and Webber, B. G. M., 2020. The effect of seasonally and spatially varying chlorophyll on Bay of Bengal surface ocean properties and the South Asian Monsoon. *Weather Clim. Dynam. Discuss.*, <https://doi.org/10.5194/wcd-2020-15>, *in review*.

JG carried out the research and prepared the paper. NPK provided the support in setting up the model. AJM, KJH, MJ and BGMW provided support for the research and gave feedback on earlier iterations of the draft paper. Figure 1 of the submitted paper has since been moved to Chapter 1 and re-numbered as Figure 1.3. Figures in Chapter 5 have been re-numbered.

Contents

Abstract	v
Acronyms	vii
Acknowledgements	ix
Publications	xiii
List of figures	xix
List of tables	xxi
1 Chapter 1	1
1.1 Optics of the oceans	2
1.2 Bio-optics of the oceans	5
1.2.1 Chlorophyll-dependent optical parameters and parameterisations	8
1.3 Chlorophyll perturbation studies using coupled and non-coupled ocean GCMs	12
1.4 The Bay of Bengal	13
1.4.1 Motivation	13
1.4.2 The South Asian monsoon	15
1.4.3 Surface ocean properties and chlorophyll concentration . .	16
1.5 The Southern Ocean	20
1.5.1 Regional climate	20
1.5.2 Surface ocean properties and chlorophyll concentration . .	21
1.6 Thesis Structure	22
2 chapter 2	25
2.1 Introduction	25
2.2 Ocean gliders and profiling floats overview	26
2.3 Ocean glider depth correction	27
2.4 Backscatter data processing	31
2.5 Chlorophyll-a fluorescence data processing	33
2.6 PAR quality control and optical parameter determination	37
2.6.1 Factors that affect optical parameter determination	37
2.6.2 Nighttime and low-light PAR profiles	40
2.6.3 Near-surface PAR perturbation flagging	41
2.6.4 Adaptation of the two-band solar absorption scheme	43
2.6.5 Further PAR perturbation flagging	46

2.6.6	Radiometer data quality control	53
2.7	Conclusion	60
3	chapter 3	63
3.1	Introduction	63
3.2	Data and methods	65
3.2.1	Observations and instruments	65
3.3	Glider and profiling float observations	67
3.4	Scale depth and chlorophyll concentration relationship with implications for BoB SST and climate	75
3.4.1	Relationship between scale depth and chlorophyll concentration	75
3.4.2	Implications for BoB SST and climate	76
3.5	Conclusions	82
4	Chapter 4	85
4.1	Introduction	85
4.2	Methods	89
4.2.1	Ocean Glider data	89
4.2.2	Satellite and reanalysis products	91
4.3	Results	92
4.3.1	Local hydrography and chlorophyll concentration during SOSCEX	92
4.3.2	Glider observations	95
4.3.3	Solar penetration depth parameterisation comparison	99
4.3.4	Upper ocean radiant heating during the spring and summer blooms	104
4.4	Discussion	106
4.5	Conclusions	110
5	chapter 5	113
5.1	Introduction	113
5.2	Methods and data	118
5.2.1	MetUM-GOML	118
5.2.2	Chlorophyll-a data	120
5.2.3	Experiment set-up	121
5.3	Results	123
5.3.1	Southwest monsoon onset (April to June)	123
5.3.2	Southwest monsoon (July to October)	127
5.3.3	Mixed layer radiant heating and SST modulation	132
5.4	Discussion	137
5.5	Conclusions	140
6	Chapter 6	143
6.1	Summary	143
6.2	Discussion and future work	148

A	Glider pitch and roll angle perturbations	153
B	Summary of solar irradiance parameterisations	157
B.1	Morel and Antoine (1994) solar irradiance parameterisation	157
B.2	Ohlmann (2003) solar irradiance parameterisation	157
	References	177

List of figures

1.1	Spectral values of e -folding depth	4
1.2	Global distribution of chlorophyll-a concentration	7
1.3	The Bay of Bengal thermal and saline surface properties during the summer and winter monsoon	14
1.4	The Bay of Bengal and surrounding region of interest	18
2.1	Position of sensors on glider SG579	28
2.2	Ocean glider depth correction schematic	29
2.3	Pitch correction	31
2.4	Backscatter quality control	32
2.5	Fluorescence quality control	34
2.6	Quenching correction method	36
2.7	Cloud and wave-focusing	39
2.8	Low-light and near-surface PAR perturbations	41
2.9	Influence of red light optical parameters and flagged depth on h_2 .	45
2.10	Downwelling irradiance fourth-degree polynomial method	47
2.11	Fourth-degree polynomial PAR profile type	48
2.12	Determination coefficient of PAR profiles for each fourth-degree polynomial step	49
2.13	Effect of polynomial flagging on h_2	50
2.14	Glider SG579 vertical speed and no. of PAR data points	52
2.15	Float residuals	53
2.16	Comparing ± 1 and ± 2 SD thresholds of $\ln E_d(490)$ float profile 34	55
2.17	Determination coefficient of $\ln E_d(490)$ profiles	57
2.18	Method 1 of K_{bio} cloud perturbation removal	58
2.19	Method 2 of K_{bio} cloud perturbation removal	59
2.20	Depth-profile section of derived Chl-a concentration from $\ln E_d(490)$	60
3.1	Bay of Bengal and SG579 trajectories	64
3.2	PAR profile and curve fit example	66
3.3	SG579 timeseries	68

3.4	h_2 timeseries	69
3.5	Bay of Bengal h_2 location	71
3.6	Float 631 timeseries	72
3.7	Float 629 timeseries	73
3.8	Float 630 timeseries	74
3.9	h_2 against chlorophyll-a concentration	77
3.10	KPP forcings and timeseries	80
4.1	Southern Ocean monthly chlorophyll-a concentration	86
4.2	MLD definition comparison	90
4.3	Hovmöller diagram of satellite altimeter products	93
4.4	Hovmöller diagram of satellite chlorophyll concentration	95
4.5	SG574 timeseries	96
4.6	Spring and summer mean temperature and chlorophyll-a profiles	98
4.7	h_2 against average chlorophyll concentration	101
4.8	Southern Ocean mean heat budget terms	108
4.9	Global shortwave radiation absorbed below the mixed layer	109
5.1	Monthly climatological precipitation rate	115
5.2	Monthly chlorophyll-a concentration climatology	116
5.3	Monsoon onset season (April to June)	125
5.4	Control run monthly average VIMF	126
5.5	Monthly average VIMF divergence difference	127
5.6	Precipitation rate model bias	129
5.7	Southwest monsoon season (July to October)	130
5.8	Monthly area-weighted average precipitation rate	131
5.9	Vertical and horizontal wind velocity mean difference for October	132
5.10	Radiant heating rate monthly average difference	134
5.11	Profiles of radiant heating rate difference	136
6.1	Schematic of the effect of chlorophyll on monsoon rainfall	146
A.1	Effect of pitch and roll angle on PAR perturbations	154

List of tables

1.1	Jerlov (1968) Water Type	9
2.1	Ocean glider and profiling float summary	27
2.2	Ocean glider and profiling float fourth-degree polynomial profile type	51
3.1	r^2 and RMSE of scale depth parameterisations (BoB)	76
4.1	r^2 and RMSE of scale depth parameterisations (SAZ)	102
4.2	Average spring and summer bloom variables and radiant heating rates	105

Chapter 1

Introduction

The physical and dynamical properties of the ocean surface are driven by the absorption of incoming solar radiation (Jerlov, 1968). It is the surface ocean properties that are readily exchanged with the atmosphere, influencing both regional and global climate at various temporal and spatial scales (Schott et al., 2009). The absorption of solar radiation in the upper ocean produces radiant heat that directly affects sea surface temperatures (SST). Through its influence on longwave radiation, sensible and latent surface heat fluxes, SST is an essential ocean property that strongly influences atmospheric processes. The tropical atmosphere is highly responsive to changes in SST due to strong air-sea coupling. Tropical SST anomalies alter atmospheric circulations and affect convective activity and rainfall that cause changes to surface heat and moisture fluxes (Graham and Barnett, 1987; Lindzen and Nigam, 1987).

Biological constituents that are suspended in the water column affect the absorption of solar radiation. Single-celled organisms called phytoplankton contain the pigment chlorophyll, which is used to absorb solar radiation during photosynthesis. The concentration of chlorophyll within the phytoplankton modulates the rate of solar radiation absorption and the depth to which solar radiation can penetrate (Smith and Baker, 1978). Thus, increasing chlorophyll concentration increases solar radiation absorption as well as increasing the radiant heating rate at the near-surface, which causes an increase in SST (Zaneveld et al., 1981; Lewis et al., 1990). Increasing the SST through chlorophyll-induced warming strongly influences regional climate and large-scale oceanic and atmospheric circulation (Sweeney et al., 2005; Turner et al., 2012; Patara et al., 2012). The concentration of chlorophyll and its direct and indirect interactions with the physics of the ocean and atmosphere is the

subject of this thesis. The aim is to quantify and analyse the effect of chlorophyll concentration on upper-ocean radiant heating, air-sea processes and regional climate.

1.1 Optics of the oceans

The absorption of solar radiation is approximately exponential with depth. In its simplest form, the change of solar irradiance (or the solar radiation flux per unit area; W m^{-2}) with depth is defined as

$$E_d(z) = E_d(0)e^{-K_d z} = E_d(0)e^{-\frac{z}{h}} \quad (1.1)$$

where $E_d(0)$ is the downwelling irradiance incident at the surface; $E_d(z)$ is the downwelling irradiance at depth z ; K_d is the diffuse attenuation coefficient that describes the fraction of solar irradiance attenuated per unit distance in the water column (m^{-1}); h is the e -folding scale depth (inverse of K_d). The value of K_d can be determined for individual wavelengths (e.g. $K_d(\lambda)$) or wavelength bands (e.g. $K_d(\text{PAR})$ where PAR is photosynthetically active radiation integrated between 400–700 nm). The value of K_d can vary with depth (e.g. $K_d(z)$) or be determined over a depth range (e.g. $K_d(z_0 \leftrightarrow z_n)$). The value of K_d represents all the constituents that attenuate solar radiation in the ocean, including all organic material, inorganic sediments and pure seawater. The versatility of K_d means it can be applied to many aspects of oceanography, such as classifying water turbidities (e.g. Jerlov, 1968), determining mixed layer heat budgets (e.g. Lewis et al., 1990) and calibrating chlorophyll fluorescence data (e.g. Xing et al., 2011).

Solar radiation incident at the ocean surface consists of near-infrared (IR; wavelength, $\lambda > 700$ nm), visible ($300 < \lambda < 700$ nm) and near ultra-violet (UV; $\lambda < 300$ nm) radiation. Once incident on the ocean surface, solar radiation is preferentially absorbed depending on its wavelength. IR radiation is completely absorbed within the top 1 m of the ocean surface, whereas UV and visible light penetrates deeper in the water column (Morel and Antoine, 1994; Sweeney et al., 2005). The absorption of visible radiation is also wavelength-dependent, with blue wavelengths (blue light) having a deeper penetration depth than red wavelengths (red light; Pope and Fry, 1997). In the clear open ocean at chlorophyll concentrations as low as 0.01 mg m^{-3} , the majority of red light is

absorbed within approximately the top 5 m, whereas the majority of blue light is absorbed within approximately the top 50 m (Fig. 1.1).

The varying absorption rate of the solar radiation spectrum means that upper ocean heat distribution is non-uniform. The radiant heat produced by the absorption of red light is restricted to the near-surface due to its small penetrative depth (<5 m). Conversely, the radiant heat produced by the absorption of blue light extends much lower in the water column due to its large penetrative depth. In fact, the penetration depth of blue light can be comparable or deeper than the depth of the mixed layer (~10–20 m), meaning the absorption of blue light effectively heats the entire mixed layer. It therefore exerts a larger control on mixed layer temperature than red light.

It is important to accurately simulate the preferential absorption of solar radiation in ocean general circulation models (GCM) as it strongly modulates SST. SST is affected by the one dimensional influences of penetrative shortwave radiation, longwave radiation, sensible and latent surface heat fluxes. Shortwave radiation heats the top tens of metres of the ocean, whereas upward longwave radiation, sensible and latent heat fluxes act to cool the top few millimetres of the ocean (Fairall et al., 1996). Turbulent mixing redistributes the cooled surface water throughout the whole depth of the mixed layer, which results in a decrease in the mixed layer temperature. The penetrative shortwave radiation absorption increases the mixed layer temperature, offsetting the cooling effect that decreases the mixed layer temperature. Hence, the penetrative shortwave radiation modulates SST and the heat balance of the mixed layer (Ohlmann et al., 1998).

The radiative heating produced by shortwave radiation absorption is an important factor in modulating the mixed layer depth (MLD). The MLD is modulated by the stratifying effects of radiative heating and the de-stratifying effects of wind-induced turbulent mixing and cooling. Increased radiative heating increases the temperature of the upper ocean, decreasing the density and increasing the thermal stratification; this decreases the MLD (Sathyendranath et al., 1991). Conversely, increasing surface wind speed increases upper-ocean turbulent mixing and cooling, and decreases thermal stratification that causes the MLD to deepen (Sallée et al., 2010). Decreasing the MLD through radiative heating reduces the effective heat capacity of the mixed layer, as less energy is required to heat a smaller volume of water. Hence, a shallow MLD means the SST rapidly responds to small changes in the net surface heat flux.

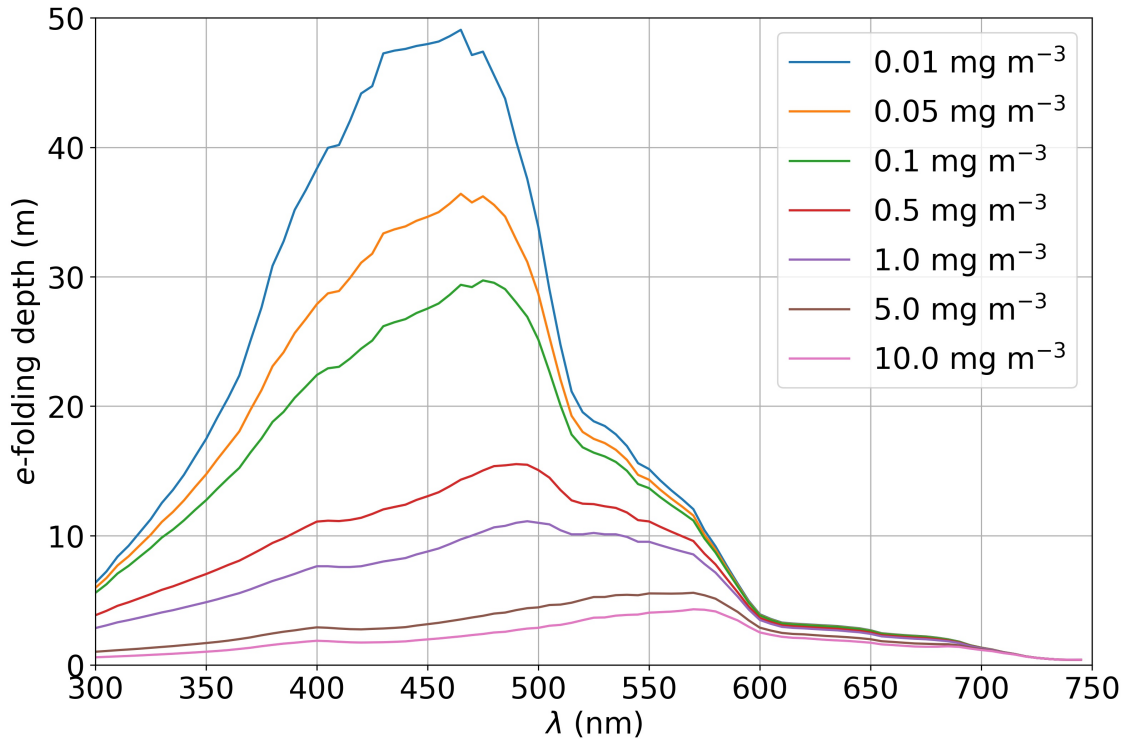


Figure 1.1: Spectral values of e -folding depth (inverse of k_d) for the 300–750 nm domain of downwelling solar irradiance for various chlorophyll- a concentrations. Figure is sourced and adapted from Figure 3a from Morel and Antoine (1994).

Recognising the wavelength-dependence of radiant heating, and its implications for MLD and SST, ocean GCMs represent solar radiation absorption as a function of depth by splitting the spectrum into multiple radiation bands. Paulson and Simpson (1977) used a double exponential function to replicate the preferential absorption of red and blue light with depth:

$$\frac{E_d(z)}{E_d(0)} = R e^{-\frac{z}{h_1}} + (1 - R) e^{-\frac{z}{h_2}} \quad (1.2)$$

where h_1 and h_2 are the scale depths of red and blue light, respectively, and R is the ratio of red light to total visible radiation. This double exponential function improves upon a single exponential function previously used by Denman (1973), which is similar to Equation 1.1. Morel and Antoine (1994) used a double exponential function for the absorption of red and blue light (300–750 nm) and included another exponential function for the absorption of IR radiation (> 750 nm). Ohlmann (2003) used a double exponential function for the absorption of UV and visible radiation (300–750 nm) and the absorption of IR radiation (750–2500 nm). Lengaigne et al. (2007) used a triple exponential function to

replicate the absorption of blue, green and red light with respect to depth. These multi-band solar absorption schemes are used in many state-of-the-art ocean GCMs, enabling them to replicate the preferential absorption of solar radiation and its effects on surface ocean properties.

1.2 Bio-optics of the oceans

The optical properties and absorption of visible radiation in the upper ocean depends on the in-water constituents. These constituents consist of: inorganic materials dissolved in sea water (Sullivan et al., 2006), organic suspended phytoplankton and coloured dissolved organic material (Morel, 1988), terrestrial material (Boss et al., 2009), and even bubbles (Zhang et al., 1998). The amount of these suspended or dissolved constituents modulates the intensity and wavelength of solar radiation that penetrates through the upper ocean. The biological constituents that effect the optical properties of the ocean are referred to as the “bio-optical state” (Smith and Baker, 1978). The biological constituent that most strongly effects the bio-optical state of the ocean is chlorophyll-a, the pigment that is commonly produced by phytoplankton for photosynthesis (Smith and Baker, 1978; Morel, 1988). Chlorophyll-a concentration strongly absorbs in the 400 to 500 nm visible domain (predominantly blue light; Fig. 1.1), with one dominant absorption spectra peak at 440 nm wavelength (Bricaud, 2004). The high sensitivity of the penetration depth of blue light to changes in chlorophyll-a concentration means chlorophyll-a concentration can modulate mixed layer radiant heating.

The physical and dynamical properties of the mixed layer influence chlorophyll concentrations as chlorophyll concentration depends on light and nutrient availability (Longhurst and Harrison, 1989; Thomalla et al., 2011). The depth of the mixed layer affects the likelihood of phytoplankton encountering light, as turbulent fluxes transport phytoplankton vertically in the mixed layer. Nutrients such as iron, silicate, nitrate and phosphate are used for phytoplankton division and growth, making them limiting factors to biological productivity (de Baar et al., 1995; Borrione and Schlitzer, 2013). When phytoplankton die, or are too heavy for suspension, they sink out of the mixed layer, taking nutrients with them (Huisman et al., 2006). Nutrients are then entrained back into the mixed layer through mixed layer deepening, which is caused by convective or wind-induced mixing (Schmittner, 2005; Behrenfeld and

Boss, 2014). Other nutrient sources include coastal upwelling, riverine input and terrestrial dust (Lévy et al., 2007; Smetacek et al., 2012; Amol et al., 2019).

The global annual 17-year climatology (2002–2018) of chlorophyll-a concentration at 9 km resolution derived from radiation measurements from the Moderate Resolution Imaging Spectroradiometer (MODIS) on the Aqua satellite is shown in Fig. 1.2. The spatial distribution and concentration of chlorophyll depends on the location of nutrient sources. Chlorophyll concentrations are high ($>1 \text{ mg m}^{-3}$) in coastal regions (e.g. The Ganges River delta in the north Bay of Bengal) and in upwelling regions (e.g. east equatorial Pacific), where nutrients are supplied to the euphotic zone (the sun-lit layer of ocean where photosynthesis occurs) through riverine input and upwelling. Conversely, chlorophyll concentrations are low ($<0.1 \text{ mg m}^{-3}$) in the subtropical gyres (e.g. South Atlantic) where downwelling limits the supply of nutrients to the euphotic zone throughout the year.

There are limitations to satellite-derived chlorophyll concentrations. Firstly, missing chlorophyll concentrations are a common occurrence. These are caused by clouds blocking backscattered visible radiation from the ocean surface. Secondly, the ocean colour algorithms used to determine chlorophyll concentration are not completely effective in turbid coastal waters where chlorophyll concentrations are high ($> 5 \text{ mg m}^{-3}$; Morel et al., 2007) and other oceanic constituents strongly attenuate solar radiation. Thirdly, chlorophyll concentrations vary sub-daily and at horizontal resolutions of less than 1 km. Satellite-derived chlorophyll concentrations are unable to capture this finescale temporal and spatial variability. In situ observations are needed to capture the sub-daily and sub-mesoscale variability of chlorophyll concentrations in regions where satellites are unable to accurately determine chlorophyll concentrations. Chapter 5 outlines the methodology of satellite-derived chlorophyll concentrations and its application in a climate sensitivity study.

The vertical distributions of chlorophyll concentration are not homogeneous. High chlorophyll concentrations can occur at the bottom of the euphotic zone, where there are just enough nutrients from below and sunlight from above for biological productivity. This region is referred to as the deep chlorophyll maximum. The deep chlorophyll maximum is a common feature in stratified subtropical gyre regions at depths of 50 to 200 m and forms when mixed layer nutrients are rapidly depleted during the start of summer (Mignot et al., 2014). The thickness of an ocean surface layer “seen” by a satellite radiance sensor is approximately one solar penetration depth (Gordon and McCluney, 1975),

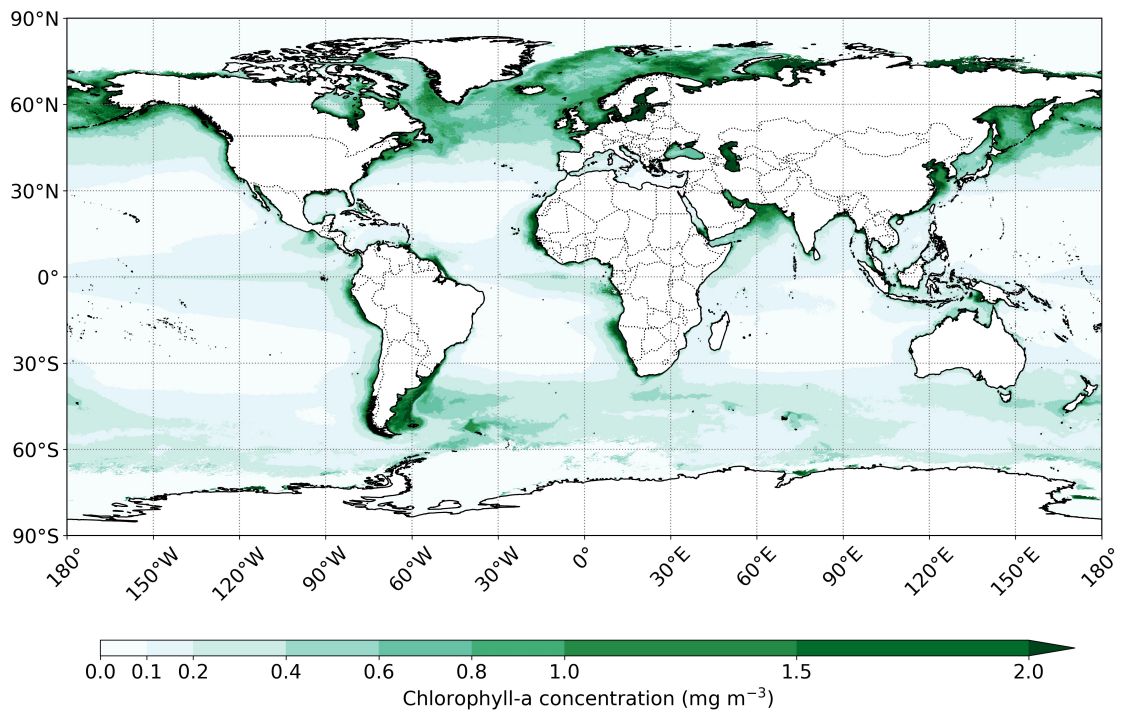


Figure 1.2: The global annual 17-year climatology (2002–2018) of chlorophyll-a concentration at 9 km resolution measured by MODIS-Aqua.

depending on the local chlorophyll concentrations. Thus, the measured global chlorophyll concentration from satellite in Fig. 1.2 represents the near-surface chlorophyll, excluding the deep chlorophyll maximum that occur at depths exceeding one solar penetration depth.

Previous observational, one-dimensional and global ocean modelling studies show the effect of chlorophyll on physical and dynamical properties of the ocean mixed layer through its modulation on solar radiation absorption. Strutton and Chavez (2004) found that observed radiant heating rates during the 1998 El Niño in the western Pacific increased from $\sim 0.1^\circ\text{C month}^{-1}$ to $\sim 1.0^\circ\text{C month}^{-1}$. It was estimated that 29% of the increase was due to an increase in chlorophyll concentration. Sathyendranath et al. (1991) found, by using a one-dimensional model, that chlorophyll contributed to a $1.0^\circ\text{C month}^{-1}$ increase in radiant heating rates in the Arabian Sea between August and September. In coastal regions, chlorophyll contributed to a $4.0^\circ\text{C month}^{-1}$ increase in radiant heating rates. Nakamoto et al. (2001) found, by using an ocean GCM, that chlorophyll concentrations increased mixed layer temperatures, which decreased MLDs in the equatorial Pacific. The chlorophyll-induced meridional thermal gradient along the equator was

then found to create anomalous geostrophic currents north and south of the equator. These currents merge at 200 m depth and strengthen upwelling in the equatorial eastern Pacific, offsetting the chlorophyll-induced surface warming by approximately 1.0°C. Chlorophyll-induced changes to the mixed layer have both positive and negative feedbacks on chlorophyll concentration, as light and nutrient availability are dependent on mixed layer processes (Manizza et al., 2005; Tian et al., 2019). The interactions between the mixed layer and chlorophyll concentrations show that the upper ocean is a complex coupled biophysical system.

1.2.1 Chlorophyll-dependent optical parameters and parameterisations

For the purposes of solar radiant heating in ocean GCMs the value of K_d represents the average solar radiation attenuation over a depth range, typically from the surface to a depth where solar radiation no longer perturbs the upper ocean temperature (<100 m). The value of K_d can represent individual wavelengths or wavelength bands depending on the solar radiation scheme used in an ocean GCM.

Ocean GCMs sometimes use the scale depth of blue light, h_2 (K_d^{-1}), to represent the solar penetration depth of blue light in the upper ocean. This is due to the strong influence blue light has on mixed layer radiant heating and the strong absorption of blue light by chlorophyll concentration. Hence, h_2 is a useful optical parameter in quantifying the effect of chlorophyll on solar radiation absorption in an ocean GCM.

The values of K_d or h_2 are determined from in situ radiometer measurements and satellite measurements. For in situ radiometer measurements, the optical parameters are determined by fitting a multi-band solar absorption function, like that of Equation 1.2, to in-water irradiance profiles (Smith and Baker, 1978; Lotliker et al., 2016). These in situ irradiance profiles are measured by radiometer sensors placed on oceanographic platforms such as ship-based tethers, buoys, profiling floats and ocean gliders (Lotliker et al., 2016; Xing et al., 2011). For satellite measurements, the optical parameters are determined by a series of empirical algorithms (Morel and Maritorena, 2001) or semi-analytical models (Lee et al., 2005).

The Jerlov water type classification is the earliest attempt to quantify and

Water Type	R	h_1 (m)	h_2 (m)	Chl-a conc. (mg m^{-3})
<i>Type I</i>	0.58	0.35	23	0–0.01
<i>Type IA</i>	0.62	0.6	20	0.05
<i>Type IB</i>	0.67	1.0	17	0.1
<i>Type II</i>	0.77	1.5	14	0.5
<i>Type III</i>	0.78	1.4	7.9	1.5–2

Table 1.1: Paulson and Simpson (1977) best-fit parameters of the five different Jerlov water type classifications and corresponding chlorophyll concentrations from Morel (1988).

classify ocean turbidity for ocean GCMs (Jerlov, 1968). This classification groups open-ocean water into five categories of turbidity depending on its solar absorption rates. Paulson and Simpson (1977) determined the optical parameters for each of the five Jerlov water types using Equation 1.2 (Table 1.1). The water type classification is a simple method that allows ocean GCMs to represent the average optical property of the global ocean or an ocean region. Water type I represents the clearest open-ocean (low turbidity), where chlorophyll concentrations are 0 to 0.01 mg m^{-3} , and h_1 and h_2 are 0.35 m and 23 m respectively (Table 1.1). Water type III represents the least clear open-ocean (high turbidity), where chlorophyll concentrations are 1.5 to 2.0 mg m^{-3} , and h_1 and h_2 are 1.4 m and 7.9 m respectively. As water type and corresponding chlorophyll concentrations increase, values of h_2 decrease, demonstrating the reduced solar penetrative depth as more solar radiation is absorbed with increasing chlorophyll concentration.

Zaneveld et al. (1981) demonstrated the effect of Jerlov water type I (low chlorophyll concentration) and III (high chlorophyll concentration) on mixed layer radiant heating rates. A 5-day simulation of two idealised one-dimensional mixed layers with a depth of 10 m and 20 m was run. Surface fluxes were assumed to be constant and incoming shortwave radiation had a diurnal cycle. Increasing the water type from I to III for a mixed layer that is 20 m deep, increased the radiant heating rate by $0.04^\circ\text{C day}^{-1}$. Increasing the water type from I to III for a mixed layer that is 10 m deep, increased the radiant heating rate by $0.08^\circ\text{C day}^{-1}$. Thus, changing the water type from I to III increases the mixed layer temperature, and decreasing the MLD further increases the radiant heating rate.

The Jerlov water type classification does have some limitations. Firstly, the classification does not define what in-water constituents affect the optical

properties of the upper ocean. Secondly, remotely sensed chlorophyll concentrations from satellites show that chlorophyll concentrations vary spatially and temporally, and are not limited to five discrete categories of concentration. Thirdly, radiative heating is sensitive to small changes in the solar penetration depth when MLDs are shallow, meaning the broad water type classification is not suitable for accurate solar radiative heating simulations in ocean GCMs (Ohlmann et al., 1998).

Morel and Prieur (1977) defined two “cases” of oceanic water based on the type of in-water constituents that effect the optical properties of the upper ocean. They are defined as:

- **Case I:** Optical properties influenced by phytoplankton, coloured dissolved organic matter and detrital organic matter, which are often referred to as “oligotrophic” waters.
- **Case II:** Optical properties influenced by all organic and inorganic matter, including sediments and dissolved yellow substance, which are often referred to as “eutrophic” waters.

Oligotrophic Case I waters represents the majority of the open ocean, accounting for approximately 98% of the global ocean (Morel, 1988). The remaining 2% accounts for coastal, eutrophic case II waters, where inorganic sediments from river outflow dominate the optical properties of the upper ocean (Morel, 1988; Boss et al., 2009). The case water classification has been crucial for the development of chlorophyll-dependent parameterisations, as it defines an important distinction between the optical properties of water masses that are either dominated by chlorophyll pigments or inorganic matter (Morel and Maritorena, 2001). For the purposes of solar radiant heating in ocean GCMs, chlorophyll-dependent parameterisations are strictly used for case I open-ocean waters, where chlorophyll pigments strongly perturb solar radiation (Morel and Antoine, 1994; Ohlmann, 2003).

Chlorophyll-dependent parameterisations have been developed through the use of in situ radiometric measurements (e.g. Morel, 1988) and radiative transfer models that use remotely sensed chlorophyll concentrations (e.g. Ohlmann, 2003). Morel and Antoine (1994) produced high-order polynomial relationships for a two-band model that related the scale depths of blue and red light (300–750 nm) to near-surface chlorophyll concentration, assuming an idealized Gaussian vertical profile of chlorophyll. Ohlmann (2003) used the

HYDROLIGHT radiative transfer model (Ohlmann and Siegel, 2000) to produce vertical profiles of solar radiation for pre-defined chlorophyll concentrations, time of day and cloud cover to determine optical parameters. A scale depth relationship was developed for the transmission of the ultraviolet-visible spectrum (300–750 nm) as part of a two-band model. Both parameterisations show a non-linear power-law relationship between solar penetration depths and chlorophyll concentration, meaning solar penetration depths are more sensitive to variations in low chlorophyll concentrations ($<0.2 \text{ mg m}^{-3}$) than high chlorophyll concentrations.

GCMs are now capable of using these parameterisations to accurately convert assimilated remotely sensed chlorophyll concentrations into solar penetration depths for the global ocean. Using remotely sensed chlorophyll concentrations, as opposed to using a single Jerlov water type to represent the average water type for the global open ocean, improves the spatial and temporal variability of chlorophyll forcing in coupled simulations.

GCMs such as the National Center for Atmospheric Research Community Climate System Model use the Ohlmann (2003) parameterisation for a two-band solar absorption scheme to convert observed chlorophyll concentrations into chlorophyll-perturbed solar penetration depths (Smith et al., 2010). The National Oceanic and Atmospheric Administration Geophysical Fluid Dynamics Laboratory Modular Ocean Model uses the Morel and Antoine (1994) parameterisation for a two-band solar absorption scheme to accurately determine solar penetration depths from observed chlorophyll concentrations (Sweeney et al., 2005). Implementing chlorophyll parameterisations in ocean GCMs would improve the accuracy of mixed layer radiant heating, and thus SST in coupled climate simulations.

Although the Morel and Antoine (1994) and Ohlmann (2003) parameterisations display a similar power-law relationship, subtle differences in the determined solar penetration depths leads to large differences in ocean GCM simulations. Sweeney et al. (2005) compared the effects of the Morel and Antoine (1994) and Ohlmann (2003) parameterisations in an ocean GCM. The difference in the parameterisations changed MLDs by up to 20 m, which affected the flux of radiant heat below the mixed layer and led to changes in the meridional overturning circulation and transport of heat polewards. The impact on large-scale circulations and horizontal and vertical heat transports highlights the sensitivity of the ocean system to different chlorophyll-dependent parameterisations.

1.3 Chlorophyll perturbation studies using coupled and non-coupled ocean GCMs

Previous studies have examined the effect of chlorophyll concentration on the tropical ocean and climate in ocean GCMs and coupled ocean-atmosphere GCMs. Particular focus has been on the effect of chlorophyll on Indian Ocean SST and the South Asian monsoon. Nakamoto et al. (2000) examined the effect of chlorophyll on Arabian Sea SST in an ocean isopycnal GCM with a two-band solar absorption scheme from Paulson and Simpson (1977). The imposed monthly climatology of chlorophyll concentrations, measured by the Coastal Zone Color Scanner (CZCS), were converted into solar penetration depths using the Morel and Antoine (1994) parameterisation. High chlorophyll concentrations during the intermonsoon were found to decrease the MLD and solar radiation penetration depth, as well as causing an increase to the SST by 0.6°C .

Wetzel et al. (2006) used a fully coupled system, linking a biogeochemistry model to an ocean-atmosphere GCM, to examine the effects of chlorophyll on the climate of the Arabian Sea. A four-band solar radiation scheme for visible, UV and IR spectral bands was used to represent the preferential absorption of solar radiation. Spring chlorophyll blooms in the western Arabian Sea were found to increase SST by 1°C at 20°N , which led to an increase in rainfall of 3 mm day^{-1} over southwest India during the southwest monsoon onset. Turner et al. (2012) showed similar results when using a coupled ocean-atmosphere GCM with a two-band solar absorption scheme from Ohlmann (2003). The imposed seasonally varying chlorophyll concentrations from SeaWiFS were converted into solar penetration depths using the Ohlmann (2003) parameterisation. The spring chlorophyll blooms in the western Arabian Sea were found to reduce MLD biases by 50%, increase SST by 0.5 to 1.0°C and increase rainfall by 2 mm day^{-1} over western India during the southwest monsoon onset.

Previous studies have examined the effect of chlorophyll on Equatorial Pacific SST. Murtugudde et al. (2002) used an ocean GCM with an annual mean of chlorophyll concentrations measured from the CZCS to show increased SST and reduced upwelling in the eastern Equatorial Pacific. Nakamoto et al. (2001) used an ocean isopycnal GCM with a monthly climatology of chlorophyll concentrations measured from the CZCS to show decreased SST and

increased equatorial upwelling in the eastern Equatorial Pacific, contradicting the results of Murtugudde et al. (2002). Other studies have also examined the impact of chlorophyll on El Niño-Southern Oscillation (ENSO) dynamics. Marzeion et al. (2005) used a coupled GCM linked to an ecosystem model to show that biophysical feedbacks increased ENSO amplitudes by warming the eastern Equatorial Pacific. Tian et al. (2019) used a coupled GCM linked to a biogeochemistry model to show that mesoscale variations of chlorophyll concentration increased the amplitude of ENSO. However, Jochum et al. (2010) found that ENSO amplitudes decreased by 9% when using a coupled GCM linked to a biogeochemistry model.

All these studies demonstrate the sensitivity of the tropical atmosphere to spatial, seasonal and even subseasonal variations in chlorophyll concentrations, which has implications for the location of convective activity within the tropics. The often contradictory results between these studies highlights the impact of using different coupled GCMs and varying experimental designs when investigating the impact of chlorophyll on surface ocean properties and climate (Park and Kug, 2014).

1.4 The Bay of Bengal

1.4.1 Motivation

The Bay of Bengal (BoB), located in the northern Indian Ocean, is a semi-enclosed basin with India to the west, Bangladesh to the north and Myanmar and Isthmus of Thailand to the east (Fig. 1.3). The BoB is an important source of heat and moisture to the South Asian monsoon system and provides essential rainfall to the densely-populated Indian subcontinent during the boreal summer. Industries such as agriculture are most reliant on monsoon rainfall for reliable crop yields and employment (Revadekar and Preethi, 2012). Variations in the amount, timing and location of monsoon rainfall leads to natural disasters such as droughts and floods, which have severe socio-economic impacts (Webster et al., 1998; Roxy et al., 2017). Improving the physical and dynamical processes of the South Asian monsoon in coupled GCMs would mean more accurate forecasting and limited socio-economic devastation.

Coupled atmosphere-ocean GCMs still show significant biases in the basic mean seasonality of South Asian monsoon precipitation. Lin et al. (2008) found

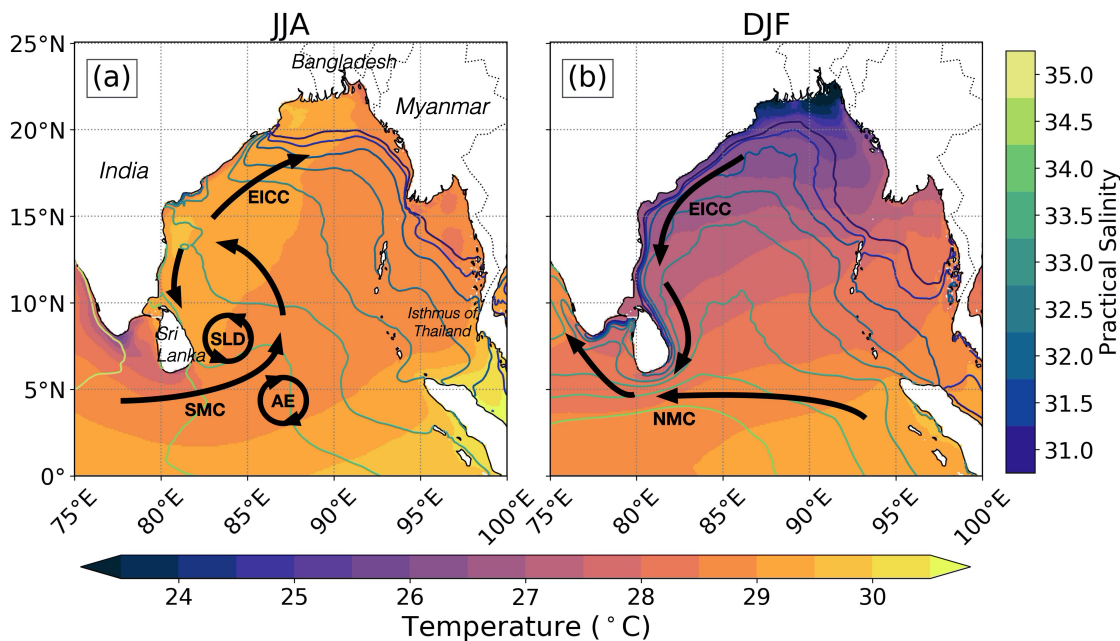


Figure 1.3: BoB SST ($^{\circ}\text{C}$) and surface practical salinity 26-year climatology during the South Asian (a) summer monsoon (June to August) and (b) winter monsoon (December to February). The data is sourced from the monthly global NEMO reanalysis dataset at 0.25×0.25 horizontal resolution from 1993 to 2019 (available at <http://marine.copernicus.eu>). During summer, the Sri Lanka Dome (SLD) is shown as a cyclonic (anticlockwise) black circle, the Southwest Monsoon Current (SMC) is shown as the black arrow south west of Sri Lanka and the East India Coastal Current (EICC) is shown as the black arrow north east of India. During winter, the Northeast Monsoon Current (NMC) is shown as the black arrow in the southern BoB and the EICC is shown as the black arrow north east of India.

that 12 out of 14 coupled GCMs from the Coupled Model Intercomparison Project Phase 3 (CMIP3) captured the seasonal-mean precipitation rate reasonably well. Nevertheless, most GCMs produced excessive precipitation at the Equator and insufficient precipitation across the northern BoB and Bangladesh during summer. Sperber et al. (2013) compared 25 CMIP5 models with 22 CMIP3 models, where CMIP5 models have higher vertical and horizontal resolutions in the ocean and atmosphere, compared with CMIP3 models. Both the CMIP5 and CMIP3 models underestimate precipitation over the BoB and India at 20°N and produce a consistent dry bias of up to 4 mm day^{-1} over central India at 25 to 30°N . The inaccuracies of the basic seasonality of summer monsoon precipitation in state-of-the-art coupled GCMs highlights the need for improved simulations of the South Asian monsoon.

Some studies have shown the effect of chlorophyll on BoB SST. Murtugudde et al. (2002) found that the annual mean SST increased by 0.2°C in the western

and northern BoB. Wetzel et al. (2006) found that surface air temperatures increased by 0.2°C across the southern and southwestern BoB from May to August. Although these studies demonstrate the effect of chlorophyll on BoB SST, the role of chlorophyll in modulating BoB mixed layer processes and the seasonal cycle of SST, and the response of SST to monsoon rainfall remains a vital knowledge gap. Without this knowledge then missing bio-physical interactions in the BoB could lead to inaccuracies in simulated air-sea interactions, which are crucial in simulating accurate monsoon behaviour over the Indian subcontinent. The purpose of this thesis aims to investigate the effect of chlorophyll on solar penetration depths, upper ocean radiant heating, air-sea surface fluxes and monsoon rainfall amount and spatial distribution in the BoB region.

1.4.2 The South Asian monsoon

The South Asian monsoon is initiated by the seasonal cycle of insolation. As insolation increases from spring to summer over the Asian continent, differential heating rates and resultant thermal gradients between land and ocean cause lower-tropospheric winds to flow northward from the equator to the Asian continent (Webster et al., 1998). Additional mid-tropospheric heating from the elevated Tibetan Plateau further increases the land-sea temperature and pressure contrast, accelerating the seasonal reversal of the large-scale circulation (Li and Yanai, 1996).

Ju and Slingo (1995) outlined three mean evolutionary phases of the South Asian monsoon. First is the onset of the monsoon, which starts with rainfall at the southernmost tip of India around 1 June. Second is the establishment of the monsoon as strong lower-tropospheric southwesterly winds, transporting heat and moisture, sustains heavy rainfall over the Indian subcontinent from June to September (JJAS). Third is the retreat of the monsoon as lower-tropospheric southwesterly winds weaken equatorward and monsoonal rainfall ceases over the Indian subcontinent from September onwards. During the established phases of the South Asian monsoon, the highest mean rainfall rates are anchored to three regions across the Indian subcontinent: the Western Ghats of southwest India, the Myanmar coast and the foothills of the Himalayas extending south across Bangladesh.

The South Asian monsoon displays strong intraseasonal variability as it is strongly influenced by the planetary-scale Madden-Julian Oscillation (MJO;

Wang and Xie, 1997). This intraseasonal variability, termed the boreal summer intraseasonal oscillation (BSISO; Wang and Xie, 1997), propagates northwards and westwards from the Equator (Gadgil and Srinivasan, 1990), affecting monsoon rainfall break and active periods over the BoB and Indian subcontinent (Webster et al., 1998). The BSISO strongly influences the intraseasonal variability of SST (Fu et al., 2003; Gao et al., 2019). Break periods correspond with calmer and less cloudy conditions, which allow for more downward shortwave radiation and reduced windspeeds that reduces the turbulent surface heat flux, shoals the mixed layer and increases the SST (Roxy et al., 2013). The strong air-sea coupling means that the SST intraseasonal variability influences the BSISO mean state and propagation, which produces a positive feedback on the SST intraseasonal variability over the BoB (Klingaman et al., 2011; Peatman and Klingaman, 2018). As demonstrated in previous coupled GCM studies (e.g., Wetzal et al., 2006; Turner et al., 2012), chlorophyll has been found to increase SST and monsoon rainfall during the South Asian summer monsoon. The effects of biological warming on BoB SST would have the potential to influence the seasonal and intraseasonal variability of summer monsoon rainfall across the BoB.

1.4.3 Surface ocean properties and chlorophyll concentration

The general circulation of the BoB varies seasonally and is forced by a combination of local and remote forcing. During the boreal summer (June to August), southwesterly monsoon winds initiate the Southwest Monsoon Current (SMC; Vinayachandran et al., 2004), which advects cooler, saline water from the Arabian Sea and the western equatorial Indian Ocean around the southernmost point of India and Sri Lanka into the warmer and fresher BoB (Fig. 1.3a; Jensen, 2003; Sanchez-Franks et al., 2019). The SMC is a shallow, fast-moving current with speeds of up to 0.6 m s^{-1} and extends to a depth of 550 m (Fig. 1.3a; Webber et al., 2018). Arabian Sea water entering the BoB typically has a high sea surface salinity of 34 and low SST of 28°C relative to the BoB (Fig. 1.3a). Two eddy features form either side of the SMC during the summer monsoon. The first is the cyclonic eddy known as the Sri Lanka Dome (SLD) located east of Sri Lanka and the second is the anticyclonic eddy (AE) located southeast of Sri Lanka (Fig. 1.3a). The cyclonic circulation of the SLD causes open-ocean upwelling, whilst the AE causes open-ocean downwelling. The eddy features have been found to be initiated by the local wind stress curl

(Vinayachandran and Yamagata, 1998) and Rossby wave propagation (Webber et al., 2018; Pirro et al., 2020). The East India Coastal Current (EICC), which is partly supplied by flow out of the SMC, bifurcates at around 10 to 15°N with a northern branch flowing northwards and a southern branch flowing southwards (Fig. 1.3a; Schott and McCreary, 2001).

During the boreal winter (December to February), northeasterly monsoon winds initiate the Northwest Monsoon Current (NMC), which advects fresher BoB water around the southernmost point of India and Sri Lanka into the saltier Arabian Sea (Fig. 1.3b; Schott et al., 2009). The EICC reverses direction due to the reversing of the monsoon winds, advecting cool, fresh river water from the northeastern BoB southward where it joins the NMC and exits the BoB (Fig. 1.3b; Han and McCreary, 2001). Hence, BoB water entering the Arabian Sea typically has a low sea surface salinity of 32 and low SST of 27°C relative to the Arabian Sea (Fig. 1.3b).

The BoB thermal and saline surface properties are forced by the monsoonal winds and large freshwater flux. However, these forcings are not uniform across the basin. In the northern BoB, there is a large freshwater flux from several rivers such as the Ganges, Brahmaputra, Mahanadi and Irrawaddy (Fig. 1.4). The large river runoff, combined with the monsoonal precipitation, leads to strong salinity stratification and the formation of a barrier layer (Vinayachandran et al., 2002; Jana et al., 2015; Sengupta et al., 2016). The barrier layer is the region between the low-density freshwater that forms a shallower halocline and the deeper thermocline, and the mixed layer is the region between the surface and the shallower halocline (Sprintall and Tomczak, 1992). Barrier layers form in the northern BoB during summer and spread equatorward across the BoB until winter (Rao and Sivakumar, 2003). The strong stratification associated with the barrier layer means vertical mixing is inhibited when exposed to monsoonal wind forcing (Sprintall and Tomczak, 1992; Rao and Sivakumar, 2003) and the mixed layer above is isolated from cooling by entrainment of colder, deeper waters (Duncan and Han, 2009). Reducing the MLD increases the sensitivity of the mixed layer temperature and SST to changes in the net surface heat flux, which are primarily controlled by variations in windspeed (Duncan and Han, 2009). In the southern BoB, the salinity stratification is weaker, meaning monsoonal winds strongly influence the thermal stratification of the upper ocean (Narvekar and Prasanna Kumar, 2006). This monsoonal wind dependence explains why the southern BoB MLD and SST show larger seasonal variability compared with the northern BoB.

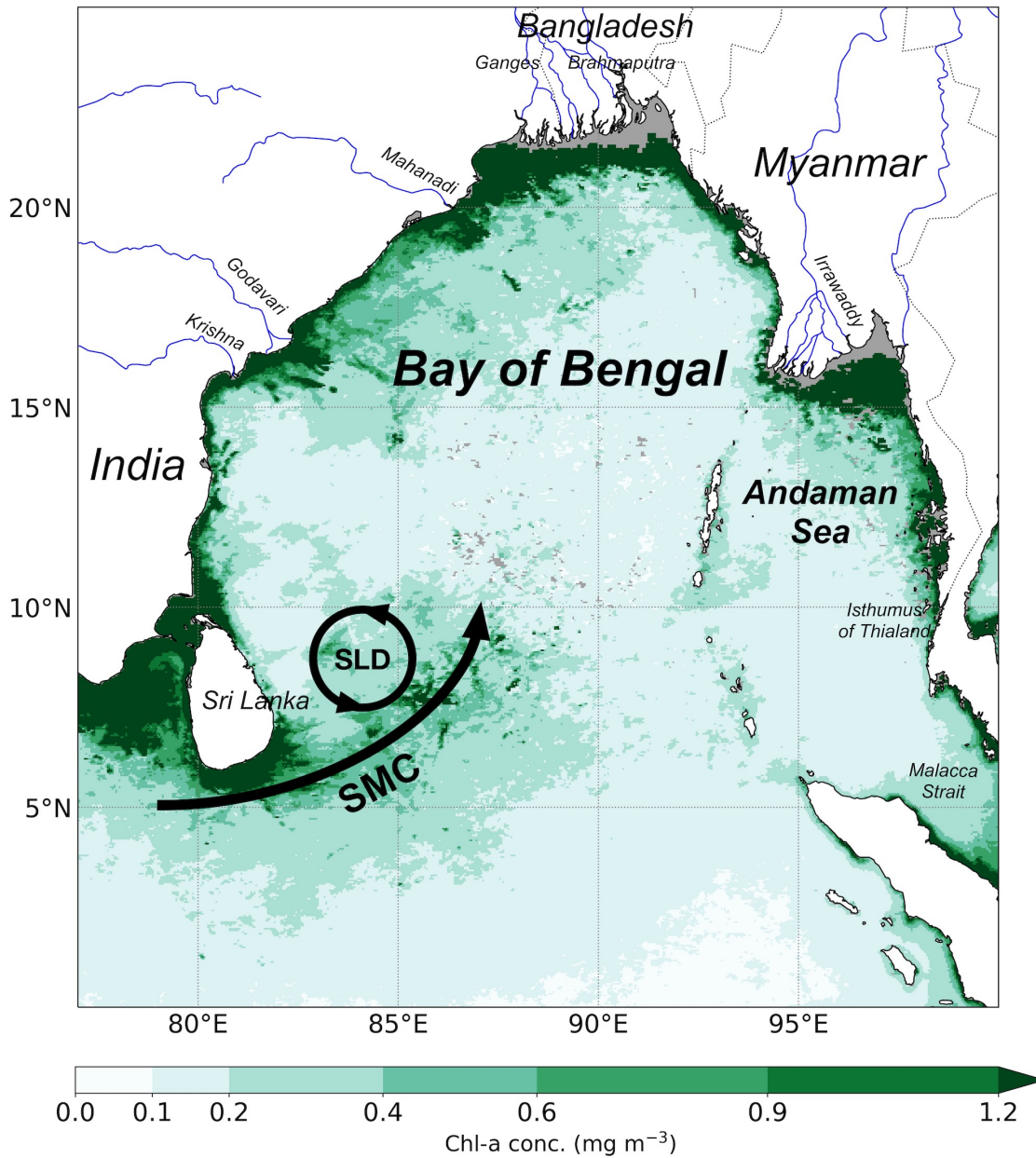


Figure 1.4: The Bay of Bengal (BoB) and surrounding region of interest. August chlorophyll-a concentration climatology measured from MODIS-Aqua at 4 km horizontal resolution is shown. The locations of major rivers are represented as blue lines. The SLD is shown as a cyclonic (anticlockwise) black circle and the SMC is shown as the solid black arrow. Missing data is shown in grey.

In the northern BoB, strong salinity stratification reduces biological productivity by inhibiting the vertical transport of nutrients to the euphotic zone (Kumar et al., 2002). Nonetheless, certain regions of the northern BoB exhibit high biological productivity. Chlorophyll concentrations in the coastal and delta regions are high ($>1 \text{ mg m}^{-3}$) due to the supply of nutrients from riverine output (Fig. 1.4; Amol et al., 2019). River discharge, and attendant nutrients, typically peak during October (Rao and Sivakumar, 2003), meaning corresponding chlorophyll concentrations also peak during October (Lévy et al., 2007). Local alongshore winds in the northwestern BoB during summer cause coastal upwelling, increasing nutrient flux to the near-surface and increasing biological productivity (Thushara and Vinayachandran, 2016).

In the southern BoB, where salinity stratification is less strong than the northern BoB, southwesterly winds across the southernmost tip of India and Sri Lanka initiate coastal upwelling, which increases biological productivity and chlorophyll concentration during the southwest monsoon (Fig. 1.4; Lévy et al., 2007). The high chlorophyll concentrations from the southernmost tip of India and Sri Lanka are entrained and advected into the southwest BoB by the SMC (Vinayachandran et al., 2004). The high chlorophyll concentrations east of Sri Lanka are located inside the cyclonic eddy of the SLD (Fig. 1.4). The open-ocean Ekman upwelling associated with the SLD transports nutrients to the near-surface, sustaining biological productivity (Vinayachandran and Yamagata, 1998; Vinayachandran et al., 2004; Thushara et al., 2019).

In the BoB open ocean, chlorophyll concentrations are periodically enhanced by transient cold-core eddies and post-monsoon cyclones, which briefly erode the strong salinity stratification and transport nutrients to the near-surface (Vinayachandran and Mathew, 2003; Prasanna Kumar et al., 2007; Patra et al., 2007). Regions that exhibit seasonal to subseasonal variations in chlorophyll concentrations would have seasonal to subseasonal variations in solar radiation penetration depths. Consequently, altering the solar radiation penetration depth for an ocean that is tightly coupled to the atmosphere, and which is sensitive to variations in surface heat fluxes, could result in changes to the South Asian summer monsoon system.

1.5 The Southern Ocean

In addition to understanding the effect of chlorophyll on surface ocean properties and regional climate in the low-latitude region of the BoB, this thesis will extend its investigation to the mid-latitude region of the Southern Ocean, after an opportunity to analyse in situ observations in the Atlantic sector of the Southern Ocean. Here, the effect of chlorophyll on surface ocean properties and climate in a region with different biological, oceanic and climate regimes to the BoB will be quantified and discussed.

Chlorophyll concentrations have been found to influence the physical upper ocean properties and regional climate of the Atlantic sector of the Southern Ocean. Using a biogeochemistry model linked to a coupled ocean-atmosphere GCM, Patara et al. (2012) found that global chlorophyll concentrations increased the annual mean SST in the Atlantic sector of the Southern Ocean by up to 0.5°C and increased annual zonally-averaged ocean temperatures by 0.1°C down to 300 m. The increase in SST led to an increase in the upward latent heat flux of 1 W m^{-2} and an increase in the precipitation rate of 0.05 mm day^{-1} . Manizza et al. (2005) found using a biogeochemistry model linked to an ocean GCM that the Southern Ocean SST in the Atlantic sector increased by 0.5°C , yet some areas SST decreased by up to 0.2°C due to increased upwelling. The increase in SST corresponds to an increase in chlorophyll concentrations during the spring and summer blooms, with an increase in the upper-ocean stratification of 3–4%. Gnanadesikan and Anderson (2009) also found using a coupled ocean-atmosphere model that Southern Ocean SST in the Atlantic sector increased by up to 0.5°C . These coupled GCMs show that the Southern Ocean SST and climate is also susceptible to the effects of chlorophyll concentration.

1.5.1 Regional climate

The Southern Ocean is a region that is strongly influenced by atmospheric forcing from midlatitude cyclones. The high activity of midlatitude cyclones decreases the mean surface pressure around the Southern Ocean, forming the Antarctic Circumpolar Trough between $50\text{--}70^{\circ}\text{S}$ (King and Turner, 1997). These midlatitude cyclones are generated from the baroclinic instability caused by the large meridional temperature gradient between cold, Antarctic air and warm, midlatitude air (King and Turner, 1997; Yuan et al., 1999). The strong meridional SST gradient across the Antarctic Circumpolar Current (ACC)

further enhances tropospheric zonal wind velocities and baroclinic instability (Hoskins and Hodges, 2005). Midlatitude cyclones are classed as synoptic-scale weather systems with a diameter of at least 1,000 km that last between one and seven days in the Southern Ocean (King and Turner, 1997). The season with the strongest cyclones (large surface pressure gradient with windspeeds exceeding 20 m s^{-1}) and highest cyclone frequency is austral winter (June to August), whereas the season with the weakest and lowest cyclone frequency is austral summer (December to February; Yuan et al., 2009). Midlatitude cyclones strongly influence the physical properties of the surface ocean.

1.5.2 Surface ocean properties and chlorophyll concentration

The thermal and saline properties of the Atlantic sector of the Southern Ocean surface are forced by the annual cycle of windspeed and buoyancy. Between early autumn and the end of winter (February to September), the increased midlatitude cyclone frequency increases the wind stress and the resultant turbulent mixing of the ocean surface. The increase in wind stress increases the upward surface heat fluxes, cooling and reducing the buoyancy of the ocean surface (du Plessis et al., 2019). The strong wind-induced turbulent mixing causes the mixed layer depth (MLD) to deepen to around $150 \pm 60 \text{ m}$ during winter (Sallée et al., 2010).

During spring and summer (October to January), the gradual increase in solar radiation increases upper-ocean thermal stratification (Sallée et al., 2010). The reduction in midlatitude cyclone frequency during spring and summer means the wind stress is reduced. This causes a reduction in the upper-ocean turbulent mixing and causes lateral density gradients to slump (where less dense water moves up and over more dense water) as meridional density gradients are unable to be maintained when windspeeds are reduced (Swart et al., 2015). The reduction in wind-induced turbulent mixing and increased slumping increases upper-ocean stratification and causes the MLD to shoal to around $50 \pm 20 \text{ m}$ during summer (Sallée et al., 2010). Mixed layer eddies that form along frontal jets also move less dense water up and over the denser side of the fronts when windspeeds are reduced or reversed over the frontal jet, which rapidly increases upper-ocean stratification (du Plessis et al., 2017; du Plessis et al., 2019).

The seasonal variability of the upper-ocean stratification in the Atlantic sector of the Southern Ocean influences the seasonal variability of biological processes.

During winter, deep mixed layers and low incoming solar radiation means the likelihood of phytoplankton receiving light to photosynthesise and produce chlorophyll is reduced, resulting in low chlorophyll concentrations (Mitchell et al., 1991; Nelson and Smith, 1991). During spring and summer, high incoming solar radiation and slumping of lateral density gradients increase upper-ocean stratification and decreases the MLD (Swart et al., 2015). Decreasing the MLD reduces the vertical extent of turbulent fluxes that transport phytoplankton in the mixed layer, increasing the likelihood of phytoplankton receiving light. The combination of reduced MLDs, cross-frontal mixing of nutrients and high incoming solar radiation results in high chlorophyll concentrations (Mitchell et al., 1991; Nelson and Smith, 1991).

The seasonal to subseasonal (weekly to monthly) and mesoscale (10–200 km) to submesoscale (1–10 km) variability of chlorophyll concentration in the Atlantic sector of the Southern Ocean are attributed to many factors. The deepening of a mixed layer can dilute the chlorophyll concentration and cause physiological adaptation of phytoplankton, altering the chlorophyll concentration that they produce (Smetacek and Naqvi, 2008). The seasonal to subseasonal changes to the MLD are not uniform across the Atlantic sector of the Southern Ocean. Different water masses with varying upper-ocean stratifications respond differently to the same atmospheric forcing, resulting in varying MLDs and chlorophyll concentrations (Swart et al., 2015). The variability in biological productivity is also dependent on the types of nutrients that are available (de Baar et al., 1995; Boyd et al., 2000) and the grazing of phytoplankton by zooplankton (Hoppe et al., 2017). These factors make it difficult to disentangle the causality of chlorophyll concentration variability on various spatial and temporal scales in the Southern Ocean. Such variability in chlorophyll concentration further suggests that there is similar variability in upper-ocean turbidity, solar penetrations depths and radiant heating rates.

1.6 Thesis Structure

This thesis will aim to (i) accurately derive solar penetration depths from optical measurements from ocean gliders and profiling floats, (ii) to determine and compare the relationship between derived solar penetration depths and observed chlorophyll concentrations with previously published relationships, and (iii) to quantify the effect of chlorophyll on upper ocean radiant heating, SST

and regional climate in the low-latitude region of the BoB and the mid-latitude region of the Southern Ocean Atlantic Sector.

In Chapter 2, a methodology of the data quality control process for physical and optical variables measured by ocean gliders and profiling floats is presented. This includes the development and application of the PAR quality control and optical parameter determination. A novel method is presented to derive chlorophyll-a concentration from profiling float radiometer measurements. An overview of the ocean glider and profiling float deployments from which the data is collected is also summarised.

In chapter 3, the spatial and temporal variability of solar penetration depths, measured from a month to 3-month glider and profiling float deployment in the BoB, is analysed. The spatial and temporal variability of chlorophyll concentration and corresponding solar penetration depths is examined. The impact of the chlorophyll-perturbed solar penetration depths on SST during the summer monsoon is investigated by using the one-dimensional K-profile parameterisation ocean mixed layer model. Further implications of the chlorophyll-perturbed surface ocean properties on monsoon climate is discussed.

Chapter 4 presents an analysis of the spatial and temporal variability of solar penetration depths in the Southern Ocean. Unlike the tropics, this mid-latitude region experiences large seasonal chlorophyll blooms with high concentrations ($> 1 \text{ mg m}^{-3}$) that are strongly modulated by the seasonal cycle of insolation and periodic atmospheric forcing. Biological, optical and physical variables are measured during a 5-month glider deployment. Similar to Chapter 3, the implications of the Southern Ocean chlorophyll blooms on mixed layer radiant heating rates are analysed and its potential impact on mid-latitudinal regional climate is discussed.

In chapter 5 (submitted to WCD), seasonally and spatially varying chlorophyll concentration in the BoB is imposed in the Global Ocean Mixed Layer 3.0 configuration of UK Met Office Unified Model (MetUM-GOML3.0). Comparing the 30-year control and chlorophyll-perturbed simulations shows the direct and indirect effects of seasonally varying chlorophyll concentration on BoB surface ocean properties and monsoon rainfall. Chapter 6 presents the conclusions where the final results of chapters 2 to 5 are summarised and discussed, and future work is proposed.

Chapter 2

Methodology of glider and profiling float data processing

2.1 Introduction

Measuring the biological and physical properties of the surface ocean at increased temporal and spatial resolutions has been made possible through the use of autonomous underwater vehicles (AUV) such as an ocean glider, and autonomous underwater platforms such as a profiling float. Ocean gliders provide continuous sampling of the upper ocean (0–1000 m) on hourly to daily time scales for time periods of weeks to months. Profiling floats provide continuous sampling of the upper ocean every 1 to 10 days for up to 4 to 5 years. Both ocean gliders and profiling floats are suitable for capturing sub-seasonal, seasonal and sub-annual changes to the upper ocean. The ocean gliders and floats are equipped with an array of sensors that measure the physical, chemical, biological and optical properties of the upper ocean.

This chapter will provide background information on the ocean glider and profiling floats used in the 2016 joint India-UK Bay of Bengal Boundary Layer Experiment (BoBBLE; Vinayachandran et al., 2018) and the ocean glider used in the 2012/13 Southern Ocean Seasonal Cycle Experiment (SOSCEX; Swart et al., 2012). This chapter will further provide an overview of the development and application of the quality control process for each physical and bio-optical variable measured during these deployments.

2.2 Ocean gliders and profiling floats overview

An ocean glider is a buoyancy-driven AUV that can be piloted via satellite communications to set locations anywhere in the global ocean. During the BoBBLE field campaign, a Seaglider (SG579) was deployed at 86°E on 30 June 2016 along the 8°N transect east of Sri Lanka and piloted to 85.3°E by 8 July, where the glider continued to take measurements until 29 July 2016 (Table 2.1). The glider profiled on a sawtooth trajectory from the surface to 700–1000 m, completing a full dive cycle approximately every 4 hours. Surface manoeuvres were initiated at 3 m depth allowing the ascending glider to sample the near-surface ocean before trimming into position to transmit data. The glider was equipped with a Seabird Electronics (SBE) conductivity (salinity), temperature and depth (CTD) sensor, a Wetlabs Triplet Ecopuck measuring chlorophyll-a fluorescence and optical backscatter at wavelengths 470 nm and 700 nm and a Biospherical Instruments quantum scalar irradiance photosynthetically active radiation (PAR; $\mu\text{E m}^{-2} \text{s}^{-1}$) sensor measuring visible wavelengths between 400 nm and 700 nm. The Wetlabs and PAR sensors sampled to a depth of 300 m with a vertical resolution of ~ 1 m.

A profiling float is a buoyancy-driven free-drifting profiler. Argo profiling floats 629, 631 and 630 that are part of the international Argo float program were deployed at 85.5°E, 87°E and 89°E on the 28 June, 1 July and 4 July respectively (Table 2.1), where they sampled to 500 m daily until mid-August and every other day until the end of September. All three floats were equipped with SBE 41N CTD and a Satlantic OCR-504 ICSW radiometer measuring downwelling irradiance at wavelengths 380 nm, 490 nm, 555 nm ($\mu\text{W cm}^{-2} \text{nm}^{-1}$) and PAR ($\mu\text{E m}^{-2} \text{s}^{-1}$). Both sensors had a vertical resolution of ~ 1 m sampling up to the near-surface to a depth of 0.5 m.

Ocean glider SG574, used in the SOSCEX campaign, was deployed in the Atlantic sector of the Southern Ocean at 42.4°S, 9.9°W on 20 September 2012 (Table 2.1). The glider continuously sampled for 5.5 months, descending to 1000 m depth with each dive taking approximately 4 to 5 hours to complete. The glider was equipped with the same sensors as glider SG579. The bio-optical sensors had a vertical resolution of 0.7 m in the top 100 m of surface ocean and then reduced vertical resolution to 1 m from 100 to 1000 m depth.

Label	Platform	Campaign	Date	Length	Variables
SG579	Ocean glider	BoBBLE	30.06.16	1 month	CTD, PAR, chl-a fluorescence, backscatter 470 nm and 700 nm
Float 629	Profiling float	BoBBLE	28.06.16	3 months	CTD, PAR, E_d at 380 nm, 490 nm, 555 nm
Float 630	Profiling float	BoBBLE	01.07.16	3 months	CTD, PAR, E_d at 380 nm, 490 nm, 555 nm
Float 631	Profiling float	BoBBLE	04.07.16	3 months	CTD, PAR, E_d at 380 nm, 490 nm, 555 nm
SG574	Ocean glider	SOSCEX	20.09.12	5.5 months	CTD, PAR, chl-a fluorescence, backscatter 470 nm and 700 nm

Table 2.1: Summary of ocean gliders and profiling floats deployed on the BoBBLE and SOSCEX campaigns including the date of deployment, mission length and oceanographic variables measured. Optical variable, E_d , is the downwelling irradiance.

2.3 Ocean glider depth correction

An ocean glider or profiling float continuously records the depth, time and location of an observation from all sensors. For ocean gliders the depth (or pressure) is recorded by the pressure sensor. A depth measurement reflects the depth of the pressure sensor and not the actual depth of the observation from the other sensors. Hence, a depth offset must be applied to find the actual depth of the observation. This depth offset depends on the variation of vertical distance between the pressure sensor and all other sensors. For profiling floats, this depth offset is considered to be negligible (Organelli et al., 2016).

The on-board instruments are placed on different parts of the glider. Most of the instruments are typically located at the aft and outer fairing of the glider. The pressure sensor is permanently located on the right side at the nose, positioned on the central axis of the glider (Fig. 2.1). If the glider were to lie horizontally in the water then PAR, dissolved oxygen and CTD sensor would be above the pressure sensor at a shallower depth relative to the recorded depth, compared with a WETLabs puck, which would be below the pressure sensor at a lower depth relative to the recorded depth. The depth offset between the

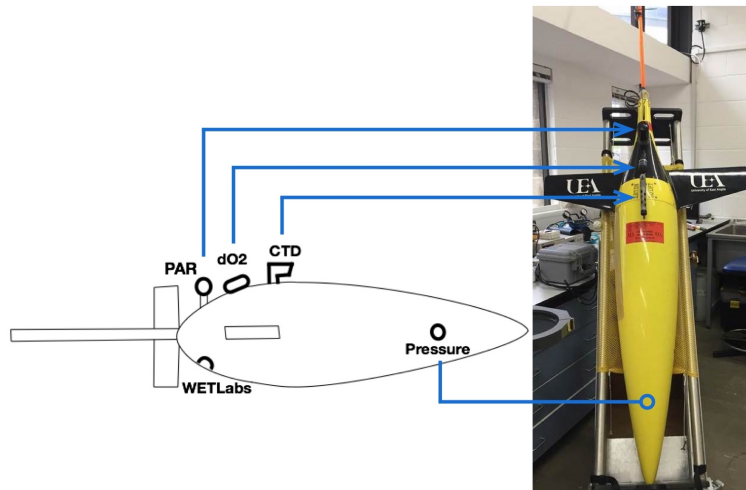


Figure 2.1: Position of individual sensors on SG579 including PAR, dissolved oxygen (dO₂), conductivity-temperature depth (CTD), WETLabs ECO Puck and pressure sensor.

pressure sensor and all other sensors on a horizontally positioned glider was calculated by measuring the horizontal and vertical dimensions between these sensors. We assume that these dimensions are fixed so the vertical distances between the central axis of the glider and all other sensors are constant on the glider.

The vertical distance between the pressure sensor and all other sensors varies with pitch angle. We can assume a glider is ascending through the water column at pitch angle Θ anticlockwise from the horizontal axis, x (Fig. 2.2). Any change to Θ varies the vertical distance between the horizontal x -axis of the pressure sensor and PAR sensor, labelled as a . To calculate a as a function of Θ , the position of the PAR sensor relative to the pressure sensor positioned on the glider have to be taken into account.

The required parameters and definitions to correct for pitch angle:

- d is the horizontal distance between a sensor and the pressure sensor on the glider, parallel to the glider central axis (bold dashed line).
- c is the vertical distance between a sensor and the pressure sensor on the glider, perpendicular to the glider central axis (bold dashed line).
- h is the shortest distance of separation between a sensor and the pressure sensor and is calculated using Pythagoras' theorem (Equation 2.1).

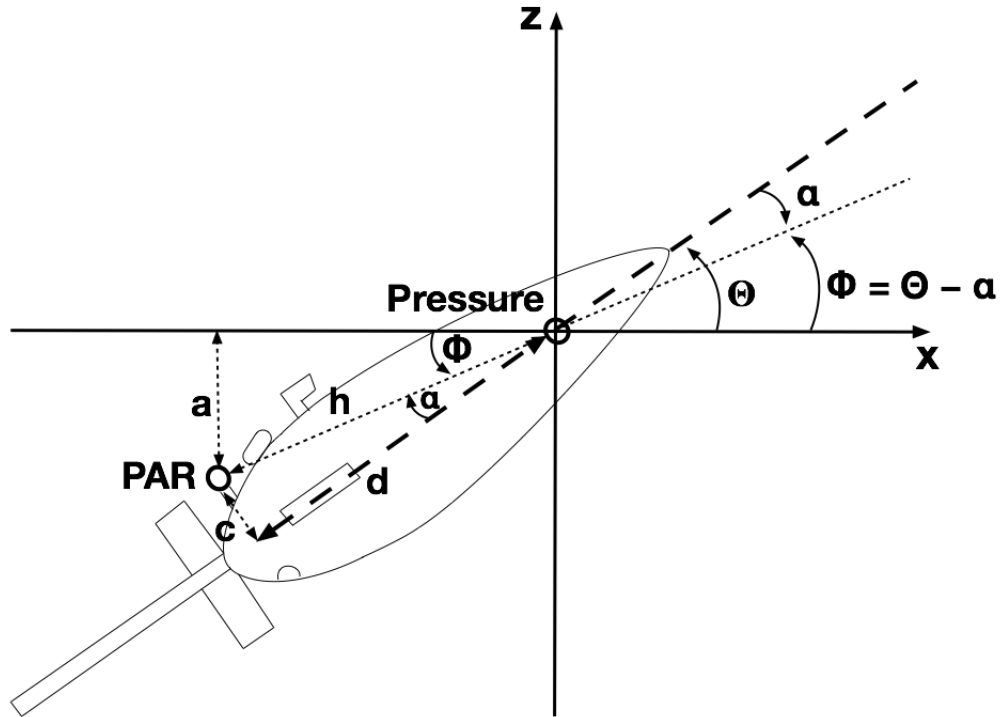


Figure 2.2: Ascending glider at pitch angle, Θ . The vertical distance, a , between the pressure and PAR sensor varies with Θ .

- α is the angle clockwise from the central axis of the glider between the pressure sensor and a sensor and is calculated from Equation 2.2.

$$h = \sqrt{c^2 + d^2} \quad (2.1)$$

$$\alpha = \arctan\left(\frac{c}{d}\right) \quad (2.2)$$

To correct for the fixed angle between the pressure sensor and a sensor on the glider (α) we define a new angle anticlockwise from the horizontal x -axis, Φ , to the line of shortest distance of separation between the pressure sensor and a sensor. The vertical distance, a , is calculated as a function of Θ :

$$a = h \sin(\Theta - \alpha). \quad (2.3)$$

For an ascending dive, Θ is positive as it rotates anticlockwise from the horizontal x -axis to the central axis of the glider (Fig. 2.2). The fixed angle,

α is negative as it rotates clockwise from the central axis of the glider to the line of the shortest distance of separation between the PAR and the pressure sensor. The resultant value of Φ remains positive, but smaller. The vertical distance between the PAR and the horizontal x -axis of the pressure sensor, a , will be positive. However, the PAR sensor is deeper than the pressure sensor, so the change of height must be negative. To ensure that the height of the PAR sensor, z_{PAR} , is less than the height, z , of the pressure sensor then:

$$z_{PAR} = z - a = z - h \sin(\Theta - \alpha). \quad (2.4)$$

A PAR profile from dive 84 from glider SG579 ascends to the surface with a positive pitch angle, Θ , and a -0.2 m change in height in the PAR measurements (Fig. 2.3a). The glider completes a surface manoeuvre at 0.8 m depth by pitching the nose down, inflating the oil bladder and rising the antenna out of the water. The change in height for the PAR measurements was 0.3 m. The glider starts to descend by deflating the oil bladder and pitching the nose down close to vertical (Fig. 2.3b). The maximum change in height between the PAR and pressure sensor was 0.8 m.

The accuracy of the PAR measurement height is improved after applying the pitch angle offset. It is important that the PAR measurement height at the near-surface is corrected as visible radiation is rapidly attenuated with depth in this region. The majority of red wavelengths of visible radiation are absorbed at a depth of ~ 1 m, which is comparable to the maximum change in height between the PAR and pressure sensor. Hence, correcting PAR measurement heights at the near-surface would ensure that the optical parameters for the attenuation of red wavelengths are accurately determined when fitting a two-band solar radiation function to PAR profiles.

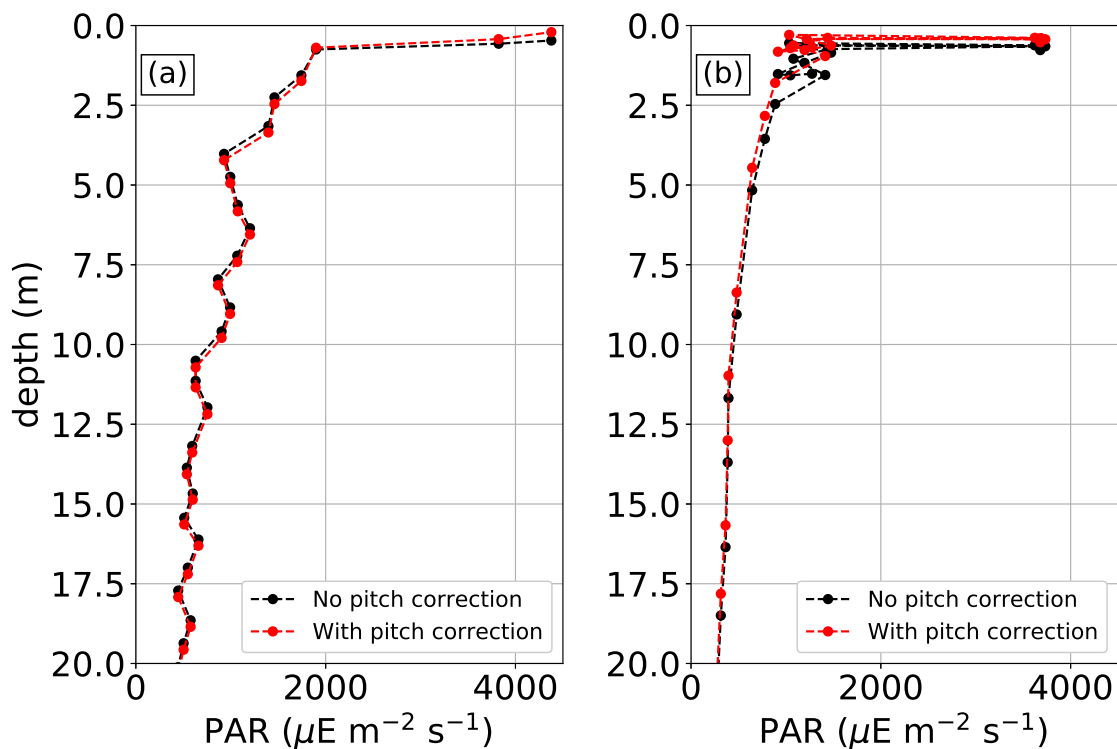


Figure 2.3: PAR profiles from dive 84 measured from SG579 during the BoBBLE campaign: (a) ascending dive 84 with no pitch correction (black dashed line and dots) and with pitch correction (red dashed line and dots); (b) descending dive 84 with no pitch correction (black dashed line and dots) and with pitch correction (red dashed line and dots).

2.4 Backscatter data processing

The backscatter measurements provide a proxy of the amount of organic and inorganic material that is suspended at a certain depth (Stramski et al., 2004). The backscatter sensor transmits visible light at two wavelengths ($\lambda = 470 \text{ nm}$ and $\lambda = 700 \text{ nm}$) and measures the returned backscattered light from suspended material in the water as a raw voltage (Fig. 2.4a). GliderTools, a Python toolbox package used to clean, calibrate and convert raw glider data was used to process the raw backscatter dataset (Gregor et al., 2019). The toolbox was used to remove profiles of raw backscatter that displayed non-physical features such as anomalously high voltage counts (Fig. 2.4b). Raw backscatter profiles were removed if the median raw backscatter for a profile was larger than one standard deviation (+1 SD) of the median raw backscatter of all the profiles. The median raw backscatter of all the profiles was calculated below a reference depth. The reference depth was defined as the average maximum depth of

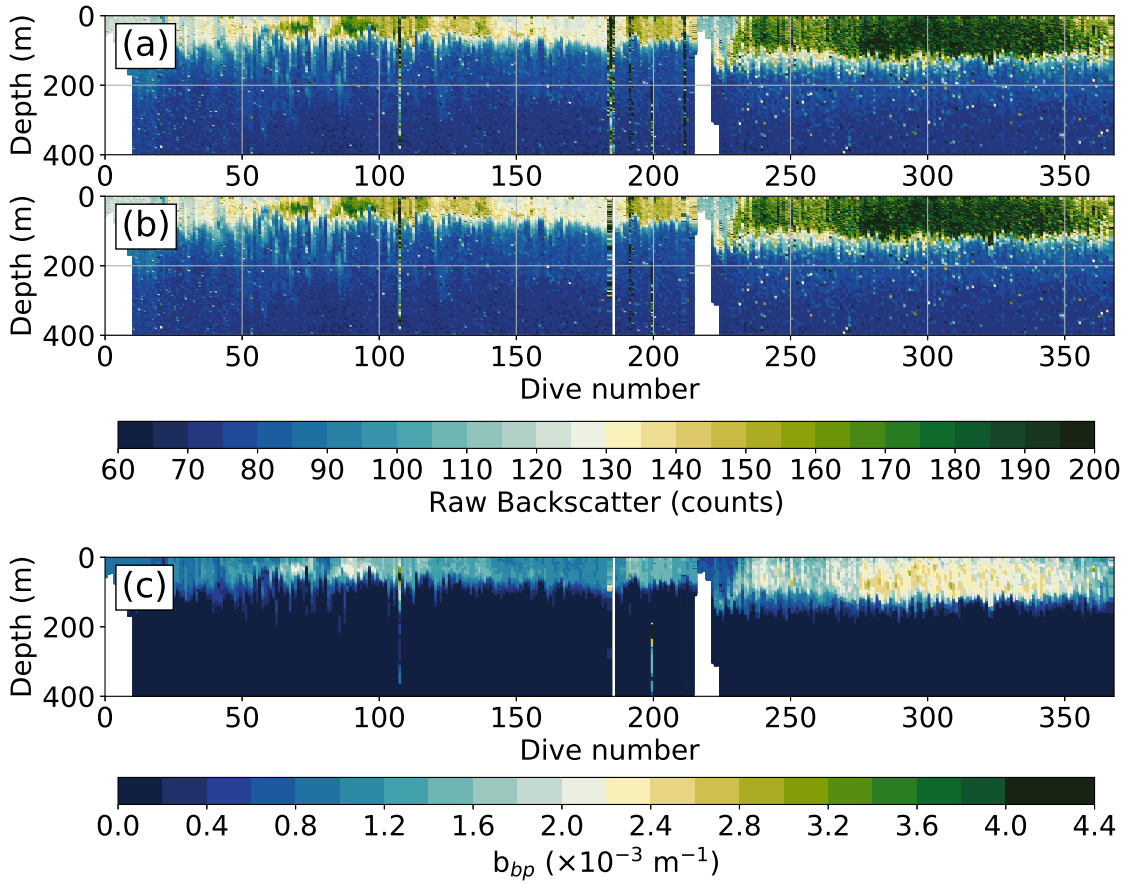


Figure 2.4: Example of backscatter at 700 nm quality control from glider SG574 from the SOSCEX campaign: (a) raw voltage counts before bad profiles are masked; (b) raw voltage counts after bad profiles are masked (masked profiles are white); (c) particulate backscatter at 700 nm ($b_{bp}(700 \text{ nm})$) after spikes are masked.

the raw backscatter profiles, which was then multiplied by three to ensure the reference depth was deep enough to avoid the sun-lit, biologically productive surface layers.

The raw backscatter voltages were converted into a volume scattering function, β , by subtracting the manufacturer's dark count and multiplying by the manufacturer's scale factor. The volume scattering function ($\text{m}^{-1} \text{sr}^{-1}$ where sr is the symbol for Steradian) was converted into particulate backscatter, b_{bp} (m^{-1}), using the following expression

$$b_{pb} = 2\pi\chi_p(\beta - \beta_{sw}) = 2\pi\chi_p\beta_p \quad (2.5)$$

where β_p is the particulate volume scattering function and is defined as the difference between the measured volume scattering function (β) and the volume

scattering function of pure sea water (β_{sw}), which depends on the salinity, temperature and scattering angle of the wavelength of light transmitted by the backscatter sensor. The value of β_{sw} was estimated using a scattering seawater model (Zhang and Hu, 2009). The conversion factor, χ_p , converts the β_p into b_{bp} . Given the backscatter sensor has a scattering angle of 124° , χ_p was equal to 1.2 (Boss and Pegau, 2001; Chami et al., 2006).

Particulate backscatter at 700 nm ($b_{bp}(700 \text{ nm})$) was used to correct daytime surface fluorescence quenching, which meant $b_{bp}(700 \text{ nm})$ spikes had to be masked to avoid contaminating the derived daytime surface fluorescence data. In the GliderTools toolbox, particulate backscatter spikes were identified and removed using a despiking method from Briggs et al. (2011). This method used a 7-point rolling minimum and maximum median filter that removed large spikes and also the smaller instrument noise (Fig. 2.4c). In regions where the upper ocean becomes increasingly more biologically productive (0 to 120 m depth between dive 280 to 350; Fig. 2.4c), then the larger the size of the particle aggregates of phytoplankton and detrital material that descend out the mixed layer. These large particles are recorded as large spikes, as they scatter a large signal to the glider backscatter sensor (Briggs et al., 2011). The backscatter quality control method presented here was applied to the backscatter datasets from the BoBBLE and SOSCEX glider deployments.

2.5 Chlorophyll-a fluorescence data processing

The fluorometer on the gliders measured chlorophyll-a concentration. The fluorometer emits blue light at a wavelength of 470 nm that is absorbed by chlorophyll-a pigments. By absorbing this particular wavelength the chlorophyll-a fluoresces light back to the fluorometer, which is then measured. The larger the amount of fluorescence measured by the fluorometer, the higher the concentration of chlorophyll-a. The fluorescence signal is approximately linearly proportional to the chlorophyll-a concentration (Xing et al., 2011). However, the amount of fluorescence per unit chlorophyll-a does vary with phytoplankton composition, physiological state and ambient light levels (Fennel and Boss, 2003), hence, the derived chlorophyll-a concentration should be appreciated as an approximation of actual chlorophyll-a concentration.

Profiles of raw fluorescence displaying non-physical features, such as anomalously high voltage counts throughout a profile were removed using

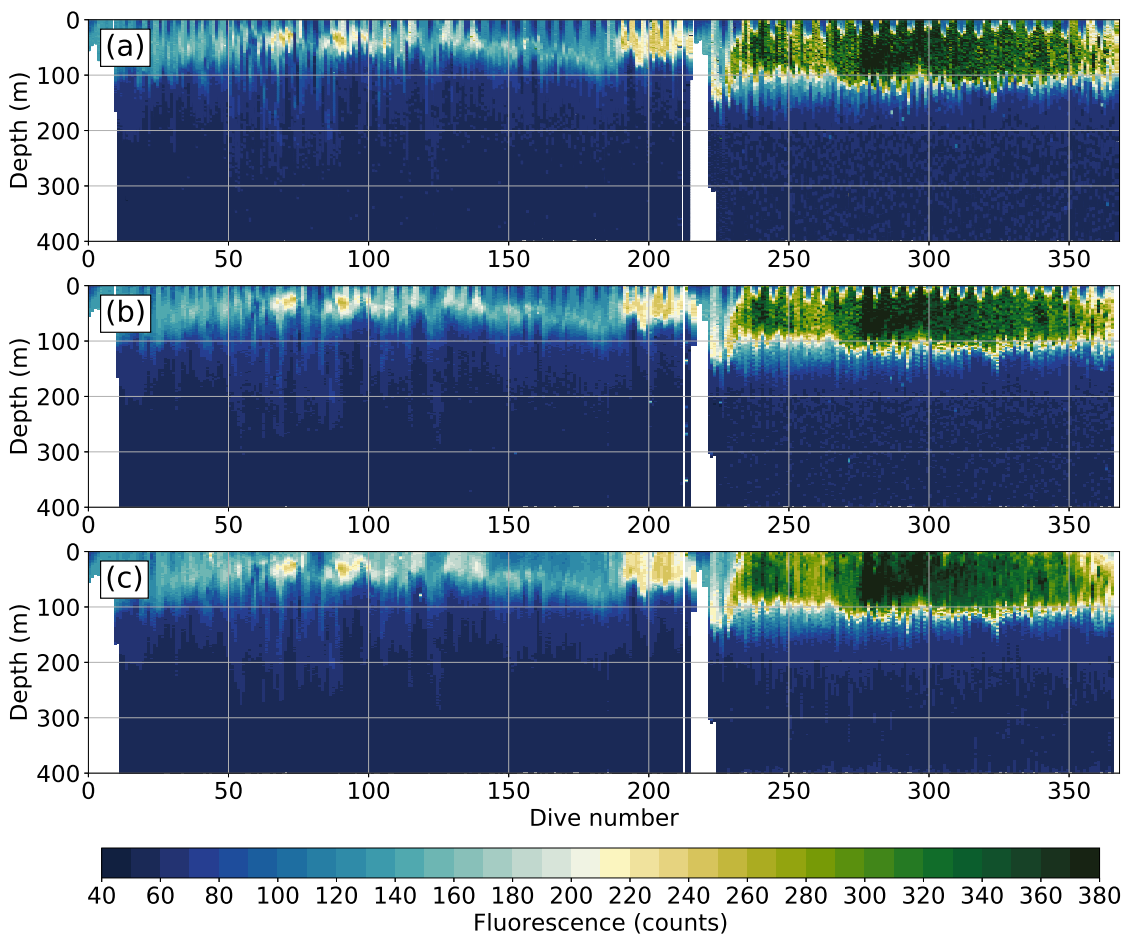


Figure 2.5: Example of fluorescence quality control from glider SG574 from the SOSCEX campaign: (a) raw fluorescence after bad profiles are masked (masked profiles are white); (b) raw fluorescence after spikes are masked; (c) raw fluorescence after quenching correction.

the same GliderTools processing as the raw backscatter profiles (Fig. 2.5a). Spikes were a common occurrence in the raw fluorescence dataset, particularly in regions of high biological productivity. GliderTools uses the method of Thomalla et al. (2018) to mask raw fluorescence spikes by using a 7-point rolling mean and subtracting this rolling mean profile from each profile to highlight the raw fluorescence perturbations. The perturbations were flagged if they were larger than +3 SD of all perturbations. Gaps were linearly interpolated and the data were smoothed using a 7-point rolling mean Hanning window. The upper ocean, above 100 m depth, had the highest concentration of removed fluorescence spikes, whereas regions below 100 m had limited fluorescence spiking (Fig. 2.5b).

When ambient light levels are too high, phytoplankton initiate a

non-photochemical quenching mechanism to reduce harmful photooxidative damage (Muller, 2001), resulting in suppressed fluorescence emission at the surface during the daytime. Fig. 2.6a shows a vertical profile of chlorophyll-a from glider SG574 during the nighttime (dive 32; black dots) and during the daytime (dive 33; red dots). The daytime profile shows a decrease in fluorescence from 35 m to the surface, whereas the nighttime profile shows relatively uniform fluorescence over the same depth. The profiles of $b_{pb}(700\text{ nm})$ during the daytime and nighttime were the same between 35 m and the surface, indicating uniform phytoplankton amount in the surface layer (Fig. 2.6b), which was not apparent in the daytime fluorescence profile (Fig. 2.6a). The b_{pb} provides a proxy of phytoplankton biomass amount, measuring the scattered light from biological material suspended in the water. Thus, b_{pb} measurements are not prone to non-photochemical quenching and can be used to identify quenching characteristics in the daytime fluorescence profiles. Hence, the decrease of fluorescence during the daytime was indicative of non-photochemical quenching.

GliderTools uses the method of Thomalla et al. (2018) to correct for daytime quenching. This method uses average nighttime profiles of fluorescence and $b_{pb}(700\text{ nm})$. The nighttime profiles were identified as the dives that occurred after sunset and before sunrise and were averaged to make one fluorescence profile for each night. The difference between the average nighttime fluorescence profile and the daytime fluorescence profile highlights the change in fluorescence at the surface caused by quenching (fig 2.6c; solid black line). The quenching depth, the deepest depth where daytime profiles begin to quench, was defined as the point of the shallowest minimum difference of the average nighttime fluorescence and the daytime fluorescence above a euphotic depth of 100 m, where light is $\sim 1\%$ of that at the surface. This shallowest minimum difference point was calculated by finding the steepest gradient (fig 2.6c; dashed green line) between the five minimum absolute fluorescence differences near the zero difference line (fig 2.6c; red dot) to the maximum fluorescence difference at the surface (top 5 m depth) (fig 2.6c; green dot). The daytime $b_{pb}(700\text{ nm})$ was then multiplied by the preceding average nighttime fluorescence to $b_{pb}(700\text{ nm})$ ratio ($Fl:b_{pb}$) from the quenching depth up to the surface. Fig. 2.6d shows the preceding average nighttime $Fl:b_{pb}$ profile (black dots) and the daytime $Fl:b_{pb}$ profile (red dots). The night time $Fl:b_{pb}$ profile remains relatively uniform above the quenching depth compared with the daytime $Fl:b_{pb}$ profile. Fig. 2.6e shows the final corrected fluorescence profile

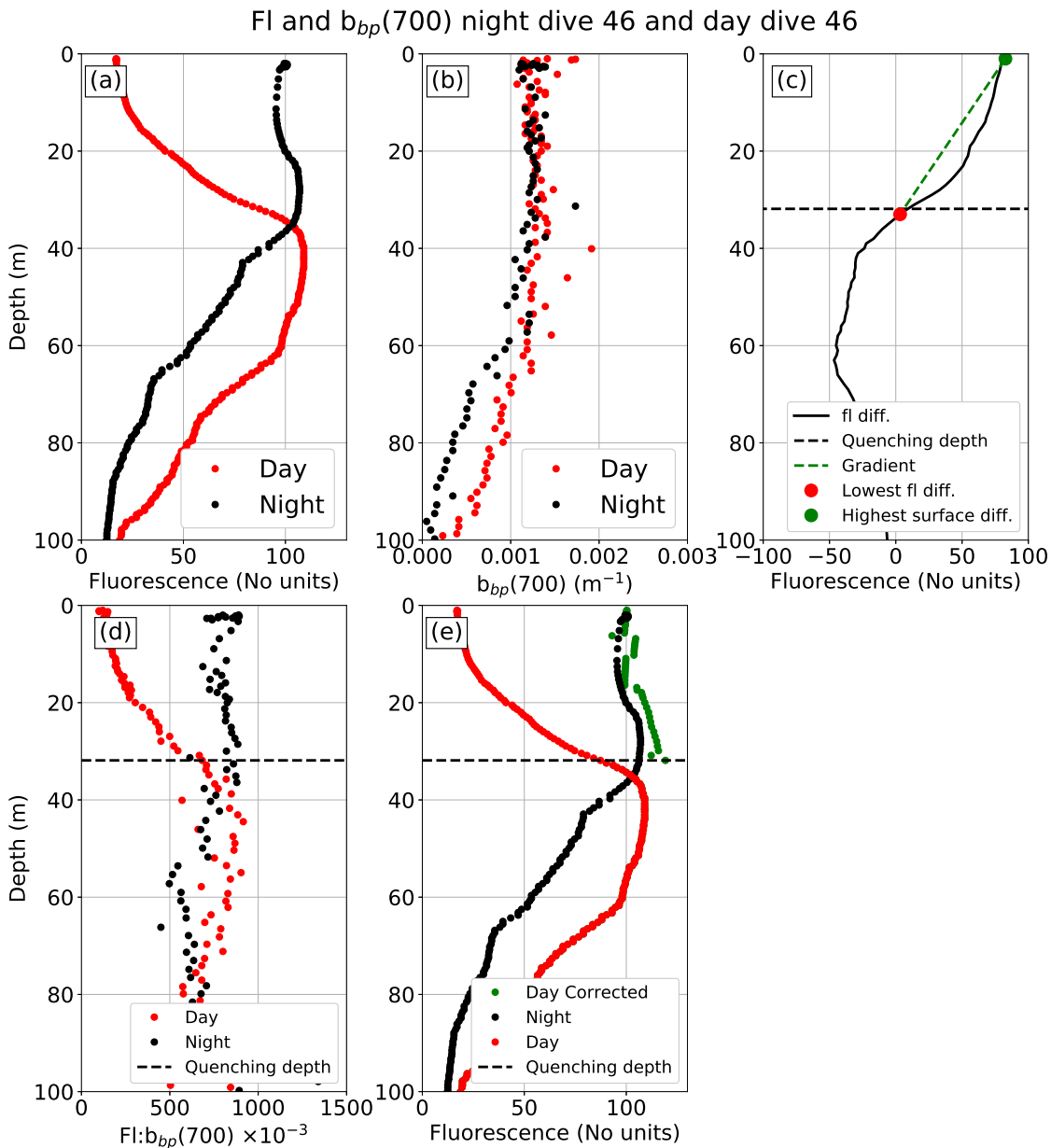


Figure 2.6: Example of quenching correction method using dive 32 (nighttime) and 33 (daytime) from glider SG574 from the SOSCEX campaign: (a) Profile of fluorescence during the nighttime (black dots) and daytime (red dots); (b) Profile of $b_{pb}(700 \text{ nm})$ during the nighttime (black dots) and daytime (red dots); (c) The difference between average nighttime fluorescence and daytime fluorescence (solid black line) with steepest gradient (dashed green line) between maximum surface fluorescence (green dot) and shallowest minimum fluorescence (red dot) to calculate quenching depth (dashed black line); (d) Average nighttime (black dots) and daytime (red dots) $Fl:b_{pb}$; (e) Quenched daytime (red dots) and quench-corrected daytime (green dots) profile of fluorescence.

from the quenching depth up to the surface (green dots).

After applying the Thomalla et al. (2018) quenching correction method, there was improvement to the daytime fluorescence profiles with an increase in fluorescence counts in the top 20 m (Fig. 2.5c). The method assumes there is no change between the nighttime and daytime $Fl:b_{pb}$ profiles and the vertical distribution of phytoplankton, but the glider may have intercepted a region with varying turbidity during the nighttime relative to the daytime introducing errors to the $Fl:b_{pb}$ profiles. Furthermore, the method does not include the changes to the chlorophyll-to-carbon ratio (the relationship between chlorophyll concentration and phytoplankton biomass), which can vary with depth and time (Mignot et al., 2014). Regardless of the drawbacks, this quenching correction method was applied to the fluorescence datasets from the BoBBLE and SOSCEX glider deployments.

2.6 PAR quality control and optical parameter determination

2.6.1 Factors that affect optical parameter determination

The gliders and floats from the BoBBLE and SOSCEX campaigns measured PAR (Table 2.1). As discussed in Chapter 1, longer visible wavelengths (red light) are quickly absorbed in the the first few metres of the upper ocean, whereas shorter wavelengths (blue light) penetrate deeper into the water column. The preferential absorption of PAR through the water column can be represented by a double exponential function, similar to Equation 1.2 from Paulson and Simpson (1977):

$$Q(z) = q_1 e^{-\frac{z}{h_1}} + q_2 e^{-\frac{z}{h_2}} + d \quad (2.6)$$

where $Q(z)$ is the PAR at depth z ; q_1 and q_2 are the surface PAR for red and blue light, respectively; h_1 and h_2 represent the scale depths of red and blue light, respectively; d has been introduced to allow for a non-zero instrument response when there is zero radiation flux applied to the PAR sensor, and in practice, d is very small ($\sim 10^4$). The scale depth of blue light, h_2 , which modulates the radiant heating rate of the mixed layer, is determined by fitting Equation 2.6 to observed PAR profiles from the gliders and floats.

The raw PAR voltages were factory calibrated and converted into PAR with units $\mu\text{E m}^{-2} \text{s}^{-1}$. Large, non-physical spikes were removed from the PAR datasets. Individual profiles of PAR were then corrected for their mean in situ dark count by using PAR measurements from below 200 m. The dark count is the background voltage count measured by the PAR sensor when there is no sun light. At depths of 200 m the dark count can be safely quantified as there is no sun light at these depths (Organelli et al., 2016).

The PAR profiles measured from the floats and gliders at this stage in the processing often varied in shape and magnitude. All profiles displayed spikes or perturbations that were caused by external environmental factors. These perturbations were found to affect optical parameter determination when fitting the double exponential function. It was vital that a universal quality control method for identifying and removing perturbations from profiles was established in order to improve optical parameter determination. However, these PAR profile perturbations were found to vary between gliders and floats. The different types of perturbations that affected glider and float PAR profiles are outlined below.

Glider PAR profiles vary in shape and magnitude as gliders surface at different times of the day. Conversely, float PAR profiles were more consistent in shape and magnitude as they were programmed to surface at around midday. It was found that low-light glider PAR profiles worsened the fit of the double exponential function, which affected the determined optical parameters. Section 2.6.2 demonstrates how low-light PAR profiles affected determined optical parameters and what conditions were used to remove low-light PAR profiles.

PAR profiles measured from the floats and gliders displayed cloud spikes. Clouds passing above the ocean surface perturb the in-water light field by temporarily reducing the light intensity and PAR (Xing et al., 2011). Cloud spikes range in size due to the varying optical thickness and speeds of the passing clouds (fig. 2.7a). Cloud spikes become less obvious with depth as light levels rapidly decrease. These cloud spikes must be identified and removed before optical parameter determination.

PAR profiles measured from the floats and gliders displayed wave-focusing perturbations. Wave-focusing can create zig-zag spiking in the vertical PAR profiles as the waves focus and de-focus the in-water light field as they pass over the sensor (Zaneveld et al., 2001). Wave-focusing perturbations predominately affected the PAR signal in the top few metres for nearly all PAR profiles (Fig.

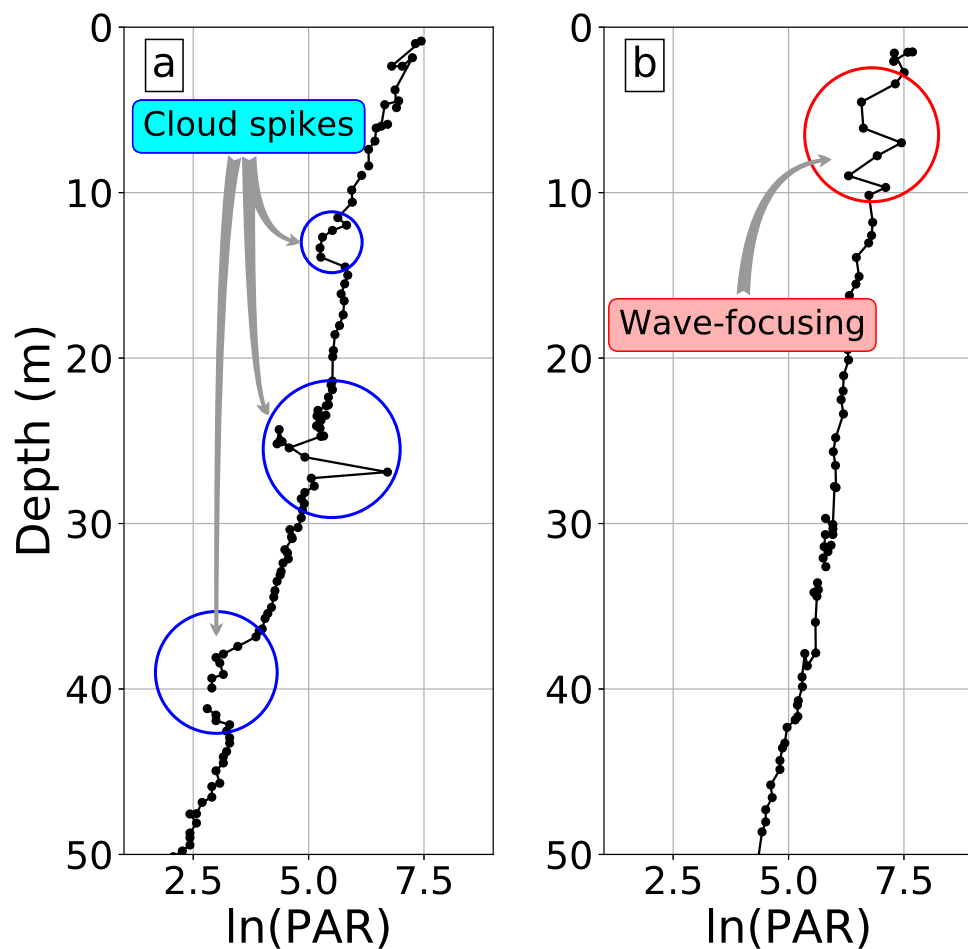


Figure 2.7: Examples of cloud spikes and wave-focusing spikes from two ln(PAR) profiles measured from glider SG579 during the BoBBLE deployment; (a) Cloud spikes in ascending dive 12; (b) Wave-focusing spikes in ascending dive 77.

2.7b). As with cloud spikes, the wave-focusing features become less obvious with depth, as light levels rapidly decrease. Even waves of small amplitude (~ 0.1 m) still have a significant effect on measured light levels (Zaneveld et al., 2001).

Ideal PAR profiles were only attainable if in-water light levels remained constant. This meant sky conditions had to be clear or overcast with calm sea surface conditions. In reality, observed PAR profiles in the top 5 m displayed excessive noise caused by cloud and wave-focusing perturbations. Section 2.6.3 demonstrates why PAR measurements in the top 5 m were removed. Section 2.6.5 outlines an adapted quality control method used to identify cloud and wave-focusing perturbations below 5 m.

The gliders continuously adjust their roll and pitch angle as they ascend and

descend through the water column, unlike floats which ascend at a constant upright position through the water column. Roll and pitch angle variations of ocean gliders have been found to cause perturbations to radiometric measurements (Hemsley et al., 2015). In this thesis, glider roll and pitch angle variations were unlikely to cause PAR perturbations (see Appendix A). The largest changes to pitch angle were found to occur between the surface and 5 m depth, as the glider performs a surface manoeuvre. This is also the depth where the largest PAR perturbations were observed. However, clouds and wave-focusing were found to be the most likely cause of large PAR perturbations. Thus, the tilt of the glider and the tilt of the PAR sensor, or the sudden change in roll and pitch angle, were unlikely to contribute to the perturbations of PAR.

2.6.2 Nighttime and low-light PAR profiles

Initial fitting of Equation 2.6 to glider PAR profiles that were subject to low-light conditions resulted in optical parameters q_1 , q_2 , h_1 and h_2 being poorly resolved with large uncertainties. Ascending PAR profile 31 from glider SG579, deployed during BoBBLE campaign, surfaced at a local time of 6:33 in the morning, when PAR levels just below the surface were around $6 \mu\text{E m}^{-2} \text{s}^{-1}$ (Fig. 2.8a). The fitted function determined the value of $h_1 = 0.2 \pm 0.7$ m and the value of $h_2 = 7.0 \pm 6.5$ m (uncertainty based on 1 SD error of fitted function). The scale depth of blue light of 7 m implies that surface chlorophyll concentrations should be higher than approximately 2 mg m^{-3} , indicative of Jerlov water type III (Morel, 1988), when instead observed average chlorophyll concentrations were only 0.3 mg m^{-3} . Furthermore, the uncertainties of determined h_2 from low-light PAR profiles based on the fitted function were very large (often double the size of determined h_2). PAR profiles in low-light conditions were therefore susceptible to inaccurate scale depth determinations with large uncertainties.

Nighttime and low-light PAR profiles were removed using two conditions. First, if the local zenith angle was greater than 70° then PAR profiles were removed. This removed all nighttime PAR profiles, but some low-light PAR profiles still remained, possibly caused by overcast conditions during the daytime. Hence, the second condition removed profiles where maximum PAR in the top 5 m was less than $100 \mu\text{E m}^{-2} \text{s}^{-1}$. For all the glider SG579 PAR profiles, 45% were removed using the first condition. A further 12% of low-light profiles were removed using the second condition (Fig. 2.8c). Values of h_2

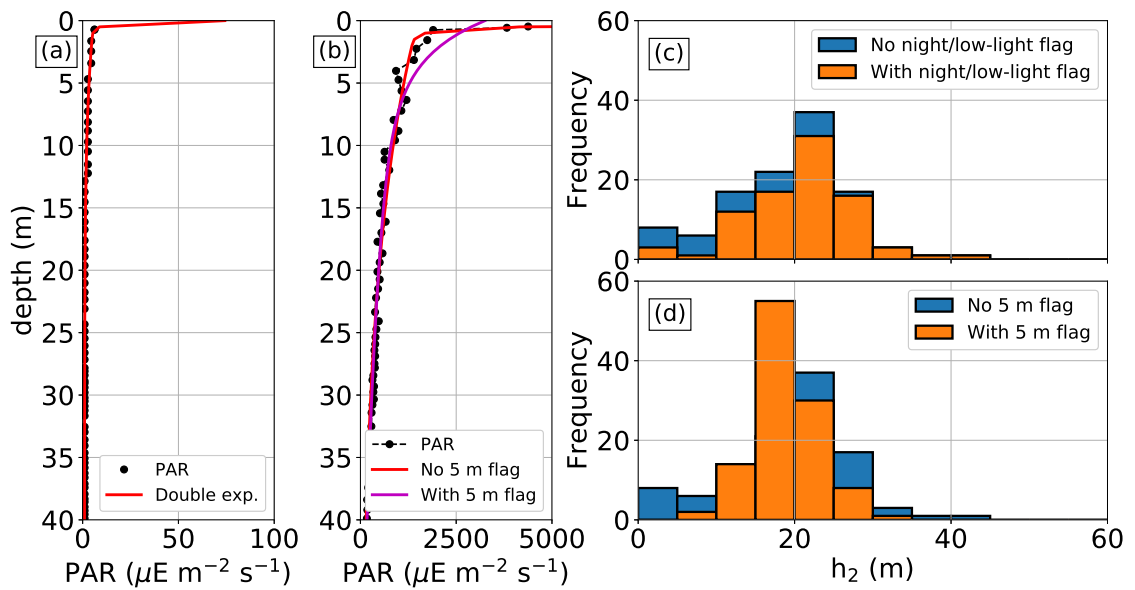


Figure 2.8: Example of a low-light and a near-surface perturbation PAR profile from glider SG579 during the BoBBLE deployment that were fitted with Equation 2.6; (a) Ascending dive 31 exhibiting low-light conditions and fitted function (red line); (b) Ascending dive 84 exhibiting wave-focusing in the top 5 m and fitted function with (magenta line) and without (red line) flagging the top 5 m; (c) Histogram of determined h_2 from all PAR profiles from SG579 with (orange bars) and without (blue bars) nighttime and low-light flagging; (d) Histogram of determined h_2 from all PAR profiles from SG579 with (orange bars) and without (blue bars) top 5 m flagging.

that were determined below 10 m and associated with very large uncertainty were reduced, as low-light profiles were discarded. Lotliker et al. (2016) also found similar variability in measured PAR in the BoB. They applied a local time threshold between 10:00 and 14:00, which approximately equals a local zenith angle threshold of 65° , similar to the threshold in this methodology.

2.6.3 Near-surface PAR perturbation flagging

Initial fitting of Equation 2.6 to glider and float PAR profiles with large surface noise resulted in poorly resolved optical parameters. Ascending PAR profile 84 from glider SG579, deployed during BoBBLE campaign, shows fluctuating PAR measurements at 5 m depth (dashed black line; Fig. 2.8b). There is a large increase in PAR from 1900 to 4400 $\mu\text{E m}^{-2} \text{s}^{-1}$ at 0.5 m depth that was caused by wave-focusing at the surface. The fitted function is unable to resolve the absorption of red light at the surface, as shown by the curve's sharp "elbow" at the near-surface and the overestimation of surface PAR of over

20,000 $\mu\text{E m}^{-2} \text{s}^{-1}$ (red line; Fig. 2.8b). Flagging the top 5 m and fitting the curve a second time removes the curve's sharp elbow and the overestimation of surface PAR (magenta line; Fig. 2.8b).

Flagging the top 5 m improves the fit of the function to the deeper, more robust part of the profile where there is less perturbation. Before and after the 5 m flag, the values of h_1 increased from 2.2 ± 0.2 m to 3.0 ± 1.0 m and the values of h_2 increased from 18 ± 1.2 m to 28.9 ± 4.1 m (Fig. 2.8b). The increase in h_1 and h_2 after the 5 m PAR flag demonstrated the effect that near-surface PAR perturbations had on determined optical parameters of red and blue light. If there were unrealistic determinations of red light optical parameters then this caused unrealistic determinations of blue light optical parameters. After applying the 5 m flag to all PAR profiles from SG579, the distribution of h_2 was skewed to lower values with a peak in the 15–20 m bin (Fig. 2.8d). There was also reduced spread in the h_2 distribution as marginal h_2 values above 30 m and below 10 m were corrected to values grouped in the 15–20 m bin, which better represented the average scale depth given that observed average chlorophyll concentrations were around 0.2 mg m^{-3} .

Previous studies have also implemented similar near-surface flagging thresholds of PAR or solar irradiance measurements. Xing et al. (2011) removed $E_d(490)$ data from the surface down to an optical depth of 0.69 by fitting a single exponential function to measured irradiance profiles. An optical depth of 0.69 is defined as the downward irradiance at a specific depth, $E_d(z)$, that is around 50% less than the irradiance at the surface, $E_d(0)$ ($E_d(z) = E_d(0)e^{-0.69z}$). Xing et al. (2011) used this depth threshold after identifying that near-surface irradiance measurements displayed large perturbations that affected determined $K_d(490)$ values, which were used to calibrate chlorophyll-a fluorescence data. Ohlmann et al. (1998) removed measured solar irradiance data from the surface down to 10 m due to potential perturbation and to determine the scale depth of the deeper penetrating blue light. Conversely, Lotliker et al. (2016) did not apply a depth threshold to measured in situ solar irradiance profiles, as they produced a daily average profile of solar irradiance, which smoothed out large perturbations at the near-surface. Hence, the purposes of applying a flagged depth threshold, as shown from previous studies, is to remove large perturbations that affect optical parameters.

With no PAR data in the top 5 m or surface PAR incident at the ocean surface, we were unable to accurately determine the absorption of red light and optical parameters q_1 , q_2 and h_1 . The next subsection (Section 2.6.4) outlines how the

absorption of red light was represented after flagging the top 5 m of PAR data and also minimising the influence that red light optical parameters have on determined h_2 .

2.6.4 Adaptation of the two-band solar absorption scheme

A pragmatic solution to represent the absorption of red light at the near-surface, yet fit to the robust part of the profile below the near-surface, was achieved by externally specifying optical parameters of red light from Paulson and Simpson (1977) and determining unknown optical parameters of blue light below a fixed depth, D . The fixed depth, D , had to be much greater than h_1 to reduce the effect that red light optical parameters had on the blue light optical parameters. A fixed depth of 5 m satisfied this requirement as h_1 is typically ~ 1 m. Paulson and Simpson (1977) defined optical parameter, R , as the ratio of the red light to the total visible light spectrum,

$$R = \frac{q_1}{q_1 + q_2}. \quad (2.7)$$

Rearranging 2.7 and substituting into Equation 2.6,

$$Q(z) = q_2 \left[\left(\frac{R}{1-R} \right) e^{-\frac{z}{h_1}} + e^{-\frac{z}{h_2}} \right] + d \quad (2.8)$$

hence, Equation 2.8 can be fitted to PAR profiles from below $D = 5$ m, resolving optical parameters of blue light such as q_2 and h_2 . The constant d is still represented as an offset. Average values of h_2 from glider SG579 were around 17 m (Fig. 2.8d), meaning the southern BoB can be classified as water type IB. Values of R and h_1 of this water type from Paulson and Simpson (1977) were used to replicate red light absorption at the near-surface. R and h_1 were equal to 0.67 and 1 m for water type IB, respectively. We can further demonstrate $D \ll h_1$ and show that Equation 2.8 can be simplified by substituting R and h_1 into the first exponential term inside the square bracket at a depth $z = 5$ m. The first exponential term becomes $2.030e^{-z/1.0} \approx 0.014$ and the second term is $e^{-z/17} \approx 0.745$, if h_2 is ~ 17 m. Hence

$$\left(\frac{R}{1-R} \right) e^{-z/1.0} \ll e^{-z/17}.$$

Therefore, Equation 2.8 below 5 m simplifies to a single exponential

$$Q(z) = q_2 e^{-\frac{z}{h_2}} + d. \quad (2.9)$$

Equations 2.8 and 2.9 are shown to be the same when $D \ll h_1$. To test if the flagged depth, D , and the chosen R and h_1 optical parameters influence determined h_2 , Equation 2.8 was individually fitted to all the PAR profiles from glider SG579 and D , R and h_1 were varied separately: (i) D varied between 0–10 m; (ii) h_1 varied within the Jerlov water type range; (iii) R varied within the Jerlov water type range. The nighttime and low-light dive thresholds were applied to all PAR profiles. Furthermore, the profiles were split into ascending and descending profiles to investigate whether there is a difference in determined h_2 depending on the vertical direction of the glider.

Values of h_2 varied more when PAR measurements at depths less than 3 m were flagged (Fig. 2.9a and 2.9d). This variation in the top 3 m was slightly larger for descending profiles compared with ascending profiles, as shown by the average h_2 fluctuating between 20 to 23 m for descending profiles (dashed black line; Fig. 2.9d). Descending profiles had lower vertical resolutions than ascending profiles, due to the descents being faster than the ascents. With fewer near-surface PAR measurements on descending profiles then the poorer the determination of h_2 when fitting Equation 2.8 (see Section 2.6.5 for further discussion; Fig. 2.14a and 2.14b). Flagging PAR measurements below 3 m depth had a small effect on determined h_2 , as values remained constant at 19 to 20 m. Some individual profiles show large variations of h_2 between flagged depths of 3 to 10 m. However, this is mostly due to cloud spikes, which have not been removed, adding uncertainty to the determined h_2 values.

Fitting Equation 2.8 with values of h_1 from the Jerlov water types has a small effect on the values of h_2 (Fig. 2.9b and 2.9e). Smaller values of h_1 , corresponding to the clearest water types (I, IA and IB), do not change h_2 . Some variation to h_2 occurs between water type IB to III, as h_2 increases by ~ 0.8 m when h_1 increases from 1 to 1.5 m for both ascending and descending profiles. Fitting Equation 2.8 with values of R from the Jerlov water types has a very small effect on the values of h_2 (Fig. 2.9c and 2.9f). Increasing the water type from I to III increases h_2 less than ~ 0.1 m for both ascending and descending profiles. Optical parameter R and h_1 , thus have the smallest influence on derived values of h_2 compared with flagged depth, D , showing that Equation 2.8 reduces the influence of determined R and h_1 on determined h_2 .

The overall uncertainty of determined h_2 is a combination of the ± 1 SD

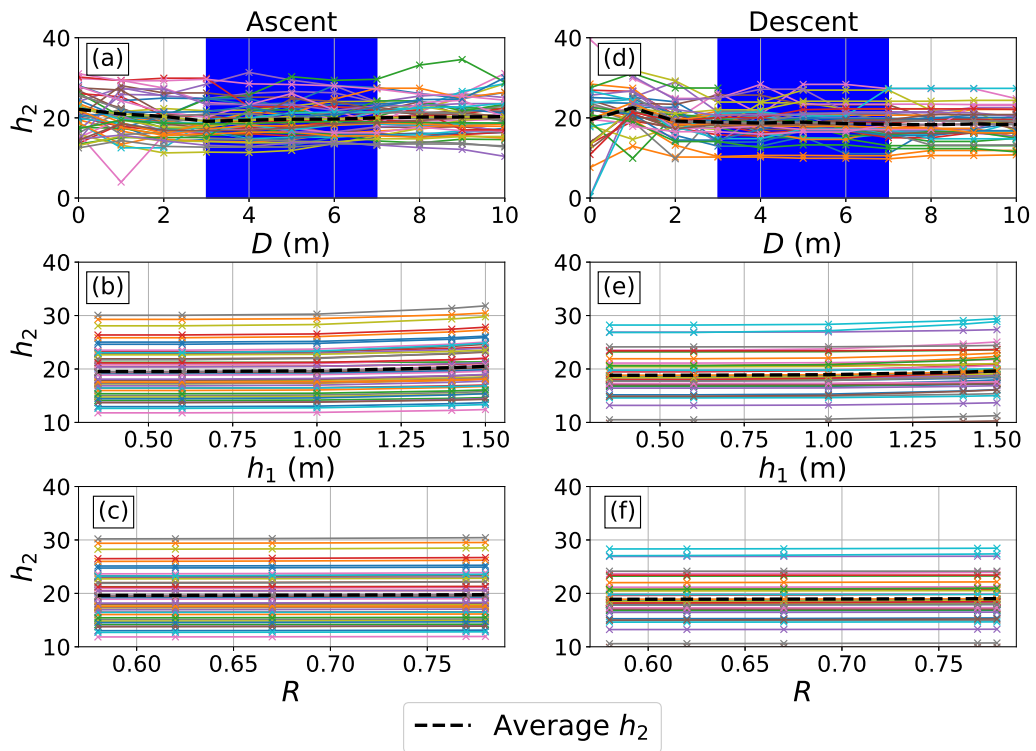


Figure 2.9: h_2 values after fitting Equation 2.8 to all ascending PAR profiles from SG579 with: (a) varying flagged depth, D , from 0 – 10 m depth; (b) varying h_1 within the Jerlov water type range I to III; (c) varying R within the Jerlov water type range I to III; (d–f) as in (a–c) but for all descending PAR profiles.

uncertainty from fitting Equation 2.8, and the uncertainty of chosen parameters R , h_1 and D between a depth of 3–7 m (blue shaded region; Fig. 2.9a and 2.9d). The maximum and minimum uncertainty is chosen out of the four uncertainties to represent the upper and lower uncertainty bounds of each determined h_2 value.

There are drawbacks to using the Jerlov water type optical parameters from Paulson and Simpson (1977) in representing the absorption of red wavelengths at the near-surface. Ohlmann et al. (1998) and Ohlmann (2003) found that h_1 and R from Paulson and Simpson (1977) are poorly approximated. The poor approximation is due to the low-resolution in-water irradiance profiles used. These profiles displayed large wave-focusing perturbations in the top 10 m, meaning the determined optical parameters for red wavelengths are subject to some uncertainty and inaccuracy. However, we have shown that h_1 and R values from the water types constrains the double exponential function to fit to the more robust PAR profile below 5 m and had a small influence on determined h_2 (<0.8 m). As long as h_1 is much smaller than D , then determined h_2 is not

affected.

2.6.5 Further PAR perturbation flagging

The fit of Equation 2.8 and determined h_2 were still influenced by PAR perturbations below 5 m depth. In order to identify perturbations below 5 m for all float and glider PAR profiles, an adapted quality-control method using a fourth-degree polynomial was used from Organelli et al. (2016). Developed to process near-real time radiometric profiles measured by Bio-Argo floats, the method is chosen for its ability to identify cloud spikes, wave-focusing spikes and other perturbations on PAR and irradiance profiles. The method can be applied to individual radiometric profiles and does not require other bio-optical or biological measurements to correct the profiles. The method preserves the shape of the profiles caused by non-uniform changes to chlorophyll concentration in the water column.

The fourth-degree polynomial method has been used for a range purposes. Firstly, it has been used to validate and calibrate ocean colour products that are measured from satellite. These ocean products include K_d and spectral water-leaving radiances, which are used to determine chlorophyll pigment concentrations. Secondly, it has been used to improve biogeochemistry and primary productivity models. In situ radiometric measurements from profiling floats that have been corrected using this method were used to identify K_d anomalies in bio-optical models, which reduced the uncertainty in satellite measurements (Organelli et al., 2017). This method has been used to correct in situ radiometric measurements that are used to validate reflectance measurements (calculated from water-leaving radiances) in remote regions of the Indian Ocean (Wojtasiewicz et al., 2018). This method has also recently been used on in situ radiometric measurements from profiling floats to improve simulations of chlorophyll concentration for biogeochemistry models (Terzić et al., 2019). For this study, the method was adapted and simplified for the purposes of determining the scale depth of blue light.

The three-step fourth-degree polynomial process, adapted for this study, identifies and flags perturbations based on statistical least squares fit of a fourth degree polynomial to individual $\ln(\text{PAR})$ profiles. Each step assigns a flag to the largest residuals (δ) of the fitted function and assigns each profile with a type number: “type 1” were good profiles, “type 2” were potentially good profiles and “type 3” were bad profiles (Fig. 2.10). The fourth-degree polynomial was

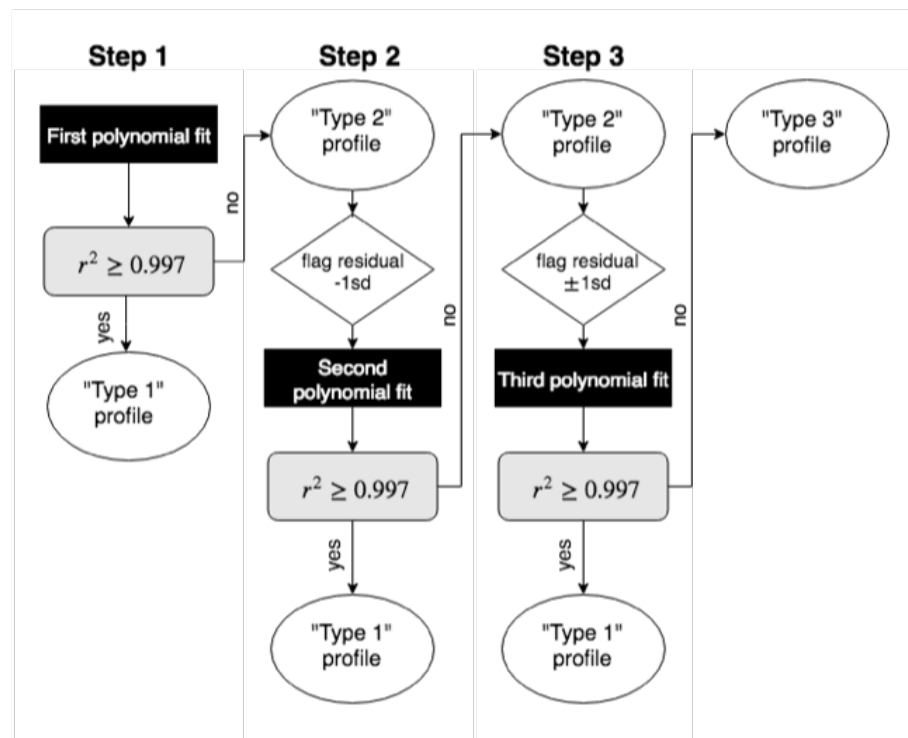


Figure 2.10: A flow chart of the fourth-degree polynomial flagging process from step 1 – 3.

fitted to each profile of the natural log of PAR from 5–70 m depth (Fig. 2.11a). If the determination coefficient, r^2 , was less than 0.997, then the profile was labelled as type 2, otherwise the profile was recorded as type 1. The type 2 profiles continue to step 2 where δ from the first polynomial fit that were -1 SD smaller than the mean of the residuals ($\bar{\delta}$) were flagged to remove spikes caused by passing clouds (Fig. 2.11b). Fitting a second polynomial to type 2 profiles with flagged spikes on the left of the profile became a type 1 profile if $r^2 \geq 0.997$. If $r^2 < 0.997$ then the type 2 profile continued to step 3. Profiles which made it to step 3 displayed an unstable light field with cloud spikes on the left of the profile. Residuals from the first fit that are $\delta > \bar{\delta} \pm 1$ SD were flagged and a third polynomial was fitted (Fig. 2.11c). Improvement of $r^2 \geq 0.997$ resulted in the type 2 profile becoming type 1. However, profiles that did not meet the threshold were labelled type 3 and were discarded from further analysis (Fig. 2.11d).

The choice of polynomial was kept at four-degrees of freedom after Organelli et al. (2016) tested the fit of a range of lower degree polynomials on PAR profiles in natural log space. The fourth degree polynomial was found to be

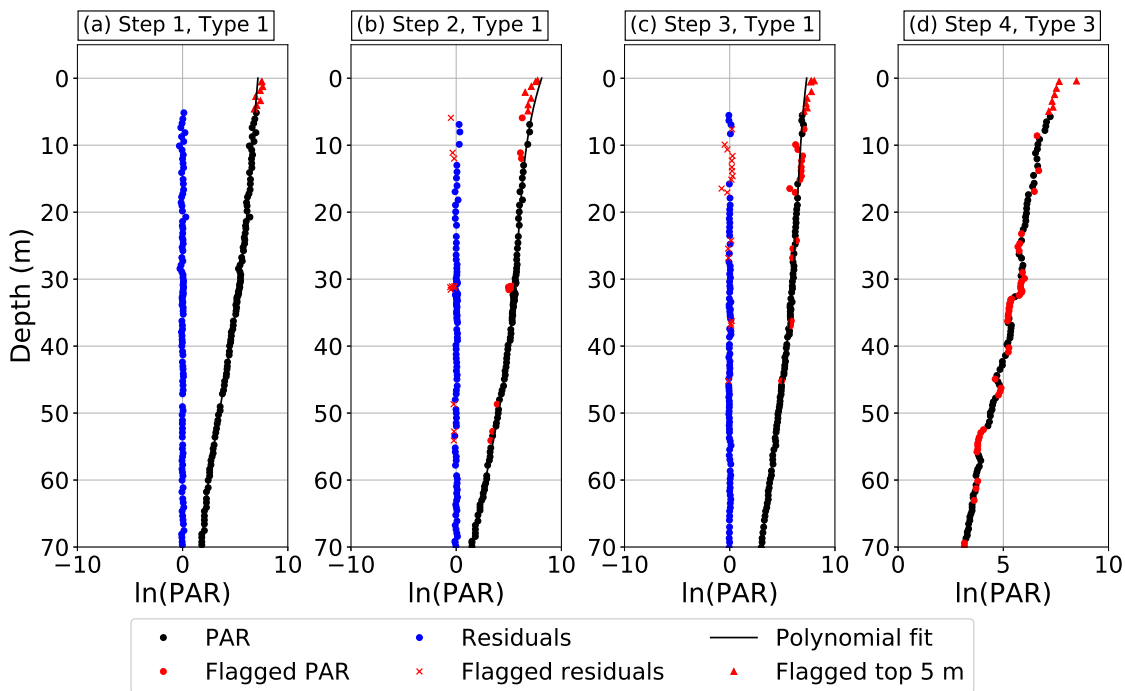


Figure 2.11: PAR profiles from glider SG579 with fitted fourth-degree polynomial and flagged spikes at each of the three steps: (a) Ascending dive 18 PAR profile recorded as “Type 1” at Step 1; (b) Ascending dive 28 PAR profile recorded as “Type 1” at Step 2; (c) Ascending dive 42 PAR profile recorded as “Type 1” at Step 3; (d) Ascending dive 102 PAR profile recorded as “Type 3” after Step 3 and was discarded from future curve-fitting processing.

the least sensitive to wave-focusing and cloud perturbations, compared with lower polynomial functions. The Organelli et al. (2016) method used slightly different r^2 thresholds to the one used in this study. For the first and second fit, they used an r^2 of 0.996. For the third fit, they used an r^2 of 0.998. The Organelli et al. (2016) method also used flagged perturbations ± 2 SD, instead of ± 1 SD in this study.

Flagging PAR perturbations exceeding ± 2 SD was ineffective in removing all of the perturbations. Cloud spikes were identified as the primary perturbation feature to flag on the PAR profiles. The cloud spikes predominantly occurred on the left of the profiles where ambient light levels decreased temporally. Flagging $\delta > \bar{\delta} - 2$ SD was effective in removing large cloud spikes, but was ineffective in removing smaller cloud spikes. Flagging $\delta > \bar{\delta} - 1$ SD was more effective in removing the smaller cloud spikes. Some PAR profiles exhibited perturbations on both the left and the right side of the profile. These profiles show unstable in-water light fields caused by wavy sea surface conditions or rapidly changing atmospheric conditions. Flagging $\delta > \bar{\delta} \pm 1$ SD was more effective in removing

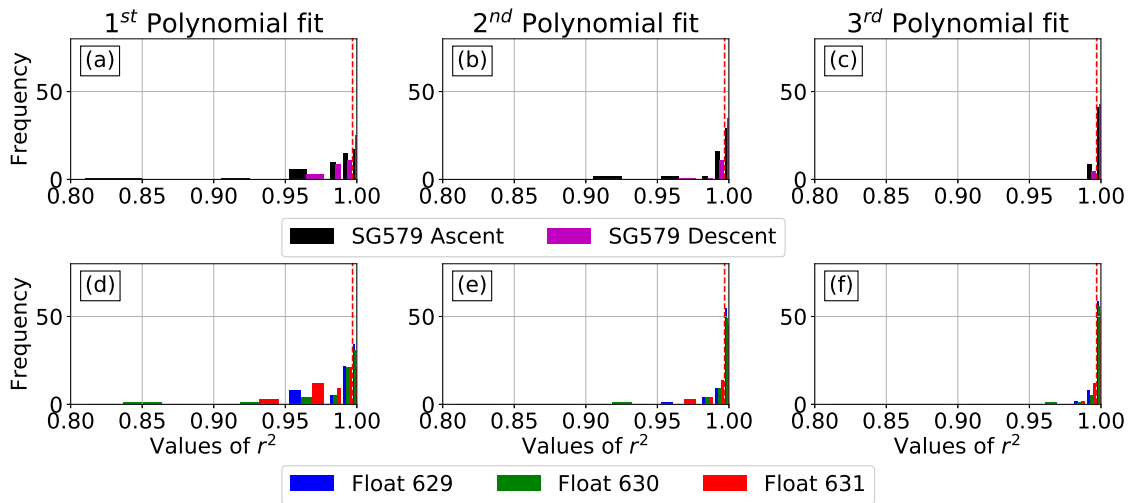


Figure 2.12: (a–c) r^2 after the first, second and third polynomial fit to ascending and descending PAR profiles from glider SG579 that was deployed during BoBBLE; (d–f) r^2 after the first, second and third polynomial fit to ascending PAR profiles from float 629, 630 and 631 that was deployed during BoBBLE.

the smaller cloud and wave-focusing spikes on both sides of the profile.

An r^2 threshold of 0.997 was suitable for classifying whether profiles were type 1, 2 or 3. Flagging δ at ± 1 SD improved the r^2 of all PAR profiles from the glider and floats deployed during BoBBLE (Fig. 2.12b and 2.12e). By the third polynomial fit, the majority of PAR profiles had $r^2 > 0.997$ (Fig. 2.12c and 2.12f). If an r^2 threshold of 0.998 from Organelli et al. (2016) was used then profiles that were suitable for h_2 determination would be discarded. In Chapter 4, a relationship between determined h_2 and average chlorophyll-a concentration is derived. It was important to not remove too many PAR profiles to ensure there was a large enough sample size to derive a chlorophyll-a concentration parameterisation. The r^2 threshold was kept at 0.997 to conserve the number of PAR profiles that were suitable for h_2 determination. Around 15% of PAR profiles were labelled type 3 and discarded from this analysis, compared with 21% of PAR profiles in Organelli et al. (2016) (Table 2.2).

A comparison of determined h_2 values before and after flagging perturbations identified by the polynomial method shows some improvement in the values and uncertainties of h_2 (Fig. 2.13). Across all platforms, the polynomial method has reduced the majority of h_2 uncertainties, as shown by the smaller vertical error bars (Fig. 2.13a–2.13d). The polynomial method is also effective in reducing h_2 values above 25 m and reducing their associated high uncertainties. There is change in the h_2 distribution with less h_2 values in the

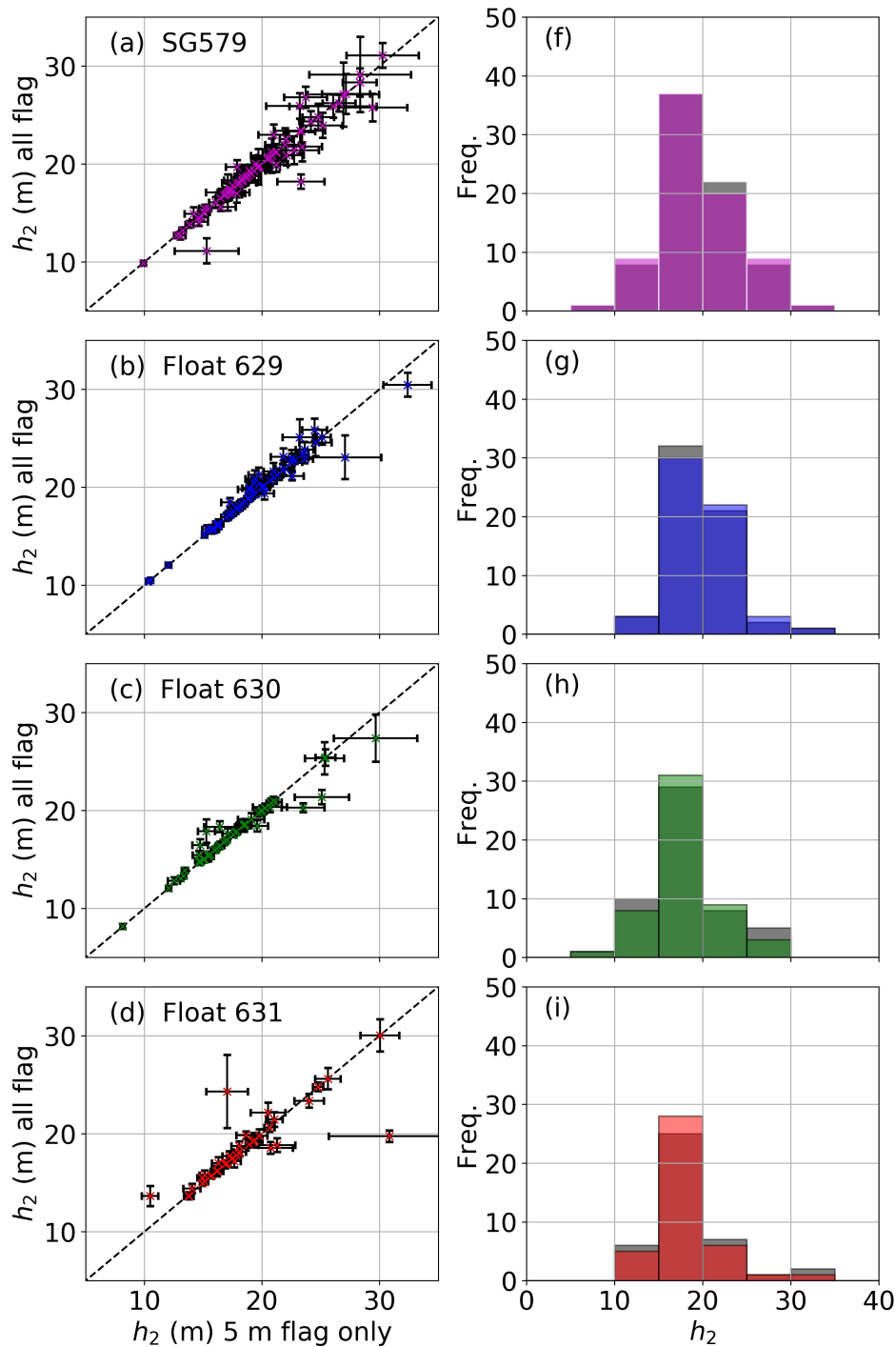


Figure 2.13: Comparison of h_2 before and after flagging perturbations identified by the polynomial method; (a) Glider SG579; (b) Float 629; (c) Float 630; (d) Float 631. Histograms of derived h_2 before (grey bars) and after (coloured bars) flagging perturbations identified by the polynomial method; (f) Glider SG579; (g) Float 629; (h) Float 630; (i) Float 631. The error bars represent the ± 1 SD error of the fit of Equation 2.8. The dashed black line represents the 1:1 ratio.

Label	Ascent/Descent	Type 1	Type 2	Type 3
SG579	Ascent	33%	49%	18%
SG579	Descent	53%	37%	10%
Float 629	Ascent	49%	38%	13%
Float 630	Ascent	49%	40%	11%
Float 631	Ascent	32%	47%	21%

Table 2.2: Percentage of PAR profiles grouped into each profile type after the fourth-degree polynomial method. These include PAR profiles from the ocean gliders and profiling floats deployed during the BoBBLE campaign.

15–20 m bin for float 629 (Fig. 2.13g). For floats 630 and 631, there is an increase in the number of h_2 values in the 15–20 m bin, as the number of h_2 values in the marginalised bins of 25 to 40 m decreases (Fig. 2.13h–2.13i). Decreasing large h_2 values and their corresponding uncertainties demonstrates an improvement in the determined values of h_2 after applying the polynomial method.

Using the polynomial method showed that the percentage of PAR profiles that were discarded were found to depend on whether the profile is measured on an ascent or descent. Ascending profiles from glider SG579 required more perturbation flagging than descending profiles. Ascending profiles had a higher percentage of type 2 and type 3 profiles compared with descending profiles, which had a higher percentage of type 1 profiles (Table 2.2). The average vertical velocity of ascending profiles was 0.1 m s^{-1} , whereas the average vertical velocity of descending profiles was -0.2 m s^{-1} (Fig. 2.14a). The difference in vertical velocities caused differences in the vertical resolutions of ascending and descending profiles. The slow ascents increased the vertical resolution of the PAR profiles (Fig. 2.14b), which meant more waves and clouds could pass over the glider resulting in more perturbations (red dots exceeding $\delta > \pm 1 \text{ SD}$; Fig. 2.14c). Conversely, the fast descents decreased the vertical resolution of the PAR profiles (Fig. 2.14b), which meant fewer waves and clouds passed over the glider resulting in fewer perturbations (blue dots exceeding $\delta > \pm 1 \text{ SD}$; Fig. 2.14c). The polynomial method highlights that ascending PAR profiles tend to be noisier than descending PAR profiles, and are therefore more likely to be discarded from the analysis as they are more likely to provide unreliable h_2 determinations.

The difference between ascending and descending vertical velocity is due to the strong stratification of the BoB upper ocean. The glider must overcome this large density difference as it ascends to the surface, pushing the glider to the

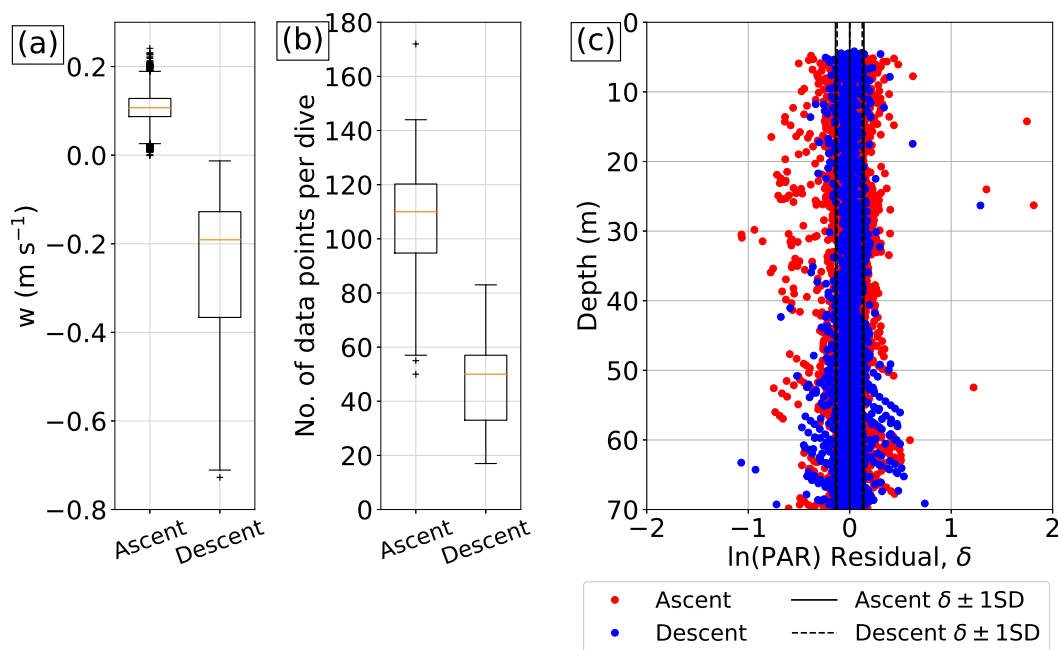


Figure 2.14: (a) The measured vertical velocity of glider SG579 ascent and descent between 5–70 m depth; (b) The number of PAR data points per dive from glider SG579 for ascents and descents between 5–70 m depth; (c) Residuals of $\ln(\text{PAR})$ and ± 1 SD after fitting a fourth degree polynomial to each individual $\ln(\text{PAR})$ profile for glider SG579 ascent (red dots) and descent (blue dots) between 5–70 m depth.

peak of its capability. More oil needs to be pumped into the external bladder to reduce the density of the glider relative to the less dense stratified upper ocean, which results in a slower ascent. Conversely, as the glider pumps oil out of the external bladder to sink, the glider would rapidly descend as it quickly becomes more dense than the surrounding upper ocean.

Float profiles required less perturbation flagging than glider profiles with a higher average percentage of profiles assigned as type 1. However, float 631 showed a lower percentage of type 1 profiles compared with the other two floats and had the highest percentage of type 3 profiles. Float 631 showed more PAR perturbations than the other two floats, which could be due to the external environmental conditions float 631 encountered during the three month deployment (red dots exceeding $\delta > \pm 1$ SD; Fig. 2.15c). Hence, differences between the number of PAR perturbations flagged for each float is dependent on the local sea-surface and atmospheric conditions of the region being sampled.

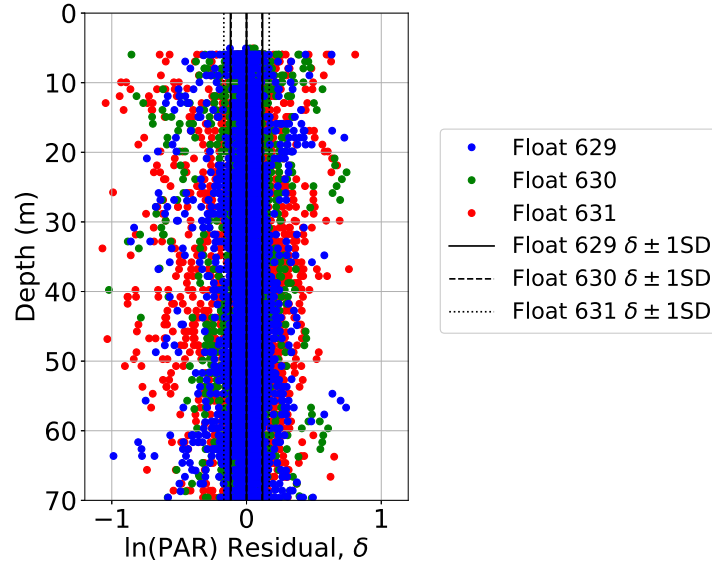


Figure 2.15: Residuals of $\ln(\text{PAR})$ and ± 1 SD after fitting a fourth degree polynomial to each individual $\ln(\text{PAR})$ profile for float 629 (blue dots), 630 (green dots) and 631 (red dots) between 5–70 m depth.

2.6.6 Radiometer data quality control

The floats that were deployed during the BoBBLE campaign measured individual visible wavelengths at 380 nm (blue light), 490 nm (blue-green light) and 555 nm (green light) with units $\mu\text{W m}^{-2} \text{nm}^{-1}$. Chlorophyll-a pigment predominantly absorbs $E_d(490)$ during photosynthesis, which means a proxy of in situ chlorophyll-a concentration can be derived from measured profiles of $E_d(490)$. This chlorophyll-a concentration proxy allows for identification of the vertical distribution of chlorophyll-a.

Xing et al. (2011) describes the method to derive the chlorophyll-a concentration. We first assume downward irradiance, E_d , at wavelength, λ , through the water column decays exponentially. The irradiance just below the surface, $E_d(\lambda, -0)$, decreases with depth, z , at a specific wavelength at each discretised layer, dz . The rate of decay of light or the diffuse attenuation coefficient, $K_d(\lambda, z)$, is allowed to vary in each discretised layer of 1 m thickness. Hence, the expression to calculate $E_d(\lambda, z)$ is

$$\ln E_d(\lambda, z) = \ln E_d(\lambda, -0) - \sum_1^n K_d(\lambda, z) \Delta z. \quad (2.10)$$

The attenuation rate of light with depth depends on the properties of pure

seawater and the biological constituents that are suspended within the water column. $K_d(\lambda)$ is defined as the sum of the attenuation of pure seawater (K_w) and the attenuation due to biological material (K_{bio}). For each discretised layer of water, K_w is assumed to remain constant at a given wavelength, but K_{bio} is allowed to vary in order to derive depth-varying chlorophyll-a concentration. Ocean water in the Southern BoB is categorised as “case 1” waters, where optical properties are affected by chlorophyll pigments and detrital organic matter (Morel, 1988). The BoB upper ocean consists of chlorophyll-a pigments, as shown from in situ water samples (Madhu et al., 2006), chlorophyll-a fluorescence measurements and remotely sensed satellite measurements (Thushara et al., 2019). For case 1 waters, K_{bio} varies as a non-linear power law function of chlorophyll-a concentration, [Chl-a] (Morel, 1988; Morel and Maritorena, 2001) meaning that $K_d(\lambda)$ is defined as

$$K_d(\lambda) = K_w(\lambda) + \chi(\lambda)[\text{Chl-a}]^{e(\lambda)} \quad (2.11)$$

where $\chi(\lambda)$ and $e(\lambda)$ are empirically determined values. Equation 2.11 then becomes,

$$\ln E_d(\lambda, z) = \ln E_d(\lambda, -0) - \sum_1^n K_w(\lambda) + \chi(\lambda)[\text{Chl-a}]^{e(\lambda)} \Delta z. \quad (2.12)$$

Morel and Maritorena (2001) derived the spectrally dependent $\chi(\lambda)$ and $e(\lambda)$ parameters for wavelengths 350 to 700 nm using linear regression analysis of the log-transformed chlorophyll-a concentration and K_d . The $\chi(\lambda)$ and $e(\lambda)$ parameters determined by Morel and Maritorena (2001) were used in this study.

Optical and bio-optical parameters $K_w(490)$, $\chi(\lambda)$ and $e(\lambda)$ were 0.0166, 0.0825 and 0.6529, respectively, for downwelling irradiance 490 nm. The empirical relationship breaks down at chlorophyll-a concentrations above 20 mg m⁻³ (Morel et al., 2007), which is considerably higher than in situ concentrations measured by glider SG579 in the Southern BoB. Hence, Equation 2.11 is suitable to determine chlorophyll-a concentration profiles from $\ln E_d(490)$.

Radiometric measurements, like PAR, were affected by the same perturbations as discussed in Section 2.6.1. These perturbations had to be removed to minimise non-biological spikes in the derived chlorophyll-a concentration profiles. All radiometric profiles exhibited considerable noise in

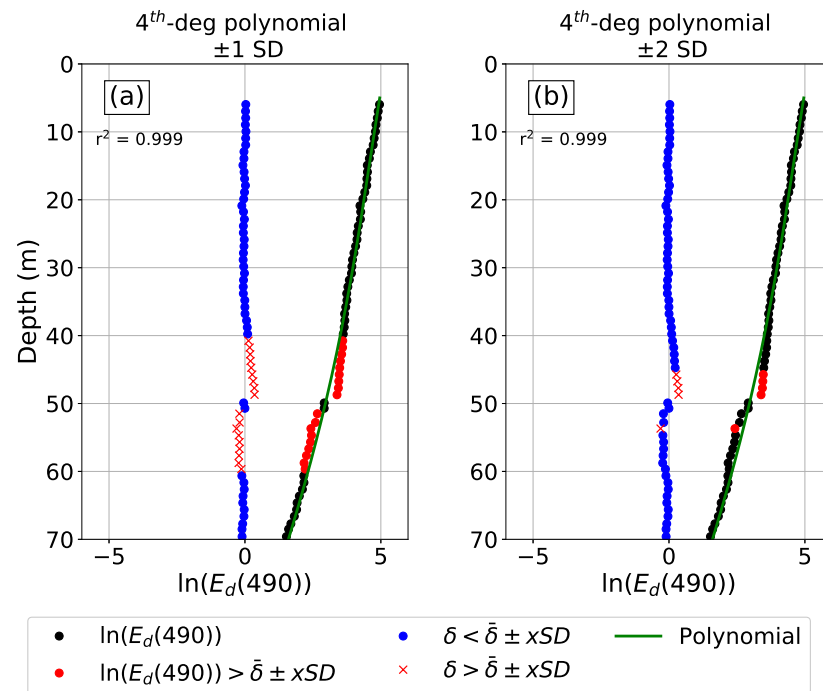


Figure 2.16: A fourth-degree polynomial was fitted to $\ln E_d(490)$ profile 34 from float 629 where; (a) $\delta > \bar{\delta} \pm 1 SD$ was flagged; (b) $\delta > \bar{\delta} \pm 2 SD$ was flagged.

the top 5 m, hence data were initially flagged to a depth of 5 m.

The same fourth-degree polynomial method adapted for the glider and float PAR measurements was not suitable in identifying and removing perturbations from radiometric profiles of $\ln E_d(490)$. As an example, a fourth-degree polynomial was fitted to float 629 profile 34 of $\ln E_d(490)$ from 5 to 100 m depth where $\delta > \bar{\delta} \pm 1 SD$ was flagged (Fig. 2.16a). The profile at 50 m depth showed a sudden increase in ambient light levels as the float ascended to the surface, which was possibly caused by cloud break-up or reduced chlorophyll concentrations, or even both. The flagging of δ at $\pm 1 SD$ removed ~ 10 m sections of the profile either side of the step-wise change in $\ln E_d(490)$ at 50 m depth. Removing large sections of data points around this one perturbation would mean removing data points that could be derived for chlorophyll-a concentration. This led to the development of an altered radiometric quality control method.

The new radiometric quality control method involved flagging $\ln E_d(490)$ where $\delta > \bar{\delta} \pm 2 SD$ to preserve data points needed to calculate chlorophyll-a concentration for each discretised layer (Fig. 2.16b). Increasing the SD threshold from 1 to 2 resulted in fewer flagged data points either side of the perturbation in

$\ln E_d(490)$ at 50 m depth and would reduce the gaps in the derived chlorophyll-a profile. However, as mentioned in Section 2.6.5, increasing the SD threshold from 1 to 2 increased the number of smaller perturbations that were not flagged, which led to large non-physical chlorophyll-a concentration spikes later in the chlorophyll-a calculation.

The new radiometric quality control method also used an r^2 threshold of 0.996 when fitting the polynomial to $\ln E_d(490)$, instead of 0.997 when fitting the polynomial to $\ln E_d(\text{PAR})$. After step 3 of the fourth-degree polynomial method, r^2 was lower for the ± 2 SD threshold compared with the ± 1 SD threshold, as fewer perturbations were flagged (Fig. 2.17). It was found that profiles with an r^2 exceeding 0.996 were suitable for chlorophyll-a concentration determination. An r^2 threshold of 0.996 was slightly lower than the r^2 threshold of 0.998 used by Organelli et al. (2016). However, as discussed in Section 2.6.5 using an r^2 threshold of 0.998 was found to remove too many profiles that could have been used to derive chlorophyll-a concentration. To flag the smaller perturbations, two methods were developed to remove these non-biological features.

The first method involved flagging $\ln E_d(490)$ where $\delta > \bar{\delta} \pm 2$ SD (red dots; Fig. 2.18a) and then linearly interpolating the $\ln E_d(490)$ profile onto a 1 m depth grid (blue circles; Fig. 2.18a). At this stage small cloud perturbations (blue circles at 23 m; Fig. 2.18b) become large positive and negative spikes in K_{bio} space (blue line and circles; Fig. 2.18c) and a large positive spikes in chlorophyll-a concentration space (blue line and squares; Fig. 2.18d). Hence, K_{bio} represents the attenuation due to biology, but also the contamination of the attenuation due to clouds. A 10-point rolling mean was used to smooth out small cloud perturbations in the $\ln E_d(490)$ profiles (magenta crosses; Fig. 2.18b). In comparison, a 10-point rolling median was found to be ineffective in removing cloud perturbations, which can be seen in K_{bio} space (green line and circles; Fig. 2.18c) and can produce anomalously high chlorophyll-a concentrations (green line and squares; Fig. 2.18d). Thus, a rolling mean effectively reduced cloud spike contamination throughout the chlorophyll-a concentration profile and is used as the first method to remove cloud perturbations.

The second method to remove cloud perturbations was dependent on the cloud perturbation pattern identified in K_{bio} space, where large positive spikes always preceded large negative spikes. An algorithm was used to flag positive spikes preceded negative spikes and the remaining positive and negative spikes were further flagged using a threshold of 0.1 m^{-1} and -0.03 m^{-1} , respectively.

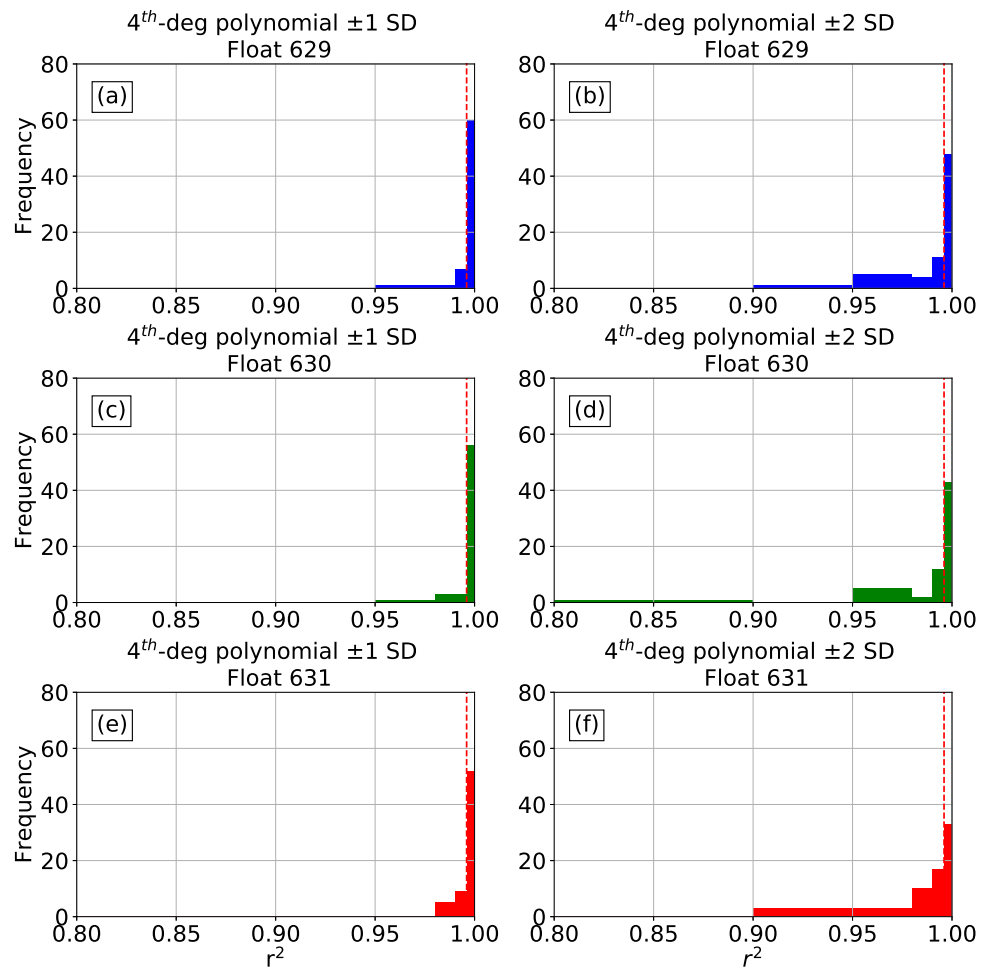


Figure 2.17: (a) The determination coefficient, r^2 , after the third polynomial step flagging $\delta > \bar{\delta} \pm 1$ SD of $\ln E_d(490)$ profiles from float 629; (b) as in (a) but flagging $\delta > \bar{\delta} \pm 2$ SD; (c–d) as in (a–b), but for float 630; (e–f) as in (a–b), but for float 631.

The K_{bio} profile was then linearly interpolated onto a 1 m depth grid to fill in missing sections of the profile that were flagged as cloud spikes (green line and circles; Fig. 2.19b). The interpolated K_{bio} profile was then smoothed using a 10-point rolling mean (red line and circles; Fig. 2.19b) and converted into chlorophyll-a concentration profile (red line and squares; Fig. 2.19c). The chlorophyll-a concentration profile using the first method (magenta line and squares; Fig. 2.19c) is less smooth than the chlorophyll-a concentration profile using the second method (red line and squares; Fig. 2.19c). By initially flagging large perturbations in K_{bio} space and then applying the rolling mean in the second method ensures more of the small cloud perturbations are removed.

Fig. 2.20 shows a depth-profile section of derived chlorophyll-a concentrations from float 631 using the two methods. Both sections show a

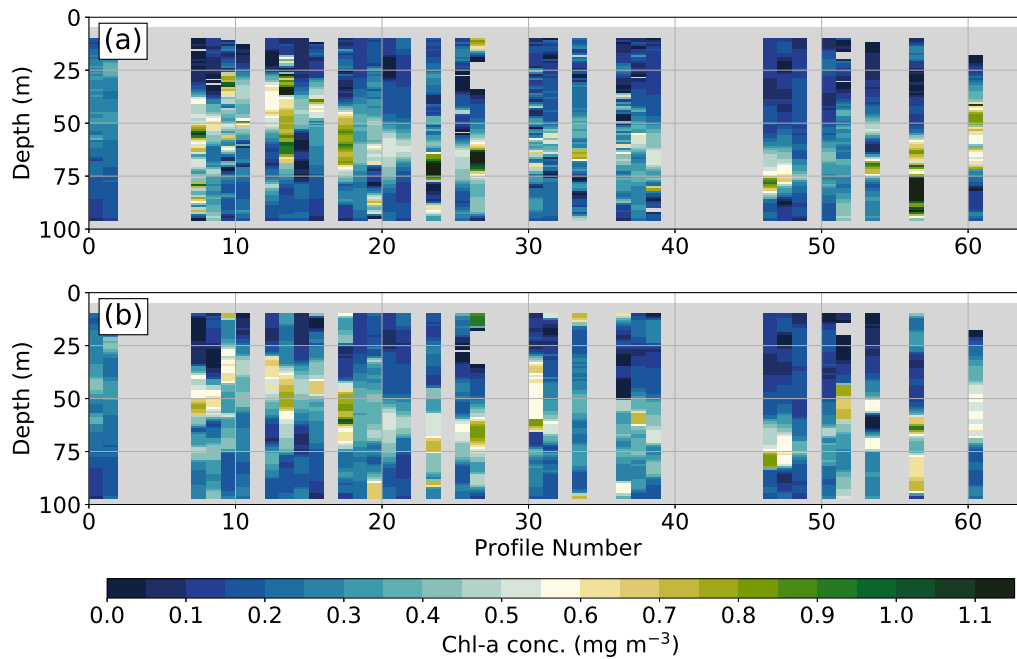


Figure 2.20: Derived chlorophyll-a concentration from float 631 $\ln E_d(490)$ profiles using two flagging and smoothing techniques, (a) 1 m interpolated $\ln E_d(490)$ and 10-point rolling mean; (b) Flagged K_{bio} cloud spikes interpolated onto a 1 m depth grid and 10-point rolling mean. Missing profiles and sections are coloured grey.

2.7 Conclusion

PAR profiles vary in magnitude and shape depending on the type of oceanographic platform. For PAR profiles measured by gliders, a nighttime and low-light threshold was introduced to remove profiles that observed low PAR intensity, which were found to affect h_2 determinations. All PAR profiles measured from both gliders and floats were affected by external environmental factors such as wave-focusing and cloud spikes. To solve this issue, the PAR profiles were split into two. First, the noisy near-surface PAR signal that was affecting h_2 determinations was flagged from the surface down to 5 m and then a double exponential function was adapted to replicate the absorption of red light, yet fit to the more robust PAR profile below 5 m. Second, the less noisy PAR signal below 5 m was still affecting h_2 determinations and so an adapted fourth-degree polynomial method from Organelli et al. (2016) was used to identify and flag perturbations, which improved h_2 determinations. Radiometric profiles measured from the floats followed a similar quality control method as the PAR profiles, except the polynomial method had different r^2 and SD thresholds and a further method was developed to flag smaller cloud

perturbations.

The use of Jerlov optical parameters was used to constrain the fit of the double exponential function to the surface, but the representation of the red light absorption at the near-surface might not be as accurate as optical parameters determined by Ohlmann (2003) and Morel and Antoine (1994). However, for the purposes of accurately determining h_2 Jerlov optical parameters R and h_1 were found to have a small influence on determined h_2 (<0.8 m) and were thus used to constrain the fit of Equation 2.8.

For the adapted polynomial method, the condition where residuals ± 1 SD of the mean of the residuals were flagged was found to be effective in flagging the majority of PAR perturbations. However, this meant PAR data points that potentially showed no perturbation were flagged. These non-perturbed data points might have shown changes in the vertical gradient of PAR that was caused by a change in the chlorophyll concentration. Hence, the fitted double exponential function might not fully quantify the chlorophyll-perturbed scale depth if those data points are removed. The occurrence of flagging non-perturbed data points were limited to PAR profiles exhibiting fluctuating PAR signals due to both external environmental conditions and the attenuation by biological constituents.

The PAR quality control process presented here has shown that there was no difference between PAR perturbations measured by gliders and floats. Instead, PAR perturbations depended on the local external environmental conditions. For the glider, more perturbations were identified on the ascents than the descents, which was due to slow ascents in the highly stratified BoB. Whilst more ascents were likely to be discarded during the polynomial method this did not mean all ascents were excluded from the h_2 determination analysis. This Chapter has shown that floats and gliders can be effective oceanographic platforms in measuring optical and bio-optical variables and should be recommended for future optical-related campaigns.

Chapter 3

Spatial and temporal variability of solar penetration depths and the impact on Bay of Bengal SST during the summer monsoon

3.1 Introduction

This Chapter focuses on the temporal and spatial variability of h_2 that is influenced by surface chlorophyll concentrations, and on how h_2 affects SST across the southern BoB. To quantify the influence of chlorophyll on radiant heating, an ocean glider and three profiling floats were deployed as part of the BoBBLE campaign to measure in situ physical, optical and biogeochemical variables in the upper ocean during July 2016 at high vertical resolution (Fig. 3.1a).

An overview of the instruments and data is presented in Section 3.2. Section 3.3 presents an analysis of the observed physical properties of the upper ocean, and temporal and spatial variability of determined h_2 . Based on these results, we compare the observed scale depth and chlorophyll concentration to two previously published parameterisations (Section 3.4.1). The impact of observed chlorophyll on upper ocean radiant heating rate in the southern BoB is investigated by running two idealised simulations with an imposed solar penetration depth from the h_2 observations. The simulations were conducted using the one-dimensional K-profile parameterisation ocean mixed layer model

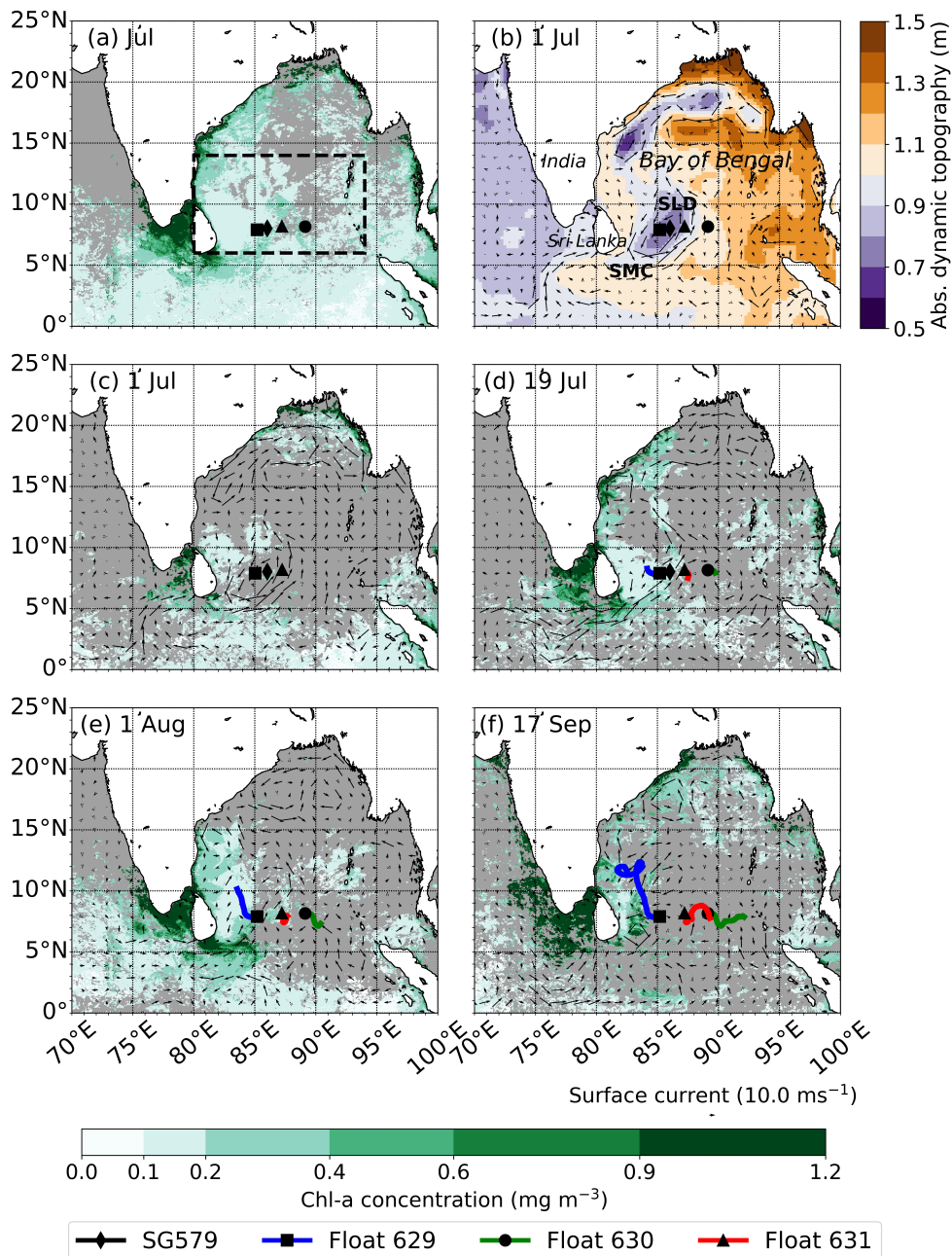


Figure 3.1: (a) Satellite composite of July 2016 average 4 km chlorophyll-a concentration (mg m^{-3}) obtained from ESA OC CCI version 3.1. The dashed black box shows the outline of Fig. 3.5a. (b) Absolute dynamic topography (m) of horizontal resolution $0.25^\circ \times 0.25^\circ$ overlaid with surface geostrophic velocity (m s^{-1}) from AVISO for 1 July 2016 plotted with a horizontal resolution $1^\circ \times 1^\circ$. (c-f) Satellite composite of 8-day averaged 4 km chlorophyll-a concentration and surface geostrophic velocities for 1–8 July, 19–27 July, 1–8 August and 17–25 September. Deployment locations and trajectories of glider SG579 (diamond marker; black line), float 629 (square marker; blue line), float 630 (circle marker; green line) and float 631 (triangle marker; red line) are overlaid. Missing data is shaded grey.

(Section 3.4.2). Conclusions are given in Section 3.5.

3.2 Data and methods

3.2.1 Observations and instruments

a. Ocean gliders and Argo profiling floats

As outlined in Chapter 2, Seaglider (SG579) was deployed at 86°E, 8°N on 30 June 2016 east of Sri Lanka and piloted to 85.3°E by 8 July, where the glider continued to take measurements until 29 July 2016. Quality control was performed on the entire conductivity-temperature (CT) dataset using Conservative Temperature–Absolute Salinity (IOC et al., 2010) space analysis and further quality control in depth space for individual vertical profiles. Salinity spikes were removed when the glider vertical speed was less than 0.035 m s^{-1} as the unpumped CT sensor relied on a suitable flow of water for reliable measurements. The ocean glider PAR measurements were factory calibrated. The CT sensor was factory calibrated and was then further calibrated against in situ ship CTD observations.

As outlined in Chapter 2, Argo profiling floats 629, 631 and 630 were deployed at 85.5°E, 87°E and 89°E on the 28 June, 1 July and 4 July respectively, where they sampled to 500 m daily until mid-August and every other day until the end of September. The CTD measurements were factory calibrated and radiometer measurements were factory calibrated with channel-specific coefficients. The vertical resolution on the ascent to the surface was $\sim 1 \text{ m}$ for the radiometer and CTD.

b. PAR

The methodology described in Chapter 2 was used to remove nighttime and low-light PAR profiles, remove all PAR data between 0–5 m depth and to flag PAR perturbations below 5 m depth. From the 1-m vertical resolution PAR measurements we are unable to determine the transmission of red wavelengths (values of q_1 and h_1). We assume Jerlov water type IB (Paulson and Simpson, 1977) to be applicable to our region, based upon initial determinations of $h_2 \sim 17 \text{ m}$ from fitting equation (2.6). We therefore constrain R to be 0.67 and h_1 to be 1 m and thus fit PAR profiles between 5 m and 70 m to the transmission of blue light with depth (h_2) using Equation 2.8 (Fig. 3.2a). The same fit plotted

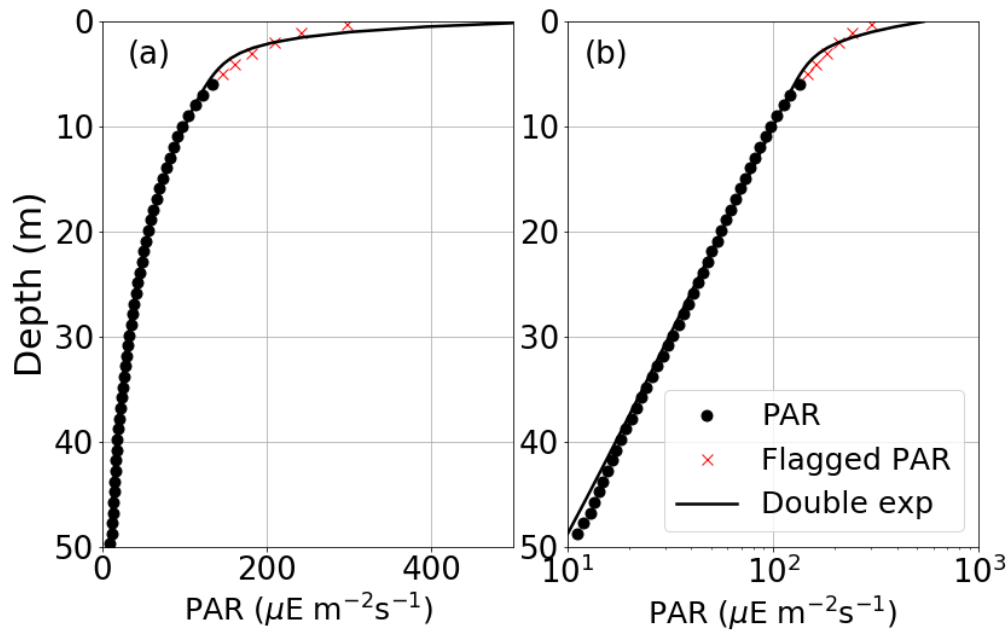


Figure 3.2: (a) Vertical profile of PAR (black circles) measured from float 629 from the surface to 50 m depth with a fitted double exponential function (black line) to PAR between 5–70 m depth. R and h_1 were specified to be 0.67 and 1.0 m respectively. Unknown parameters include: the offset of fitted function, d ; the surface value of blue wavelengths of PAR, q_2 ; the scale depth of blue wavelengths, h_2 . Red crosses show flagged PAR values that were excluded from the curve fit. (b) Same vertical profile of PAR and fitted double exponential function as (a) but presented in log space.

in log space (Fig. 3.2b) demonstrates the approximate linear absorption of blue light with depth below 5 m.

c. Chlorophyll

The gliders raw fluorescence voltages were converted into chlorophyll-a concentrations according to the manufacturer calibrations. The quenching correction method described in Chapter 2 was used to corrected daytime non-photochemical quenching in the chlorophyll-a fluorescence profiles. The glider fluorescence-derived chlorophyll-a concentrations, after correcting for non-photochemical quenching, showed values that were higher than those derived from the shipboard CTD chlorophyll-a fluorescence sensor. Concentrations were calibrated by applying a scale factor and offset derived using linear regression between the glider and CTD chlorophyll-a profiles.

The profiling floats did not make chlorophyll-a fluorescence measurements, so a novel approach was developed to derive chlorophyll-a concentration

from radiometer data alone (see Chapter 2.6.6 for method details). The chlorophyll-a pigment concentration that was derived from radiometry data or remotely sensed by satellite will henceforth be referred to as “chlorophyll” for convenience.

d. Satellite products

The remotely sensed chlorophyll concentrations used in this Chapter are sourced from the European Space Agency's Ocean Colour - Climate Change Initiative (ESA OC-CCI; Lavender et al., 2015) version 3.1 (available at <http://www.esa-oceancolour-cci.org>). The OC-CCI project involved the merging of remotely sensed chlorophyll concentrations from MODIS, MERIS, SeaWiFS and VIIRS radiance sensors to provide a continuous dataset ranging from 1997–2016 with increased spatial coverage of the global oceans. 8-daily and monthly composite of chlorophyll concentration with spatial resolutions of 4 km have been used to investigate the weekly and monthly variability of chlorophyll concentration influencing solar penetration depths in the deployment region across the southern BoB from July to September 2016.

Satellite-derived absolute geostrophic velocities (meridional and zonal components) and absolute dynamic topography are altimeter products produced by SSALTO/Duacs, distributed by AVISO (<https://www.aviso.altimetry.fr>) and are available through the Copernicus Marine Environment Monitoring Service (<http://marine.copernicus.eu>). The daily composites of absolute geostrophic velocities and absolute dynamic topography have a spatial resolution of $0.25^\circ \times 0.25^\circ$ and are used to investigate the surface current velocities that control chlorophyll concentration advection from July to September 2016.

3.3 Glider and profiling float observations

The SLD is a prominent feature in the southwest BoB during the summer monsoon and is typically associated with high surface chlorophyll concentrations (Thushara et al., 2019). At the start of July 2016, the SLD is centered around $85\text{--}86^\circ\text{E}$ and $5\text{--}10^\circ\text{N}$ to the west of the SMC (Fig. 3.1b). Glider SG579 is located inside the SLD from 30 June and observes the weakening of this cyclonic eddy after 2 July, remaining in a localized region between $85\text{--}86^\circ\text{E}$ (Fig. 3.1c; black diamond). The average mixed layer salinity and temperature are 34 g kg^{-1} and 28°C respectively (Fig. 3.3a and 3.3b). Chlorophyll concentrations peak on 1 July at 0.8 mg m^{-3} at a depth of 18 m, indicating high surface

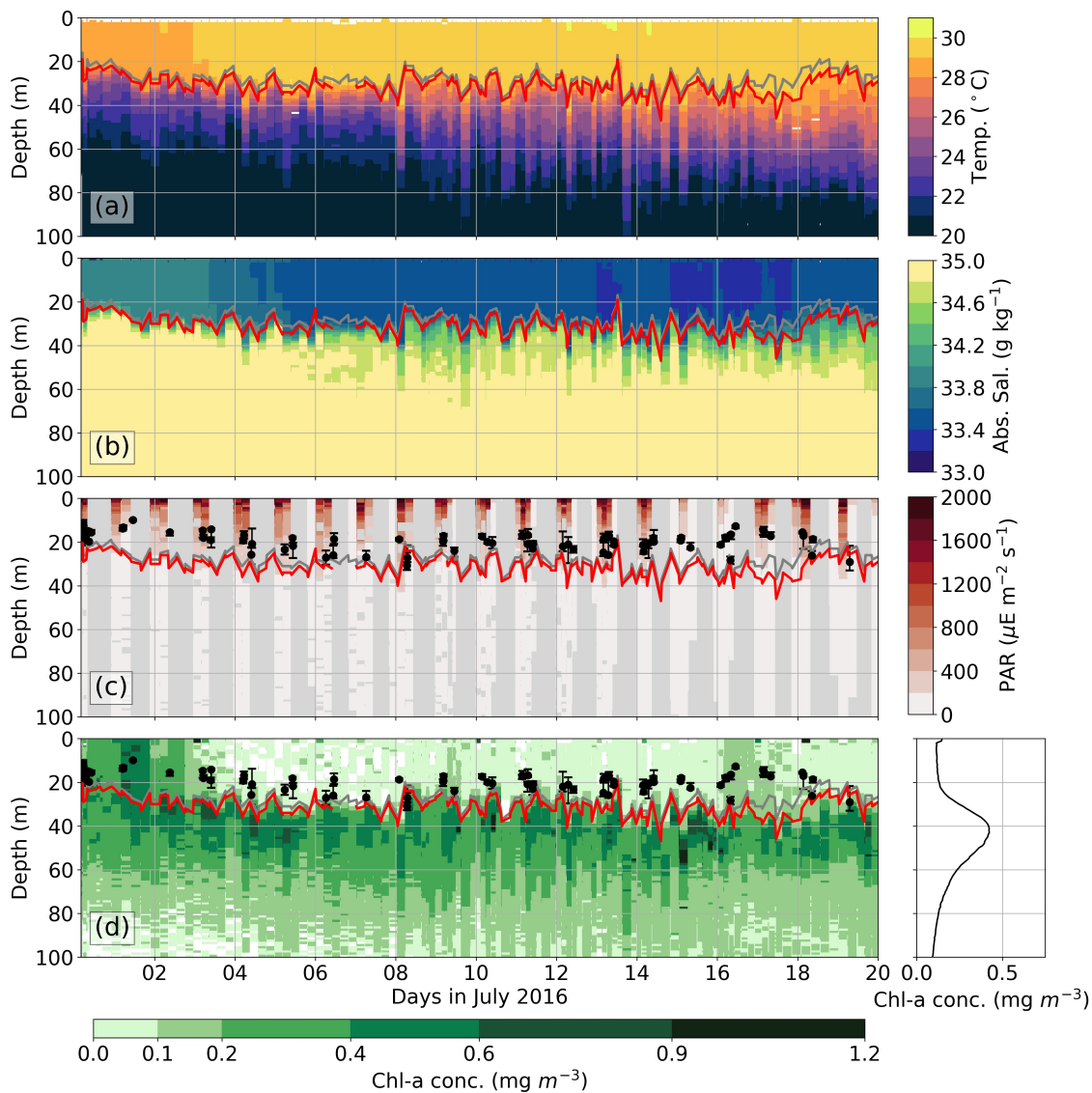


Figure 3.3: Time series of observations measured by glider SG579, linearly interpolated to 1 m depth intervals down to 100 m: (a) conservative temperature ($^{\circ}\text{C}$), (b) absolute salinity (g kg^{-1}), (c) PAR ($\mu\text{E m}^{-2} \text{s}^{-1}$), (d) chlorophyll concentration and vertical profile of the average chlorophyll concentration (mg m^{-3}). The black circles are scale depth values, h_2 (m). The mixed layer depth is defined as the depth where density is same as the surface density plus an increase in density equivalent to a 0.8°C decrease in temperature, and the isothermal layer depth is calculated as the depth where temperature is 0.8°C cooler than SST (Kara et al., 2000; Thushara et al., 2019). The region between the mixed layer depth (grey line) and isothermal layer depth (red line) is the barrier layer.

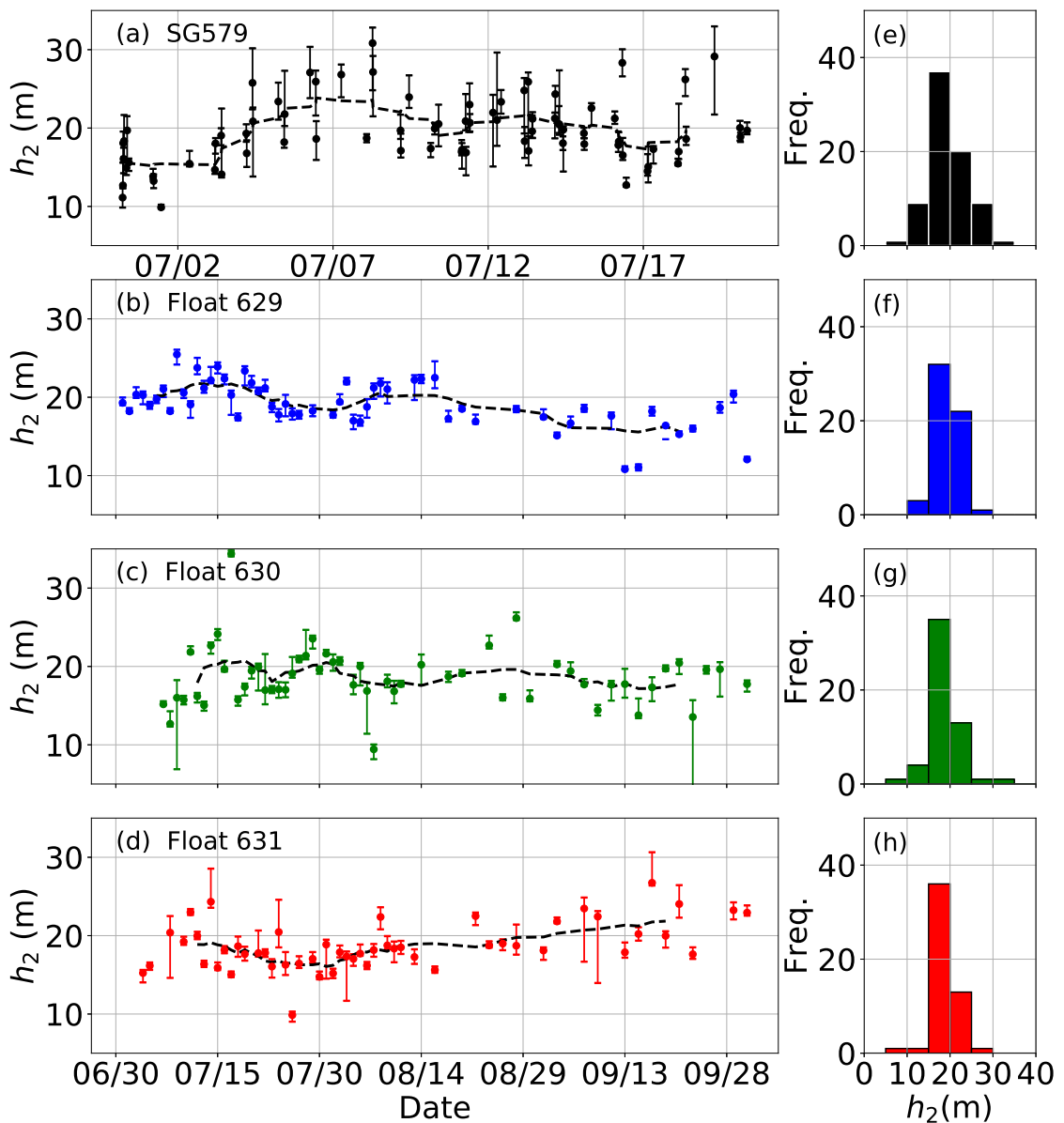


Figure 3.4: (a–d) Time series of observed h_2 : (a) glider SG579 (black), (b) float 629 (blue), (c) float 630 (green) and (d) float 631 (red). Dashed black lines represents a centered moving average of h_2 values with window size of 10 data points. (e–h) Histograms of observed h_2 for each glider and floats with the same colour scheme as the time series.

chlorophyll concentrations (Fig. 3.3d). Corresponding values of h_2 decrease from an average of 16 m on 30 June to 13 m on 1 July, as the average 0–30 m chlorophyll concentration increases from 0.2 mg m^{-3} to 0.5 mg m^{-3} in one day (Fig. 3.3d; black circles).

After 2 July, the SLD weakens and shifts towards the northwest, but the SMC continues to flow into the south-central BoB. Patches of surface chlorophyll, with concentrations of $0.1\text{--}0.4 \text{ mg m}^{-3}$ (Fig. 3.1d), continue to be advected by the

SMC into the glider SG579 deployment region (85–86°E) until 19 July. Within the SMC, the mixed layer warms to 29°C and freshens to 33.3 g kg⁻¹ (Fig. 3.3a and 3.3b). Chlorophyll concentrations below the mixed layer remain around 0.5 mg m⁻³ forming a deep chlorophyll maximum between 30–50 m depth (Fig. 3.3d). Meanwhile average 0–30 m chlorophyll concentrations decrease to less than 0.2 mg m⁻³ (Fig. 3.3d) and the corresponding average values of h_2 increase to more than 20 m until 16 July (Fig. 3.4a; dashed black line). The position and velocity of the SMC relative to the biologically-productive southern coast of Sri Lanka (Lévy et al., 2007) determines how much surface chlorophyll is entrained and advected into the south-central BoB (Vinayachandran et al., 2004). Throughout most of July the SMC is too far south to intercept the high surface chlorophyll concentrations along the southern coast of Sri Lanka (Fig. 3.1d), explaining why in situ surface chlorophyll concentrations are relatively low after 2 July (Fig. 3.3d). The variability of h_2 in the SMC is large (Fig. 3.4a). Values ranged between 15–31 m from 4 July onwards, which we partly attribute to sub-daily temporal variability in the mixed layer and surface chlorophyll concentrations. However, the derived h_2 values from glider SG579 are associated with relatively high uncertainty (typically ~2 m) due to the fitting of the double exponential function to noisy vertical PAR profiles, which may contribute to this apparent variability.

The profiling float dataset allows us to extend the glider dataset temporally and spatially, providing daily measurements of solar penetration depths until mid-August and then measurements every 2 days until the end of September, spanning much of the southern BoB. The vertical profiles of downwelling irradiance measured from the profiling floats are less noisy than those measured from the glider. Hence, the profiling floats display lower uncertainty in determined values of h_2 when compared with the glider (Fig. 3.4 a–d). As the SMC flows northeastward into the south-central BoB during early July, the surface current bifurcates. The main branch flows northward towards 10°N and the smaller branch flows eastward towards 90°E (Fig. 3.1d). Fig. 3.5b shows the longitudinal variations of h_2 across the SLD and SMC. Values of h_2 decrease as remotely sensed chlorophyll concentrations increase towards the center of the SMC (Fig. 3.5a and 3.5b), consistent with previous studies that show the SMC increasing chlorophyll concentrations in the region (e.g., Vinayachandran et al., 2004; Thushara et al., 2019). Float 631 is deployed on the eastern flank of the SMC and completes an anticyclonic loop, intercepting the eastern flank of the SMC a second time on 20 July at 87°E (Fig. 3.1d). Between 20–24 July the time

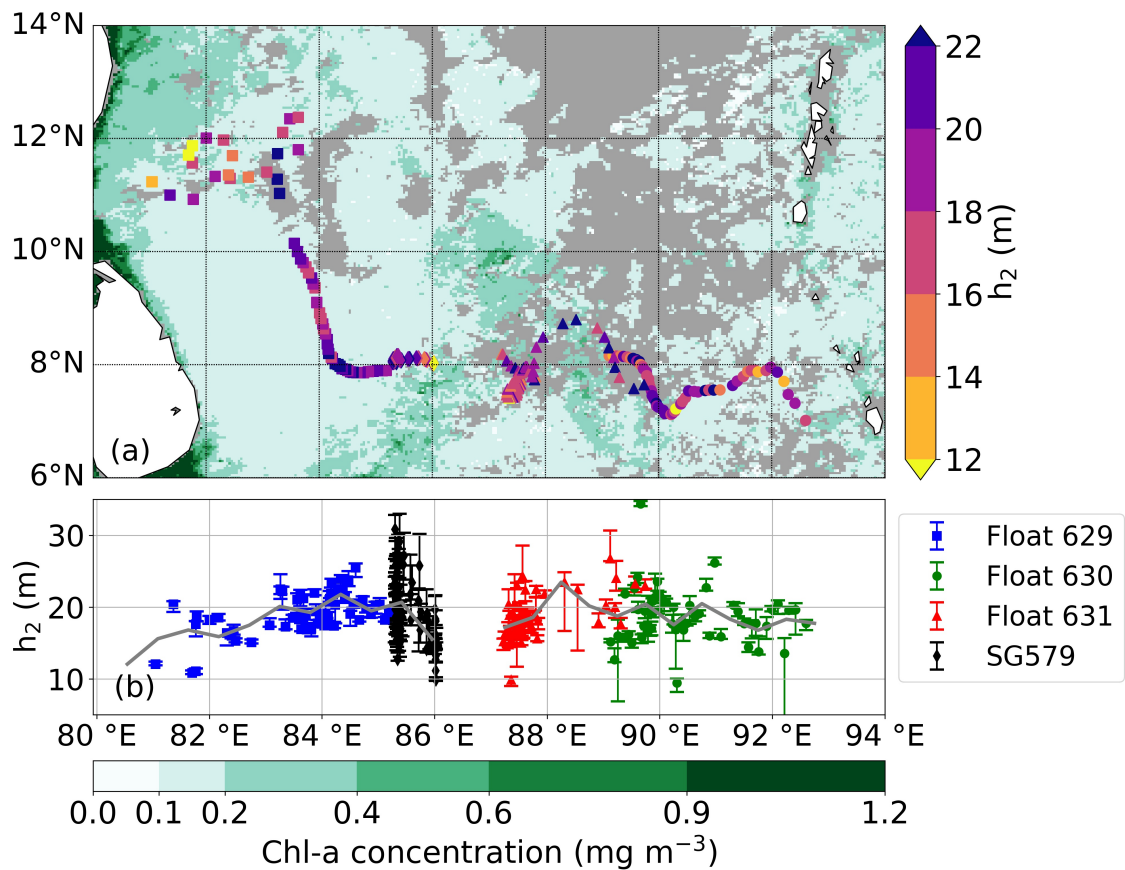


Figure 3.5: (a) Location of each profile for glider SG579 (diamond), float 629 (square), float 630 (circle) and float 631 (triangle) across the southern BoB coloured by the observed h_2 value. ESA OC CCI version 3.1 satellite composite of 4 km chlorophyll-a concentration for the month of July 2016 is shown in the background. (b) h_2 variability with longitude across the basin for glider SG579 (black diamond), float 629 (blue square), float 630 (green circle) and float 631 (red triangle). The grey solid line represents the mean h_2 value binned at 0.5° intervals.

series shows the mixed layer cooling, increasing in salinity and deepening to 40 m depth, as barrier layer thickness increases to 40 m (Fig. 3.6a and 3.6b). Surface chlorophyll concentrations are patchy as the float intercepts the SMC with average mixed layer chlorophyll concentrations varying daily between 0.1–0.4 mg m⁻³ (Fig. 3.6d). Average values of h_2 are around 16 m, although vary between 10 to 20 m, similar to the sub-daily variability of h_2 observed from the glider in the SMC.

Observations on the western side of the basin from 8–11°N show average h_2 values of 20 m compared with the average h_2 values of 16 m in the SMC (Fig. 3.5a). The timeseries of chlorophyll concentration from float 629 shows the mixed layer depth increasing from 25 m to below 50 m and the deep

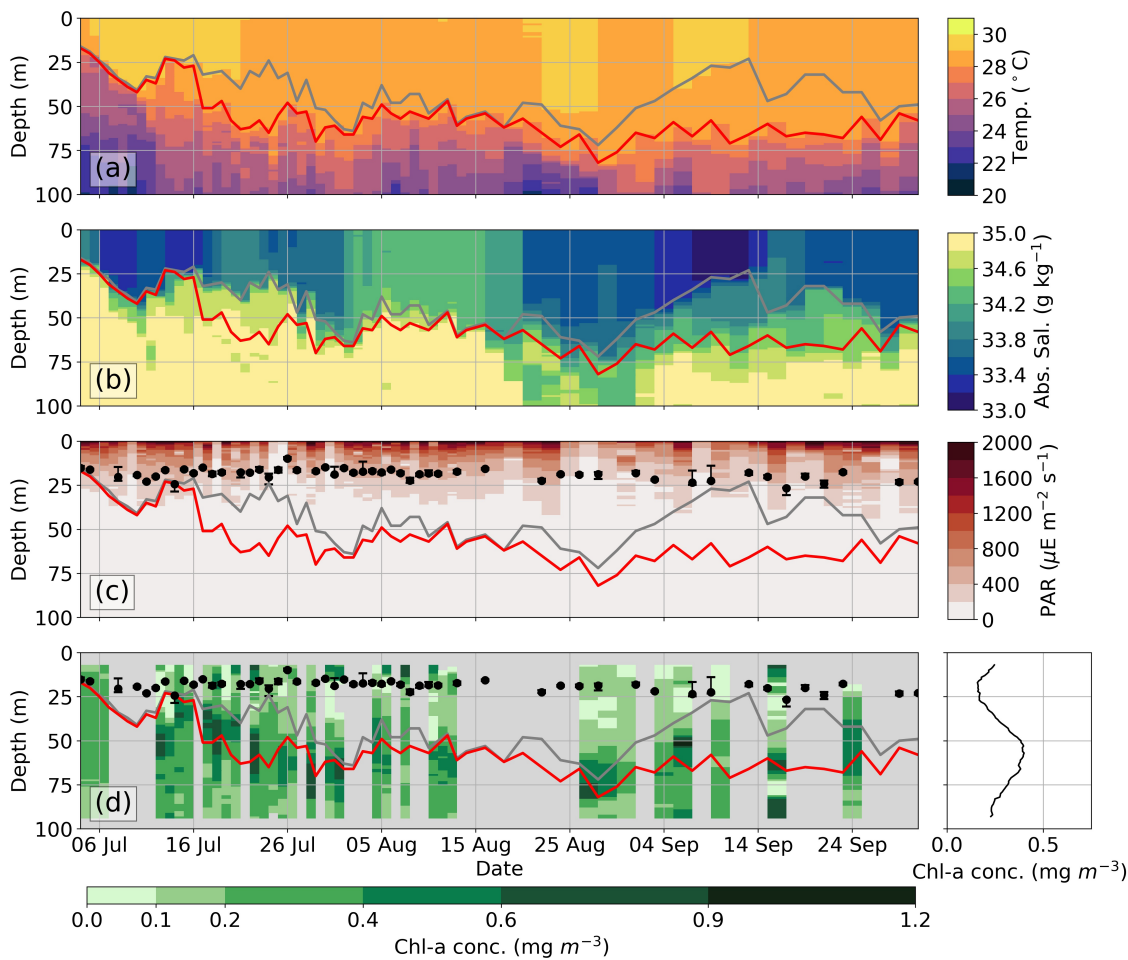


Figure 3.6: Time series of observations measured by float 631, linearly interpolated to 1 m depth intervals: (a) temperature ($^{\circ}\text{C}$), (b) absolute salinity (g kg^{-1}), (c) PAR ($\mu\text{E m}^{-2} \text{s}^{-1}$), (d) chlorophyll concentration and vertical profile of the average chlorophyll concentration (mg m^{-3}). Grey sections in the chlorophyll time series represent removed $E_d(490)$ profiles that displayed excessive noise. The black dots are scale depth values, h_2 (m). The grey line for each time series represents the mixed layer depth. The red line represents the isothermal layer depth.

chlorophyll maximum deepening from 30 m to 50 m between 16 July to 13 August (Fig. 3.7d). Away from the SLD and SMC float 629 encounters a more transparent upper ocean with increased h_2 and reduced mixed layer chlorophyll concentration of $0.2\text{--}0.3 \text{ mg m}^{-3}$. Closer to the East India continental shelf, the influence of the freshwater runoff from rivers entering the basin enhances the supply of biological material and the nutrient supply to the upper water column (Lotliker et al., 2016). Sedimentary material also reduces the solar penetrative depths and increases solar absorption in the surface layers of the coastal region. As a result, h_2 is reduced to the west of 83°E (Fig. 3.5b), associated with higher remotely sensed chlorophyll concentrations in this region (Fig. 3.5a).

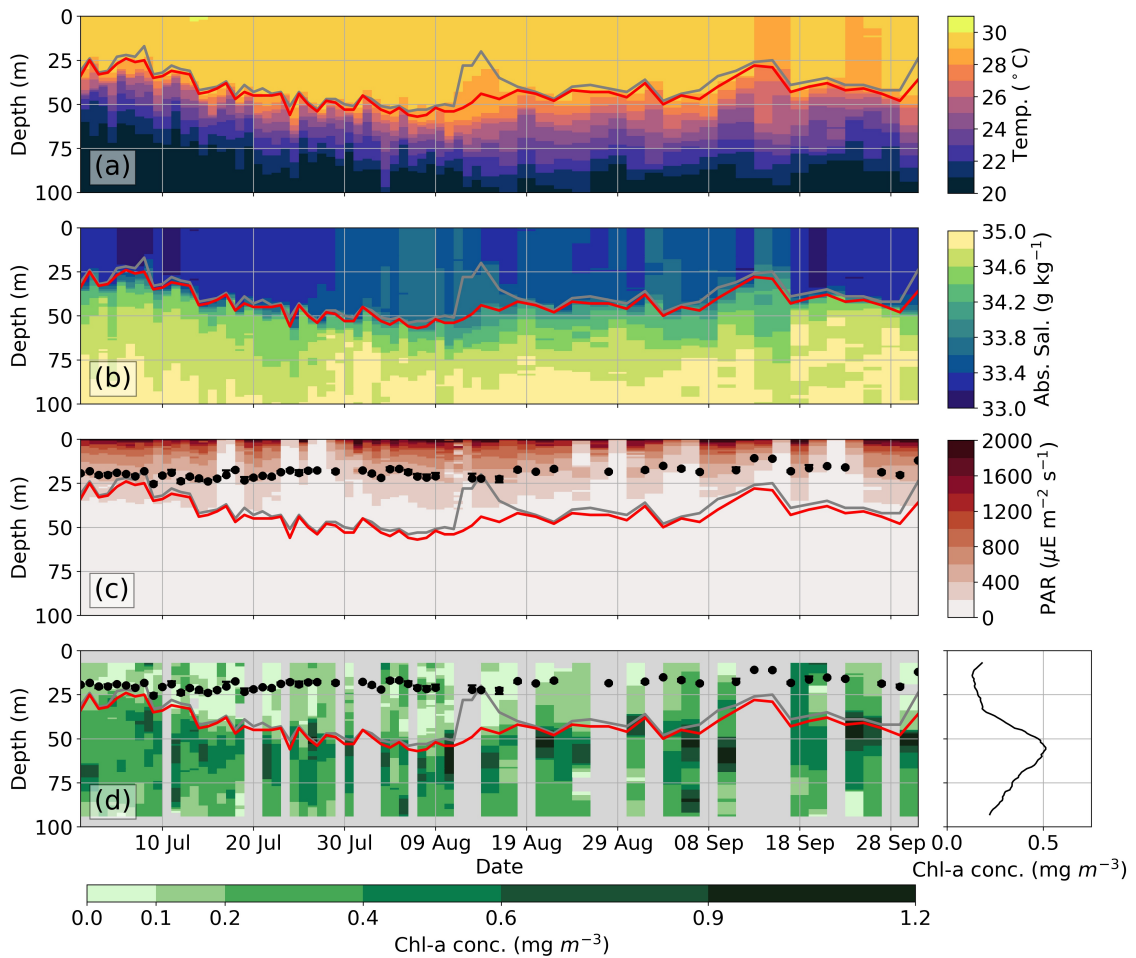


Figure 3.7: As in Fig. 3.6, but for float 629.

On 13 September, surface geostrophic velocities from satellite altimetry show an anticyclonic eddy moving eastward away from the East India coast (not shown) intercepting the path of float 629, causing the mixed layer to shoal and salinity to increase by 0.6 g kg^{-1} in two days (Fig. 3.7b). Average 0–30 m chlorophyll concentrations increase to 0.4 mg m^{-3} and corresponding h_2 values decrease to a minimum of 11 m (Fig. 3.7d).

Daily variations in salinity of 0.2 g kg^{-1} are observed by float 630 during 6–12 July, with the highest salinity recorded at 34.4 g kg^{-1} in the mixed layer and the barrier layer on 10 July (Fig. 3.8b), possibly due to eddies shearing off from the main SMC flow (Fig. 3.1d). Values of h_2 are around 16 m as average 0–30 m chlorophyll concentrations of $\sim 0.2 \text{ mg m}^{-3}$ (Fig. 3.8d) are entrained by the SMC and advected into the path of float 630 at around 89°E in early July. Towards the end of September, the SMC influence at 89°E reduces and the current shifts to the western side of the basin (Fig. 3.1f), consistent

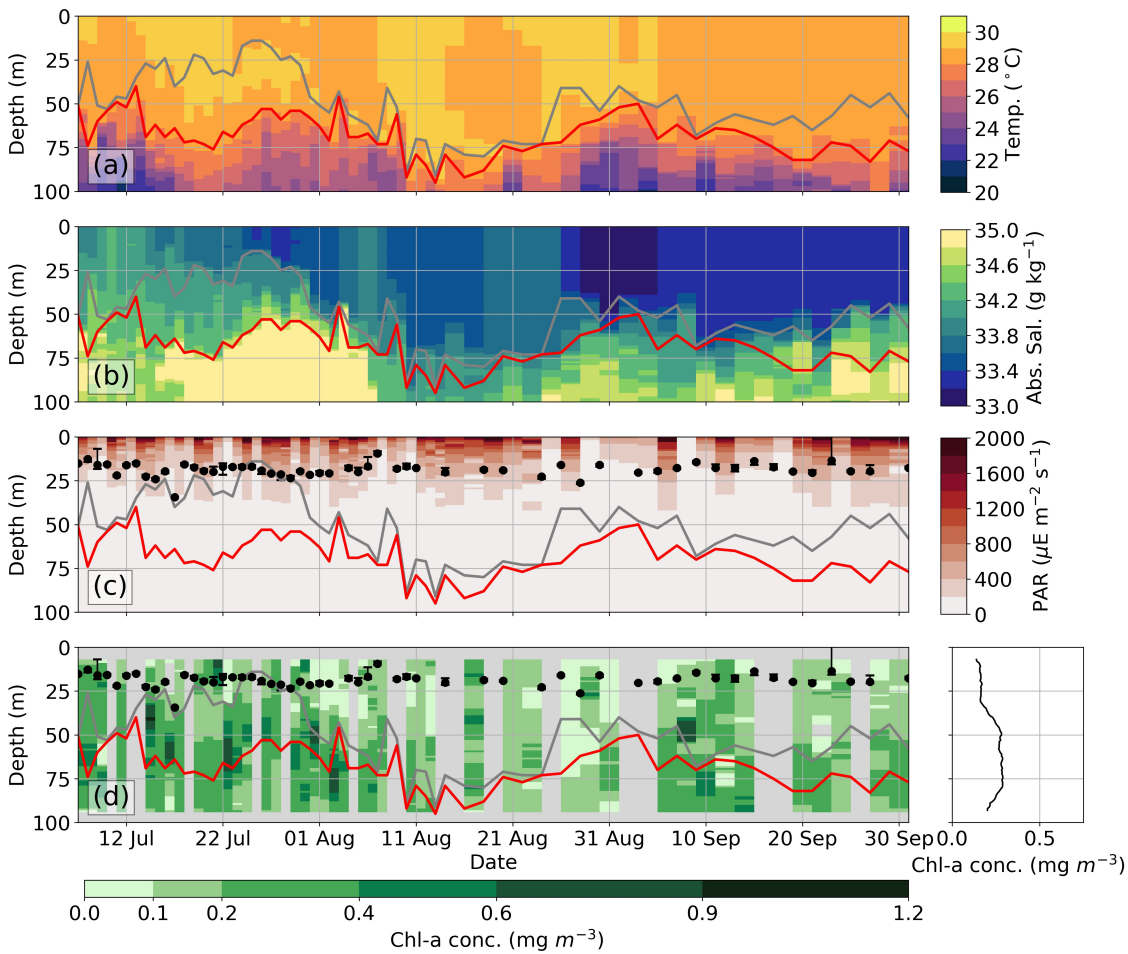


Figure 3.8: As in Fig. 3.6, but for float 630.

with climatological observations (Webber et al., 2018). Consequently, at 89°E a southeastward flow containing water from the eastern side of the basin along with some recirculated surface water from the SMC is observed (Fig. 3.1e and 3.1f). Float 631 yields h_2 values greater than 20 m (Fig. 3.6d), possibly indicating that the southeastward flow advects low surface chlorophyll concentrations from the biologically-unproductive eastern side of the BoB. We hypothesize that the displacement of the SMC to the western BoB would lead to reduced solar penetration depth in the west and increased solar penetration depth in the east during the summer.

3.4 Scale depth and chlorophyll concentration relationship with implications for BoB SST and climate

3.4.1 Relationship between scale depth and chlorophyll concentration

Visible radiation in the upper ocean decreases by approximately 63% ($1 - e^{-1}$) from the surface to a depth equal to one scale depth. Glider observations show that over 80% of PAR is absorbed to a depth of 30 m (Fig. 3.3c). The chlorophyll concentration of the surface layer, where the majority of visible radiation is absorbed, is a key control on the amount of visible radiation absorbed and thus on the radiant heating rate of the surface layer. We examine the relationship between the average chlorophyll concentration in the surface layer and h_2 , both observed by the glider. The average mixed layer depth in the glider time series (Fig. 3.3d) and the approximate observed maximum h_2 is approximately 30 m. Hence, we calculate the average chlorophyll concentration in the surface layer between 0 and 30 m depth. We do not derive a relationship between chlorophyll and h_2 from the float data, since the float chlorophyll concentration is itself derived from profiles of light absorption ($E_d(490)$) or K_d (inverse of h_2), using a known empirical relationship from Morel and Maritorena (2001). Instead, we derive an unknown relationship between chlorophyll and h_2 from the glider data, since the glider chlorophyll concentration is measured from chlorophyll fluorescence, which is independent of K_d , and hence h_2 .

As expected, h_2 is inversely related to chlorophyll concentration (Fig. 3.9). Observed average chlorophyll concentrations from glider SG579 vary by a factor of 6 during the BoBBLE campaign. Larger h_2 values of ~ 20 m are associated with lower mixed layer chlorophyll concentrations of less than 0.1 mg m^{-3} ; smaller h_2 values of ~ 12 m are associated with higher mixed layer chlorophyll concentrations of 0.5 mg m^{-3} .

The observations compare well with two commonly-used double exponential parameterisations in ocean GCMs relating light absorption to chlorophyll concentration (Fig. 3.9; Table 3.1), from Morel and Antoine (1994) [MA94] and Ohlmann (2003) [O03]. We assume for the O03 two-band solar absorption scheme that the incident angle of solar radiation on the ocean surface, $H(\theta)$, and the cloud index, $G(\text{ci})$, are both zero (see Equation B.3 in Appendix B). Both the

Parameterisation	r^2	RMSE (m)
MA94	0.16	0.24
O03	0.16	0.24

Table 3.1: Two parameterisations (MA94 and O03) and their determination coefficients (r^2) and root-mean-square errors (RMSE) after fitting to ocean glider (SG579) observed scale depth, h_2 , and average 0–30 m mixed layer chlorophyll concentrations, [Chl] (Fig. 3.9)

parameterisations define a power law dependence in scale depth as a function of chlorophyll, with the greatest change in scale depth occurring at lower chlorophyll concentrations, between 0.08–0.1 mg m⁻³, and the smallest change in scale depth occurring at higher chlorophyll concentrations above 0.2 mg m⁻³ (Fig. 3.9). The r^2 of O03 and MA94 against the observations show that these functions fit similarly to the observed h_2 . The parameterisations predict scale depths to be within ~ 3.6 m of the observed h_2 . For chlorophyll concentrations larger than 0.2 mg m⁻³ MA94 and O03 predict scale depths smaller than the observed h_2 , although the number of observations above this concentration is limited. From our results, we cannot definitively select the most appropriate parameterisation given the spread and uncertainty in the h_2 estimates.

3.4.2 Implications for BoB SST and climate

The observed h_2 for each glider and float timeseries varies by a factor of two (Fig. 3.4; e–h). The 5th and 95th percentile of all observed h_2 values are 14 m and 26 m respectively. With the majority of solar radiation absorbed in the surface mixed layer, then the difference between $h_2 = 14$ m and $h_2 = 26$ m would have significant effects on the radiant heating of the surface layer and SST. We can compare the impact that these two values of h_2 would have on the temperature change for an idealized water column. The temperature change is related to the daily average solar radiant heating rate of a layer of upper ocean with thickness, H , as

$$\left. \frac{dT}{dt} \right|_Q = \frac{\overline{Q_0} - \overline{Q_H}}{\rho c_p H} = \frac{\overline{Q_0} - (1 - R)\overline{Q_0}e^{-\frac{H}{h_2}}}{\rho c_p H} \quad (3.1)$$

where we specify $H = 30$ m to represent the average mixed layer depth from the glider, $\rho = 1021$ kg m⁻³ to represent the average density of seawater in the upper 30 m from the glider dataset and $c_p = 4100$ J kg⁻¹ K⁻¹ to represent

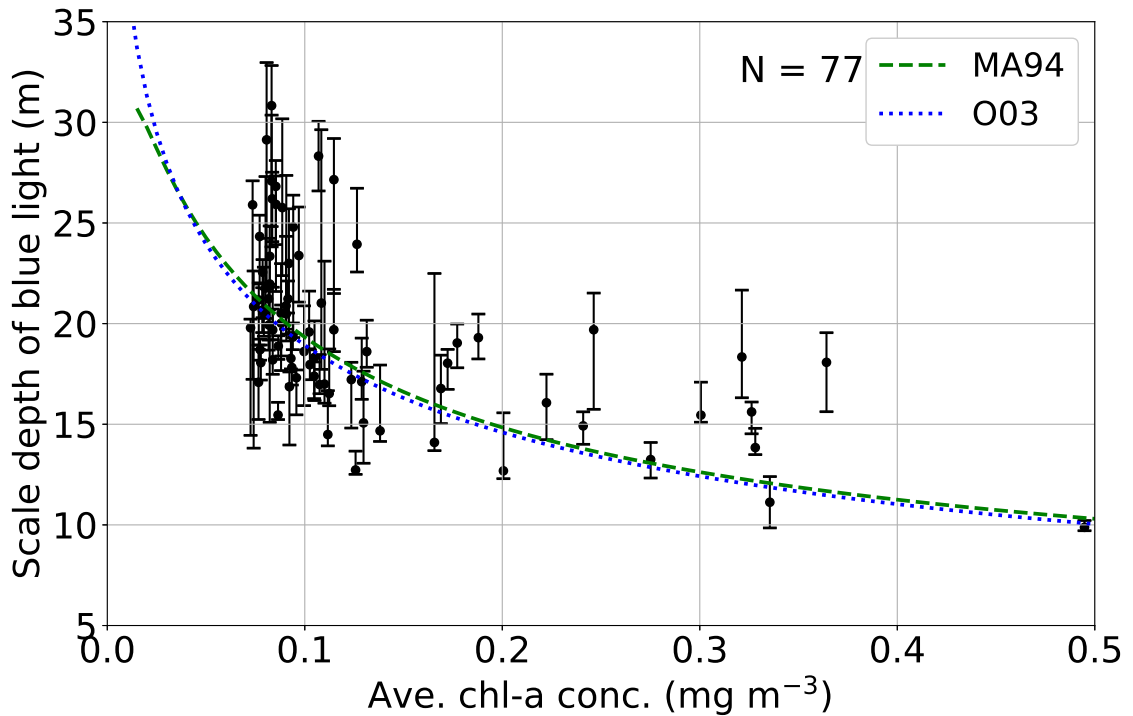


Figure 3.9: Observed h_2 against average chlorophyll-a concentration between the surface to 30 m depth from glider SG579 (black circles). Parameterisations of scale depth of blue light (equivalent to h_2) for chlorophyll concentrations between 0–0.5 mg m^{-3} are presented with the observational data: Morel and Antoine (1994) [MA94] (dashed green line) and Ohlmann (2003) [O03] (dotted blue line).

the specific heat capacity of sea water. The daily average net solar irradiance absorbed in this mixed layer is calculated by taking the difference between the daily average net solar irradiance incident just below the ocean surface, $\overline{Q_0}$, and daily average net solar irradiance at the base of the mixed layer, $\overline{Q_H}$. At depths greater than 5 m, we assume all red light is absorbed and $\overline{Q_H}$ is then the blue light radiation flux that penetrates the base of the mixed layer.

The daily average net solar irradiance incident on the column surface is estimated to be 280 W m^{-2} based on solar irradiance measurements during clear sky conditions during the observation period (Vinayachandran et al., 2018). For the purposes of this calculation, we ignore the effects of albedo, advection, entrainment and mixing, as well as any atmospheric feedbacks from changing SST. The average observed h_2 for July, August and September is indicative of Jerlov water type IB where $h_2 = 17 \text{ m}$ (Fig. 3.4; e–h), hence we use a constant value of $R = 0.67$ for the same Jerlov water type. If the water column has an h_2 value of 26 m, then the solar irradiance absorbed in the upper 30 m would be 251 W m^{-2} with 29 W m^{-2} absorbed below 30 m. If the water column has an

h_2 value of 14 m then the solar irradiance absorbed in the upper 30 m would be 269 W m^{-2} with 11 W m^{-2} absorbed below 30 m. Using Equation 3.1 the increased absorption of solar irradiance in the mixed layer when h_2 decreases from 26 m to 14 m leads to a $0.35^\circ\text{C month}^{-1}$ increase in radiant heating rate. The increase in radiant heating rate confirms that chlorophyll-induced heating over the observed range of h_2 will lead to significantly different values of SST, assuming no atmospheric feedbacks.

These idealized calculations are now extended to investigate further the influence of near-surface chlorophyll concentrations on SST and heat distribution of the upper ocean. A one-dimensional K-profile parameterisation (KPP) model (Large et al., 1994) is used to run two idealized simulations with two constant h_2 values of 14 m and 26 m respectively throughout July 2016. The model has a simple two-band solar radiation scheme, identical to Paulson and Simpson (1977), to replicate the transmission of solar radiation in the upper ocean. Initial KPP sensitivity experiments, not presented in this Chapter, show that the influence of R on SST is not negligible. Hence, two constant values of R from Paulson and Simpson (1977) are chosen with $R = 0.58$ when $h_2 = 26$ m (Jerlov water type I), and $R = 0.77$ when $h_2 = 14$ m (Jerlov water type II). The influence of h_1 on SST is negligible and is fixed at 1 m (Jerlov water type IB) when h_2 is 26 m and 14 m. Horizontal advection, Ekman pumping and atmospheric feedbacks are absent from the model.

The mean vertical profiles of temperature and salinity from the glider for 1–10 July provide the subsurface (0–1000 m depth) initial conditions. Hourly solar shortwave flux is derived from the downwelling shortwave radiation observed every 2 minutes from the RAMA (Research Moored Array for African-Asian-Australian Monsoon Analysis and Prediction; McPhaden et al., 2009) mooring at 8°N , 90°E in the southern BoB approximately 4° east of the glider location. The hourly rainfall data are interpolated from three-hourly rainfall rate from the Tropical Rainfall Measuring Mission (TRMM) for the same location. The sensible and latent heat fluxes and the surface wind stress are sourced from TropFlux (Kumar et al., 2012) at a daily resolution, which are then linearly interpolated to an hourly resolution. TropFlux is used as it provides an accurate representation of heat fluxes during the boreal summer in the BoB (Sanchez-Franks et al., 2018). Evaporation rates are calculated from the latent heat flux from TropFlux at the same hourly resolution. The model is spun up for one month using the surface forcing data for June 2016. For this spin up period, the scale depth of blue light was fixed at the Jerlov water type IB value

of $h_2 = 17$ m. After the spin up, the model was run through July 2016 in two configurations, one with $h_2 = 14$ m and one with $h_2 = 26$ m.

The BoBBLE campaign took place during a suppressed period of convection or a break phase in the South Asian monsoon. The South Asian monsoon is subject to active-break cycles driven by the Boreal Summer Intraseasonal Oscillation (BSISO; Wang and Xie, 1997), which are strongly influenced by air-sea interactions (Sengupta et al., 2001). Associated with this break phase, no precipitation is recorded, and solar shortwave flux remains high during the campaign between 4–15 July (Fig. 3.10b and 3.10c), allowing for strong diurnal heating of the ocean surface during this period. By 15 July, precipitation increases (Fig. 3.10c) as deep atmospheric convection enters the campaign region marking the transition into an active phase of the BSISO.

The experiment demonstrates that changing h_2 from 26 m to 14 m leads to an increase in SST of 0.37°C by the end of July 2016 (Fig. 3.10d). The average mixed layer depth is 32 m and remains relatively constant during July. Hence, the previous idealized calculation is relevant here as we estimated a similar amount of radiant heating for a mixed layer of similar thickness. From 1–15 July the SST from the $h_2 = 14$ m simulation warms at the greatest rate of $0.04^\circ\text{C day}^{-1}$, compared with $0.02^\circ\text{C day}^{-1}$ for the $h_2 = 26$ m simulation. From 15 July onwards, during an active phase of the BSISO, SST warming for the $h_2 = 14$ m simulation is just $0.01^\circ\text{C day}^{-1}$, compared with the slight SST cooling in the $h_2 = 26$ m simulation. Decreased solar penetration depth leads to increased absorption of solar radiation over a shallower depth of ocean. Hence, the mixed layer warms and the water below the mixed layer cools as less solar radiation penetrates deeper in the water column (Fig. 3.10f).

A blue-light scale depth value of 14 m is likely to occur within the SMC and SLD due to the higher surface chlorophyll concentrations. The width of the SMC is approximately 300 km (Webber et al., 2018) and surface chlorophyll concentrations begin in April and typically peak in July (Lévy et al., 2007) resulting in a considerable area and time-period of biologically-induced surface warming. Likewise, the Indian coastal region in the west and the Andaman and Nicobar Islands in the east also display smaller solar penetration depths, further widening the region impacted by biologically-induced surface warming.

The additional biologically-induced surface warming is likely to be non-uniform across the basin and subject to variability during the summer season. As identified by the observations from the glider and float 631, the

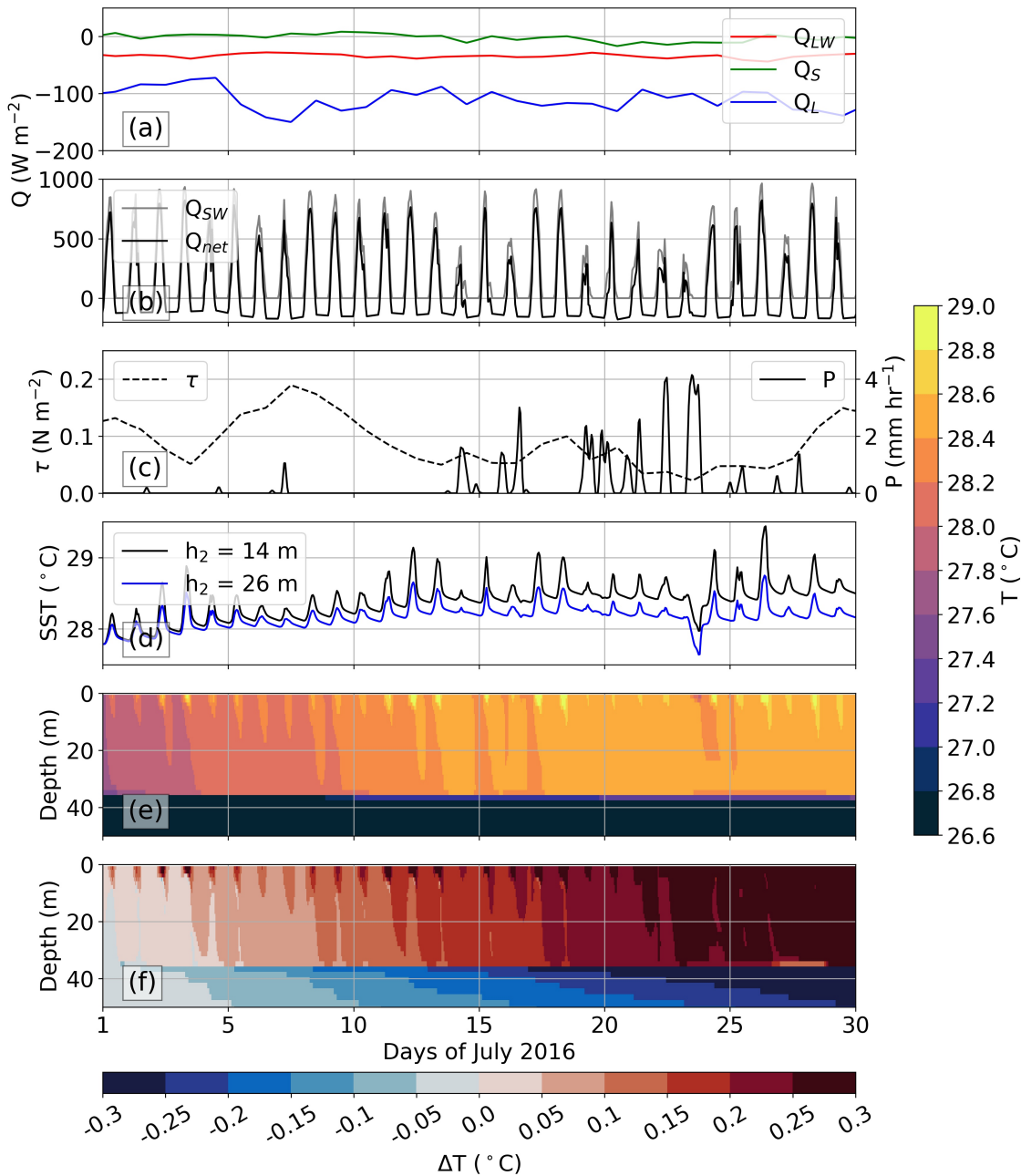


Figure 3.10: (a) Hourly surface longwave (red line), sensible (green line) and latent (blue line) heat fluxes (W m^{-2}) for July 2016; (b) Hourly surface shortwave (grey line) and net (black line) heat fluxes (W m^{-2}) for July 2016; (c) Resultant wind stress (dashed black line; N m^{-2}) and precipitation rate (solid black line; mm day^{-1}); (d) Time series of model SST when h_2 is 14 m (black line) and h_2 is 26 m (blue line); (e) Depth-time section of temperature from the $h_2 = 14$ m simulation ($^{\circ}\text{C}$); (f) Depth-time section of temperature difference calculated as T_{14m} minus T_{26m} ($^{\circ}\text{C}$).

SMC contains patches of higher surface chlorophyll concentration within the main flow and within the eddies and filaments that split off from the SMC. The amount of chlorophyll concentration within the SMC depends on its strength and location, which affect the entrainment of phytoplankton from the coastal region of Sri Lanka (Vinayachandran et al., 2004). The SMC strength and location are influenced by the strength of the SLD and the propagation of Rossby waves from the eastern side of the basin (Webber et al., 2018). Hence, if conditions are conducive for a strong SMC intercepting the biologically-productive coastal regions from June to July, then surface chlorophyll concentration increases and enhances surface warming. The SLD also fluctuates in strength and position depending on the local wind stress curl and the propagation of Rossby waves (Webber et al., 2018). Variability in SLD peak strength determines the upwelling of nutrients to the sun-lit layers that sustain high surface chlorophyll concentrations (Thushara et al., 2019). Hence, this would vary solar penetration depths and periods of enhanced surface warming in the SLD throughout the summer.

The modulation of SST has important feedbacks to the Indian monsoon system. The SST gradients strongly influence surface pressure gradients that can then initiate low-level convergence (Lindzen and Nigam, 1987), resulting in the vertical advection of moisture and heat that triggers strong convection. The higher the SST, the more moisture and heat exchanged to the atmosphere, which can shorten the response time between the occurrence of the highest SST and following precipitation events (Roxy et al., 2013). The SMC and SLD region is known as the southern BoB “cold pool”, caused by intense cooling periods during the onset phases of the South Asian monsoon (Das et al., 2016). The high surface chlorophyll concentrations in the SMC and SLD could be acting to increase SST and potentially to reduce SST gradients, potentially altering the location of convergence and strength of convection across the BoB. The additional presence of a thick oceanic barrier layer positioned below a thin mixed layer inhibits cooling due to entrainment and results in SST being primarily controlled by surface turbulent heat fluxes across much of the BoB (Duncan and Han, 2009). The glider and float observations show a small barrier layer (thickness ~ 1 m) within the SLD and SMC (Fig. 3.3a and 3.3b). The central-eastern BoB (89°E) displayed the thickest barrier layers of up to 50 m in July (Fig. 3.8a) and September (Fig. 3.6a) and thin mixed layer depths of around 30 m. Reduced scale depths in this latter region have the potential to increase SST and strongly influence surface fluxes exchanged to the atmosphere above.

The enhanced surface warming during a 15-day break phase in the BSISO, as shown from the $h_2 = 14$ m simulation, demonstrates the influence that high surface chlorophyll concentrations could have on SST intraseasonal variability (10–30 day time scales). The intraseasonal SST anomalies during the start of the BoBBLE campaign (1–15 July) are $\sim 0.6^\circ\text{C}$ higher (Vinayachandran et al., 2018) and previous studies have found the June–July intraseasonal SST variability to be less than 1°C (Duncan and Han, 2009; Vinayachandran et al., 2012). Our simulations suggest that higher surface chlorophyll (decreasing h_2 to 14 m) could generate an SST perturbation equal to $\sim 60\%$ of the intraseasonal SST variability that is observed during the first half of the BoBBLE campaign. This is a significant modulation of SST and shows the potential influence of varying chlorophyll concentrations on SST in the BoB.

The SST intraseasonal variability is strongly coupled to active and break periods of the BSISO (Fu et al., 2003), and even partly contributes to the northward and northwestward propagation of convective bands (Gao et al., 2019). Typically, positive (negative) SST anomalies are ahead of (behind) the band of convection, as conditions are calmer (windier), and there is more (less) incoming shortwave radiation. Turbulent heat fluxes are reduced (increased), and smaller (larger) ocean mixing shoals (deepens) the mixed layer (Roxy et al., 2013). The $h_2 = 14$ m simulation showed increased warming of the ocean surface and hence a more rapid recovery of SST anomalies during the BSISO break period. This would increase the turbulent heat fluxes to the atmosphere, destabilize the atmospheric boundary layer, and potentially trigger convection for the following active period sooner. Fig. 3.1c and 3.1d shows that surface chlorophyll concentrations are particularly low in the central BoB at 8°N at the beginning of July, during the break period. However, surface chlorophyll concentrations increase by the start of August as the SMC intercepts the chlorophyll blooms off the southern coast of Sri Lanka. The timing of the chlorophyll blooms in the central BoB relative to the break periods of the BSISO is an additional factor to consider when modelling intraseasonal convective events.

3.5 Conclusions

Observed and inferred chlorophyll concentrations show a deep chlorophyll maximum at 50 to 80 m across the Southern BoB during the southwest monsoon,

with higher near-surface chlorophyll concentrations occurring intermittently within the SMC, SLD and coastal regions. The average blue-light scale depth, h_2 , for July, August and September is indicative of Jerlov water type IB ($h_2 = 17$ m). The h_2 values display temporal and spatial variability on sub-daily timescales, a consequence of sub-daily variability of surface chlorophyll concentrations entrained by the SMC. In the SLD and SMC, where high surface chlorophyll concentrations are advected into the southern BoB, h_2 is generally shallower. The bifurcation of the SMC, and hence of the chlorophyll entrained in its flow, reduces h_2 values to the south and east of the SMC as filaments and eddies break off from the main current. Away from the SMC, the upper ocean is more transparent with h_2 values of more than 20 m. In coastal regions, h_2 values occasionally reduce to 11 m due to high surface chlorophyll concentrations, as well as other chlorophyll pigments, detritus material and other biological constituents.

The O03 and MA94 scale depth parameterisations demonstrate similar correlation and RMSE when compared to observed h_2 and average 0–30 m chlorophyll concentrations. Both parameterisations demonstrate a power law relationship of scale depth as a function of chlorophyll and predict scale depths to be within ~ 3.6 m of the observed h_2 , although both tend to underestimate h_2 for chlorophyll concentrations of $0.2\text{--}0.5$ mg m^{-3} . The spread and uncertainty of the observed h_2 means we cannot robustly select the most appropriate parameterisation to predict scale depth in this region.

Idealized KPP simulations show that changing h_2 from 14 m to 26 m would lead to an SST trend difference of $0.37^\circ\text{C month}^{-1}$. The $h_2 = 14$ m simulation, corresponding to greater surface chlorophyll concentrations, shows an increase in SST of $0.04^\circ\text{C day}^{-1}$ during the BSISO break phase, which is equivalent to $\sim 60\%$ of the intraseasonal SST variability that is observed during the first half of the BoBBLE campaign. If high surface chlorophyll concentrations advected by the SMC coincide with the BSISO break phase then the SST would recover more rapidly, amplifying the subsequent active phases through increased turbulent heat fluxes into the atmospheric boundary layer. This underlines the importance of accounting for near-surface chlorophyll and its variability in studies of the BSISO.

The 300 km-wide SMC and its continuous presence during summer monsoon means that a large area of the BoB would have regions of high surface chlorophyll that would warm more rapidly than regions of low surface chlorophyll, changing the horizontal temperature gradient,

resulting in varied regions of moisture convergence and convection. Further simulations using coupled atmosphere-ocean GCMs are required to investigate biologically-induced modulation of SST in the southern BoB, and its impact on the spatial and temporal distribution of monsoon rainfall. These simulations should include temporally and spatially varying scale depths for light absorption to replicate the observed variability of surface chlorophyll across the basin. Only then could the effect of chlorophyll on the summer monsoon climate be fully quantified.

Chapter 4

The spatial and temporal variability of solar penetration depths in the Southern Ocean

4.1 Introduction

This chapter focuses on the Sub-Antarctic Zone (SAZ) in the Atlantic sector of the Southern Ocean. The SAZ is located in the ACC and is bounded between the Subtropical Front to the north (STF; $\sim 40^\circ\text{S}$) and the Sub-Antarctic Front to the south (SAF; $\sim 50^\circ\text{S}$). During austral winter, deep MLDs and low incoming solar radiation result in low chlorophyll concentrations between 30 and 60°S ($< 0.3 \text{ mg m}^{-3}$; Fig. 4.1a). During austral summer, shallow MLDs and high incoming solar radiation result in high chlorophyll concentrations between 30 and 60°S ($> 1.2 \text{ mg m}^{-3}$; Fig. 4.1d). The band of high chlorophyll concentration at approximately 40°S shows the location of the STF and the band of high chlorophyll concentration at approximately 50°S shows the location of the northern branch of the SAF (Fig. 4.1d). Chlorophyll concentrations in the SAZ show strong seasonal to subseasonal and synoptic to submesoscale variability as filaments and eddies form and dissipate along the fronts, altering upper-ocean stratification, in-water light conditions and nutrient availability (Swart et al., 2015). The corresponding solar absorption and radiant heating rates in the upper ocean of the SAZ are expected to be as variable as the regional chlorophyll concentration.

The upper ocean of the SAZ in the Atlantic sector is characterised by the

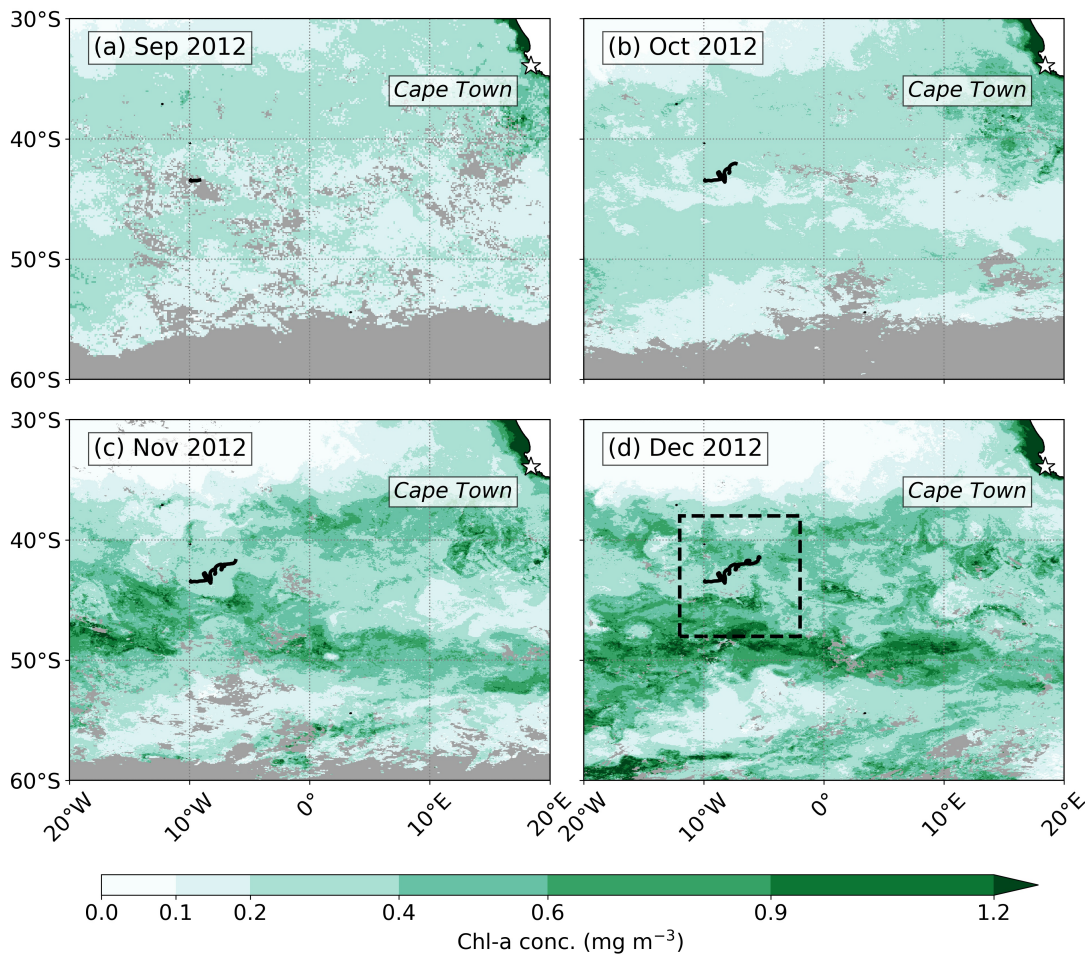


Figure 4.1: Monthly chlorophyll-a concentration (mg m^{-3}) in the Southern Ocean at 4 km horizontal resolution obtained from ESA OC CCI version 4.0: (a) September 2012; (b) October 2012; (c) November 2012; (d) December 2012. The solid black line shows the trajectory of ocean glider SG574 during the SOSCEX deployment. The dashed black box outlines the latitudinal extent of the Hovmöller diagrams shown in Fig. 4.3 and Fig. 4.4. The grey shading represents missing satellite data.

Sub-Antarctic Mode Water and the Antarctic Intermediate Water, which forms the southern part of the subtropical gyre of the South Atlantic and has a predominantly eastward surface flow (Talley et al., 2011). The cool, upwelled Upper Circumpolar Deep Water south of the SAF move northwards through meridional Ekman and eddy transport. The positive net heat flux from solar radiant heating and warm, maritime air, warms the cool upwelled waters. This process of converting cool, dense upwelled waters into warm, less dense surface waters forms the upper part of the meridional overturning circulation. The strength of the overturning in the SAZ depends on the buoyancy flux gain in the upper ocean (Morrison et al., 2011).

The buoyancy flux gain through solar radiative heating has been shown to be affected by chlorophyll concentrations. Groeskamp and Iudicone (2018) found that using chlorophyll-dependent parameterisations (e.g. Morel and Antoine, 1994; Ohlmann, 2003) improved the horizontal distribution of chlorophyll-perturbed solar penetration depths, which improved global air-sea flux variations and thus water mass transformations that are essential for the meridional overturning circulation. Some upper-ocean heat budget studies of the ACC do not include the positive net heat flux effects of chlorophyll concentration and instead use constant optical parameters from the Jerlov water types (e.g. Tamsitt et al., 2016). Groeskamp and Iudicone (2018) demonstrates the need to include the spatial and temporal effects of biological heating for accurate heat flux products used in ocean GCMs. However, their study lacked the quantification of the seasonal and subseasonal effects of biological heating specific to the SAZ region, which would be potentially important for meridional overturning circulation simulations.

Previous studies that were mentioned in Chapter 1 (e.g. Manizza et al., 2005; Gnanadesikan and Anderson, 2009; Patara et al., 2012) have shown that global chlorophyll concentrations in coupled GCM simulations perturb the upper-ocean physical and dynamical properties and regional climate of the SAZ. However, there are drawbacks to the experimental design and results of these coupled GCM studies.

Firstly, using global chlorophyll concentration increases the difficulty in identifying the causality of perturbations in the ocean and atmosphere. Such perturbations could be directly or indirectly caused by local or remote chlorophyll perturbations. Mid- to high-latitude regions are particularly susceptible to tropical SST anomalies, as these anomalies alter the strength and location of tropical convective activity, which can alter upper tropospheric winds and excite Rossby waves that influence mid- to high-latitude climate (Barsugli and Sardeshmukh, 2002). Hence, chlorophyll-perturbed SST in the tropics would indirectly influence SAZ climate, masking the direct effect of chlorophyll-perturbed SST on SAZ climate.

Secondly, these studies compared oceanic and atmospheric variables from two model runs, where one run had "clear" water (e.g. constant global h_2 of 23 m) and the other run had seasonally varying chlorophyll concentrations that were derived from satellite measurements or from a biogeochemistry model. Comparing runs with very large differences in solar penetration depths would undoubtedly lead to large differences in physical variables such as SST.

However, such large variations from clear water to turbid water are unrealistic and do not represent the actual variations in solar penetration depths that are observed in the SAZ.

Finally, these coupled GCM studies show the average annual and seasonal oceanic and atmospheric changes from climate-length simulations (ranging from 10 to 300 years), smoothing out year-to-year seasonal and subseasonal effects of chlorophyll concentration. Thus, the direct effect of SAZ chlorophyll on radiant heating and SST on seasonal to subseasonal timescales remains unclear.

This chapter aims to investigate: (i) the seasonal to subseasonal variability of solar penetration depths and corresponding chlorophyll concentrations during the spring and summer chlorophyll blooms in the SAZ; (ii) to propose and compare a new chlorophyll-dependent parameterisation with two other parameterisations; (iii) to examine the seasonal to subseasonal influence of spring and summer chlorophyll blooms on radiant heating rates, and to discuss its potential implications for net surface heat fluxes, SST, regional climate and the meridional overturning circulation.

High-resolution ocean glider observations from the 2012/13 Southern Ocean Seasonal Cycle Experiment (SOSCEX; Swart et al., 2012) are used to analyse the physical, biological and optical properties of the SAZ upper ocean on seasonal to subseasonal timescales. Two ocean gliders, SG573 and SG574, owned by the University of Cape Town, were deployed by PI Sebastiaan Swart from RV S.A. Agulhas II as part of the first SOSCEX campaign. A total of four SOSCEX campaigns have been completed between 2012 and 2016. Observations from glider SG573 have been analysed by several studies (e.g. Swart et al., 2015; Thomalla et al., 2015; du Plessis et al., 2017; Little et al., 2018; du Plessis et al., 2019), whereas observations from glider SG574 have been mostly overlooked. This chapter focuses on the dataset from glider SG574 from the first SOSCEX deployment. Observations from glider SG574 were processed by Sebastiaan Swart and kindly provided by Prof. Marcello Vichi, based at the Department of Oceanography at the University of Cape Town.

A description of the methodology, including the glider and remotely sensed datasets, is presented in Section 4.2. Section 4.3 presents the results of the satellite and glider observations, with further analysis on the relationship between observed chlorophyll concentration and optical parameters. Section 4.4 provides a discussion of the implications of chlorophyll on radiant heating rates and conclusions are given in Section 4.5.

4.2 Methods

4.2.1 Ocean Glider data

Seaglider SG574 was deployed in the southeast Atlantic at 43°S, 11°W on 25 September 2012 and retrieved on 15 February 2013. Glider SG574 performed a zig-zag trajectory through the water column from the surface to 1000 m depth, completing a full dive in 4 to 5 hours. The number of dives for this deployment was 683 dives. Glider SG574 was equipped with the same sensors as glider SG579 that was deployed during BoBBLE. A summary of the sensors on SG574 is presented in Table 2.1 in Chapter 2.

The processing and calibration of the CT data was already completed following the methodology of Swart et al. (2015). The raw data were initially processed using the University of Washington's base station toolbox that corrected for thermal lags and converted the CT dataset into conservative temperature and absolute salinity (IOC et al., 2010). Swart et al. (2015) further checked and corrected the absolute salinity measurements for conductivity sensor drift.

Swart et al. (2015) witnessed bio-fouling on the outside of SG574. The growth of goose barnacles on the unpumped CT sensor reduced the flow of water through the sensor, which relies on a continuous flow rate for reliable measurements. Bio-fouling also affected the optical sensors. The final 63 days of the processed glider data were removed due to erroneous salinity and optical measurements.

The MLD in this chapter was defined as the depth where the change in temperature from a reference depth of 10 m exceeds a threshold of 0.2°C ($\Delta T = 0.2^\circ\text{C}$, de Boyer Montégut et al., 2004). This MLD definition has been used by previous SOSCEX glider studies (e.g. Swart et al., 2015; Thomalla et al., 2015; Little et al., 2018). However, some SOSCEX modelling studies (e.g. du Plessis et al., 2017; du Plessis et al., 2019) have defined the MLD as the depth where the change in density from a reference depth of 10 m exceeds a threshold of 0.03 kg m⁻³ ($\Delta\rho = 0.03 \text{ kg m}^{-3}$, de Boyer Montégut et al., 2004). Swart et al., 2015 outlined two reasons as to why the temperature based MLD definition is used by the previous glider studies: (i) the salinity data, and thus density data, became increasingly contaminated by bio-fouling during the summer, (ii) there were still thermal lag errors and spiking in the salinity measurements. The salinity spiking caused by biofouling and thermal lags produced false and

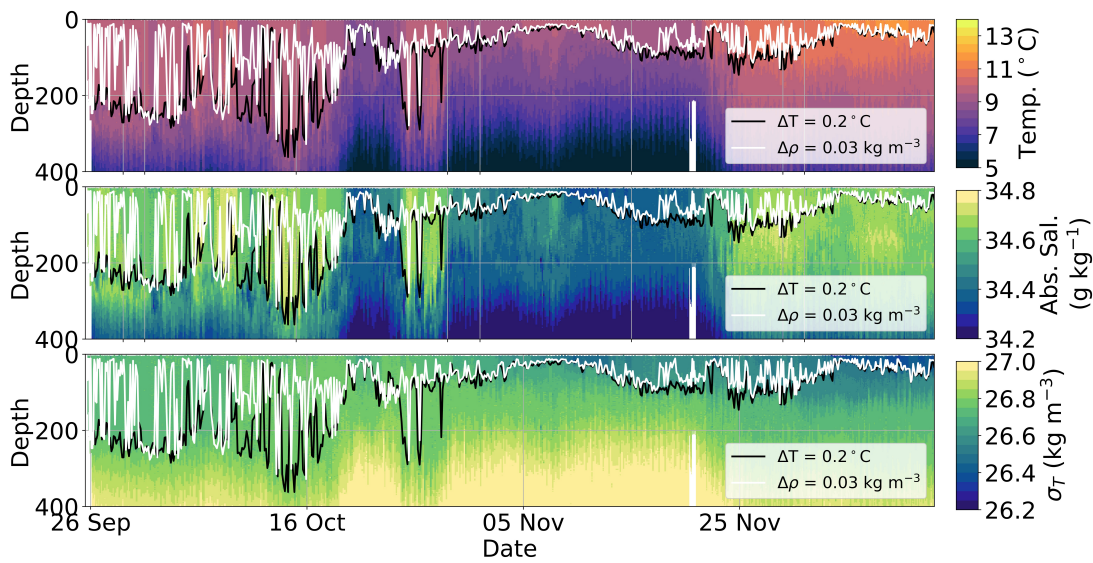


Figure 4.2: Comparison of two MLD definitions using a temperature (black line) and density (white line) based criteria. Top panel shows conservative temperature ($^{\circ}\text{C}$), middle panel shows absolute salinity (g kg^{-1}) and bottom panel shows density (kg m^{-3}).

unrealistic MLD determinations when using a density based MLD definition (white line; Fig. 4.2). Using a temperature based MLD definition reduced the false MLD determinations and was therefore used for this study (black line; Fig. 4.2).

a. PAR data

The raw PAR measurements that were provided were initially factory calibrated, but no further quality control was carried out. Hence, the methodology described in Chapter 2 was used to flag PAR perturbations. We constrain h_1 and R to be 1 m and 0.67 (Jerlov water type IB) when fitting Equation 2.8 to PAR profiles between 5–70 m to determine optical parameters of blue light (e.g. h_2). Water type IB was chosen for two reasons. Firstly, the large seasonality of SAZ chlorophyll concentrations means the water type ranges between IA and III. du Plessis et al., 2017 found that water type IA (h_2 of 20 m) best suites the turbidity of the SAZ region in their study. Conversely, initial h_2 determinations from the glider SG574 showed that h_2 values ranged between water type IA to III (h_2 of 20 to 7.9 m). Water type IB best represents the average water type of the SAZ region due to the large range of turbidity. Secondly, the influence of h_1 and R on determined values of h_2 when fitting Equation 2.8 was negligible when using water type IB (see Chapter 2.6.4).

b. Optical backscatter data

As with PAR, the raw backscatter voltages at channels 470 and 700 nm were factory calibrated, but no further quality control was carried out. The methodology described in Chapter 2 was used to clean and calculate the backscatter dataset.

Further cleaning and smoothing was applied by flagging spikes larger than 0.004 m^{-1} in the top 350 m and spikes larger than 0.0001 m^{-1} below 350 m where there is no biological productivity due to light limitation. A final 7-point rolling median was applied to smooth the dataset.

c. Chlorophyll-a fluorescence data

The methodology described in Chapter 2 was used to clean, smooth and correct large quenching signals from the raw chlorophyll-a fluorescence measurements. The fluorescence was then converted into a chlorophyll-a concentration using the manufacturer's specific scale factor. A linear regression described by Swart et al. (2015) between the glider and in situ bottle samples of chlorophyll-a was used to calculate a scale factor and offset to calibrate the glider chlorophyll-a concentration. Chlorophyll-a will henceforth be referred to as "chlorophyll" for convenience.

4.2.2 Satellite and reanalysis products

This Chapter presents remotely sensed chlorophyll-a concentrations from the European Space Agency's Ocean Colour - Climate Change Initiative (ESA OC-CCI; Lavender et al., 2015) version 4.0 (available at <http://www.esa-oceancolour-cci.org>). The 8-day and monthly average chlorophyll concentration products at a horizontal resolution of 4 km were used to analyse the seasonal and subseasonal variations of chlorophyll concentrations in the vicinity of the glider.

This Chapter presents satellite-derived meridional and zonal components of absolute geostrophic velocity and absolute dynamic topography, which are produced by SSALTO/Duacs (distributed by AVISO; <https://www.aviso.altimetry.fr>) and are available through the Copernicus Marine Environment Monitoring Service (<http://marine.copernicus.eu>). The daily average absolute dynamic topography at a horizontal resolution of $0.25^\circ \times 0.25^\circ$ are used to investigate the hydrographical features in the vicinity of the glider on a seasonal to subseasonal timescale.

The reanalysis product ERA-5 is the fifth generation of global atmospheric

reanalyses from ECMWF (Hersbach and Dee, 2016) that is available through the Copernicus Climate Change Service (C3S) Climate Data Store (CDS; <https://cds.climate.copernicus.eu>). The ERA-5 product provided the downward shortwave radiation flux data at one hourly time intervals and at $0.25^\circ \times 0.25^\circ$ horizontal resolution. No measurements of downward shortwave radiation flux were made during the deployment of the glider, hence, the ERA-5 reanalysis product provided the required solar radiation data. ERA-5 Southern Ocean surface heat fluxes have high uncertainty due to sparse in situ surface measurements; however, the standard deviation error of surface heat fluxes in the SAZ region is low compared with surface heat fluxes south of the ACC, which is affected by the Antarctic sea-ice edge (Swart et al., 2019). For the purposes of this study, an equal area-weighted mean of the downward shortwave radiation flux is calculated in the vicinity of the glider ($40\text{--}44^\circ\text{S}$, $11\text{--}2^\circ\text{W}$), which is then used to estimate radiant heating rates during the spring and summer seasons in the SAZ.

4.3 Results

4.3.1 Local hydrography and chlorophyll concentration during SOSCEX

The reproduced and modified Hovmöller diagram of absolute dynamic topography and geostrophic velocity from Swart et al. (2015) shows the seasonal evolution of the surface ocean dynamics from the start of spring (September) to summer (December; Fig. 4.3). During spring, the latitudinal position of the glider varies by up to 1° over a time period of a week (black dots; Fig. 4.3). The absolute dynamic topography varies by 0.3 m over a monthly timescale. The high mesoscale and submesoscale variability of the absolute dynamic topography is attributed to the local hydrographic features, such as meandering fronts and eddies. From 20 to 25 October the glider briefly passes across a meandering front. The surface geostrophic velocities of the meander have a predominantly northward component, as cooler, fresher water is transported north (Fig. 4.3). From 30 October to 23 November the glider passes across the same meander that has now shed an eddy. The surface geostrophic velocities in the vicinity of the glider have an initial northward component and then switches to an eastward component by 18 November. This meander and eddy explain

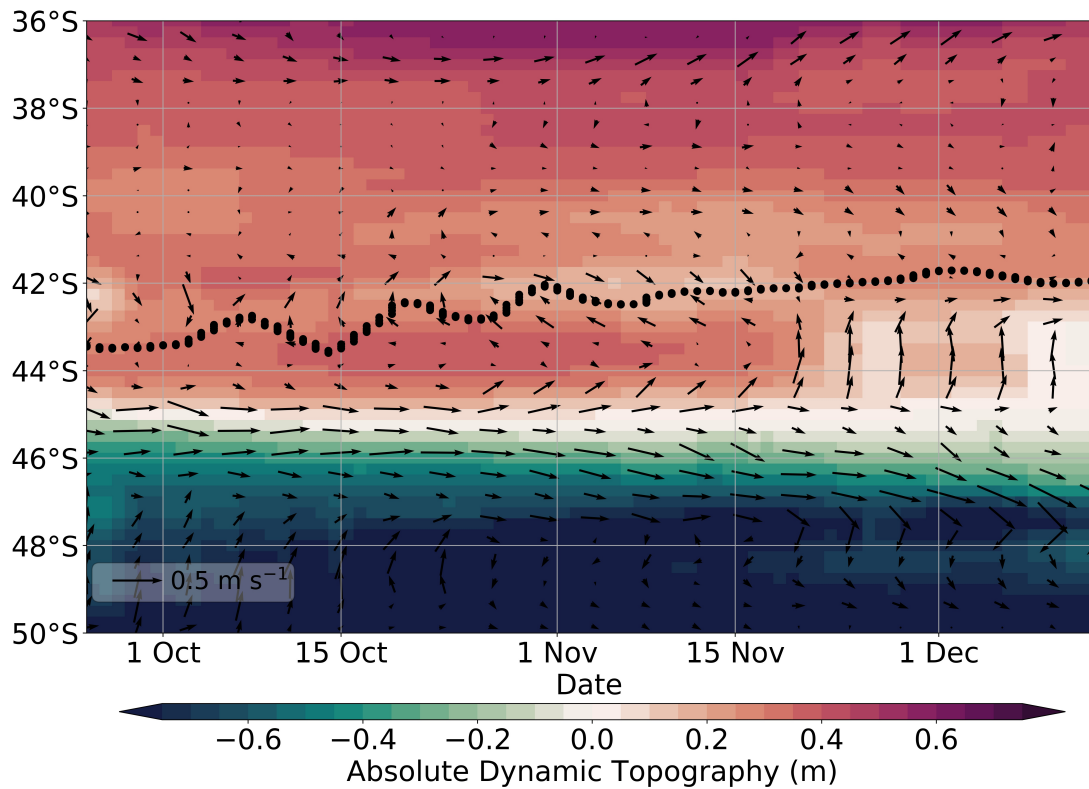


Figure 4.3: Hovmöller diagram of absolute dynamic topography (shaded) and geostrophic velocities (vector arrows) for the deployment period of SG574. The Hovmöller is created by extracting the latitudinal extent of the satellite observations at the longitude nearest to the daily average longitude of the glider. The black dots show the daily average latitude of the glider. Figure has been reproduced and adapted from Figure 2a from Swart et al. (2015).

why large temperature, salinity and MLD changes occur on daily to weekly timescales in the glider timeseries during spring (Fig. 4.5 in Section 4.3.2).

During summer, the glider passes through a less dynamic region compared with the spring period, as fewer meanders and eddies are encountered by the glider (Fig. 4.3). The absolute dynamic topography encountered by the glider varies by up to 0.1 m over the summer season and the geostrophic velocities are less than 0.3 m s^{-1} in an eastward direction. The reduced variation of absolute dynamic topography explains why changes to the physical properties of the upper ocean on daily to weekly timescales are relatively small compared with the spring period in the glider timeseries (Fig. 4.5 in Section 4.3.2).

The reproduced and modified Hovmöller diagram of 8-day average chlorophyll concentration from Swart et al. (2015) shows the seasonal evolution of the chlorophyll blooms from the start of spring to summer in the SAZ

(Fig. 4.4). In spring, average 8-day chlorophyll concentrations remain low ($\sim 0.2 \text{ mg m}^{-3}$; Fig. 4.4). Swart et al. (2015) identified the start of the spring bloom along the Polar Frontal Zone (PFZ) south of the glider during November, as chlorophyll concentrations increase to 1.0 mg m^{-3} . Approximately at the same time as the PFZ spring chlorophyll bloom, Swart et al. (2015) identified the start of the SAZ spring chlorophyll bloom in the vicinity of the glider, as chlorophyll concentrations increase to 0.3 mg m^{-3} . In the first week of December the glider encounters chlorophyll concentrations of up to 0.7 mg m^{-3} , as high chlorophyll concentrations are sustained during the summer months in the SAZ. The seasonal increase in chlorophyll concentration from spring to summer would suggest increased solar absorption and radiant heating rates in the upper ocean as turbidity decreases.

The onset and duration of the spring and summer chlorophyll blooms are not the same each year. du Plessis et al. (2019) found that the onset dates of the spring chlorophyll blooms vary by up to 36 days, as shown from four previous SOSCEX campaigns. The variation in the spring chlorophyll bloom timing is attributed to the variation in wind-induced mesoscale mixing and restratification timings during spring. Differences in the onset timings and duration of these blooms would mean that there are similar differences in the onset timings and duration of chlorophyll-induced warming, which would potentially have implications for regional climate and the meridional overturning circulation.

The influence of upper-ocean dynamics on mixed layer restratification and chlorophyll bloom initiation decreases from spring to summer in the SAZ region. Little et al. (2018) found that chlorophyll concentrations during the spring bloom are highly responsive to mesoscale restratification events, which are mainly due to temperature based changes in density that are likely to be caused by eddies. This localised restratification is sporadic across the SAZ and leads to patchy increases in chlorophyll concentration. Conversely, chlorophyll concentrations during the summer bloom are more responsive to the seasonal increase in shortwave heat flux that warms and restratifies the entire SAZ region. This regional restratification allows for higher and more spatially homogeneous chlorophyll concentrations in summer, demonstrating that upper-ocean dynamics have a smaller influence on the summer chlorophyll bloom than the spring chlorophyll bloom. The seasonal increase in chlorophyll concentration magnitude and spatial extent would also mean a similar seasonal increase in chlorophyll-induced warming that may further enhance regional

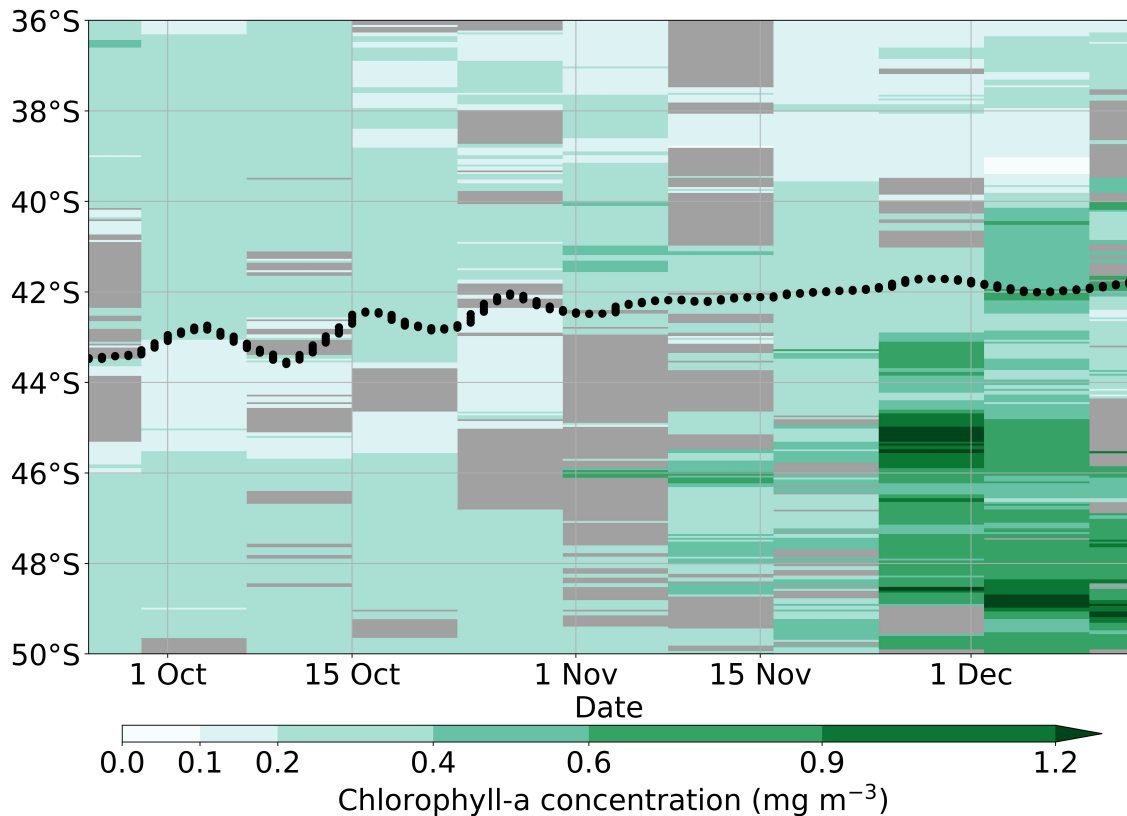


Figure 4.4: As in Fig. 4.3, but for remotely sensed 8-day average chlorophyll concentration measured from satellite. Figure has been reproduced and adapted from Figure 2b from Swart et al. (2015).

restratification during summer.

4.3.2 Glider observations

The time series of the glider observations and determined values of h_2 show the initiation of the spring chlorophyll bloom during the start of October (Fig. 4.5). Between 25 September and 20 October, warm, salty water in the top 200 to 300 m is observed by the glider. Chlorophyll concentrations in the top 30 m between September and the start of October are low (0.25 mg m^{-3}) and MLDs are around 250 m deep (Fig. 4.5e). The corresponding average h_2 remains at 15 m. On 13 October onwards a deep chlorophyll maximum begins to form and gradually extends closer to the surface, increasing the average 0 to 30 m chlorophyll concentration to 0.5 mg m^{-3} . The corresponding average h_2 decreases from 15 to 12 m, as less solar radiation penetrates through the upper ocean with increasing chlorophyll concentration.

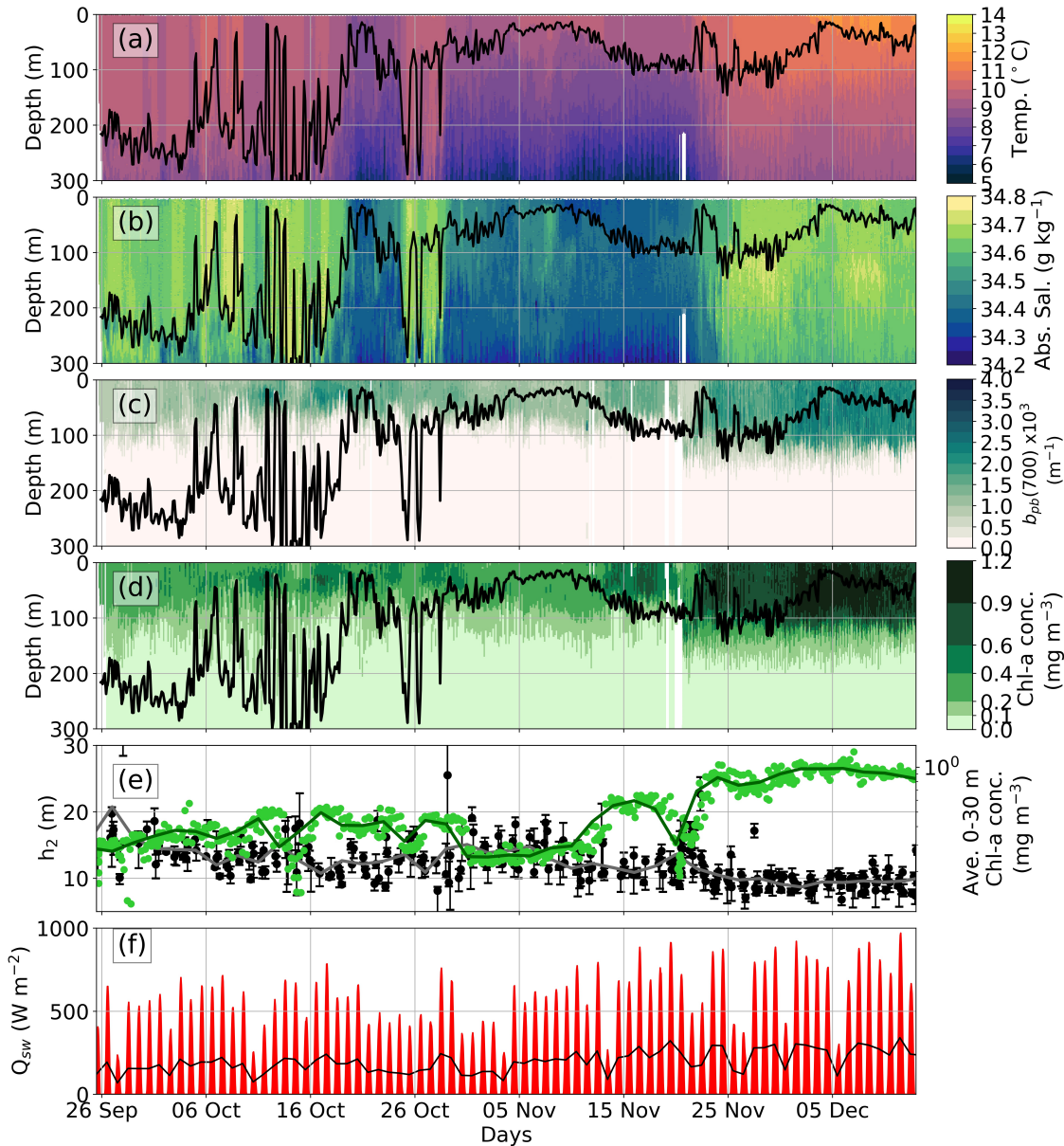


Figure 4.5: Timeseries of observations from SG574: (a) conservative temperature ($^{\circ}C$); (b) absolute salinity ($g kg^{-1}$); (c) particulate backscatter at 700 nm (m^{-1}); (d) chlorophyll concentration ($mg m^{-3}$); (e) h_2 (black dots with error bars; m), average 0–30 m chlorophyll concentration (green dots; $mg m^{-3}$), average h_2 binned every two days (grey line) and average 0–30 m chlorophyll concentration binned every two days (dark green line); (f) hourly (red shading) and daily (solid black line) area-weighted average of downward shortwave radiation flux from ERA-5 reanalysis ($W m^{-2}$). The black line in (a)–(d) represents the MLD.

Values of h_2 fluctuate as corresponding chlorophyll concentrations fluctuate during the spring bloom. Average values of h_2 increase by 5 m between 14 and 16 October, as chlorophyll concentrations briefly decrease over a two-day period by 0.3 mg m^{-3} (Fig. 4.5e). This decrease in chlorophyll concentration is likely due to phytoplankton encountering less sunlight, as the MLD deepens to a depth of around 350 m. Meanwhile, salinity and temperature decrease by 0.1 g kg^{-1} and 0.5°C , respectively (Fig. 4.5a and 4.5b). The values of h_2 , and thus chlorophyll concentration during spring are strongly dependent on the MLD. Furthermore, the 5 m deepening in h_2 after a 0.3 mg m^{-3} decrease in chlorophyll concentration demonstrates the high sensitivity of solar penetration depths to small changes in chlorophyll concentrations.

Between 20 and 30 October the glider moves across a meandering front, as shown by the decrease in the absolute dynamic topography in Fig. 4.3. As the glider enters the cooler, fresher water on the eastern side of the meandering front, the temperature and salinity in the top 50 m rapidly decrease by 0.8°C and 0.3 g kg^{-1} , respectively in one day (Fig. 4.5a and 4.5b). Meanwhile, the change in h_2 and corresponding chlorophyll concentration is small, as h_2 increases by 2 m and chlorophyll concentrations decrease by 0.1 mg m^{-3} (Fig. 4.5d). As the glider moves westward and eastward again to cross the meandering front a second time, the average h_2 and corresponding chlorophyll concentrations vary by same small amount as before (Fig. 4.5e). This small change in h_2 across the front demonstrates that h_2 does not depend on the water mass type. In fact, Little et al. (2018) found a weak correlation between chlorophyll concentration and salinity variations, which are associated with density changes across a front. Instead, up to 50% of the chlorophyll concentration variability can be explained by finer scale windstress and MLD variations. This suggests that a similar percentage of h_2 variability can also be explained by the same finer scale mixed layer stratification changes, seen as stratification modulates the chlorophyll concentration and thus the turbidity.

Between 20 November and 15 December, average values of h_2 decrease to approximately 10 m, with some values as low as 7 m during the start of December (Fig. 4.5e). The biological productivity of the SAZ increases as average chlorophyll concentrations in the top 30 m increase by up to 1.2 mg m^{-3} (Fig. 4.5e). Individual dives show chlorophyll concentrations of 0.5 mg m^{-3} and a backscatter of 0.002 m^{-1} at depths of 130 m (Fig. 4.5c and 4.5d). Temperatures in the top 5 m increase by 3.5°C and the MLD shoals from 100 to 20 m as the mixed layer warms and restratifies. Persistently low values of h_2

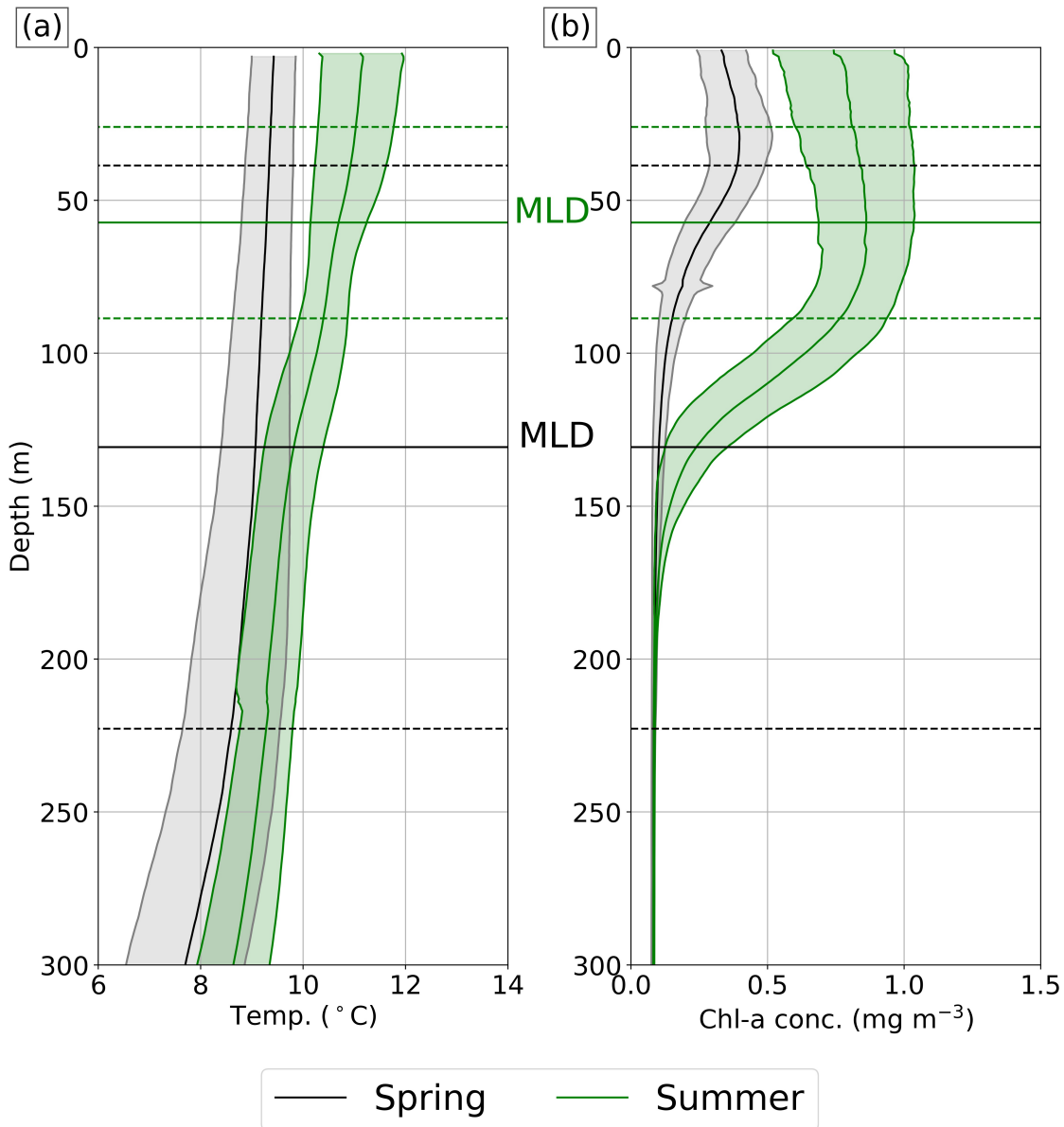


Figure 4.6: Spring (5 October to 5 November) and summer (20 November to 20 December) mean profiles of: (a) conservative temperature ($^{\circ}\text{C}$); (b) chlorophyll concentration (mg m^{-3}). Shaded regions represent the ± 1 SD variability. The horizontal solid black and green line represents the average MLD during spring and summer respectively and the dashed lines represent the ± 1 SD MLD variability.

during December would mean a prolonged period of increased solar absorption, increasing radiant heating rates and SST in the SAZ region.

The observed temperature and chlorophyll concentration profiles show two distinct seasonal blooms that occur during the glider deployment: the spring chlorophyll bloom and the summer chlorophyll bloom (Fig. 4.6). The average h_2 during the spring bloom (5 October to 5 November) is 13 m, which is deeper

than the average h_2 of 10 m during the summer bloom (20 November to 20 December). The average chlorophyll concentration profile during the spring bloom shows chlorophyll concentrations that are smaller, less variable and peak higher in the water column compared with chlorophyll concentrations during the summer bloom (Fig. 4.6b). The average chlorophyll concentration maximum during the spring bloom is $0.4 \pm 0.1 \text{ mg m}^{-3}$ at a depth of 28 m, whereas the maximum during the summer bloom is $0.9 \pm 0.2 \text{ mg m}^{-3}$ at a depth of 66 m. The seasonal change in chlorophyll concentration corresponds to a seasonal change in temperature and MLD, where the upper ocean increases in temperature by 1.7°C and the average MLD shoals by 73 m from spring to summer (Fig. 4.6a). Section 4.4.1 presents results and a discussion on how this seasonal increase in temperature could be due to chlorophyll-induced warming during the spring to summer blooms.

4.3.3 Solar penetration depth parameterisation comparison

We examine the relationship between derived solar penetration depths and average in situ measurements of chlorophyll concentration. We further examine how our own chlorophyll-dependent solar penetration depth parameterisation that is fitted to the glider observations compares with parameterisations from previous studies.

As in Chapter 3, the MA94 and O03 solar penetration depth parameterisations are fitted to the determined h_2 and observed chlorophyll concentrations. However, both parameterisations might not provide appropriate determinations of h_2 specific for the SAZ region. MA94 and O03 are based on modelled in-water solar irradiance profiles that use remotely sensed chlorophyll-a concentrations measured from satellite. MA94 assumes that the chlorophyll concentrations have a Gaussian distribution over the depth of one scale depth and O03 assumes that chlorophyll concentrations are uniformly spread over a depth range of 2 to 80 m. The observed chlorophyll concentration in the SAZ shows that it is not necessarily homogeneous with depth, and that features such as a deep chlorophyll maximum occur deeper than one scale depth. This therefore weakens the assumptions of both MA94 and O03 and would mean that neither would necessarily provide appropriate determinations of h_2 for the SAZ region.

We therefore propose a new function [henceforth referred to as G20] to accurately predict h_2 values from a range of average chlorophyll concentrations

observed in the SAZ region:

$$h_2 = \frac{1}{a[\text{Chl}]^b} \quad (4.1)$$

where [Chl] is the average chlorophyll concentration; a is an unknown coefficient; b is an unknown exponent. The function is based on a previous power law function from Morel (1988) that predicts the diffuse attenuation coefficient as a function of chlorophyll concentration ($k_d = a[\text{Chl}]^b$) for case I ocean waters, where biological constituents such as chlorophyll pigments, coloured dissolved organic matter and detrital material influence the optical parameters in the upper ocean. The function has been previously used to convert chlorophyll concentrations into k_d for chlorophyll sensitivity experiments in a coupled GCM (e.g. Manizza et al., 2005; Gnanadesikan and Anderson, 2009). Hence, given that the function has been previously used to parameterise chlorophyll and that the upper ocean of the SAZ region predominantly consists of chlorophyll pigments, the function is therefore suitable for our new h_2 parameterisation.

The G20 parameters are determined using least squares fit to the determined h_2 and observed average chlorophyll concentrations. The fit of MA94 and O03 to the glider data is compared with the fit of G20. As in Chapter 3, for the O03 parameterisation we assume that the incident angle of solar radiation on the ocean surface ($H(\theta)$) and the cloud index ($G(\text{ci})$) are zero (see Equation B.3 in Appendix B).

The average chlorophyll concentration varies depending on the depth range over which the average is calculated (Fig. 4.7). The average chlorophyll concentration between 0 and 20 m is around 0.2 mg m^{-3} , which is less than the average chlorophyll concentration between 0 and 80 m, which is around 0.4 mg m^{-3} (Fig. 4.7a and 4.7d). Averaging chlorophyll concentrations over a deeper depth means high chlorophyll concentration features such as deep chlorophyll maxima are included in the calculation, which increases the overall magnitude of average chlorophyll concentrations.

As with G20 (red line; Fig. 4.7), MA94 (blue line) and O03 (green line) show a power law dependence in h_2 as a function of chlorophyll concentration. Varying the average chlorophyll concentration depth range changes the r^2 and RMSE of the fitted parameterisations (Table 4.1). The values of r^2 for MA94 and O03 are the same as G20 at each depth range. Increasing the depth range from 0 to

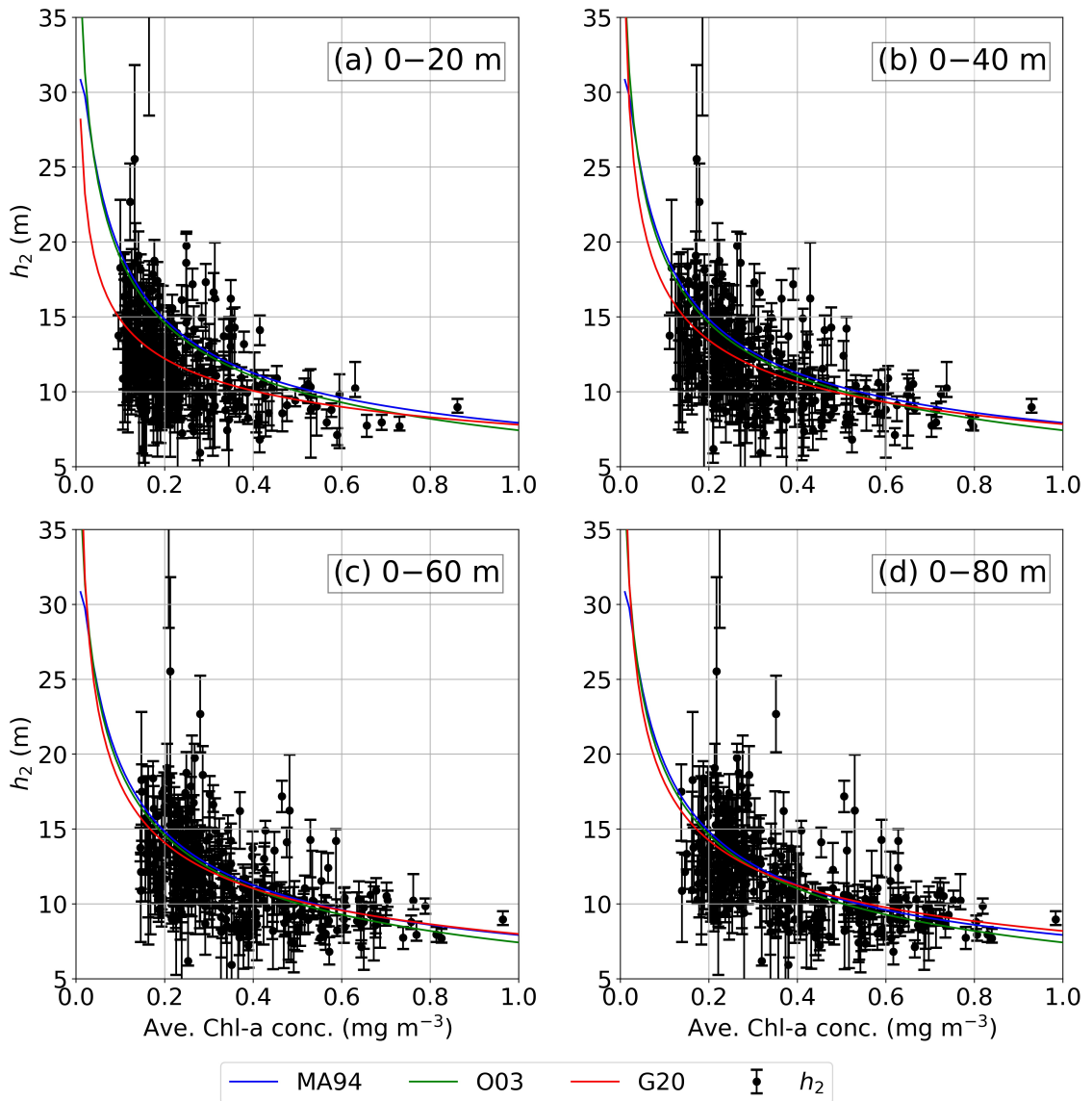


Figure 4.7: Relationship between determined h_2 and chlorophyll concentration, where chlorophyll concentration is averaged at a range of depths: (a) 0–20 m; (b) 0–40 m; (c) 0–60 m; (d) 0–80 m. Three parameterisations of chlorophyll-dependent solar penetration depths are plotted with the observed data: Morel and Antoine (1994) [MA94] (blue line); Ohlmann (2003) [O03] (green line); parameterisation of present study [G20] (red line).

20 m, to 0 to 80 m increases r^2 , showing that there is an improvement in the fit of the functions with an increase in depth range. The improvement in the fit is also shown by the reduction in the RMSE, as the depth range increases from 0 to 20 m to 0 to 80 m. For the G20 parameterisation the RMSE remains the same for all depth ranges above 0 to 40 m, but the r^2 is shown to improve with increasing depth range. Increasing the depth range to 0 to 100 m shows no further improvement in r^2 and RMSE. Hence, the depth range of 0 to 80 m is

Parameterisation	r^2					RMSE (m)				
	0–20	0–40	0–60	0–80	0–100	0–20	0–40	0–60	0–80	0–100
MA94	0.16	0.24	0.25	0.26	0.26	4.2	3.3	3.1	3.1	3.1
O03	0.16	0.24	0.25	0.26	0.26	4.1	3.2	3.1	3.1	3.1
G20	0.16	0.24	0.25	0.26	0.26	3.3	3.1	3.1	3.1	3.1

Table 4.1: The determination coefficients (r^2) and root-mean-square errors (RMSE) of the parameterisations when fitted to the determined scale depth and average chlorophyll concentrations for depth ranges: 0–20 m, 0–40 m, 0–60 m, 0–80 m and 0–100 m (see Fig. 4.7).

the shallowest depth range where the correlation is at its highest and the RMSE is at its lowest.

Determining the most appropriate parameterisation to predict the scale depth in the SAZ strongly depends on the depth range over which the average chlorophyll concentration is calculated. Blue light approximately decreases exponentially with depth meaning the largest rate of absorption of blue light occurs at the near-surface. The derived value of h_2 represents one scale depth or the first penetration depth of blue light, where blue light is approximately 63% less than its surface value ($1 - e^{-1}$). At a depth of two scale depths ($2h_2$), blue light is 86% less than its surface value ($1 - e^{-2}$). Hence, the majority of solar radiation that is absorbed occurs at a depth of one scale depth. Changes to chlorophyll concentration at the near-surface would have a larger influence on the absorption of blue light, and thus near-surface radiant heating and SST, than changes to chlorophyll concentration lower in the water column, where solar radiation and radiant heating is considerably weaker. However, the parameter h_2 in this study is determined by fitting the double exponential function to a vertical profile of PAR from the surface to a depth of 70 m. Therefore, the biological constituents over this depth range would influence the absorption of blue light, the fit of the double exponential function and determined values of h_2 .

The correlation between the parameterisations and the observed dataset is at its highest at a depth range between 0 and 80 m (Table 4.1), which is similar to the depth range of the fitted double exponential function to the PAR profiles. Hence, the average chlorophyll concentration depth range of 0 to 80 m is suitable for deriving the parameters of G20 and comparing G20 with MA94 and O03. The determined G20 function at a depth range of 0 to 80 m is

$$h_2 = \frac{1}{0.12[\text{Chl}]^{0.34}} \quad (4.2)$$

where $a = 0.12 \pm 0.01 \text{ mg m}^{-2}$ and $b = 0.34 \pm 0.04$. The uncertainty associated with a and b represents the 1 SD error of the fitted function. G20 determines slightly different values of h_2 than that of MA94 and O03. G20 determines h_2 values that are less than MA94 and O03 at chlorophyll concentrations smaller than 0.4 and 0.25 mg m^{-3} , respectively. Conversely, G20 determines h_2 values that are more than MA94 and O03 at chlorophyll concentrations higher than 0.4 and 0.25 mg m^{-3} , respectively. Using G20 instead of MA94 and O03 in an ocean GCM would therefore reduce the solar irradiance absorption at high chlorophyll concentrations ($>0.4 \text{ mg m}^{-3}$), which would reduce the influence of chlorophyll-induced warming during the spring and summer blooms.

Using determined h_2 from the glider, G20 would provide a better representation of the attenuation of blue light due to the occurrence of inhomogeneous chlorophyll concentrations in the SAZ region. However, there are additional uncertainties associated with the derived parameters of G20 that depend on the uncertainty and reliability of the observed glider data. Firstly, determined values of h_2 have their own individual uncertainties, which have not been considered when deriving G20. Applying more weighting on h_2 values with low uncertainties and less weighting on h_2 values with high uncertainties when fitting G20 would improve the determined parameters of G20. An appropriate weight function is required when fitting G20 and is the source of future work. Secondly, the average observed chlorophyll concentration from the glider is a proxy to actual chlorophyll-a concentration, and does not include other chlorophyll pigment concentrations. Determined h_2 values would be affected by other biological constituents that strongly attenuate blue light. Hence, the chlorophyll-a concentration measured from the glider underestimates the actual chlorophyll concentration that attenuates blue light and potentially skews the data and the fit of G20. Further investigation into the type and amount of biological constituents that affect h_2 is required. Considering these additional uncertainties we do not have sufficient confidence in the robustness of the derived parameters of G20 and whether G20 further improves upon MA94 and O03 in parameterising chlorophyll concentration in the SAZ.

4.3.4 Upper ocean radiant heating during the spring and summer blooms

The increases in chlorophyll concentration during the spring and summer chlorophyll bloom have the potential to increase the radiant heating rates. The glider time series suggests that the radiant heating rate during the summer bloom is larger than the radiant heating rate during the spring bloom due to lower values of h_2 in summer than spring. The values of h_2 also show subseasonal fluctuations during the bloom events that would potentially cause subseasonal fluctuations in the radiant heating rate. Furthermore, the radiative heating of the upper ocean not only depends on h_2 , but also on the amount of shortwave radiation flux absorbed in the mixed layer and the amount incident on the ocean surface that vary on seasonal to subseasonal timescales.

Here, we compare the influence h_2 has on the radiant heating rate of the SAZ mixed layer on a seasonal timescale (spring to summer) and on a subseasonal timescale (monthly to weekly). We further examine how factors such as MLD and shortwave radiative flux modulates the chlorophyll-induced warming of the mixed layer.

We use Equation 3.1 from Chapter 3 to quantify the average radiant heating rate of an idealised mixed layer during the spring and summer bloom. The glider observations and reanalysis data of shortwave radiative flux are averaged for the spring bloom (5 October to 5 November) and the summer bloom (20 November to 20 December), and are presented in Table 4.2. The depth of the idealised water column, H , represents the average MLD. We assume R is 0.67 for Jerlov water type IB, which is an appropriate water type to represent the SAZ region, given h_2 varies between water type IA to III. As in Chapter 3, for the purposes of this calculation, we ignore the effects of advection, entrainment and mixing, and atmospheric feedbacks.

Using the variables from Table 4.2 the difference in radiant heating rate of the mixed layer between the spring and summer bloom is $1.7^\circ\text{C month}^{-1}$. An idealised sensitivity experiment shows whether this increase in radiant heating rate between spring and summer is due to a decrease in h_2 , associated with an increase in chlorophyll concentration. If the average MLD and shortwave radiative flux remained constant, a change in h_2 of 3 m results in a near-zero change in the mixed layer radiant heating rate. A change in the shortwave radiative flux of 78 W m^{-2} increases the mixed layer radiant heating rate by $0.3^\circ\text{C month}^{-1}$, whereas a change in the MLD of 73 m increases the mixed layer

Average variables	Season	
	Spring	Summer
h_2 (m)	13	10
MLD (m)	130	57
Q_0 (W m^{-2})	165	243
ρ (kg m^{-3})	1026	1026
dT/dt ($^{\circ}\text{C month}^{-1}$)	0.7	2.4

Table 4.2: Average variables during the spring bloom (5 October to 5 November) and summer bloom (20 November to 20 December) that are used to quantify the mixed layer radiant heating rate (dT/dt). The variables include average h_2 , average MLD, daily average shortwave heat flux (Q_0) and average mixed layer density (ρ).

radiant heating rate by $0.9^{\circ}\text{C month}^{-1}$. The seasonal change in MLD has the largest influence on the upper ocean radiant heating rate and temperature in the SAZ from spring to summer, followed by the seasonal increase in incoming shortwave radiative flux. The seasonal change in chlorophyll concentration has a negligible affect on the radiant heating rate by comparison with MLD and shortwave radiative flux.

The 5th and 95th percentile of h_2 during the spring and summer blooms are used to represent the subseasonal fluctuations in h_2 . These two h_2 values are then used to quantify potential subseasonal fluctuations in the radiant heating rates of an idealised mixed layer.

During spring, the 5th and 95th percentiles of h_2 are 10 m and 18 m, respectively. If the average spring MLD and shortwave radiative flux remains constant, a change in h_2 of -8 m results in negligible difference to the mixed layer radiant heating rate. During summer, the 5th and 95th percentiles of h_2 are 8 m and 16 m, respectively. If the average summer MLD and shortwave radiative flux remains constant, a change in h_2 of -8 m increases the mixed layer radiant heating rate by $0.01^{\circ}\text{C month}^{-1}$. Although the subseasonal variations in h_2 during summer cause larger differences in the radiant heating rate than spring, the difference in radiant heating rate during summer is still small. Hence, fluctuations in h_2 , and in the corresponding chlorophyll concentration, during both bloom events have a negligibly small effect on the radiant heating rate.

There are multiple occurrences where the MLD in the glider timeseries shoals to a depth comparable to h_2 and amplifies the chlorophyll-induced warming during both chlorophyll blooms. On 20 October during the spring bloom, the mixed layer shoals to a depth of 17 m, which means a subseasonal change in

h_2 from 18 to 10 m increases the radiant heating rate by $0.3^\circ\text{C month}^{-1}$. On 4 December during the summer bloom, the mixed layer also shoals to a depth of 17 m, which means a subseasonal change in h_2 from 16 to 8 m increases the mixed layer radiant heating rate of $0.5^\circ\text{C month}^{-1}$. This increase in radiant heating rate shows that when the mixed layer extends to a depth comparable to the solar penetration depth, subseasonal changes to h_2 have a larger influence on mixed layer radiant heating rates. Previous studies have found that a decrease in the MLD reduces the effective heat capacity of the mixed layer, as less shortwave radiation is required to heat a smaller volume of water (Wetzel et al., 2006; Turner et al., 2012). Hence, the temperature of the mixed layer in the SAZ rapidly responds to increases in the absorption of shortwave radiation that are due to increases in chlorophyll concentration. These radiant heating rates are larger during the summer bloom than that of the spring bloom due to lower values of h_2 and an increase in the incoming solar radiation.

The occurrences of shallow MLDs in the glider timeseries are shortlived (approximately lasting 1-2 days), meaning the amplification of the chlorophyll-induced warming is also shortlived. Furthermore, it is unlikely that the chlorophyll blooms modulate the rapid restratification of the upper ocean, as chlorophyll-induced radiant heating rates are too weak. Instead, the rapid restratification is strongly modulated by atmospheric forcing.

The quantified radiant heating rates presented here do not represent the actual radiant heating rates that would be observed in the SAZ. We assume that the MLD and daily average shortwave heat flux remains constant during the bloom seasons, which in reality are not true as both variables display large temporal variability in the glider timeseries. Excluding effects such as advection, entrainment and mixing, and atmospheric feedbacks means other horizontal and vertical heat fluxes that dominate the mixed layer heat budget are not represented.

4.4 Discussion

The radiant heating rates calculated in the previous subsection have limited implications for the wider SAZ region during spring and summer. During spring, the SAZ is a dynamic region of meandering fronts and eddies, meaning surface chlorophyll concentrations are continuously advected horizontally and mixed vertically. Localised mesoscale restratification events that are caused

by eddies (du Plessis et al., 2017) or wind velocity reversals (du Plessis et al., 2019) leads to patchy increases in chlorophyll concentration, as shown from the glider timeseries and satellite measurements. Patches of high chlorophyll concentration, associated with low values of h_2 and shallow MLDs, would have higher mixed layer radiant heating rates than patches of low chlorophyll concentration. However, depending on the frequency and timing of these mesoscale restratification events these patches of high chlorophyll concentration could be reduced in number and occur later in spring, reducing the effect of chlorophyll on radiant heating rates.

During summer, the glider timeseries and satellite measurements show that chlorophyll concentrations are relatively uniform across the SAZ compared with the spring. Little et al. (2018) found that regional restratification, caused by the seasonal increase in shortwave heat flux, decreases the influence of mesoscale restratification events and shoals the MLD across the entire SAZ region. The effect of chlorophyll on radiant heating rates found in this study are small, as MLDs extend far below the solar penetration depths. The MLD occasionally reduces to a depth comparable to the solar penetration depth, increasing radiant heating rates during summer. However, these shallow MLDs occur on timescales of less than two days as periodic wind-induced turbulent mixing events cause rapid MLD deepening, which would cause a reduction in the effect of chlorophyll on radiant heating rates.

The effect of chlorophyll on the mean net air-sea heat flux across the SAZ is likely to be negligible. Tamsitt et al. (2016) used the Southern Ocean State Estimate (SOSE) model to simulate the 2005 to 2010 mean heat budget terms across the global Southern Ocean. Focusing on the SOSCEX campaign region (approximately 40–50°S, 10–0°W) the net air-sea heat fluxes are generally positive (~ 40 to 50 W m^{-2}) with heat going into the ocean, as cool, upwelled upper circumpolar deep waters are transformed into more buoyant Sub-Antarctic mode waters (Fig. 4.8a). This positive net heat flux increases from spring to summer, as more shortwave radiative flux is available (Tamsitt et al., 2016). As shown in this study and by Groeskamp and Iudicone (2018), the MLD extends far beyond the penetration depth of shortwave radiation across the Atlantic Sector of the SAZ region, meaning nearly all the shortwave radiation is absorbed within the mixed layer in the SAZ (Fig. 4.9). Decreasing h_2 would increase radiant heating rates closer to the near-surface and decrease radiant heating rates below the near-surface. Following mixed layer turbulent mixing processes the vertical differences in radiant heating are mixed, resulting in a

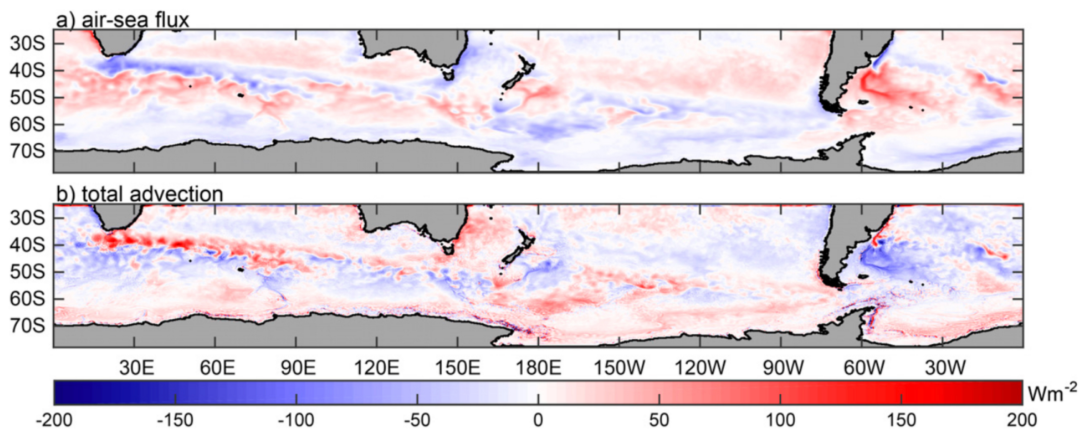


Figure 4.8: The 2005 to 2010 mean heat budget from SOSE model integrated over a depth of 624 m. These terms include: (a) air-sea heat flux; (b) total divergence of temperature advection calculated as the sum of total geostrophic and ageostrophic horizontal and vertical advection. Positive (Red) represents warming and negative (blue) represents cooling. Sourced and adapted from Figure 2 of Tamsitt et al. (2016).

zero net increase in radiant heating and zero change to the net air-sea heat flux. With no change in the net air-sea heat flux then this suggests that the effect of chlorophyll on the overturning circulation is negligible, as there is limited chlorophyll-induced warming to further increase the buoyancy of the cool, upwelled upper circumpolar deep waters.

There are isolated patches of low h_2 and shallow MLDs with enhanced radiant heating rates, which would lead to mixed layer warming and SST increase. Although these patches of enhanced radiant heating would reduce the positive net heat flux by increasing SST, the subseasonal and meso-spatial scales they occur on means that their affect is shortlived and spatially limited. Hence, the effect of chlorophyll on mixed layer and SST warming in the SAZ remains mostly negligible.

The effects of advection cannot be ignored in the SAZ region, as there is a predominantly strong eastward geostrophic surface flow associated with the ACC (Fig. 4.3). The total divergence of temperature advection, calculated as the sum of total geostrophic and ageostrophic horizontal and vertical advection, is the same order of magnitude and opposite sign to the net air-sea heat flux in the SAZ region (Fig. 4.8b). This negative advective heat transport or a decrease in upper-ocean temperature is mainly due to the Ekman transport of cold water moving equatorward (Tamsitt et al., 2016). The strong horizontal advection of temperature in the SAZ demonstrates that additional heat flux into the SAZ

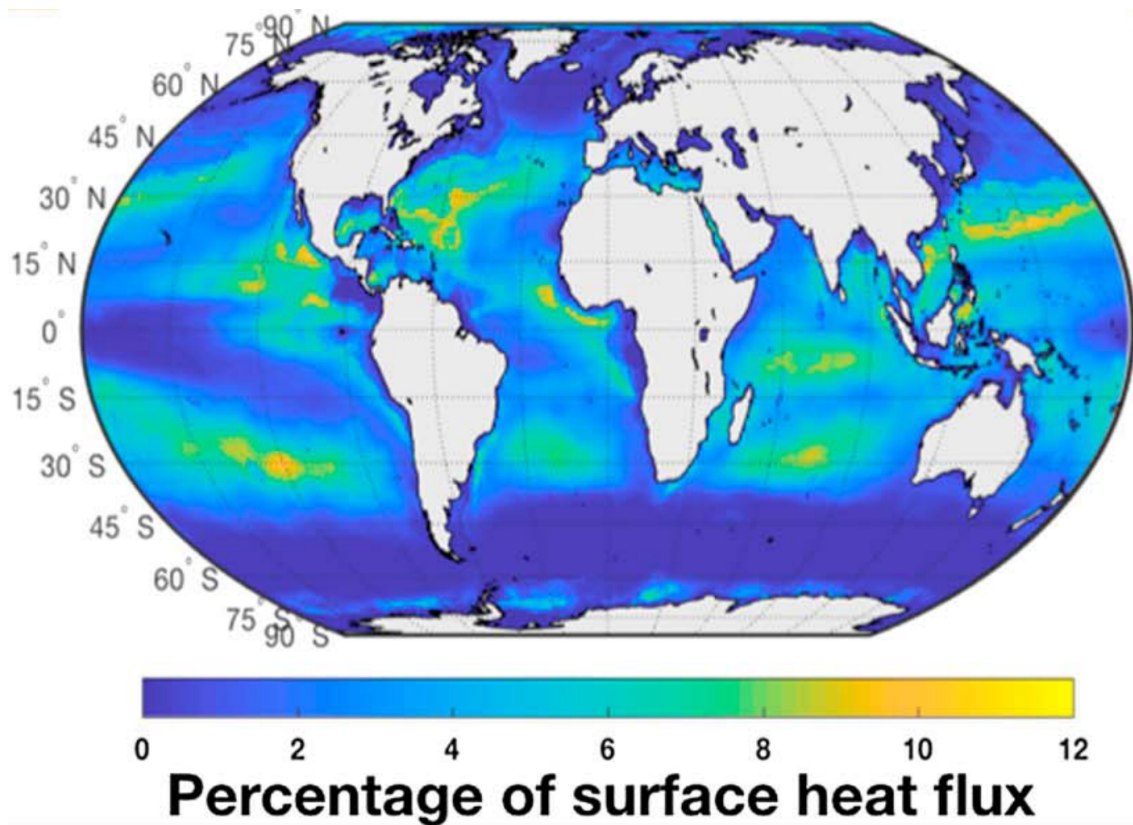


Figure 4.9: Percentage of shortwave radiation absorbed below the mixed layer for O3 solar penetration depth parameterisation. Sourced and adapted from Figure 4 of Groeskamp and Iudicone (2018).

surface ocean is rapidly transported out of the region. Conversely, patches of low h_2 and enhanced radiant heating would be horizontally advected in the flow and continuously exchanging heat between the atmosphere and ocean. However, this additional heat flux into localised regions of shallow and highly turbid mixed layers would be considerably smaller than the total divergence of temperature advection in the SAZ.

Previous studies have shown that chlorophyll concentrations have an affect on the SST across the SAZ region, but have not shown this affect on seasonal and subseasonal timescales. Patara et al. (2012), Manizza et al. (2005) and Gnanadesikan and Anderson (2009) found that the annual mean SAZ SST increased by 0.2 to 0.5°C. Conversely, this study found that chlorophyll has a negligible affect on SAZ SST during the spring and summer bloom, except for patches of shallow and highly turbid mixed layers, which increase at a rate of 0.3 to 0.5°C month⁻¹. However, considering the excluded effects of advection, entrainment and mixing, and atmospheric feedbacks our estimated radiant heating rates are likely to be smaller. Hence, chlorophyll-induced SST

increases on seasonal and subseasonal timescales in this study are much smaller compared with the annual mean SST increases found in previous coupled GCM studies.

If the effect of chlorophyll concentration on SAZ SST is mostly negligible, then this suggests the effect of chlorophyll on SAZ climate is also negligible. Moisture and heat sourced from the SAZ region is needed for cyclogenesis and the intensification of mid-latitude cyclones (Yuan et al., 2009). With the region experiencing a storm event every 4 to 10 days during the spring and summer seasons (Swart et al., 2015), additional moisture and heat fluxes would intensify wind velocities and increase precipitation rates in midlatitude cyclones. Midlatitude cyclones during the summer have a positive feedback on chlorophyll concentrations where wind-induced turbulent mixing entrains dissolved iron up into the mixed layer, enhancing biological productivity (Nicholson et al., 2016). However, the negligible effect of chlorophyll concentration on SST means mid-latitude cyclone intensification and positive feedbacks on biological productivity are also negligible in the SAZ.

4.5 Conclusions

The additional near-surface solar radiation absorption due to changes in chlorophyll concentration during the spring and summer chlorophyll blooms, are found to have a negligible effect on radiant heating rates in the SAZ region. The effect of chlorophyll concentration on radiant heating rates strongly depends on the MLD, which is dependent on the physical and dynamical properties of the upper ocean and the strength of wind-induced turbulent mixing.

The determined values of h_2 and corresponding observed chlorophyll concentrations are found to vary on seasonal to daily timescales during the spring and summer blooms. During the spring bloom, rapid MLD variations intermittently increase and decrease h_2 and corresponding chlorophyll concentrations. The fluctuations in h_2 have no effect on mixed layer radiant heating rates seen as the mixed layer extends far below the penetration depth of solar radiation. Periods of shallow MLDs that are comparable to h_2 amplifies the increase in the radiant heating rate. The mixed layer shoaling events often last one to two days and are spatially inhomogeneous across the SAZ, which means the rate of near-surface biological warming across the majority of the SAZ is

negligible. Instead, mixed layer temperatures and SSTs are strongly modulated by horizontal advection of heat and wind-induced vertical mixing.

During the summer bloom, the glider observes sustained high chlorophyll concentrations. Chlorophyll concentrations remain high before and after the mixed layer shoals as more incoming solar radiation increases biological productivity. Values of h_2 are lower than the spring bloom (~ 8 m), increasing the absorption of solar radiation at the near-surface. Although the radiant heating rate increases with increasing chlorophyll concentration, it is too small to increase mixed layer temperature and upper-ocean thermal stratification. As with spring, wind-induced turbulent mixing strongly influences the MLD, which strongly modulates the radiant heating rate in the SAZ.

The negligible increase in the seasonal and subseasonal radiant heating rates during the spring and summer blooms improves upon previous chlorophyll-perturbation studies that do not show the finer scale variations in chlorophyll-induced warming. Furthermore, the negligible increase in radiant heating rates has limited implications on SAZ climate, chlorophyll production feedbacks and the overturning circulation.

The G20 relationship would better represent h_2 in the SAZ region compared with MA94 and O03 relationships, as G20 is based on determined h_2 values from in situ PAR measurements and not based on modelled in-water solar irradiance profiles. However, considering the uncertainties associated with the determined values of h_2 and observed chlorophyll concentrations from the glider we do not have sufficient confidence in the robustness of the derived parameters of G20. Considering these additional uncertainties is the source of future work.

Chapter 5

The effect of seasonally and spatially varying chlorophyll on Bay of Bengal surface ocean properties and the South Asian Monsoon

5.1 Introduction

The strong coupling of the Indian Ocean to the atmosphere is a major factor in South Asian monsoon seasonal variability (Ju and Slingo, 1995). During the boreal summer, strong southwesterly winds transport heat and moisture from the Indian Ocean surface to sustain deep convection over the Indian subcontinent. The South Asian summer monsoon provides up to 90% of the annual rainfall for the Indian subcontinent (Vecchi and Harrison, 2002), so it is important to accurately predict the seasonal variability of monsoon rainfall given its economic importance to agriculture and other water-intensive industries.

The thermal and saline surface properties of the Bay of Bengal (BoB; Fig. 1.3), in the northeast Indian Ocean, are strongly forced by the monsoonal winds and large freshwater flux. In the north BoB, the large freshwater flux from river discharge and precipitation leads to strong salinity stratification and barrier-layer formation above the thermocline and below the mixed layer (Vinayachandran et al., 2002; Jana et al., 2015; Sengupta et al., 2016). The barrier layer inhibits vertical mixing (Sprintall and Tomczak, 1992; Rao and Sivakumar,

2003) and isolates the mixed layer above from cooling by entrainment (Duncan and Han, 2009), modulating the seasonal mixed layer depth (MLD) and its temperature (Girishkumar et al., 2011; Shee et al., 2019).

From June to September (JJAS) high climatological precipitation rates ($>20 \text{ mm day}^{-1}$), associated with the South Asian southwest monsoon, are anchored to three locations across the Indian subcontinent: the western Ghats of southwest India, the Myanmar coast and from Bangladesh north into the Himalayan foothills (Fig. 5.1f–5.1i). Coupled atmosphere-ocean general circulation models (GCMs) have improved their representations of the seasonal variability and spatial distribution of South Asian southwest monsoon precipitation, but substantial biases remain. Lin et al. (2008) found that 12 out of 14 coupled GCMs from the Coupled Model Intercomparison Project Phase 3 (CMIP3) captured the South Asian southwest monsoon seasonal-mean precipitation rate reasonably well. However, most GCMs simulated excessive precipitation at the Equator and insufficient precipitation across the northern BoB and Bangladesh region from May to October. Sperber et al. (2013) compared 25 CMIP5 models with 22 CMIP3 models. CMIP5 models have higher vertical and horizontal resolutions in the ocean and atmosphere and include additional earth system processes, compared with CMIP3 models. CMIP5 multi-model means have a better representation of precipitation rates over the western Ghats, Myanmar and Bangladesh than CMIP3 multi-model means from June to September. However, both the CMIP5 and CMIP3 models underestimate precipitation over the BoB and India at 20° N . There is also a consistent dry bias over central India at $25\text{--}30^\circ \text{ N}$ of up to 4 mm day^{-1} and a delay to the summer monsoon onset and peak over most of India in both CMIP5 and CMIP3 models. The significant biases from JJAS show that state-of-the-art coupled GCMs still struggle to capture the basic seasonality of summer monsoon precipitation across the BoB and the wider Indian subcontinent.

The BoB sea surface temperature (SST) rapidly responds to variations in the net surface heat flux, which in turn are primarily controlled by variations in windspeed (Duncan and Han, 2009). Although BoB SST decreases with increasing windspeed during the southwest monsoon (JJAS), SST remains high enough ($> 28^\circ \text{ C}$) to sustain high precipitation rates across the Indian subcontinent, consequently strengthening the salinity stratification and further reinforcing convection across the basin (Shenoi et al., 2002). The salinity stratification is weaker in the southern BoB, allowing monsoonal winds to primarily control the upper-ocean thermal structure (Narvekar and Prasanna

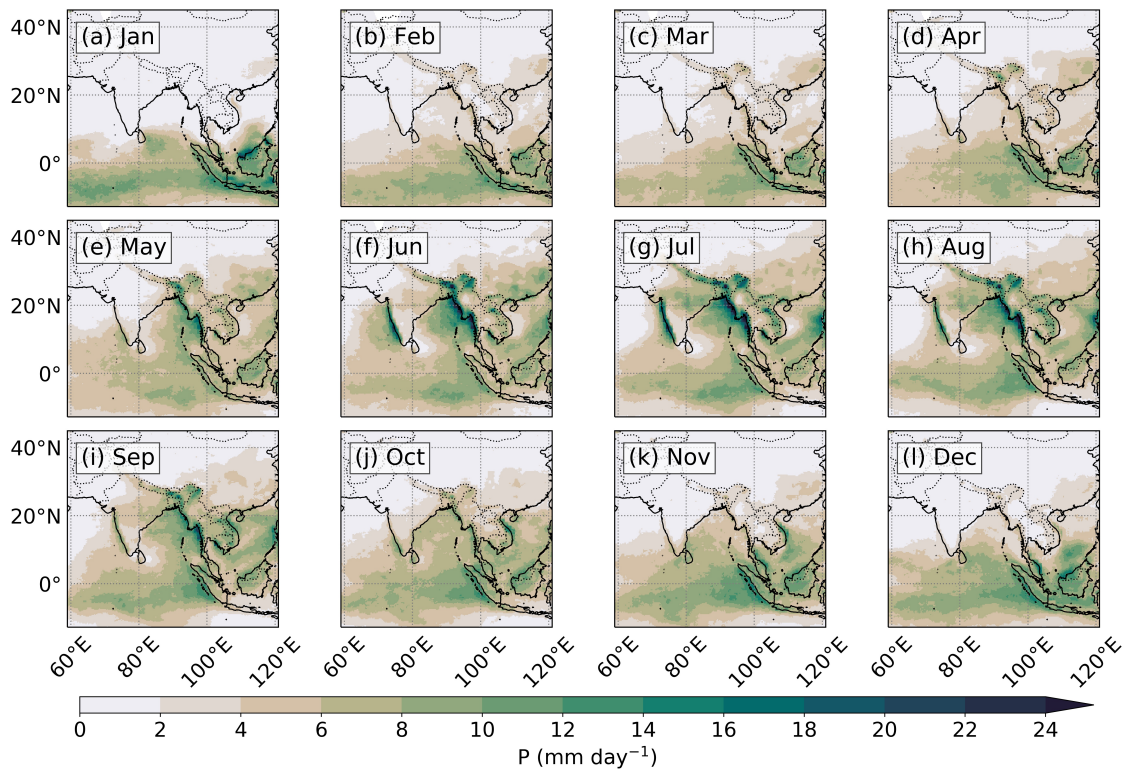


Figure 5.1: Monthly climatological precipitation rate measured from the TRMM 3B42 satellite product from January to December.

Kumar, 2006). Hence, the southern BoB MLD and SST display larger seasonal variability compared with the northern BoB (Narvekar and Prasanna Kumar, 2006).

The strong BoB salinity stratification reduces biological productivity by inhibiting the vertical transport of nutrients to the sun-lit surface layers (Kumar et al., 2002; McCreary et al., 2009). Biological productivity during JJAS is also inhibited by cloud cover and by the infiltration of river sediments, which respectively reduce the incoming solar radiation at the ocean surface and the in-water penetration depth of solar radiation (Gomes et al., 2000; Kumar et al., 2010). However, in certain regions of the BoB, localised seasonal physical forcing breaks the strong stratification and increases the vertical transport of nutrients to the sun-lit surface layers, increasing biological productivity. Chlorophyll concentrations in the coastal regions are high ($> 1 \text{ mg m}^{-3}$; Fig. 1.4), especially near large rivers such as the Ganges, Brahmaputra, Mahanadi and Irrawaddy, because of nutrients supplied by these rivers during June–October (Amol et al., 2019). Chlorophyll concentrations in the northern coastal region typically peak in October (Fig. 5.2j; Lévy et al., 2007) when river discharge and nutrients

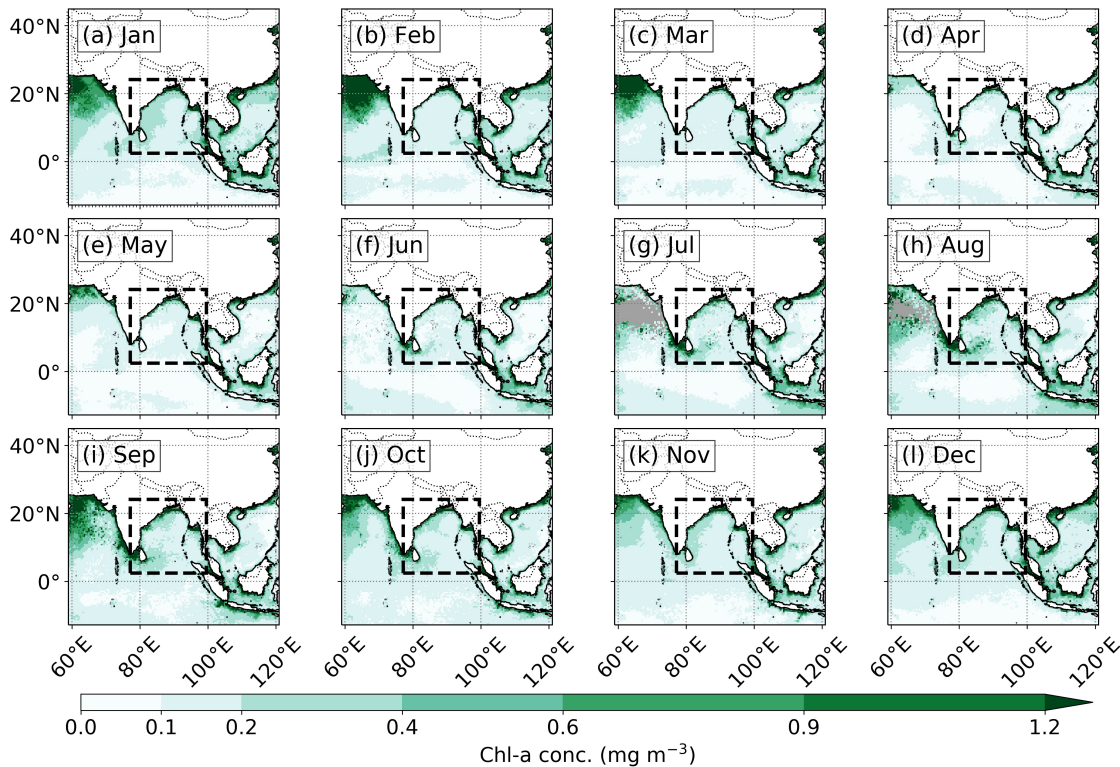


Figure 5.2: Monthly chlorophyll-a concentration climatology measured from MODIS-Aqua at 4 km horizontal resolution from January to December. The BoB domain is outlined by a black dashed box ($77\text{--}99.5^\circ\text{E}$, $2.5\text{--}24^\circ\text{N}$), which shows the location where an imposed annual cycle of chlorophyll concentration is added to a perturbation simulation, as discussed later in this Chapter.

also peak (Rao and Sivakumar, 2003). High chlorophyll concentrations are then transported along the northeast coast of the BoB (Amol et al., 2019).

In the southern BoB, strong southwesterly winds across the southernmost tip of India and Sri Lanka initiate coastal upwelling and thus biological productivity, leading to a maximum in chlorophyll concentration there in August (Fig. 1.4; Lévy et al., 2007). The Southwest Monsoon Current (SMC), a shallow, fast current, advects these high chlorophyll concentrations to the southwest BoB (Fig. 1.4; Vinayachandran et al., 2004). High chlorophyll concentrations are sustained east of Sri Lanka by the cyclonic (anticlockwise) eddy of the Sri Lanka Dome (SLD), where open ocean Ekman upwelling transfers nutrients to the near surface during JJAS (Fig. 1.4; Vinayachandran and Yamagata, 1998; Vinayachandran et al., 2004; Thushara et al., 2019). In the west and southwest BoB in winter, northeasterly winds induce open-ocean Ekman upwelling, leading to increased chlorophyll concentrations peaking in December and January (Fig. 5.2l–5.2a; Vinayachandran and Mathew, 2003; Lévy

et al., 2007). Chlorophyll concentrations in the open BoB also show sub-seasonal and mesoscale variability. Surface chlorophyll concentrations are periodically enhanced by transient cold-core eddies and post-monsoon cyclones, where the strong salinity stratification is briefly eroded and nutrients are transported to the near-surface in the western and central BoB (Vinayachandran and Mathew, 2003; Prasanna Kumar et al., 2007; Patra et al., 2007).

Chlorophyll significantly affects Indian Ocean SST and the South Asian monsoon through the absorption of sunlight (Nakamoto et al., 2000; Wetzel et al., 2006; Turner et al., 2012; Park and Kug, 2014). Nakamoto et al. (2000) used an ocean isopycnal GCM, with a two-band solar absorption scheme from Paulson and Simpson (1977), to investigate SST modulation in the Arabian Sea. Imposing a monthly climatology of chlorophyll concentrations, measured by the Coastal Zone Color Scanner (CZCS), decreased the MLD and solar radiation penetration depth during the intermonsoon, and increased SST by 0.6°C . Wetzel et al. (2006) used a biogeochemistry model coupled to an ocean-atmosphere GCM to show that spring chlorophyll blooms in the western Arabian Sea increased SST by 1°C at 20°N that led to an increase in rainfall of 3 mm day^{-1} over western India during the southwest monsoon onset. Turner et al. (2012) showed similar results when they imposed seasonally varying chlorophyll concentrations from SeaWiFS in a coupled ocean-atmosphere GCM. The spring chlorophyll blooms in the western Arabian Sea reduced MLD biases by 50%, increased SST by $0.5\text{--}1.0^{\circ}\text{C}$ and increased rainfall by 2 mm day^{-1} over southwest India during the southwest monsoon onset. Park and Kug (2014) used a biogeochemistry model coupled to an ocean GCM to investigate the biological feedback on the Indian Ocean Dipole (IOD). The response to interactive biology enhanced both warming during a positive IOD (cooling in the eastern Equatorial Indian Ocean) and cooling during a negative IOD (warming in the eastern Equatorial Indian Ocean), thus dampening the IOD magnitude, which could have significant effects on the South Asian summer monsoon.

A few studies have briefly analysed the effect of seasonally varying chlorophyll concentrations on BoB upper ocean dynamics and SST, whilst also speculating how this may affect the South Asian monsoon (Murtugudde et al., 2002; Wetzel et al., 2006). However, this is the first study to analyse the direct effect of BoB seasonally varying chlorophyll concentrations on the South Asian monsoon in a coupled GCM. A description of the experimental design, model and observed datasets used in this study is presented in Section 5.2. Section 5.3 presents the results of the control and chlorophyll-perturbed model outputs.

Section 5.4 discusses the results from the chlorophyll-perturbed experiment and conclusions are given in Section 5.5.

5.2 Methods and data

5.2.1 MetUM-GOML

This study uses the Global Ocean Mixed Layer 3.0 configuration of UK Met Office Unified Model (MetUM-GOML3.0), which comprises the Multi-Column K Profile Parameterisation ocean (MC-KPP version 1.2) coupled to the MetUM Global Atmosphere 7.0 (Walters et al., 2019). The atmospheric horizontal resolution is N216, which corresponds to a horizontal grid spacing of approximately 90 km. There are 85 vertical levels in the atmosphere, with approximately 50 vertical levels in the troposphere. MetUM-GOML3.0 is configured similarly to MetUM-GOML2.0 (Peatman and Klingaman, 2018) and MetUM-GOML1.0 (Hirons et al., 2015), except that the atmospheric model is updated to GA7.0 and the air-sea coupling routines are updated to couple the models via the Ocean-Atmosphere-Sea Ice-Soil (OASIS) Model Coupling Toolkit (Valcke, 2013).

MC-KPP consists of a grid of independent one-dimensional columns, with one column positioned under each atmospheric grid point. The ocean columns are 1000 m with 100 vertical points, with 70 points in the top 300 m; the near-surface resolution is approximately 1 m. This improves the representation of MLD and SST, which has been shown to improve tropical convection and circulation on subseasonal scales when coupled to an atmospheric GCM (Bernie et al., 2005; Bernie et al., 2008; Klingaman et al., 2011). Each column is subject to surface forcing from freshwater, heat and momentum fluxes; vertical mixing is parameterised using the KPP scheme from Large et al. (1994). The MLD is defined as the depth where the bulk Richardson number equals the critical Richardson number of 0.3 (Large et al., 1994).

Solar radiation absorption is represented as a wavelength-dependent penetration depth, with blue wavelengths penetrating deeper than red wavelengths. The decay of solar irradiance through the water column is represented as a simple two-band double-exponential function (Paulson and Simpson, 1977):

$$\frac{I(z)}{I_0} = Re^{-\frac{z}{h_1}} + (1 - R)e^{-\frac{z}{h_2}} \quad (5.1)$$

where $I(z)$ is the solar irradiance at depth z ; I_0 is the solar irradiance at the ocean surface; R is the ratio of red light to the total visible spectrum; and h_1 and h_2 are the e -folding depths or scale depths of red and blue light, respectively. Paulson and Simpson (1977) determined the optical parameters based on each of the five Jerlov water types that categorise open ocean turbidity (Jerlov, 1968). Water type IB represents the average open ocean turbidity, where chlorophyll concentrations are $\sim 0.1 \text{ mg m}^{-3}$ (Morel et al., 1988); h_1 and h_2 are 1 m and 17 m, respectively. Increasing upper-ocean turbidity to water type III, where chlorophyll concentrations exceed $1.5\text{--}2.0 \text{ mg m}^{-3}$ (Morel et al., 1988), yields h_1 and h_2 of 1.4 m and 7.9 m, respectively. The scale depth for red light ($h_1 \sim 1\text{--}1.4$ m) for all water types is much less than the typical MLD (> 10 m). Hence, all red light is absorbed at the top of the mixed layer. However, the scale depth for blue light ($h_2 \sim 8\text{--}17$ m) is comparable to the typical MLD; a significant fraction of blue light will penetrate below the mixed layer. Hence, the reduction of h_2 with increasing turbidity controls the radiant heating of the mixed layer and thus SST (Zaneveld et al., 1981; Lewis et al., 1990; Morel and Antoine, 1994).

MC-KPP uses the Paulson and Simpson (1977) scheme (Eq. 5.1) for the absorption of red and blue light with depth through the upper ocean. Chlorophyll and biogeochemical processes are not included. The effect of chlorophyll on the ocean is modelled by specifying h_2 .

MC-KPP does not represent horizontal or vertical advection. The ocean temperature and salinity correction method of Hirons et al. (2015) is used to constrain the MC-KPP mean state to account for missing advection and biases in atmospheric surface fluxes. The method uses a 10-year MetUM-GOML simulation in which temperature and salinity are relaxed (with a 15-day timescale) to an observed seasonal cycle, here the 1980-2009 climatology of Smith and Murphy (2007). A mean seasonal cycle of daily temperature and salinity tendencies is computed from this simulation. The absence of ocean dynamics means MetUM-GOML does not represent coupled modes of variability (e.g. ENSO or IOD) that rely on a dynamical ocean (Hirons et al., 2015). The benefit of not representing these modes of variability is that the signal from the chlorophyll perturbation experiment will not be obscured by the “noise” of these interannual climate variations. The absence of full ocean dynamics also reduces computational cost and allows the model to be used for

climate-length coupled simulations with shorter spin-up periods (Hirons et al., 2015).

We directly impose a seasonally varying h_2 value (representative of chlorophyll concentration) to selected columns within the BoB region whilst the global ocean outside the BoB region has a constant h_2 value (chlorophyll concentration). This set-up enables us to investigate the direct impact of chlorophyll on BoB surface ocean properties, atmospheric surface fluxes and the regional climate. Furthermore, the absence of biological and physical feedbacks on chlorophyll development means that a consistent seasonally varying h_2 value (i.e. chlorophyll concentration) is directly imposed on columns within the BoB throughout the simulation.

5.2.2 Chlorophyll-a data

To produce a temporally and spatially varying field of h_2 for MC-KPP, a monthly climatology of chlorophyll-a concentration, measured from the Moderate Resolution Imaging Spectroradiometer (MODIS) on the Aqua satellite, was used. MODIS-Aqua chlorophyll-a concentration (available from NASA's ocean color database; <https://oceancolor.gsfc.nasa.gov>) is available as a 17-year climatology (2002–2018) at a spatial resolution of 4 km. The backscattered solar radiation from the ocean surface (water-leaving radiance) in nine spectral bands between 412–869 nm measured by MODIS-Aqua were used to calculate chlorophyll-a concentration (Hu et al., 2012). Chlorophyll-a concentration retrievals below 0.25 mg m^{-3} were calculated using the Color Index (CI) three-band reflectance algorithm (Hu et al., 2012). Chlorophyll-a retrievals above 0.3 mg m^{-3} were calculated using the Ocean Color 3 (OC3) algorithm, which is a fourth-degree polynomial relating three wavelengths of water-leaving radiance (433, 490 and 550 nm) to chlorophyll-a concentration (O'Reilly et al., 2000). Chlorophyll-a retrievals from 0.25 to 0.3 mg m^{-3} were calculated by merging the CI and OC3 algorithms to create the Ocean Color Index (OCI) algorithm (Wang and Son, 2016; Hu et al., 2019). Chlorophyll-a concentration retrievals above 5 mg m^{-3} reduce the effectiveness of the OC3 algorithm (Morel et al., 2007). Organic and terrestrial material, introduced by rivers or mixed by tidal currents in coastal regions, change the scattering of visible light, affecting the water-leaving radiances (Boss et al., 2009) and leading to an overestimate in chlorophyll-a concentration (Morel et al., 2007). Hence, remotely sensed chlorophyll-a concentrations were not determined in the eutrophic coastal regions of the

Ganges and Irrawady river deltas because of the large amount of suspended organic and terrestrial material (Tilstone et al., 2011). MODIS sensor degradation on the Aqua satellite has been small (Franz et al., 2008) and all ocean color products have since been corrected and improved after cross-calibration with the SeaWiFS climatology (Meister and Franz, 2014). Chlorophyll-a will henceforth be referred to as “chlorophyll” for convenience.

In Chapter 3, in situ observations highlighted the sub-daily and sub-mesoscale variability of chlorophyll concentration across the southern BoB. Due to the limited spatial and temporal extent of the glider observations, the glider data are not appropriate to produce a seasonally varying h_2 field for the perturbation simulation. Instead, satellite-derived chlorophyll concentrations provide the most appropriate spatial and temporal extent for the perturbation simulation. In general, in situ observations of chlorophyll concentration have been essential in deriving and validating satellite chlorophyll concentrations (e.g., Morel and Maritorena, 2001), which have then been assimilated into GCMs. Here, the glider observations in Chapter 3 have not been used to derive or validate satellite chlorophyll concentrations in this Chapter due to the observational dataset being too small.

5.2.3 Experiment set-up

To investigate the impact of the seasonal and spatial variability of chlorophyll-induced heating in the BoB, two 30-year simulations were completed, with differing prescribed h_2 (chlorophyll concentrations): a control run using $h_2 = 17$ m globally and a perturbation run using an annual cycle of h_2 at daily resolution for the BoB region (defined below) and $h_2 = 17$ m over the rest of the global ocean. In both simulations, R and h_1 were kept constant, at 0.67 and 1.0 m respectively, representative of water type IB. The first year of both simulations was discarded due to spin up; the analysis was carried out on the remaining 29 years.

The control simulation used an effective constant global chlorophyll concentration of $\sim 0.15 \text{ mg m}^{-3}$, which corresponds to $h_2 = 17$ m (Jerlov water type IB; Morel, 1988). Previous studies have used control simulations with zero chlorophyll concentrations to see the full impact of chlorophyll on physical and dynamical processes (e.g. Gnanadesikan and Anderson, 2009), whilst other studies have used constant scale depths determined from parameterisations of the lowest chlorophyll concentrations encountered (e.g. Shell et al., 2003; Turner

et al., 2012). Satellite observations show that the global average chlorophyll concentration for oceans deeper than 1 km is 0.19 mg m^{-3} (Wang et al., 2005), similar to the value in our control simulation.

For the perturbation simulation, the BoB region was defined as the area $77\text{--}99.5^\circ \text{ E}$ and $2.5\text{--}24^\circ \text{ N}$ (black dashed box; Fig. 5.2). The region extends far enough south and west to incorporate the high surface chlorophyll around the southernmost tip of India and Sri Lanka, but excludes the relatively low near-equatorial surface chlorophyll concentrations (Fig. 5.2f–5.2j). The isthmus of Thailand and Myanmar to the east, and India and Bangladesh to the north and west, form a natural boundary to the defined BoB region (Fig. 1.4). An annual cycle of daily chlorophyll concentration for MetUM-GOML was derived by linearly interpolating the monthly climatology to daily values, then regridding from the resolutions of the observations (4 km) to MetUM-GOML ($\sim 90 \text{ km}$).

Satellite derived chlorophyll concentrations were converted to h_2 using a fifth-order polynomial parameterisation from Morel and Antoine (1994) (Fig. 5.3a–5.3c). This high-order polynomial relationship relates blue light from a two-band solar absorption scheme to surface chlorophyll concentrations that are assumed to have a Gaussian vertical profile in the upper ocean. The relationship shows scale depth varying as a power law function of surface chlorophyll concentration with the largest variability of scale depth ($> 18 \text{ m}$) at the lowest concentrations ($< 0.1 \text{ mg m}^{-3}$).

Missing h_2 data were common in regions such as the Ganges River delta due to undetermined remotely sensed chlorophyll concentrations from highly turbid coastal waters. Missing h_2 data in this delta extend further out onto the continental shelf during JJAS as floodwaters drain into the BoB transporting finer silt and clay further offshore (Kuehl et al., 1997). The missing h_2 data were typically associated with regions where the land fraction was less than 1, which includes the narrow isthmus of Thailand and the low-lying land of the Ganges delta. A minimum of two h_2 values from two neighbouring data points were required to find an average h_2 value to fill in the missing data point. At the boundary of the BoB domain, to avoid sharp gradients the seasonally varying h_2 values within the BoB domain were smoothly transitioned (linearly) to the constant $h_2 = 17 \text{ m}$ outside the BoB domain, over a buffer region of three grid points.

The statistical significance of the differences between the two simulations

was examined using the two-tailed Students t -test. Vertically integrated moisture fluxes (VIMF) were used to evaluate the water vapour transport sourced from the chlorophyll-forced BoB to the surrounding Indian subcontinent. The VIMF was calculated as

$$\text{VIMF} = \frac{1}{g} \int \vec{u}q \, dp \quad (5.2)$$

where \vec{u} is the horizontal wind velocity, q is the specific humidity, g is the acceleration due to gravity, p is pressure and the integration was between 1000 and 100 hPa. Note that $\vec{u}q$ was output directly by the model as monthly mean values. Although VIMF would show changes in the moisture transport caused by chlorophyll-induced SST warming, VIMF is not an appropriate diagnostic for assessing whether changes in moisture transport leads to changes in rainfall. Moisture transported into a region must converge or diverge for there to be a change in rainfall. Thus, VIMF divergence is an appropriate diagnostic for assessing whether chlorophyll-induced changes in moisture transport leads to changes in rainfall over the Indian Subcontinent. The VIMF divergence was calculated as

$$\text{VIMFD} = \frac{1}{g} \int \frac{\delta \vec{u}q}{\delta x} + \frac{\delta \vec{v}q}{\delta y} \, dp \quad (5.3)$$

where the integration was between 1000 and 100 hPa. An area-weighted re-gridding scheme was used to reduce the 0.25° horizontal resolution of the observed monthly 18-year (1998–2015) climatological precipitation rate measured from the Tropical Rainfall Measuring Mission (TRMM) 3B42 satellite product (Huffman et al., 2007) to match the horizontal resolution of MetUM-GOML. The observed monthly climatological precipitation rate was used to diagnose the bias in the model precipitation rate.

5.3 Results

5.3.1 Southwest monsoon onset (April to June)

The BoB surface ocean responds to the imposed annual cycle of h_2 in the perturbation run during the onset of the southwest monsoon. Values of h_2 increase above the global constant of 17 m, as surface chlorophyll concentrations

are low in the central BoB during April (Fig. 5.3a). The values of h_2 are as low as 5 m along the northern BoB coast, as surface chlorophyll concentrations in coastal areas are higher than those in the central BoB (Fig. 5.3a). In May, the imposed h_2 in the southwest BoB begins to decrease (this corresponds to the advection of high chlorophyll concentrations from the south coast of India and Sri Lanka; Fig. 5.3b). By June, h_2 shoals to 14 m, as the strengthening SMC increases the chlorophyll concentration across the southern BoB (Fig. 5.3c). The values of h_2 decrease and mixed-layer solar absorption increases, as high coastal chlorophyll concentrations in the northwest BoB extend oceanward across the continental shelf during May and June.

The imposed annual cycle of h_2 directly affects coastal SST. During April the increase in solar absorption by chlorophyll along the northern and western coastal regions significantly (at 5% level) increases monthly average SST by 0.5°C (Fig. 5.3d). Correspondingly, the monthly average 1.5 m air temperature increases by 0.5°C in the perturbation run (Fig. 5.3g). The strengthening alongshore wind over the warmer western coast results in a large increase in upward latent heat flux of 20 W m^{-2} (Fig. 5.3j). This increase in atmospheric moisture leads to an anomaly in the VIMF of $30 \text{ kg m}^{-1} \text{ s}^{-1}$ (Fig. 5.5a) that is in the same direction as the mean VIMF in the control run (Fig. 5.4a). The increase in VIMF converges over northeast India and Bangladesh as shown by the negative VIMF divergence (Fig. 5.5a), supplying extra moisture needed for the increase in precipitation rate of 2 mm day^{-1} (significant at the 5% level; Fig. 5.3m).

The increase in solar absorption in the mixed layer by high chlorophyll concentrations persists during May and June along the coasts (Fig. 5.3b and 5.3c). Low h_2 along the northern and western BoB coastal regions acts to increase monthly average SST by 0.5°C (Fig. 5.3e and 5.3f). This is offset by negative feedback from the latent heat flux (Fig. 5.3k and 5.3l), which is due to an increase in the surface specific humidity associated with the higher SST.

In June, the precipitation rate over the Myanmar coast increases by 3 mm day^{-1} (significant at the 5% level; Fig. 5.3o). Comparing the monthly average precipitation rate difference (Fig. 5.3o) with the control simulation bias (Fig. 5.6a and 5.6c) shows that the model dry bias of 4 mm day^{-1} over the Myanmar coast is partly removed in the perturbation run. The monthly average 1.5 m air temperature increases by 0.4°C (Fig. 5.3i), which corresponds to an increase in SST (Fig. 5.3f) where h_2 along the western BoB is shallow (Fig. 5.3c). The upward latent heat flux increases by 10 W m^{-2} (Fig. 5.3l) and the

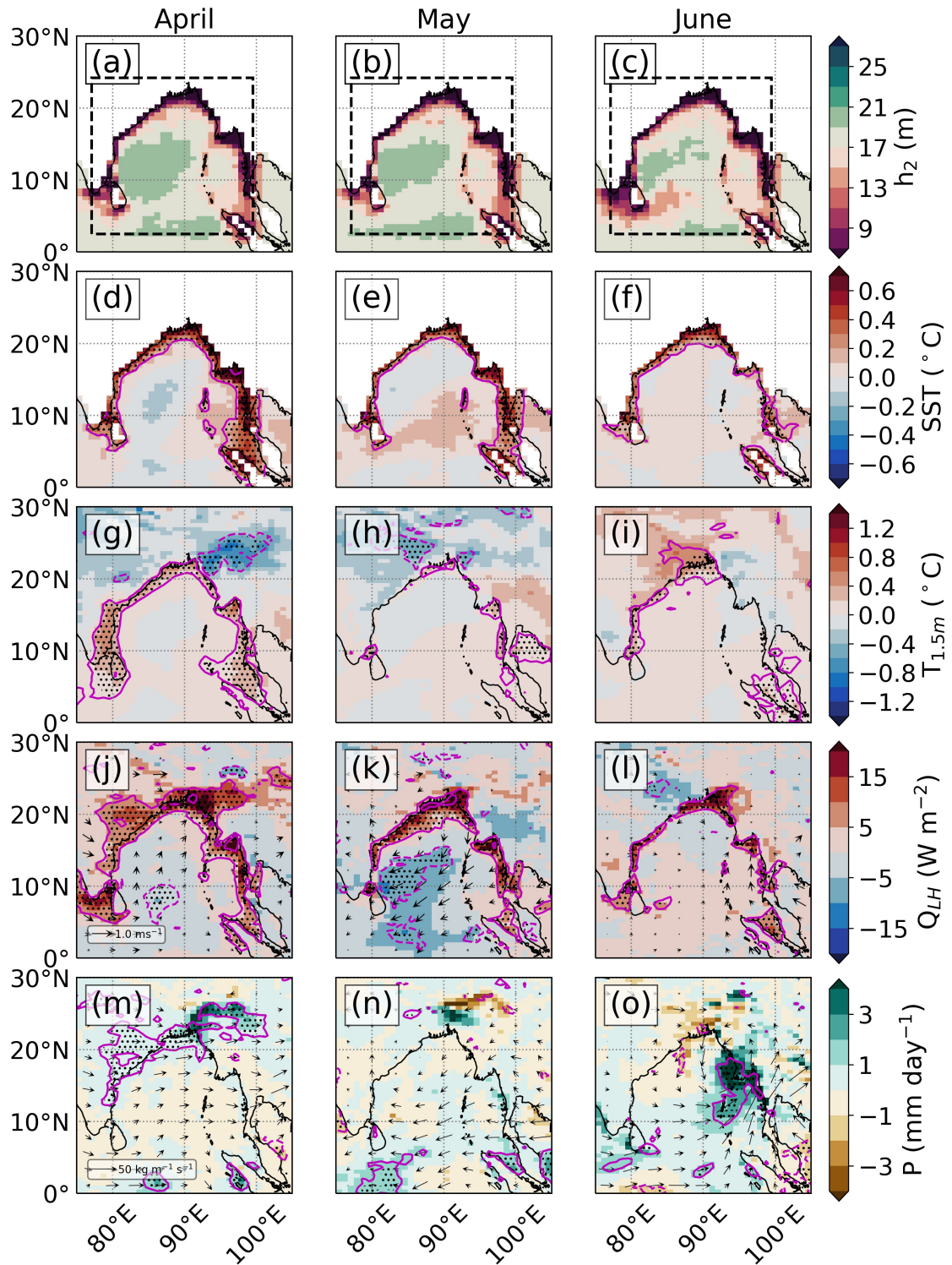


Figure 5.3: Monsoon onset season (April to June). (a-c) Monthly average h_2 (m) in the perturbation run. Monthly 29-year average difference (perturbation minus control) of: (d-f) SST ($^{\circ}\text{C}$); (g-i) 1.5 m air temperature ($^{\circ}\text{C}$); (j-l) upward latent heat flux (W m^{-2}) and 10 m wind velocity (m s^{-1}); (m-o) model precipitation rate (mm day^{-1}). The magenta line shows the 10% significance level and the black stippling shows the 5% significance level.

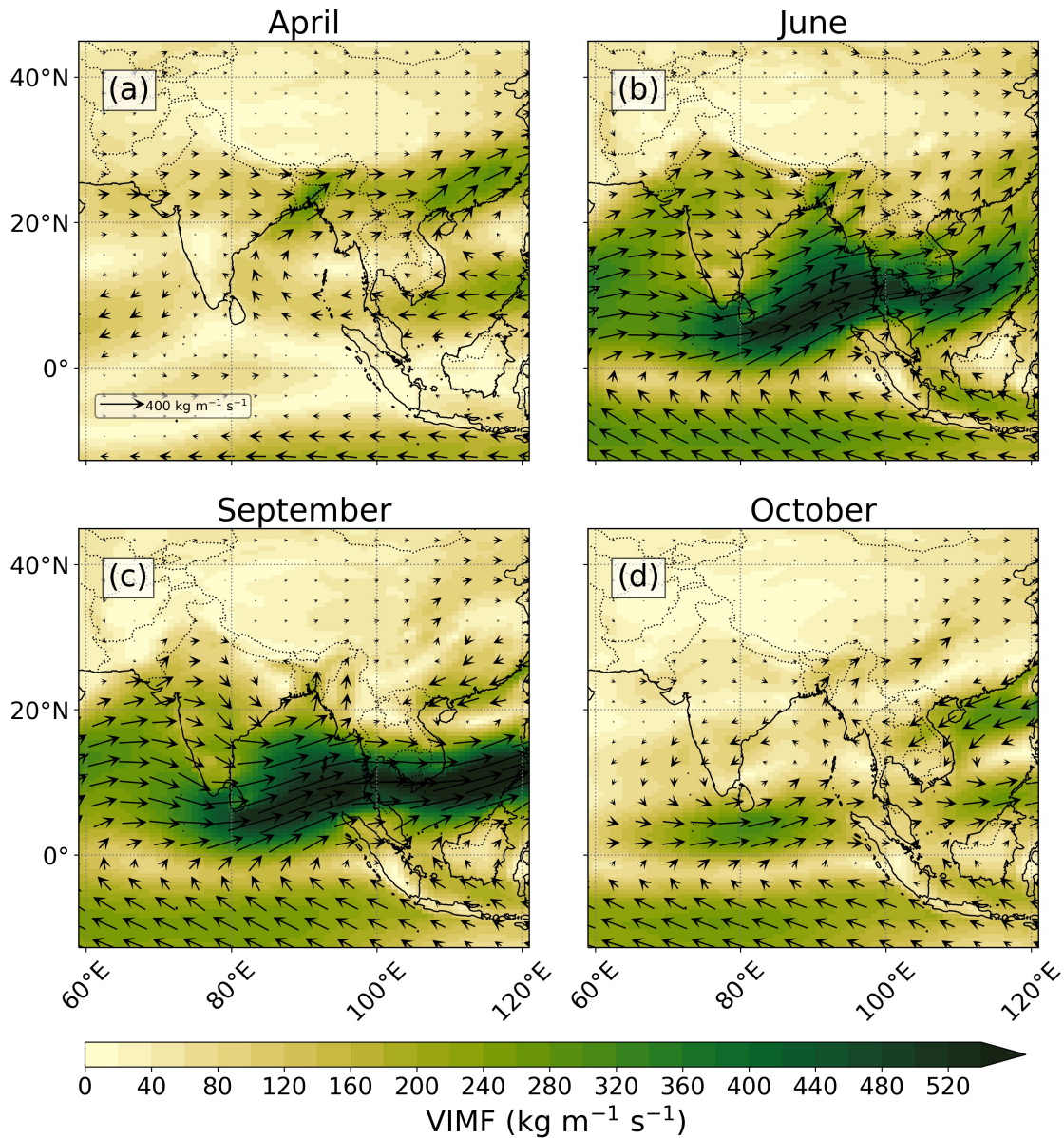


Figure 5.4: Monthly 29-year average VIMF from the control run for: (a) April; (b) June; (c) September; (d) October.

VIMF increases by $20 \text{ kg m}^{-1} \text{ s}^{-1}$ (Fig. 5.5b) in addition to a strengthening southwesterly moisture transport during the southwest monsoon onset (Fig. 5.4b). The enhanced convergence of VIMF over the Myanmar coast (Fig. 5.5b) supplies the moisture for the increase in precipitation rate (Fig. 5.3o).

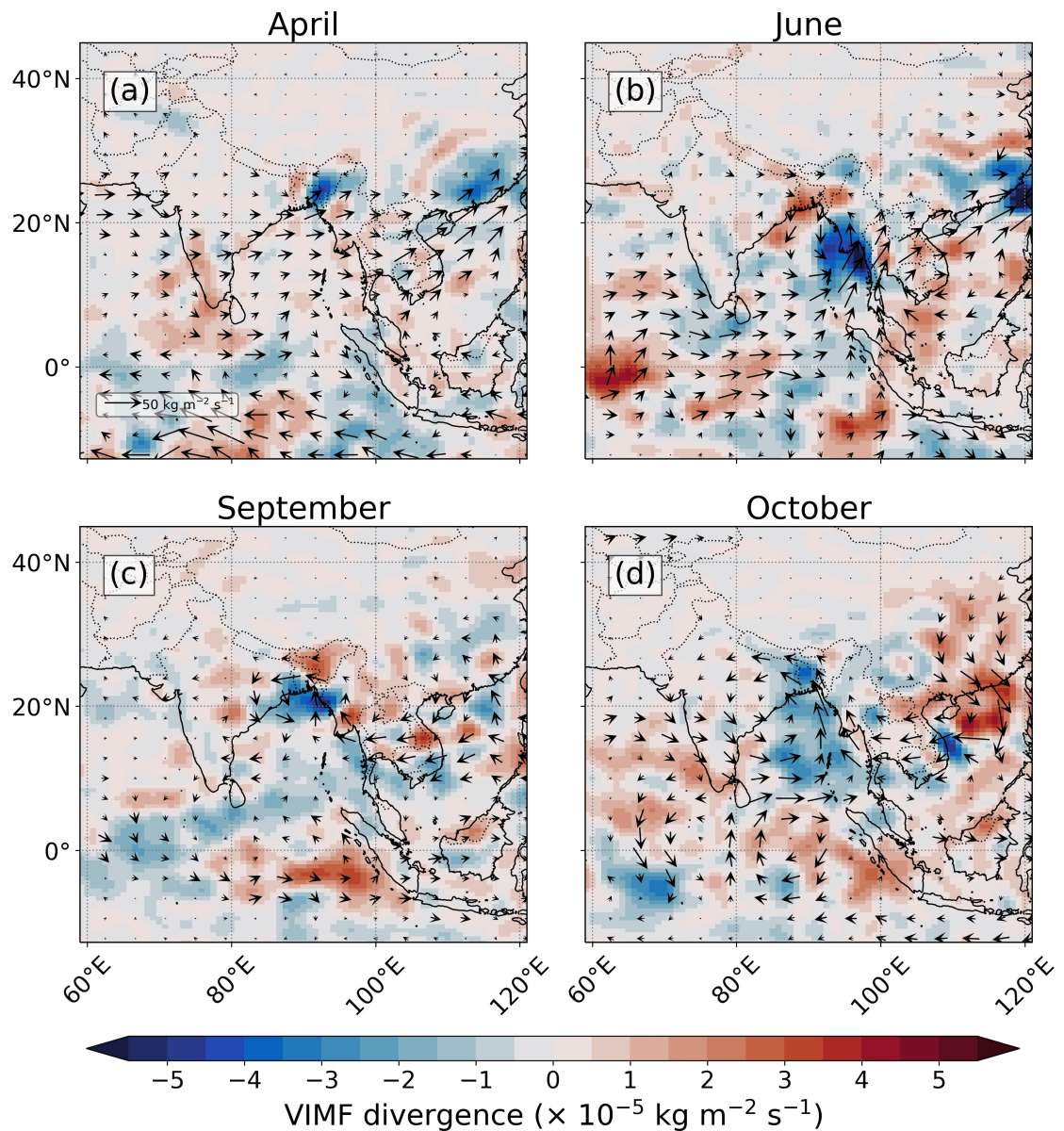


Figure 5.5: Monthly 29-year average difference (perturbation minus control) of VIMF (vector arrows) and VIMF divergence (shaded) for: (a) April; (b) June; (c) September; (d) October.

5.3.2 Southwest monsoon (July to October)

The values of h_2 continue to decrease in the southwestern BoB into July and August (Fig. 5.7a and 5.7b), associated with the advection of high chlorophyll concentrations from the south coast of India and Sri Lanka. The monthly average h_2 is 11 m along the northwest BoB (Fig. 5.7b), corresponding to an increase in chlorophyll concentration. The lowest monthly average h_2 in the SMC region (southwestern BoB) occurs in August with a value of 12 m, before

increasing to 15 m in October as the SMC weakens (Fig. 5.7b and 5.7d). In the central BoB, average h_2 decreases to 16 m, as chlorophyll concentrations increase (Fig. 5.7a). The August average h_2 decreases further to 15 m, as high chlorophyll concentrations off the continental shelf and SMC encroach further into the open ocean (Fig. 5.7b). The September and October average h_2 increases to 16 m, as the SMC weakens and high chlorophyll concentrations retreat back to the coast (Fig. 5.7c and 5.7d). In October, monthly average h_2 decreases to 13 m along the northwest BoB, as high chlorophyll concentrations retreat back onto the continental shelf (Fig. 5.7d).

BoB surface ocean and regional climate respond to the above changes in h_2 during JJAS. Higher coastal SSTs (significant at the 10% level) are collocated with the high coastal chlorophyll concentrations, whereas, open-ocean SST is largely unchanged by BoB chlorophyll forcing (Fig. 5.7e–5.7g). In July, a slight increase in alongshore windspeed over the west BoB increases the upward latent heat flux (Fig. 5.7m), but this does not significantly change precipitation rate (Fig. 5.7q). In August, a further increase in the alongshore windspeed increases the magnitude and spatial extent of the upward latent heat flux across the northern BoB (Fig. 5.7n). During September an increase in windspeeds over the northern Myanmar coast increases surface ocean evaporation (Fig. 5.7o). The VIMF increases in magnitude and remains approximately in the same direction as the mean VIMF in the control run (Fig. 5.4c and 5.5c). VIMF convergence over the northern Myanmar and Bangladeshi coast in the perturbation run (Fig. 5.5c) supplies moisture for the increase in precipitation rate in this region (significant at the 5% level; Fig. 5.7s).

By October the combined atmospheric moisture sourced from the warmer western BoB and Andaman Sea leads to an increase in precipitation rate of up to 3 mm day⁻¹ over west Bangladesh and northeast India (significant at the 5% level; Fig. 5.7t). The spatial extent of the increased precipitation rate is considerably larger than previous months, extending further west over the Indo-Gangetic plain and encompassing megacities such as Kolkata and Dhaka. An area-weighted 29-year monthly average precipitation rate over west Bangladesh and northeast India (20–25° N, 85–90° E; black dashed box in Fig. 5.7t) shows a rainfall maximum in August in both simulations (Fig. 5.8a). The precipitation rate differences gradually increase from July to August and peak in October at 2 mm day⁻¹ (Fig. 5.8b). Comparing the precipitation differences (Fig. 5.7t) with the model bias (Fig. 5.6b and 5.6d) shows that the model dry bias of up to 3 mm day⁻¹ over northeast India is removed in the perturbation

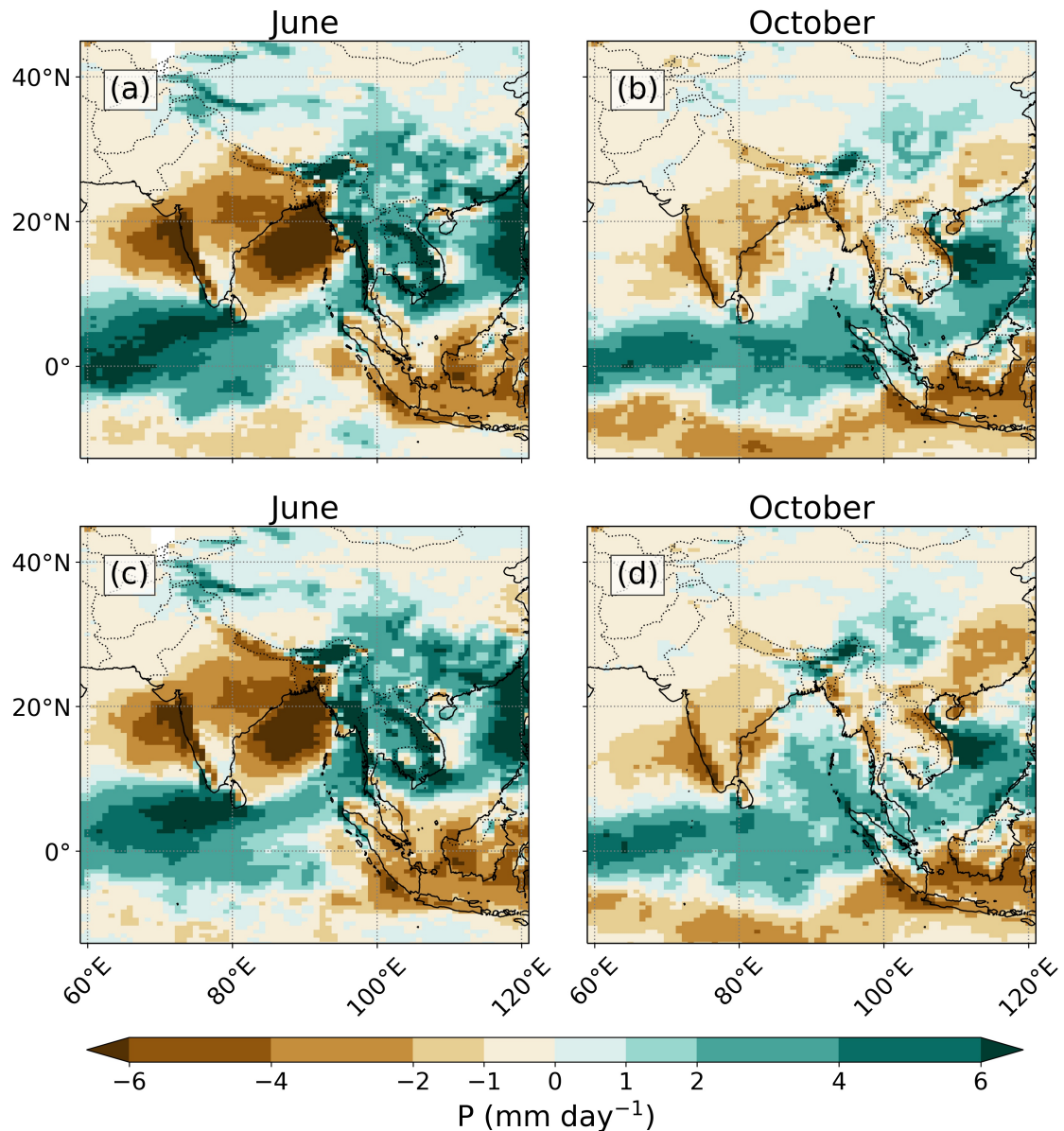


Figure 5.6: Model bias of precipitation rate during June and October. (a, b) Bias calculated as the monthly 29-year average precipitation rate from the control run minus the monthly climatological precipitation rate observed from TRMM satellite; (c, d) same as (a, b) but perturbation run minus TRMM.

run. Alongshore winds over the warmer isthmus of Thailand and the coast of Myanmar further increase atmospheric moisture transport to the northern BoB (Fig. 5.4d). The upward latent heat flux increases by 13 W m^{-2} (Fig. 5.7p) and the VIMF increases by $30 \text{ kg m}^{-1} \text{ s}^{-1}$ over the coast of Myanmar (Fig. 5.5d). The VIMF convergence over west Bangladesh and northeast India supplies moisture for the increase in precipitation rates in this region (Fig. 5.5d).

The enhanced convective activity over west Bangladesh and northeast India

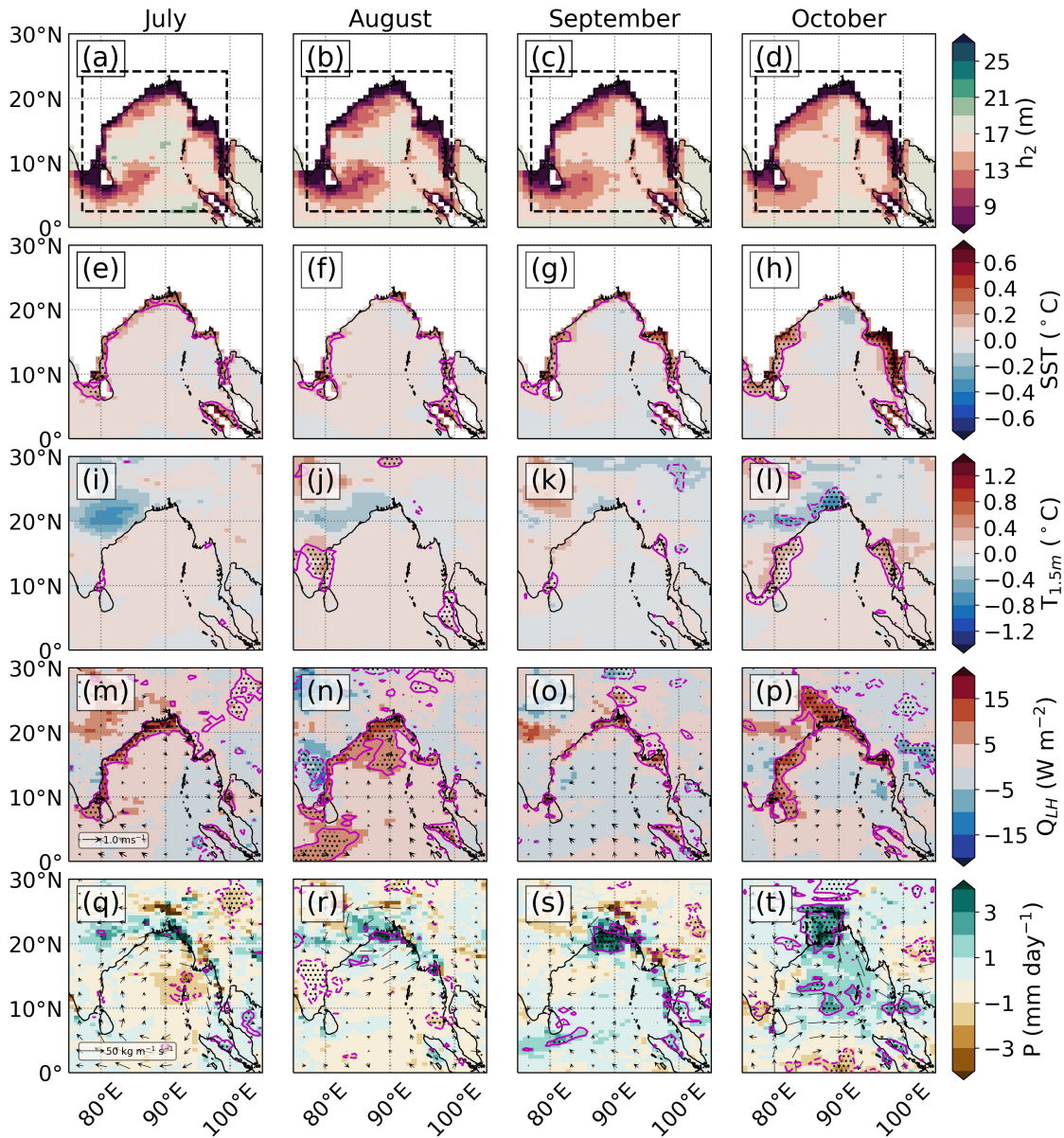


Figure 5.7: As Figure 5.3 but for the southwest monsoon season (July to October). (t) The location of the monthly 29-year area-weighted average precipitation rate in Figure 5.8 is shown as a black dashed box ($85\text{--}90^\circ\text{E}$, $20\text{--}25^\circ\text{N}$).

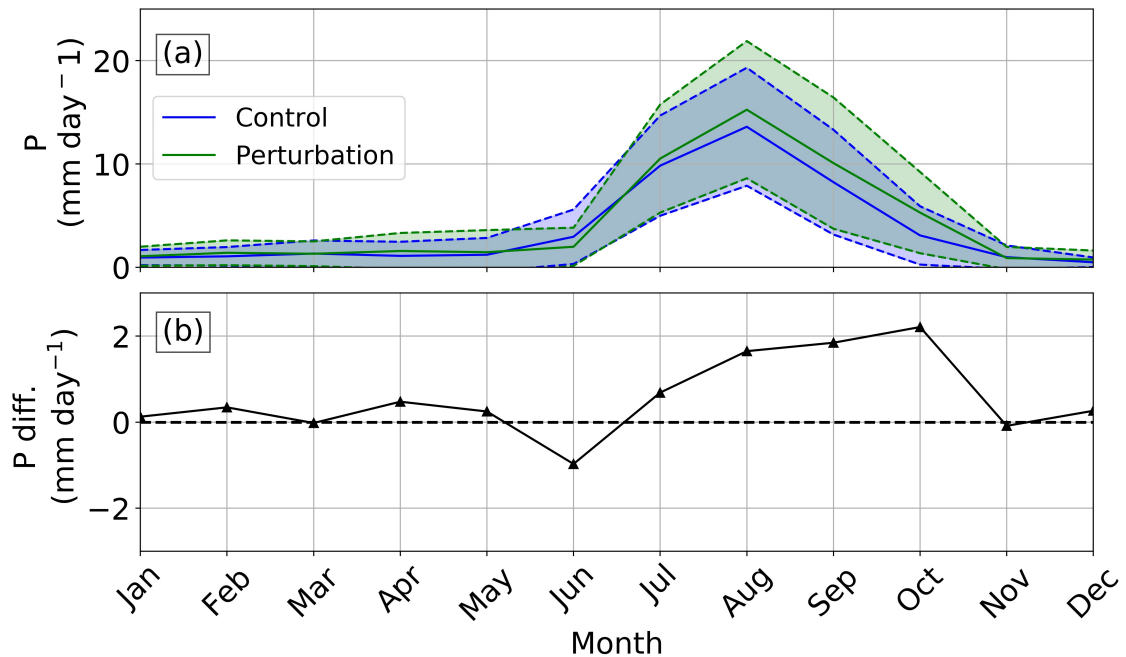


Figure 5.8: (a) Monthly 29-year area-weighted average precipitation rate for the control run (blue solid line) and the perturbation run (green solid line) for the region 85–90° E, 20–25° N. Shaded region between the dashed lines shows the one standard deviation variability. (b) The difference between the monthly 29-year area-weighted average precipitation rate between the control and perturbation run.

during October is associated with an increase in the vertical wind velocity at the 500 hPa pressure level (Fig. 5.9a). At the 200 hPa pressure level enhanced westerly winds converge over eastern China (Fig. 5.9b), which leads to increased subsidence (Fig. 5.9a) and increased positive VIMF divergence (Fig. 5.5d). This subsidence reduces precipitation and increases surface temperature over eastern China (significant at the 5% level; Fig. 5.7t). This indirect remote response resembles the effect of the “Silk Road” pattern; a stationary Eurasian-Pacific Rossby wave train that occurs during the Northern Hemisphere summer (Ding and Wang, 2005). The Silk Road pattern has been found to influence extreme heat waves over eastern China, causing considerable socio-economic devastation (Thompson et al., 2019). Indeed, the model does display significantly warmer surface temperatures in this region at this time (see Fig. 5.7l). The Silk Road pattern dynamics have been previously linked to the South Asian summer monsoon (Stephan et al., 2019). Diverging upper-tropospheric winds associated with precipitation anomalies over the Indian subcontinent interact with midlatitude westerlies, which influences the strength and positioning of the subtropical northwestern Pacific anticyclone over eastern China (Ding and

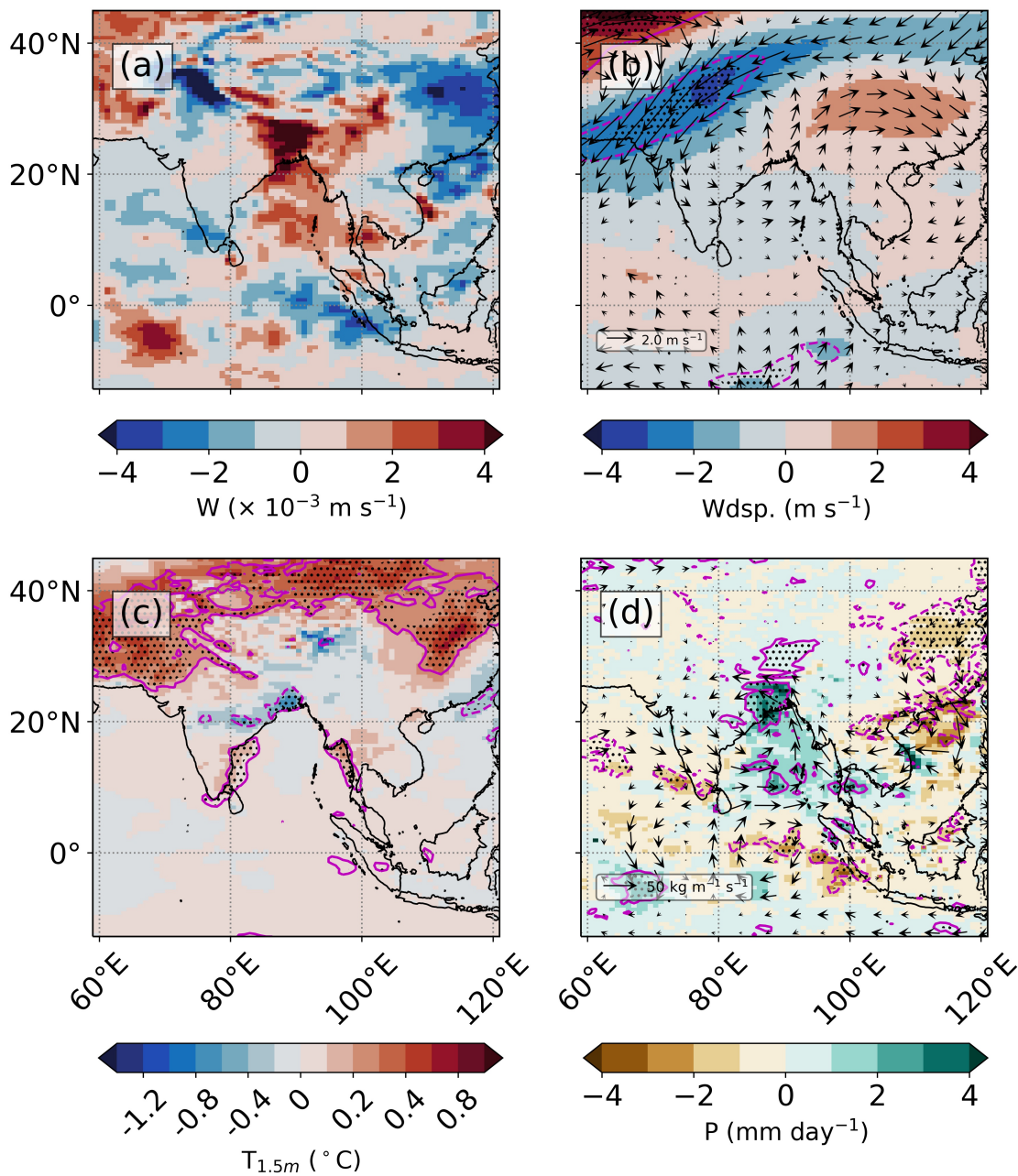


Figure 5.9: October mean difference (perturbation minus control) of: (a) 500 hPa vertical velocity; (b) 200 hPa horizontal vector wind. The magenta line shows the 10% significance level and the black stippling shows the 5% significance level.

Wang, 2005; Hu et al., 2012).

5.3.3 Mixed layer radiant heating and SST modulation

The hypothesised direct link between a change in h_2 and a resultant change in SST is examined in more detail in this subsection. The radiant heating rate of the

mixed layer, and resultant change in SST, depends not only on h_2 , but also on changes in the surface flux of shortwave radiation, which is dependent on cloud cover, and changes in the depth of the mixed layer. Here, we assess which of these three factors is primarily responsible for the changes in the radiant heating rate of the mixed layer.

We assume that the red-light radiative flux is absorbed within approximately the top 1 m and entirely within the mixed layer, and only the blue-light radiative flux can partially penetrate below the mixed layer. The radiant heating rate of the mixed layer is calculated as

$$\text{RHR} = \left. \frac{dT}{dt} \right|_Q = \frac{\overline{Q_0} - (1 - R)\overline{Q_0}e^{-\frac{H}{h_2}}}{\rho c_p H} \quad (5.4)$$

where T is the temperature of the mixed layer; t is time; $\overline{Q_0}$ is the monthly 29-year average downward shortwave radiation flux incident just below the ocean surface; $\rho = 1025 \text{ kg m}^{-3}$ is the density of the mixed layer; $c_p = 4100 \text{ J kg}^{-1} \text{ K}^{-1}$ is the specific heat capacity of sea water; $R = 0.67$ is the ratio of red light to total visible light for Jerlov water type IB; H is the monthly 29-year average MLD; and h_2 is the monthly average h_2 that was imposed in the control and perturbation run.

Within the BoB, the largest imposed change in h_2 is 13 m. Assuming that the other variables remain constant, a change in h_2 of 13 m changes the radiant heating rates by $0.3^\circ\text{C month}^{-1}$. The largest model change in downward shortwave radiation is 14 W m^{-2} , which changes the radiant heating rates by $0.2^\circ\text{C month}^{-1}$, comparable to the change from h_2 variations. The largest model MLD change is 3 m, which changes the radiant heating rates by $0.4^\circ\text{C month}^{-1}$, also comparable to the change from h_2 variations.

We compare the mixed layer radiant heating rates of the control and perturbation runs during June and October (Fig. 5.10a–5.10b). We focus on two regions: the open ocean region of the SMC ($83\text{--}86^\circ \text{ E}$, $5\text{--}8^\circ \text{ N}$; black boxes in Fig. 5.10) and the coastal region of the Irrawaddy Delta ($95\text{--}98^\circ \text{ E}$, $14\text{--}17^\circ \text{ N}$; black boxes in Fig. 5.10). In June and October, coastal regions have the highest radiant heating rate difference between the control and perturbation runs (Fig. 5.10a and 5.10b). In June, the area-weighted mean radiant heating rate in the coastal region of the Irrawaddy Delta increases by $0.4^\circ\text{C month}^{-1}$ in the perturbation run (Fig. 5.10a). An h_2 decrease of 9 m has the largest contribution to the radiant heating rate increase of $0.5^\circ\text{C month}^{-1}$, compared

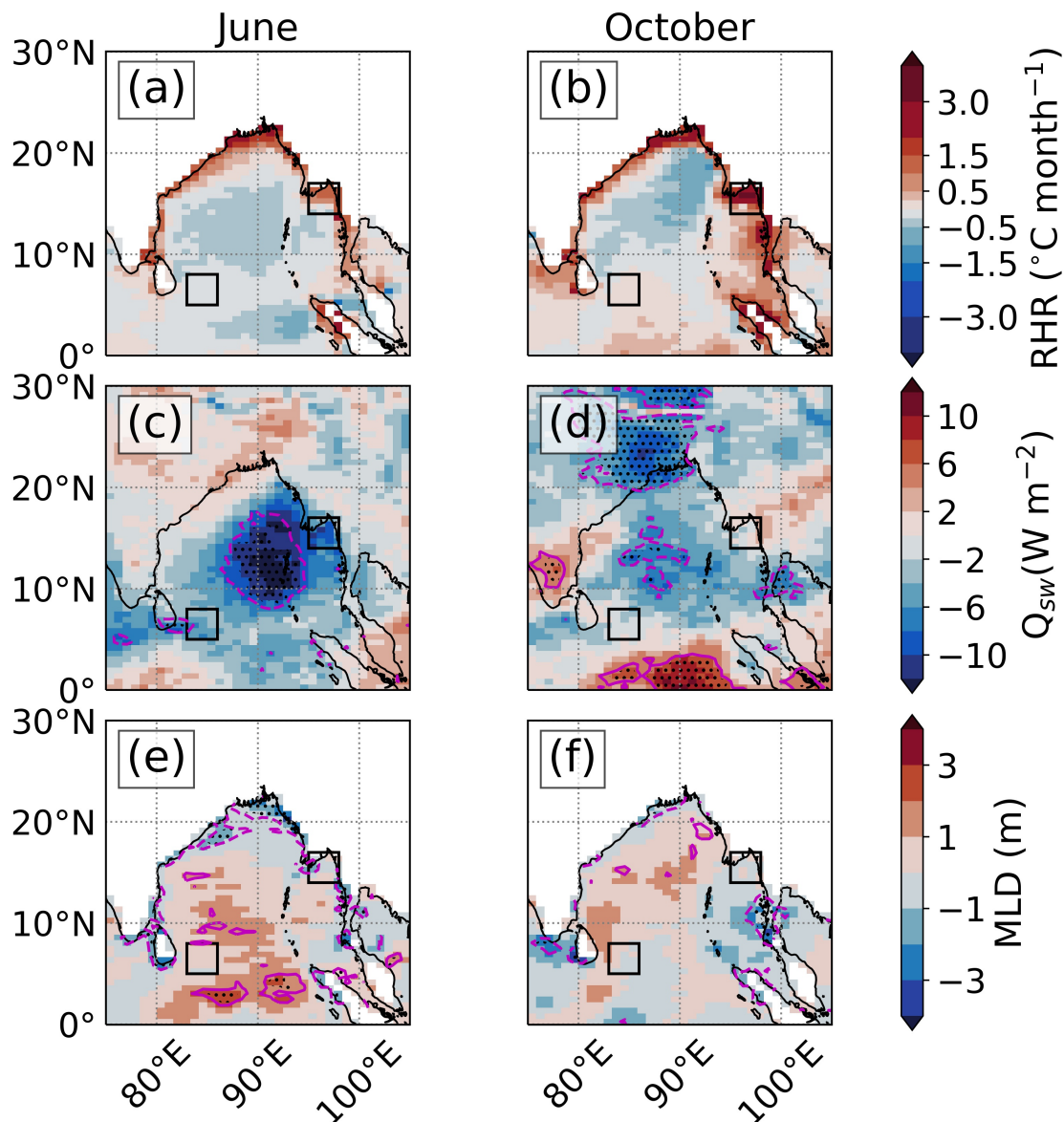


Figure 5.10: Monthly 29-year average difference (perturbation minus control) for June and October of: (a,b) radiant heating rate ($^{\circ}\text{C month}^{-1}$); (c,d) downward shortwave radiation flux (W m^{-2}); (e,f) mixed layer depth (m). The black boxes show the location of the open ocean region of the SMC (southwest BoB; $83\text{--}86^{\circ}\text{ E}$, $5\text{--}8^{\circ}\text{ N}$) and the coastal region of the Irrawaddy Delta (northeast BoB; $95\text{--}98^{\circ}\text{ E}$, $14\text{--}17^{\circ}\text{ N}$). The magenta line shows the 10% significance level and the black stippling shows the 5% significance level.

with an MLD decrease of 0.2 m (Fig. 5.10e), which contributes to an increase of $0.1^{\circ}\text{C month}^{-1}$. A decrease in downward shortwave radiation flux of 8 W m^{-2} (Fig. 5.10c), associated with an increase in monsoon cloud cover, cools the region by $0.2^{\circ}\text{C month}^{-1}$. In October, the radiant heating rate difference in the Irrawaddy Delta increases by $1.7^{\circ}\text{C month}^{-1}$ in the perturbation run. The radiant heating rate difference is larger than June because of an increase in

monthly average downward shortwave radiation flux and a shallower MLD in both the control and perturbation runs. A decrease in h_2 of 9 m has the largest contribution to the radiant heating rate increase of $1.5^\circ\text{C month}^{-1}$, whereas, a decrease in the MLD of 0.1 m (Fig. 5.10f) and an increase in downward shortwave radiation flux of 1 W m^{-2} (Fig. 5.10d) only contribute to $0.1^\circ\text{C month}^{-1}$ of the increase in radiant heating rate respectively. The changes in h_2 are more influential on mixed layer radiant heating rates and SSTs compared with small changes in MLD and downward shortwave radiation flux in the Irrawaddy Delta during June and October.

In June, the area-weighted mean radiant heating rate difference in the SMC region decreases by $0.1^\circ\text{C month}^{-1}$ in the perturbation run. A decrease in the downward shortwave radiation flux of 5 W m^{-2} (Fig. 5.10c) has the largest contribution to the radiant heating rate decrease of $0.1^\circ\text{C month}^{-1}$, whereas, a decrease in h_2 of 2 m and an increase in MLD of 0.4 m (Fig. 5.10e) contribute less than $0.1^\circ\text{C month}^{-1}$ to the radiant heating rate. In October, the radiant heating rate difference of the SMC region shows an increase of $0.1^\circ\text{C month}^{-1}$. A decrease in h_2 of 3 m has the largest contribution to the radiant heating rate increase of $0.1^\circ\text{C month}^{-1}$, whereas, a decrease in downward shortwave radiation flux of 1 W m^{-2} (Fig. 5.10d) and an increase in MLD of 0.2 m (Fig. 5.10f) contribute less than $0.1^\circ\text{C month}^{-1}$ to the radiant heating rate. In the SMC region, changes in h_2 are smaller than those in coastal regions during June and October. Thus, changes in h_2 and indirect changes in MLD and downward shortwave radiation exert a comparable control on open ocean mixed layer radiant heating rate and SST.

The radiant heating rate of the mixed layer, and resultant change in SST, further depends on the seasonal changes to the depth of the mixed layer relative to the solar penetration depth (Turner et al., 2012). Here, we examine how the depth of the mixed layer relative to the solar penetration depth affects mixed layer radiant heating rates and SSTs for the open ocean region of the SMC and the coastal region of the Irrawaddy Delta during June and October.

In the Irrawaddy Delta region during October, the MLD shoals to 9 m (green dashed line; Fig. 5.11b), which is similar to the perturbed h_2 (green dot; Fig. 5.11b). When the mixed layer is shallow, the increased near-surface radiant heating from reducing h_2 is distributed to a shallower depth, increasing the average change in the radiant heating rate by $1.2^\circ\text{C month}^{-1}$ ($\Delta dT/dt$; Fig. 5.11f). Below 10 m depth radiant heating rates reduce due to reduced h_2 . In June, the MLD is 16 m (Fig. 5.11a), meaning the effects of the increased

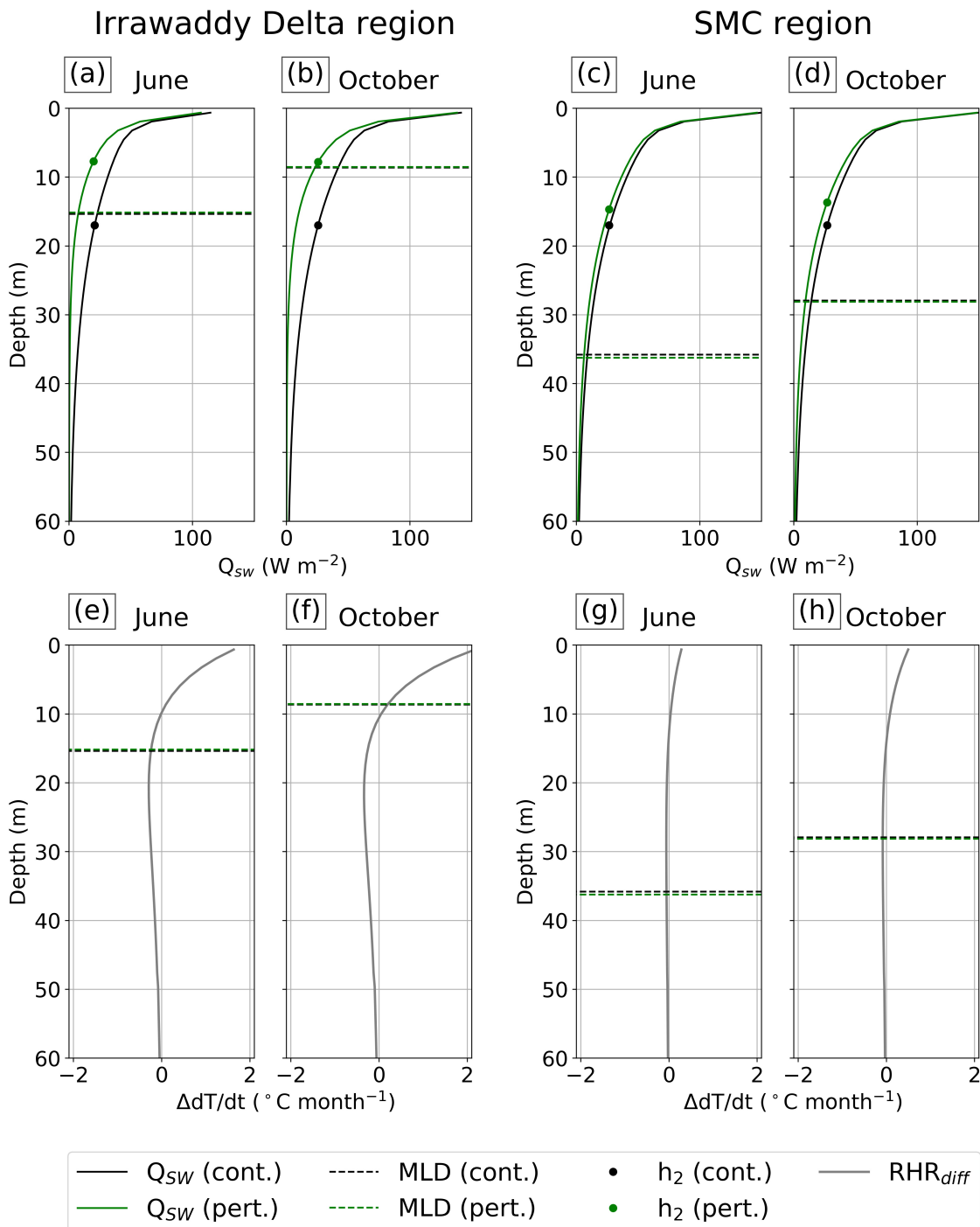


Figure 5.11: Top panels show vertical profiles of downward shortwave radiation flux from 0 to 60 m for the control (black) and perturbation (green) run for the Irrawaddy Delta region and SMC region during: (a,c) June; (b,d) October. Bottom panels show vertical profiles of radiant heating rate difference from 0 to 60 m during: (e,g) June; (f,h) October. Dashed lines show the area-weighted 29-year average mixed layer depth and coloured dots show the area-weighted average scale depth.

radiant heating rates above 10 m and reduced radiant heating rates below 10 m are mixed, resulting in a smaller average radiant heating rate change of $0.4^{\circ}\text{C month}^{-1}$ (Fig. 5.11e). Consequently, the October SST increases by 0.5°C , compared with a smaller increase of 0.2°C in June. Hence, shoaling the mixed layer to a depth comparable to the perturbed solar penetration depth in October limits the turbulent mixing processes to a depth where chlorophyll perturbs solar radiation absorption, and makes SST more sensitive to chlorophyll concentration changes.

In the SMC region during October, the MLD shoals to 28 m (Fig. 5.11d), approximately twice the depth of the perturbed h_2 , resulting in an average change in the mixed layer radiant heating rate of $0.1^{\circ}\text{C month}^{-1}$ (Fig. 5.11h). During June, the MLD extends to 36 m (Fig. 5.11c), resulting in an average change in the mixed layer radiant heating rate below $0.1^{\circ}\text{C month}^{-1}$ (Fig. 5.11g). As in the Irrawaddy Delta region, the effect of chlorophyll on upper ocean temperature depends on the MLD in the SMC region, with the shallowest MLD and largest change in radiant heating rate in October. With lower chlorophyll concentrations in the SMC region than the Irrawaddy Delta region, the resultant change in SMC regional average radiant heating rate in the top 10 m is considerably lower.

5.4 Discussion

Turner et al. (2012) identified a similar modulation of the seasonal SST cycle by MLD after imposing seasonally varying chlorophyll concentrations in the Arabian Sea. High surface chlorophyll concentrations and shallow MLDs led to an increase in SST that peaked in May. In October, another peak in surface chlorophyll concentration led to a similar, but weaker increase in SST due to deeper MLDs and stronger turbulent surface fluxes. The BoB has less biological productivity than the Arabian Sea because of light and nutrient limitation (Kumar et al., 2002), though chlorophyll concentrations in the coastal BoB can be as high as in the Arabian Sea. The BoB is also exposed to the same monsoonal winds as the Arabian Sea. Such localised, physical forcing modulates the MLD, which in turn modulates the biological warming. Hence, the SST increase of 0.5°C in coastal regions of the BoB during the spring and autumn intermonsoons is similar to the increase in SST in the Arabian Sea during the spring intermonsoon.

Previous studies show that the effect of biological warming is amplified due to secondary feedbacks on MLD. In the Arabian Sea, high chlorophyll concentrations increase solar radiation absorption and so increase thermal stratification, which inhibits vertical mixing, shoals the MLD and further increases SST (Nakamoto et al., 2000; Wetzel et al., 2006; Turner et al., 2012). In our study, secondary feedbacks on the MLD are consistent in magnitude with the Arabian Sea studies. The maximum MLD difference is 3 m in the central BoB during June. Coastal MLDs shoaled around the southernmost tip of India and the northern BoB in June by ~ 1 m and MLDs shoaled around the Isthmus of Thailand in October by ~ 1 m (fig. 5.10e and 5.10f). The effect of high chlorophyll concentrations in these coastal regions has altered upper-ocean thermal stratification, while in the open ocean, changes to windspeed primarily alter upper-ocean thermal stratification.

In our study, a realistic chlorophyll distribution increased open ocean SST by $\sim 0.1^\circ\text{C}$ and increased coastal SST by $\sim 0.5^\circ\text{C}$ during the intermonsoons and onset of the southwest monsoon. The simulated increase in open ocean SST is consistent with previous work (Murtugudde et al., 2002; Wetzel et al., 2006). However, the increase in coastal SST, primarily in the eastern BoB coastal region, is larger in magnitude than previous work: Wetzel et al. (2006) underestimated seasonal chlorophyll concentrations in the BoB coastal regions, while Murtugudde et al. (2002) used a low-resolution annual mean chlorophyll concentration which removed the seasonal variability of chlorophyll concentration, whereas we impose an annual cycle of daily h_2 across the BoB. Hence, the coastal and open ocean SST responses are more accurately represented here than in previous work.

There are limitations to using an imposed annual cycle of h_2 . The derived values of h_2 only incorporate the bio-optical property of chlorophyll-a pigment concentration that is remotely sensed by satellite. There are other biological constituents that perturb solar penetration depths, and thus vertical heat distributions. Coloured Dissolved Organic Matter (CDOM) increases the radiant heating rate of nearshore coastal waters of North America (Chang and Dickey, 2004) and in the Arctic (Hill, 2008). Imposing an annual mean of remotely sensed CDOM absorption coefficients in a coupled ocean-atmosphere GCM reduced solar penetration depths and increased coastal SST in the Northern Hemisphere during the summer (Kim et al., 2018). CDOM concentrations are high in the western and northern coastal regions of the BoB at the mouths of major rivers (Pandi et al., 2014). Thus, including the bio-optical properties of

CDOM and other biological constituents would likely increase coastal SST in the BoB, with additional implications for regional climate.

A further limitation of the imposed annual cycle of h_2 is the use of a monthly mean climatological chlorophyll concentration at a reduced horizontal resolution, which smooths over the large subseasonal variability of chlorophyll concentration observed in the BoB. In reality, the advection of high surface chlorophyll concentrations into the south and central BoB varies with the strength and positioning of the SLD and SMC (Vinayachandran et al., 2004), which is itself further influenced by local wind stress and seasonal Rossby waves (Webber et al., 2018). Surface chlorophyll concentrations are periodically enhanced by transient cold-core eddies and postmonsoon cyclones in the central BoB, which briefly upwell nutrients to the ocean surface (Vinayachandran and Mathew, 2003; Patra et al., 2007). In coastal regions, nutrient concentrations, which affect surface chlorophyll concentrations, vary with river discharge (Kumar et al., 2010). Suspended terrestrial sediment that perturbs solar penetration depths on the continental shelf also depend on river discharge (Kumar et al., 2010; Lotliker et al., 2016). All these factors influence solar penetration depths on timescales of days to weeks and on spatial scales of less than 1 km. By smoothing over the large subseasonal variability of chlorophyll concentration, such variations in solar penetration depth are not represented in the present study.

The absence of subseasonal variations of the perturbed solar penetration depths has implications for the mixed layer radiative heating rate and SST on subseasonal timescales (10 to 30 days). Varying SST on subseasonal timescales might also affect the active and break periods of the Boreal Summer Intraseasonal Oscillation, which are strongly coupled to intraseasonal variability of SST (Fu et al., 2003; Gao et al., 2019). Break periods are typically associated with calmer conditions, which allows for more downward shortwave radiation that reduces the turbulent heat flux, shoals the mixed layer and increases SST (Roxy et al., 2015). Positive intraseasonal SST anomalies in the BoB during break periods are typically 0.6–1.0°C (Duncan and Han, 2009; Vinayachandran et al., 2018). High chlorophyll concentrations, triggered by cold-core eddies or an increase in river discharge, could enhance the radiant heating rate of the mixed layer and increase SST during a break period. The enhanced SST increase could potentially enhance convection and monsoon precipitation rates during the next active period. Imposing subseasonal variations of chlorophyll concentration into a coupled ocean-atmosphere GCM is accordingly a source for future work.

5.5 Conclusions

The effect of chlorophyll perturbations on BoB surface ocean properties and the South Asian monsoon is examined using a coupled ocean-atmosphere GCM. The effect of chlorophyll on SST is amplified during the intermonsoon periods when shallow MLDs are comparable to the perturbed solar penetration depths. The MLD, and its effect on the biological warming, varies seasonally and spatially in the BoB. Coastal regions experience larger SST increases than open ocean regions because of higher chlorophyll concentrations and shallower MLDs. The SST increase is larger during the autumn intermonsoon (September–October) than the spring intermonsoon (April–May) and southwest monsoon onset (June). During the spring intermonsoon, chlorophyll concentrations are low across open BoB, but remain high in coastal regions. During the southwest monsoon onset chlorophyll concentrations are high when the MLD is relatively shallow (< 30 m) in the northern and western coastal BoB, leading to increased SST. During the autumn intermonsoon, high chlorophyll concentrations extend over the continental shelf in the northern BoB, the SMC region and the eastern BoB, in contrast to the spring intermonsoon where high chlorophyll concentrations are confined to the coasts. The chlorophyll concentrations in the southwest and northwest BoB peak in August and October respectively (Lévy et al., 2007), whilst the MLD is shallowest across the basin, which results in an increase in mixed layer radiant heating rate and SST in the western BoB in autumn.

The direct changes in h_2 in coastal regions are large, and thus more influential on mixed layer radiant heating rate and SST. The resultant increase in the radiant heating rate of the coastal mixed layer and SST during the southwest monsoon onset and autumn intermonsoon increases the latent heat flux and transport of moisture to the Indian subcontinent. Precipitation rates over the Myanmar coast during the southwest monsoon onset increase by 3 mm day^{-1} , which decreases the model bias. Precipitation rates over western Bangladesh and northeastern India during the autumn intermonsoon increase by 3 mm day^{-1} , which also decreases the model bias. During October, the enhanced precipitation rate and convective activity in the northern BoB perturbs upper-tropospheric winds, potentially causing reduced precipitation rates over eastern China, similar to the Silk Road effect. The effect of chlorophyll on the midlatitude Rossby wave train and its potential impact on East Asian climate needs further investigation.

Biological heating has complex physical and dynamical feedbacks in the ocean, which in turn imply similar feedbacks on BoB biological processes. A coupled biogeochemistry model linked to an ocean-atmosphere GCM is needed to further understand secondary feedbacks on phytoplankton productivity. Secondary feedbacks may include changes to cloud cover that affect the incoming shortwave radiation needed for biological productivity; changes to thermal and salinity stratification that affect the vertical mixing of nutrients to the ocean surface; or changes to rainfall that affect river discharge and nutrient availability on the continental shelf that influence biological productivity. The resultant changes to biological productivity could either enhance or deplete chlorophyll concentrations at the surface, with further implications to the spatial and temporal extent of biological heating. It is important that realistic simulations of chlorophyll concentrations are included as an additional Earth system process in high-resolution coupled ocean-atmosphere GCMs, which may improve the simulated seasonality and intraseasonal variability of the South Asian monsoon.

Chapter 6

Conclusions

6.1 Summary

This thesis has investigated the effect of chlorophyll concentrations on the temporal and spatial distribution of solar penetration depths, mixed layer radiant heating rates, SSTs and regional climate.

Chapter 2 has outlined the quality control method for deriving solar penetration depths. For both gliders and floats, PAR profiles are affected by external environmental factors such as wave-focusing and cloud spikes. The noisy near-surface PAR signal is flagged from the surface down to 5 m and Equation 2.8 is used to replicate the absorption of red light above 5 m and fit to the more robust PAR profile below 5 m. Previous studies that have measured downward solar irradiance have used depth thresholds of 10 m (Ohlmann et al., 1998; Ohlmann, 2003) or an optical depth threshold of 0.69 (Xing et al., 2011), whilst some studies have not used a depth threshold (Morel and Maritorena, 2001; Lotliker et al., 2016). The 5 m depth threshold is suitable for this study as we can safely assume red light is absorbed to a depth of 5 m and that large perturbations that affect h_2 determinations are removed. The PAR perturbations below 5 m are identified and flagged using a modified fourth-degree polynomial method from Organelli et al. (2016), which improves h_2 determinations and their associated uncertainties, and removes excessively noisy PAR profiles from the analysis. However, there are occurrences where the polynomial method would flag non-perturbed PAR data points. This occurrence is limited to profiles that still show fluctuating PAR signals due to both external environmental conditions and the attenuation by biological constituents. A

novel approach is developed to derive chlorophyll-a concentration from float radiometer data. A new method is also developed to flag and smooth cloud spikes from calculated k_{bio} profiles. The derived chlorophyll-a concentration would likely overestimate the total chlorophyll-a concentration present in the water column, as the empirical relationship that is used assumes the attenuation due to biology is caused by chlorophyll-a pigment concentration alone, which is not necessarily the case. Although the vertical distribution of chlorophyll concentration could be inferred, the derived chlorophyll concentration was not suitable for quantitative comparisons with determined h_2 .

Chapter 3 revealed that the observed chlorophyll concentrations and corresponding solar penetration depths in the BoB vary on seasonal to sub-daily temporal scales and on synoptic to mesoscales. Determined values of h_2 from SG579 are generally low (~ 14 m) in localised regions of high chlorophyll concentration such as the SMC, SLD and coastal regions, similar to the h_2 values determined by Lotliker et al. (2016) during JJA. Meanders and eddies, and the chlorophyll concentrations entrained in their flow, continuously break away from the main branch of the fast-flowing SMC, causing sub-daily variations in h_2 and corresponding chlorophyll concentrations. As identified in Chapter 3 and by Vinayachandran et al. (2004), the chlorophyll concentrations entrained in the flow of the SMC depend on the strength and positioning of the SMC relative to the biologically active southernmost tip of India and Sri Lanka. Away from the SMC, SLD and coastal regions, chlorophyll concentrations decrease and corresponding h_2 values increase to more than 20 m, which are comparable to the h_2 values determined from Lotliker et al. (2016) of 19 ± 3 m. The sub-daily variability in scale depth highlights the importance of near-surface ocean processes in modulating high mixed layer chlorophyll concentrations in the SMC, SLD and coastal regions.

In Chapter 3, the effect of chlorophyll concentration in the SMC has been shown to increase mixed layer temperature and SST. Two values of h_2 that are equal to 14 m and 26 m, and represent the lowest and highest h_2 values in the SMC, are imposed in the one-dimensional KPP ocean mixed layer model. The one-month surface-forced idealised simulation shows that decreasing h_2 from 26 m to 14 m increases the SST by 0.37°C , a warming of $0.04^\circ\text{C day}^{-1}$. This study found that this warming is approximately equivalent to 60% of the intraseasonal SST variability that is observed during the first half of the BoBBLE campaign. This study also demonstrates that the increase in SST in the SMC is sensitive to changes in h_2 when the MLD is shallow at a depth

of 32 m. The increased sensitivity of SST to chlorophyll concentration when MLDs are shallow has been found by previous one-dimensional modelling studies (e.g. Ohlmann et al., 1998) and coupled GCM studies (e.g. Turner et al., 2012). However, identifying this process in the SMC region, where strong air-sea coupling strongly influences the southwest monsoon, means the effect of chlorophyll concentration on the southwest monsoon required further investigation.

In Chapter 5, imposing seasonally and spatially varying chlorophyll concentrations in a coupled ocean-atmosphere GCM highlights the spatial and temporal effects of chlorophyll on BoB SST. The effect of chlorophyll on SST is enhanced during the spring and summer intermonsoon periods due to shallow MLDs (<30 m) that are comparable to the perturbed h_2 . Coastal regions experience the largest increase in SST due to high chlorophyll concentrations and continuously shallow MLDs. The autumn intermonsoon has the largest increase in SST and spatial extent compared with the spring intermonsoon and southwest monsoon onset. During the autumn intermonsoon, MLDs are shallow across the BoB and chlorophyll concentrations are high ($>1 \text{ mg m}^{-3}$) off the continental shelf in the northern and southwestern BoB. The coastal and open ocean SST responses to perturbed values of h_2 are more accurately represented in Chapter 5 than in previous work by Murtugudde et al. (2002) and Wetzel et al. (2006).

The seasonally and spatially varying chlorophyll concentrations further highlight the effects of chlorophyll on precipitation rates during the onset and retreat of the southwest monsoon. The SST increase in the southwest BoB coastal region during June provides additional moisture for increasing precipitation rates of 3 mm day^{-1} over coastal Myanmar. The SST increase in the northeast BoB coastal region during October provides additional moisture for increasing precipitation rates of 3 mm day^{-1} over Bangladesh. The increase in precipitation rates decreases or removes the model dry biases when comparing the monthly 29-year average control run precipitation rate with the monthly 18-year average observed precipitation rate. Imposing a spatially and temporally varying field of chlorophyll-perturbed h_2 shows improvement in the intermonsoon rainfall amount and distribution.

The effect of chlorophyll concentration on monsoon rainfall shown in Chapter 5 is illustrated and summarised in Fig. 6.1. We consider the western BoB during the summer monsoon onset where mixed layers are shallow (<30 m) and where there is a zonal gradient in mixed layer turbidity, with the highly

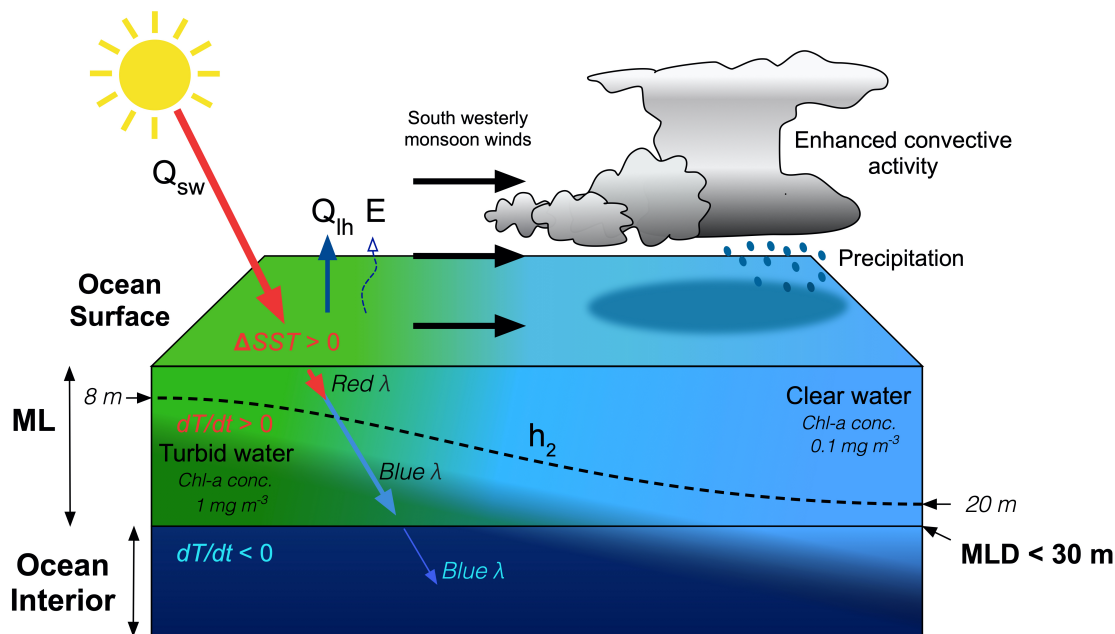


Figure 6.1: Schematic of the effect of chlorophyll concentration on the penetration of shortwave radiative heat flux (Q_{sw}), scale depth of blue light (h_2), mixed layer radiant heating rates (dT/dt), change in SST (ΔSST), surface latent heat fluxes (Q_{lh}), evaporation (E), and convective rainfall. The thick red and blue arrows pointing downwards in the mixed layer illustrates the preferential absorption of the shallow penetrating red light and the deep penetrating blue light. The thin blue arrow pointing downwards below the mixed layer shows the small fraction of penetrative blue light below the mixed layer. The dashed black line in the mixed layer represents h_2 .

turbid coastal region of Sri Lanka and India to the west and the clearer, open-ocean region of the central BoB to the east. Chlorophyll concentrations are high (1 mg m^{-3}) to the west and low (0.1 mg m^{-3}) to the east, meaning corresponding values of h_2 are low (8 m) to the west and high (20 m) to the east. The high chlorophyll concentration region would experience an increase in mixed layer radiant heating rates ($dT/dt > 0$), which causes a reduction in radiant heating rates ($dT/dt < 0$) below the mixed layer. Increasing the mixed layer radiant heating rate increases mixed layer temperature and SST ($\Delta SST > 0$). Strengthening monsoon winds over this region of increased SST increases the upward latent heat flux and evaporation. Convergence of the additional lower-tropospheric moisture that is transported by the monsoon winds increases the convective activity and precipitation rate eastwards towards the Myanmar coast.

The relationship between determined scale depths and observed average chlorophyll concentrations in Chapters 3 and 4 shows that there is a power-law

dependence in h_2 as a function of chlorophyll in both the BoB (Fig. 3.9) and SAZ (Fig. 4.7). Such a relationship has been previously found in observational (e.g. Morel, 1988) and modelling studies (e.g. Ohlmann, 2003). As shown in Chapter 4, the relationship strongly depends on the depth range over which the average chlorophyll concentration is calculated (Fig. 4.7). The appropriate depth range to calculate the average chlorophyll concentration must extend from the surface to a depth of no more than 80 m, as this is the depth by which the majority solar radiation is absorbed and where chlorophyll concentration strongly influences the determined values of h_2 . In Chapter 3, the previous parameterisations of MA94 and O03 generally underestimate h_2 in the BoB, whereas in Chapter 4, these parameterisations generally overestimate h_2 in the SAZ. Differences between in situ and parameterised h_2 occur due to the parameterisations misrepresenting the attenuation of blue light for inhomogeneous profiles of chlorophyll-a concentration and excluding other biological constituents that strongly attenuate blue light. Differences also occur due to the underestimation of actual in situ chlorophyll concentration that affects the relationship between average chlorophyll concentration and determined h_2 . In Chapter 4, a proposed new parameterisation, G20, determines larger values of h_2 than MA94 and O03 when average 0 to 80 m chlorophyll concentrations are more than 0.4 mg m^{-3} . However, considering the uncertainties associated with the determined values of h_2 and observed chlorophyll concentrations we do not have enough confidence in the robustness of the derived parameters of G20 to argue that it should replace the previously published parameterisations.

Unlike the BoB, Chapter 4 shows that the SAZ in the Southern Ocean is dominated by strong wind forcing and seasonally varying solar irradiance, which induces strong horizontal advection and vertical mixing that cause larger seasonal to subseasonal variations in h_2 and chlorophyll concentration. During spring, strong wind-induced turbulent mixing in weakly stratified mixed layers cause rapid daily variations in the MLD and the chlorophyll concentration. The effect of chlorophyll on the radiant heating rate is found to be negligible, as MLDs far exceed the depth of determined h_2 . During summer, the mixed layer becomes increasingly stratified, as wind-induced turbulent mixing is reduced and solar irradiance increases. This re-stratifying effect increases the chlorophyll concentration and decreases h_2 . Although the radiant heating rate increases from spring to summer, the additional effect of increased summer chlorophyll on the radiant heating rate is very small, as summer MLDs extend far below the depth of determined h_2 . The near-zero penetration of solar irradiance below the

mixed layer and the negligible effect of chlorophyll on upper ocean temperature is similar to the findings from Groeskamp and Iudicone (2018). Conversely, there are localised patches of low h_2 (<10 m) and shallow MLDs (<30 m) that have high radiant heating rates of 0.3 to $0.5^\circ\text{C month}^{-1}$. However, their effect is shortlived (1 to 2 days in the SG574 timeseries) and spatially limited, as these patches are typically a mesoscale feature (Little et al., 2018). Hence, the effect of chlorophyll on mixed layer and SST warming in the SAZ remains mostly negligible on seasonal to subseasonal timescales.

6.2 Discussion and future work

This thesis has demonstrated that gliders are a useful observational platform to collect PAR measurements and determine solar penetration depths. Gliders provide high vertical resolution (~ 1 m) observations of the upper ocean, especially at the near-surface where solar radiation is strongly absorbed. Gliders are able to provide continuous observations in a fixed location or across a section of ocean during any time of day, whilst remaining in the water for several months, as shown from the BoBBLE and SOSCEX deployments. Gliders can be programmed to complete shallower dives to measure finer sub-daily variations of solar penetration depths and PAR sensors can be programmed to restrict sampling to the top 100 m in order to optimise battery usage. Furthermore, shadows have not been found to be an issue for glider PAR measurements in this thesis.

There are drawbacks to using gliders to collect PAR measurements. Gliders are susceptible to biofouling, as they spend a majority of their time in the upper ocean where it is hospitable for biological growth. As found in Chapter 4, biofouling covers the on-board sensors, causing erroneous measurements that have to be discarded. Another disadvantage is that in highly stratified regions such as the BoB, ascending and descending PAR profiles have different vertical resolutions due to differences in ascending and descending vertical velocities. Glider SG579 displayed faster descents than ascents, leading to lower resolution descending profiles than ascending profiles. Ascending PAR profiles tend to be noisier than descending PAR profiles, and are therefore more likely to be discarded, as they are not as suitable for reliable h_2 determinations.

Unlike gliders, floats are not as susceptible to biofouling, as they spend the majority of their time at 1000 m depth where it is unfavourable for

biological growth (Organelli et al., 2016). Both gliders and floats should be considered in any future work regarding the spatial and temporal distribution of solar penetration depths. Gliders are suitable for short-term deployments (approximately three months) in fixed locations sampling on sub-daily timescales, and floats are suitable for long-term deployments (approximately one year) sampling on daily timescales over synoptic spatial scales.

One of the major drawbacks of the BoBBLE glider deployment is the absence of surface PAR measurements. The absence of surface PAR measurements means the fit of the double exponential function to in-water PAR profiles is not constrained to the surface, meaning optical parameters of both red and blue light are not accurately determined. Moreover, the non-dimensional parameter R can not be determined, as the in-water PAR can not be normalised without the surface PAR measurements. Surface PAR measured by satellite has been used by Strutton and Chavez (2004) to determine solar irradiance just above the ocean surface. However, surface PAR measured by satellite is not used in this thesis due to its coarse temporal and spatial resolution and due to the monsoonal cloud cover obscuring the surface PAR signal. Instead, optical parameters R and h_1 from Paulson and Simpson (1977) allowed us to replicate red light absorption in the top 5 m of PAR profiles in the absence of surface PAR measurements. These optical parameters are found to have a small influence (<0.8 m) on the determined values of h_2 below 5 m when using Equation 2.8.

In the future, surface PAR measurements should be collected using an autonomous surface oceanographic platform such as a Wave Glider (Daniel et al., 2011). Surface and in-water PAR can be measured simultaneously by piloting a Wave Glider close to an ocean glider or float. The surface PAR measurements can then be used to constrain the fit of a double exponential function to in-water PAR profiles, improving the accuracy of determined optical parameters. As found with the glider and floats, the influence of solar radiation angle and clouds would affect surface PAR measurements. Surface ocean albedo is an additional factor that must also be considered when determining PAR just below the surface, as previously found from ship-based optical measurements (e.g. Ohlmann et al., 1998). A new quality control method would be required to clean and correct for such perturbations and additional factors.

The Paulson and Simpson (1977) optical parameters have been found to misrepresent red light absorption for a broad range of chlorophyll concentrations (Ohlmann et al., 1998; Ohlmann, 2003). Paulson and Simpson (1977) found, using low-resolution in-water irradiance profiles, that h_1 and

R increases with increasing water type (increasing turbidity). Conversely, Ohlmann (2003) and Morel and Antoine (1994) found, using radiative transfer models, that h_1 and R should decrease with increasing water type, as less red wavelengths of solar irradiance penetrate to a deeper depth with increasing turbidity. Furthermore, Lotliker et al. (2016) found using high-resolution in-water PAR measurements that the BoB R value is 0.41 ± 0.03 during JJA, which is smaller than the R value used in this study (0.67 for water type IB). The use of models and high-resolution in-water PAR measurements improves the determinations of h_1 and R at the near-surface, and highlights the potential inaccuracy of the optical parameters determined by Paulson and Simpson (1977).

The choice of h_1 and R from the Jerlov water types thus introduces some uncertainty into the KPP and MC-KPP simulations in Chapters 3 and 5, respectively. A sensitivity test using the same idealised KPP simulation from Chapter 3 showed the effect of h_1 and R from Paulson and Simpson (1977) on BoB SST. Varying h_1 between water type I and III had a negligible affect on SST due to the small penetration depth of red light. However, varying R between water type I and III changed SST by 0.1°C . The effect of R on SST is non-negligible and introduces SST uncertainties that are of the same order of magnitude as the one found in this sensitivity test. Future work should involve the quantification and comparison of SST uncertainties associated with varying values of R from Morel and Antoine (1994) and Paulson and Simpson (1977) in KPP. This would highlight which parameterisation of R reduces SST uncertainty.

In Chapter 3, the idealised one-dimensional KPP simulations could be improved by imposing time-varying h_2 values to simulate corresponding time-varying chlorophyll concentrations. The time-varying h_2 should be represented by the determined h_2 from glider SG579 in the SMC region. Comparing two simulations with a time varying h_2 and time-mean h_2 would demonstrate how daily to sub-daily variations of chlorophyll concentration effect the SST evolution during a break phase of the BSISO. Furthermore, the absence of horizontal advection, Ekman pumping and atmospheric feedbacks in KPP means the full dynamics of the mixed layer are not simulated. However, for the purposes of this thesis it is important not to obscure the direct effects of chlorophyll on mixed layer properties, making the KPP model suitable for this experiment.

In Chapter 5, the use of MetUM-GOML3.0 to analyse the effect of BoB chlorophyll on surface ocean properties and atmospheric processes has

advantages and disadvantages. The advantages are that the model does not include modes of variability (e.g. ENSO and IOD) that obscure the effects of chlorophyll on interannual timescales. This is due to the model using fixed temperature and salinity corrections that represent a mean seasonal cycle of ocean dynamics, allowing the model to be used for climate-length simulations with shorter spin-up periods (Hirons et al., 2015). However, the disadvantage of representing ocean dynamics as a mean seasonal cycle means that if chlorophyll concentrations change ocean properties, which subsequently change ocean dynamics, then the model would not capture this dynamical response. Previous studies have shown the influence of enhanced biological warming on ocean dynamics in the equatorial Pacific (e.g. Nakamoto et al., 2001; Murtugudde et al., 2002) and in mid- to high-latitude regions (e.g. Manizza et al., 2005; Patara et al., 2012). It could be possible that the dynamics of SMC and SLD in the BoB could be affected by enhanced biological warming at the surface or perhaps enhanced solar radiation penetration below the mixed layer. Furthermore, missing ENSO and IOD dynamics might have non-linear effects on the chlorophyll-perturbed ocean properties, which potentially impacts on monsoon rainfall. Using a fully coupled dynamical GCM, instead of MetUM-GOML3.0, would show chlorophyll-perturbed dynamical changes and feedbacks on the oceanic and atmospheric system.

In summary, this thesis has demonstrated that solar penetration depths are able to be determined from PAR measurements from gliders and floats without the need for surface PAR measurements, coarse-resolution satellite measurements or costly, labour-intensive ship-based measurements. The determined solar penetration depths have been shown to be easily incorporated into solar radiation schemes in ocean models at no additional computational expense. Finally, including chlorophyll-perturbed solar penetration depths in a coupled GCM has been shown to improve the intermonsoon rainfall amount and spatial distribution over the Indian Subcontinent. This thesis highlights an exciting new chapter in autonomous ocean data collection to improve the parameterisation of chlorophyll in ocean GCMs and to improve simulations of the South Asian monsoon.

Appendix A

Glider pitch and roll angle perturbations

To investigate whether the roll and pitch angle magnitude or variability were the cause of PAR perturbations in our glider dataset, roll and pitch angle measurements and their variability were assessed against corresponding PAR perturbation measurements. The profiles of the natural log of PAR were fitted with a fourth degree polynomial from the surface to a depth of 70 m. The PAR perturbations were defined as the residuals of $\ln(\text{PAR})$ that were above and below the one standard deviation of all PAR residuals for each profile after fitting a fourth degree polynomial. The variability of the pitch and roll angle was defined as the change in pitch and roll angle between measurements.

Ascending dives showed positive pitch angle measurements as the nose of the glider pitches up (Fig. A.1a), whereas descending dives showed negative pitch angle measurements as the nose of the glider pitches down (Fig. A.1e). The largest PAR perturbations occur in the top 5 m when the glider moved into a horizontal position or near-zero pitch angle. The change in pitch angle was often up to 30° between measurements as the glider performed a surface manoeuvre at around 3 m depth or started its descent from the surface (Fig. A.1b and A.1f). This large change in pitch angle did correspond with a limited number of large PAR perturbations, particularly for ascending dives (Fig. A.1b). However, with no clear relationship between pitch angle variation and PAR perturbation and considering the additional effect of external environmental factors that strongly perturb near-surface PAR measurements, there was little evidence to show that pitch angle had an effect on PAR perturbation.

For the glider roll angle, PAR perturbations of all magnitudes were grouped

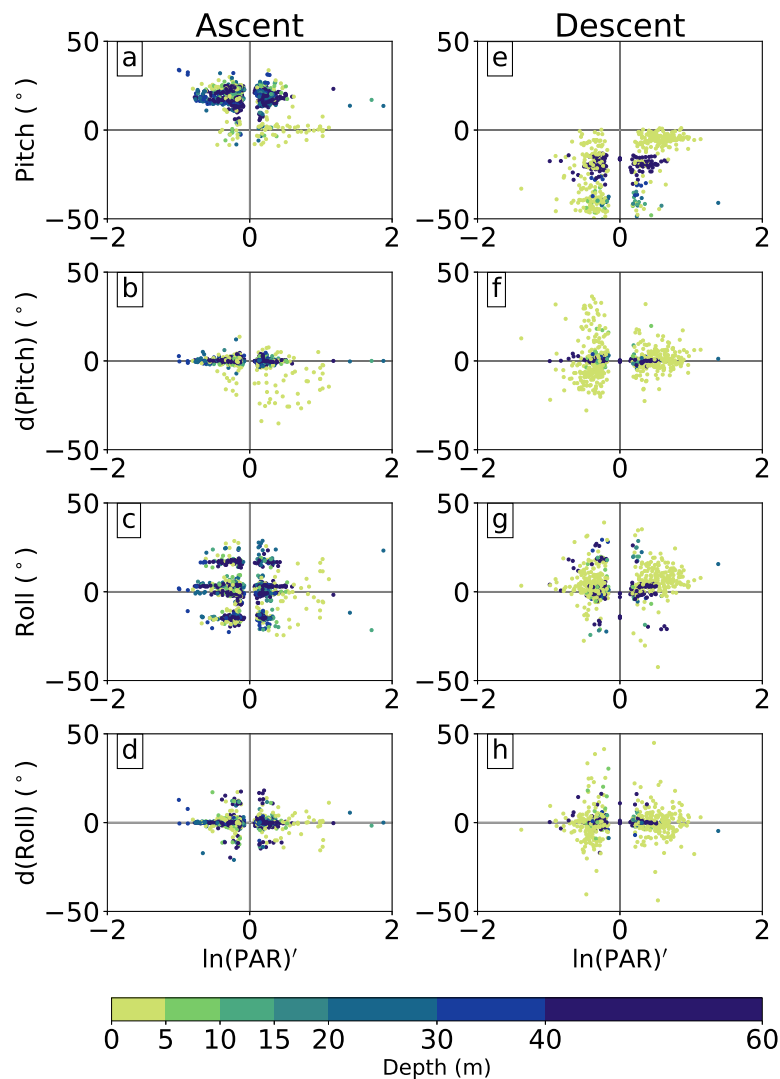


Figure A.1: Pitch and roll angle against PAR perturbation measurements from the surface to 70 m depth from Glider SG579: (a) Ascending pitch angle and PAR perturbation measurements; (b) Ascending pitch angle variation and PAR perturbation measurements; (c) Ascending roll angle and PAR perturbation measurements; (d) Ascending roll angle variation and PAR perturbation measurements; (e–h) As in (a–d) but for descending dives.

at three roll angles of 20, 0 and -20° (Fig. A.1c and A.1g). The change in roll angle was observed to be up to 20° between measurements, yet the majority of the PAR perturbations that were both negative and positive occurred when the change in roll angle was near-zero (Fig. A.1d and A.1h). Hence, there was no relationship between PAR perturbation and roll angle or roll angle variation.

In summary, the tilted and sudden variations in the position of the PAR sensor on the glider was unlikely to cause PAR perturbations and affect determined optical parameters. Instead, it was more likely that the PAR

perturbations were caused by random external environmental factors that mainly affected near-surface PAR measurements. Recognising that these perturbations were in fact random and caused by unquantified external factors meant that perturbations could not be predicted and easily identified.

Appendix B

Summary of solar irradiance parameterisations

B.1 Morel and Antoine (1994) solar irradiance parameterisation

Morel and Antoine (1994) uses a double exponential function to describe the penetration of solar irradiance in the visible range (300–750 nm):

$$E(z) = E_{0-} \left[V_1 e^{-\frac{z}{h_1}} + V_2 e^{-\frac{z}{h_2}} \right] \quad (\text{B.1})$$

where E is the solar irradiance at depth z ; E_{0-} is the solar irradiance incident just below the surface; V_1 and V_2 partitions the visible irradiance into the long wavelengths (red light) and short wavelengths (blue light), respectively, and where $V_1 + V_2 = 1$; h_1 and h_2 are the scale depths of long and short wavelengths of solar irradiance. The parameter, h_2 , is determined using the log of remotely sensed chlorophyll-a concentrations ($C = \log_{10}(\text{Chl-a})$):

$$h_2 = 7.925 - 6.644C + 3.662C^2 - 1.815C^3 - 0.218C^4 + 0.502C^5 \quad (\text{B.2})$$

B.2 Ohlmann (2003) solar irradiance parameterisation

Ohlmann (2003) uses a double exponential function to describe the penetration of solar irradiance in the infrared range (750–2500 nm) and UV and visible range

(300–750 nm):

$$E(z) = E_{0-} \left[a_1 e^{-b_1 z} + a_2 e^{-b_2 z} \right] [1 + H(\theta)G(\text{ci})] \quad (\text{B.3})$$

where E is the solar irradiance at depth z ; E_{0-} is the solar irradiance incident just below the surface; a_1 and a_2 partitions the UV-visible irradiance into the long wavelengths (red light) and short wavelengths (UV and blue light), respectively; b_1 and b_2 are the attenuation coefficients, respectively; $H(\theta)$ is the incident angle of solar radiation on the ocean surface; $G(\text{ci})$ is the cloud index. The parameter, b_2 , is determined using remotely sensed chlorophyll-a concentrations (Chl; mg m^{-3}):

$$b_2 = 0.015 + 0.176 \left(\sqrt{0.462[\text{Chl}]} \right) \quad (\text{B.4})$$

References

- Amol, P., Vinayachandran, P., Shankar, D., Thushara, V., Vijith, V., Chatterjee, A., Kankonkar, A., 2019. Effect of freshwater advection and winds on the vertical structure of chlorophyll in the northern Bay of Bengal. *Deep Sea Res. Part II Top. Stud. Oceanogr.*, 104622 URL: <https://linkinghub.elsevier.com/retrieve/pii/S0967064518301218>, doi:10.1016/j.dsr2.2019.07.010.
- de Baar, H.J.W., de Jong, J.T.M., Bakker, D.C.E., Löscher, B.M., Veth, C., Bathmann, U., Smetacek, V., 1995. Importance of iron for plankton blooms and carbon dioxide drawdown in the Southern Ocean. *Nature* 373, 412–415. URL: <http://www.nature.com/articles/373412a0>, doi:10.1038/373412a0.
- Barsugli, J.J., Sardeshmukh, P.D., 2002. Global atmospheric sensitivity to tropical SST anomalies throughout the Indo-Pacific basin. *J. Clim.* 15, 3427–3442. URL: [http://journals.ametsoc.org/doi/abs/10.1175/1520-0442\(2002\)015<3427:GASTTS>2.0.CO;2](http://journals.ametsoc.org/doi/abs/10.1175/1520-0442(2002)015<3427:GASTTS>2.0.CO;2), doi:10.1175/1520-0442(2002)015<3427:GASTTS>2.0.CO;2.
- Behrenfeld, M.J., Boss, E.S., 2014. Resurrecting the ecological underpinnings of ocean plankton blooms. *Ann. Rev. Mar. Sci.* 6, 167–194. URL: <http://www.annualreviews.org/doi/10.1146/annurev-marine-052913-021325>, doi:10.1146/annurev-marine-052913-021325.
- Bernie, D.J., Guilyardi, E., Madec, G., Slingo, J.M., Woolnough, S.J., Cole, J., 2008. Impact of resolving the diurnal cycle in an ocean-atmosphere GCM. Part 2: A diurnally coupled CGCM. *Clim. Dyn.* 31, 909–925. URL: <http://link.springer.com/10.1007/s00382-008-0429-z>, doi:10.1007/s00382-008-0429-z.
- Bernie, D.J., Woolnough, S.J., Slingo, J.M., Guilyardi, E., 2005. Modeling diurnal and intraseasonal variability of the ocean mixed layer. *J. Clim.* 18, 1190–1202. URL: <http://journals.ametsoc.org/doi/10.1175/JCLI3319.1>, doi:10.1175/JCLI3319.1.
- Borrione, I., Schlitzer, R., 2013. Distribution and recurrence of phytoplankton blooms around South Georgia, Southern Ocean. *Biogeosciences* 10, 217–231. URL: <https://www.biogeosciences.net/10/217/2013/>, doi:10.5194/bg-10-217-2013.
- Boss, E., Pegau, W.S., 2001. Relationship of light scattering at an angle in the backward direction to the backscattering coefficient. *Appl. Opt.* 40,

- 5503–5507. URL: <https://www.osapublishing.org/abstract.cfm?URI=ao-40-30-5503>, doi:10.1364/AO.40.005503.
- Boss, E., Slade, W., Hill, P., 2009. Effect of particulate aggregation in aquatic environments on the beam attenuation and its utility as a proxy for particulate mass. *Opt. Express* 17, 9408–9420. URL: <https://www.osapublishing.org/oe/abstract.cfm?uri=oe-17-11-9408>, doi:10.1364/OE.17.009408.
- Boyd, P.W., Watson, A.J., Law, C.S., Abraham, E.R., Trull, T., Murdoch, R., Bakker, D.C.E., Bowie, A.R., Buesseler, K.O., Chang, H., Charette, M., Croot, P., Downing, K., Frew, R., Gall, M., Hadfield, M., Hall, J., Harvey, M., Jameson, G., LaRoche, J., Liddicoat, M., Ling, R., Maldonado, M.T., McKay, R.M., Nodder, S., Pickmere, S., Pridmore, R., Rintoul, S., Safi, K., Sutton, P., Strzepke, R., Tanneberger, K., Turner, S., Waite, A., Zeldis, J., 2000. A mesoscale phytoplankton bloom in the polar Southern Ocean stimulated by iron fertilization. *Nature* 407, 695–702. URL: <http://www.nature.com/articles/35037500>, doi:10.1038/35037500.
- Bricaud, A., 2004. Natural variability of phytoplanktonic absorption in oceanic waters: Influence of the size structure of algal populations. *J. Geophys. Res.* 109, C11010. URL: <http://doi.wiley.com/10.1029/2004JC002419>, doi:10.1029/2004JC002419.
- Briggs, N., Perry, M.J., Cetinić, I., Lee, C., D'Asaro, E., Gray, A.M., Rehm, E., 2011. High-resolution observations of aggregate flux during a sub-polar North Atlantic spring bloom. *Deep Sea Res. Part I Oceanogr. Res. Pap.* 58, 1031–1039. URL: <https://linkinghub.elsevier.com/retrieve/pii/S0967063711001361>, doi:10.1016/j.dsr.2011.07.007.
- Chami, M., Marken, E., Stamnes, J.J., Khomenko, G., Korotaev, G., 2006. Variability of the relationship between the particulate backscattering coefficient and the volume scattering function measured at fixed angles. *J. Geophys. Res.* 111, C05013. URL: <http://doi.wiley.com/10.1029/2005JC003230>, doi:10.1029/2005JC003230.
- Chang, G.C., Dickey, T.D., 2004. Coastal ocean optical influences on solar transmission and radiant heating rate. *J. Geophys. Res.* 109, C01020. URL: <http://doi.wiley.com/10.1029/2003JC001821>, doi:10.1029/2003JC001821.
- Daniel, T., Manley, J., Trenaman, N., 2011. The Wave Glider: enabling a new approach to persistent ocean observation and research. *Ocean Dyn.* 61, 1509–1520. URL: <http://link.springer.com/10.1007/s10236-011-0408-5>, doi:10.1007/s10236-011-0408-5.
- Das, U., Vinayachandran, P.N., Behara, A., 2016. Formation of the southern Bay of Bengal cold pool. *Clim. Dyn.* 47, 2009–2023. URL: <http://link.springer.com/10.1007/s00382-015-2947-9>, doi:10.1007/s00382-015-2947-9.
- de Boyer Montégut, C., Madec, G., Fischer, A.S., Lazar, A., Iudicone, D., 2004. Mixed layer depth over the global ocean: An examination of profile

- data and a profile-based climatology. *J. Geophys. Res.* 109, C12003. URL: <http://doi.wiley.com/10.1029/2004JC002378>, doi:10.1029/2004JC002378.
- Denman, K.L., 1973. A time-dependent model of the upper ocean. *J. Phys. Oceanogr.* 3, 173–184. URL: [http://journals.ametsoc.org/doi/abs/10.1175/1520-0485\(1973\)003<0173:ATDMOT>2.0.CO;2](http://journals.ametsoc.org/doi/abs/10.1175/1520-0485(1973)003<0173:ATDMOT>2.0.CO;2), doi:10.1175/1520-0485(1973)003<0173:ATDMOT>2.0.CO;2.
- Ding, Q., Wang, B., 2005. Circumglobal teleconnection in the Northern Hemisphere summer. *J. Clim.* 18, 3483–3505. URL: <http://journals.ametsoc.org/doi/10.1175/JCLI3473.1>, doi:10.1175/JCLI3473.1.
- Duncan, B., Han, W., 2009. Indian Ocean intraseasonal sea surface temperature variability during boreal summer: Madden-Julian Oscillation versus submonthly forcing and processes. *J. Geophys. Res.* 114, C05002. URL: <http://doi.wiley.com/10.1029/2008JC004958>, doi:10.1029/2008JC004958.
- Fairall, C.W., Bradley, E.F., Godfrey, J.S., Wick, G.A., Edson, J.B., Young, G.S., 1996. Cool-skin and warm-layer effects on sea surface temperature. *J. Geophys. Res. Ocean.* 101, 1295–1308. URL: <http://doi.wiley.com/10.1029/95JC03190>, doi:10.1029/95JC03190.
- Fennel, K., Boss, E., 2003. Subsurface maxima of phytoplankton and chlorophyll: Steady-state solutions from a simple model. *Limnol. Oceanogr.* 48, 1521–1534. URL: <http://doi.wiley.com/10.4319/lo.2003.48.4.1521>, doi:10.4319/lo.2003.48.4.1521.
- Franz, B.A., Kwiatkowska, E.J., Meister, G., McClain, C.R., 2008. Moderate Resolution Imaging Spectroradiometer on Terra: limitations for ocean color applications. *J. Appl. Remote Sens.* 2, 023525. URL: <http://remotesensing.spiedigitallibrary.org/article.aspx?doi=10.1117/1.2957964>, doi:10.1117/1.2957964.
- Fu, X., Wang, B., Li, T., McCreary, J.P., 2003. Coupling between northward-propagating, intraseasonal oscillations and sea surface temperature in the Indian Ocean. *J. Atmos. Sci.* 60, 1733–1753. URL: [http://journals.ametsoc.org/doi/abs/10.1175/1520-0469\(2003\)060<1733:CBNIOA>2.0.CO;2](http://journals.ametsoc.org/doi/abs/10.1175/1520-0469(2003)060<1733:CBNIOA>2.0.CO;2), doi:10.1175/1520-0469(2003)060<1733:CBNIOA>2.0.CO;2.
- Gadgil, S., Srinivasan, J., 1990. Low frequency variation of tropical convergence zones. *Meteorol. Atmos. Phys.* 44, 119–132. URL: <http://link.springer.com/10.1007/BF01026814>, doi:10.1007/BF01026814.
- Gao, Y., Klingaman, N.P., DeMott, C.A., Hsu, P., 2019. Diagnosing ocean feedbacks to the BSISO: SST-modulated surface fluxes and the moist static energy budget. *J. Geophys. Res. Atmos.* 124, 146–170. URL: <https://onlinelibrary.wiley.com/doi/abs/10.1029/2018JD029303>, doi:10.1029/2018JD029303.

- Girishkumar, M.S., Ravichandran, M., McPhaden, M.J., Rao, R.R., 2011. Intraseasonal variability in barrier layer thickness in the south central Bay of Bengal. *J. Geophys. Res.* 116, C03009. URL: <http://doi.wiley.com/10.1029/2010JC006657>, doi:10.1029/2010JC006657.
- Gnanadesikan, A., Anderson, W.G., 2009. Ocean water clarity and the ocean general circulation in a coupled climate model. *J. Phys. Oceanogr.* 39, 314–332. URL: <http://journals.ametsoc.org/doi/abs/10.1175/2008JPO3935.1>, doi:10.1175/2008JP03935.1.
- Gomes, H.R., Goes, J.I., Saino, T., 2000. Influence of physical processes and freshwater discharge on the seasonality of phytoplankton regime in the Bay of Bengal. *Cont. Shelf Res.* 20, 313–330. URL: <https://linkinghub.elsevier.com/retrieve/pii/S0278434399000722>, doi:10.1016/S0278-4343(99)00072-2.
- Gordon, H.R., McCluney, W.R., 1975. Estimation of the depth of sunlight penetration in the sea for remote sensing. *Appl. Opt.* 14, 413–416. URL: <https://www.osapublishing.org/abstract.cfm?URI=ao-14-2-413>, doi:10.1364/AO.14.000413.
- Graham, N.E., Barnett, T.P., 1987. Sea surface temperature, surface wind divergence, and convection over tropical oceans. *Science* (80-). 238, 657–659. URL: <https://www.sciencemag.org/lookup/doi/10.1126/science.238.4827.657>, doi:10.1126/science.238.4827.657.
- Gregor, L., Ryan-Keogh, T.J., Nicholson, S.A., du Plessis, M., Giddy, I., Swart, S., 2019. GliderTools: A python toolbox for processing underwater glider data. *Front. Mar. Sci.* 6, 1–13. URL: <https://www.frontiersin.org/article/10.3389/fmars.2019.00738/full>, doi:10.3389/fmars.2019.00738.
- Groeskamp, S., Iudicone, D., 2018. The effect of air-sea flux products, shortwave radiation depth penetration, and albedo on the upper ocean overturning circulation. *Geophys. Res. Lett.* 45, 9087–9097. URL: <http://doi.wiley.com/10.1029/2018GL078442>, doi:10.1029/2018GL078442.
- Han, W., McCreary, J.P., 2001. Modeling salinity distributions in the Indian Ocean. *J. Geophys. Res. Ocean.* 106, 859–877. URL: <http://doi.wiley.com/10.1029/2000JC000316>, doi:10.1029/2000JC000316.
- Hemsley, V.S., Smyth, T.J., Martin, A.P., Frajka-Williams, E., Thompson, A.F., Damerell, G., Painter, S.C., 2015. Estimating oceanic primary production using vertical irradiance and chlorophyll profiles from ocean gliders in the North Atlantic. *Environ. Sci. Technol.* 49, 11612–11621. URL: <http://pubs.acs.org/doi/10.1021/acs.est.5b00608>, doi:10.1021/acs.est.5b00608.
- Hersbach, H., Dee, D., 2016. ERA5 reanalysis is in production. *ECMWF Newsl.* 147, 7.
- Hill, V.J., 2008. Impacts of chromophoric dissolved organic material on surface ocean heating in the Chukchi Sea. *J. Geophys. Res.* 113, C07024. URL: <http://doi.wiley.com/10.1029/2007JC004119>, doi:10.1029/2007JC004119.

- Hirons, L.C., Klingaman, N.P., Woolnough, S.J., 2015. MetUM-GOML1: a near-globally coupled atmosphere-ocean-mixed-layer model. *Geosci. Model Dev.* 8, 363–379. URL: <https://www.geosci-model-dev.net/8/363/2015/>, doi:10.5194/gmd-8-363-2015.
- Hoppe, C., Klaas, C., Ossebaar, S., Soppa, M., Cheah, W., Laglera, L., Santos-Echeandia, J., Rost, B., Wolf-Gladrow, D., Bracher, A., Hoppema, M., Strass, V., Trimborn, S., 2017. Controls of primary production in two phytoplankton blooms in the Antarctic Circumpolar Current. *Deep Sea Res. Part II Top. Stud. Oceanogr.* 138, 63–73. URL: <https://linkinghub.elsevier.com/retrieve/pii/S0967064515003367>, doi:10.1016/j.dsr2.2015.10.005.
- Hoskins, B.J., Hodges, K.I., 2005. A new perspective on Southern Hemisphere storm tracks. *J. Clim.* 18, 4108–4129. URL: <http://journals.ametsoc.org/doi/10.1175/JCLI3570.1>, doi:10.1175/JCLI3570.1.
- Hu, C., Feng, L., Lee, Z., Franz, B.A., Bailey, S.W., Werdell, P.J., Proctor, C.W., 2019. Improving satellite global chlorophyll a data products through algorithm refinement and data recovery. *J. Geophys. Res. Ocean.* 124, 1524–1543. URL: <https://onlinelibrary.wiley.com/doi/abs/10.1029/2019JC014941>, doi:10.1029/2019JC014941.
- Hu, C., Lee, Z., Franz, B., 2012. Chlorophyll a algorithms for oligotrophic oceans: A novel approach based on three-band reflectance difference. *J. Geophys. Res. Ocean.* 117, 1011. URL: <http://doi.wiley.com/10.1029/2011JC007395>, doi:10.1029/2011JC007395.
- Huffman, G.J., Bolvin, D.T., Nelkin, E.J., Wolff, D.B., Adler, R.F., Gu, G., Hong, Y., Bowman, K.P., Stocker, E.F., 2007. The TRMM Multisatellite Precipitation Analysis (TMPA): Quasi-global, multiyear, combined-sensor precipitation estimates at fine scales. *J. Hydrometeorol.* 8, 38–55. URL: <http://journals.ametsoc.org/doi/10.1175/JHM560.1>, doi:10.1175/JHM560.1.
- Huisman, J., Pham Thi, N.N., Karl, D.M., Sommeijer, B., 2006. Reduced mixing generates oscillations and chaos in the oceanic deep chlorophyll maximum. *Nature* 439, 322–325. URL: <http://www.nature.com/articles/nature04245>, doi:10.1038/nature04245.
- IOC, SCOR, IAPSO, 2010. The international thermodynamic equation of seawater – 2010: Calculation and use of thermodynamic properties. UNESCO Intergover, 1–196. URL: <http://www.teos-10.org/pubs/TEOS-10{ }Manual.pdf>.
- Jana, S., Gangopadhyay, A., Chakraborty, A., 2015. Impact of seasonal river input on the Bay of Bengal simulation. *Cont. Shelf Res.* 104, 45–62. URL: <http://dx.doi.org/10.1016/j.csr.2015.05.001>, doi:10.1016/j.csr.2015.05.001.
- Jensen, T.G., 2003. Cross-equatorial pathways of salt and tracers from the northern Indian Ocean: Modelling results. *Deep Sea Res. Part II Top. Stud.*

- Oceanogr. 50, 2111–2127. URL: <https://linkinghub.elsevier.com/retrieve/pii/S0967064503000481>, doi:10.1016/S0967-0645(03)00048-1.
- Jerlov, N.G., 1968. *Optical oceanography*. Elsevier Oceanography Series 5, Elsevier Publishing Company, Amsterdam.
- Jochum, M., Yeager, S., Lindsay, K., Moore, K., Murtugudde, R., 2010. Quantification of the feedback between phytoplankton and ENSO in the Community Climate System Model. *J. Clim.* 23, 2916–2925. URL: <http://journals.ametsoc.org/doi/10.1175/2010JCLI3254.1>, doi:10.1175/2010JCLI3254.1.
- Ju, J., Slingo, J., 1995. The Asian summer monsoon and ENSO. *Q. J. R. Meteorol. Soc.* 121, 1133–1168. URL: <http://doi.wiley.com/10.1002/qj.49712152509>, doi:10.1002/qj.49712152509.
- Kara, A.B., Rochford, P.A., Hurlburt, H.E., 2000. An optimal definition for ocean mixed layer depth. *J. Geophys. Res. Ocean.* 105, 16803–16821. URL: <http://doi.wiley.com/10.1029/2000JC900072>, doi:10.1029/2000JC900072.
- Kim, G.E., Gnanadesikan, A., Del Castillo, C.E., Pradal, M.A., 2018. Upper ocean cooling in a coupled climate model due to light attenuation by yellowing materials. *Geophys. Res. Lett.* 45, 6134–6140. URL: <http://doi.wiley.com/10.1029/2018GL077297>, doi:10.1029/2018GL077297.
- King, J.C., Turner, J., 1997. *Antarctic Meteorology and Climatology*. volume 56. Cambridge University Press. URL: <https://www.cambridge.org/core/product/identifier/9780511524967/type/book>, doi:10.1017/CB09780511524967.
- Klingaman, N.P., Woolnough, S.J., Weller, H., Slingo, J.M., 2011. The impact of finer-resolution air-sea coupling on the intraseasonal oscillation of the Indian monsoon. *J. Clim.* 24, 2451–2468. URL: <http://journals.ametsoc.org/doi/abs/10.1175/2010JCLI3868.1>, doi:10.1175/2010JCLI3868.1.
- Kuehl, S.A., Levy, B.M., Moore, W.S., Allison, M.A., 1997. Subaqueous delta of the Ganges-Brahmaputra river system. *Mar. Geol.* 144, 81–96. URL: <https://linkinghub.elsevier.com/retrieve/pii/S0025322797000753>, doi:10.1016/S0025-3227(97)00075-3.
- Kumar, B.P., Vialard, J., Lengaigne, M., Murty, V.S.N., McPhaden, M.J., 2012. TropFlux: air-sea fluxes for the global tropical oceans – description and evaluation. *Clim. Dyn.* 38, 1521–1543. URL: <http://link.springer.com/10.1007/s00382-011-1115-0>, doi:10.1007/s00382-011-1115-0.
- Kumar, S.P., Muraleedharan, P.M., Prasad, T.G., Gauns, M., Ramaiah, N., de Souza, S.N., Sardesai, S., Madhupratap, M., 2002. Why is the Bay of Bengal less productive during summer monsoon compared to the Arabian Sea? *Geophys. Res. Lett.* 29, 2235. URL: <http://doi.wiley.com/10.1029/2002GL016013>, doi:10.1029/2002GL016013.

- Kumar, S.P., Narvekar, J., Nuncio, M., Kumar, A., Ramaiah, N., Sardesai, S., Gauns, M., Fernandes, V., Paul, J., 2010. Is the biological productivity in the Bay of Bengal light limited? *Curr. Sci.* 98, 1331–1339. URL: <https://www.jstor.org/stable/24107511>.
- Large, W.G., McWilliams, J.C., Doney, S.C., 1994. Oceanic vertical mixing: A review and a model with a nonlocal boundary layer parameterization. *Rev. Geophys.* 32, 363–403. URL: <http://doi.wiley.com/10.1029/94RG01872>, doi:10.1029/94RG01872.
- Lavender, S., Jackson, T., Sathyendranath, S., 2015. The Ocean Colour Climate Change Initiative: Merging ocean colour observations seamlessly. *Ocean Chall.* 21, 29–31. URL: <https://esa-oceancolour-cci.org/sites/esa-oceancolour-cci.org/files/oc-cci{ }article{ }ocean{ }challenge{ }v21.pdf>.
- Lee, Z.P., Darecki, M., Carder, K.L., Davis, C.O., Stramski, D., Rhea, W.J., 2005. Diffuse attenuation coefficient of downwelling irradiance: An evaluation of remote sensing methods. *J. Geophys. Res.* 110, C02017. URL: <http://doi.wiley.com/10.1029/2004JC002573>, doi:10.1029/2004JC002573.
- Lengaigne, M., Menkes, C., Aumont, O., Gorgues, T., Bopp, L., André, J.M., Madec, G., 2007. Influence of the oceanic biology on the tropical Pacific climate in a coupled general circulation model. *Clim. Dyn.* 28, 503–516. URL: <http://link.springer.com/10.1007/s00382-006-0200-2>, doi:10.1007/s00382-006-0200-2.
- Lévy, M., Shankar, D., André, J.M., Shenoi, S.S.C., Durand, F., de Boyer Montégut, C., 2007. Basin-wide seasonal evolution of the Indian Ocean's phytoplankton blooms. *J. Geophys. Res.* 112, C12014. URL: <http://doi.wiley.com/10.1029/2007JC004090>, doi:10.1029/2007JC004090.
- Lewis, M.R., Carr, M.E., Feldman, G.C., Esaias, W., McClain, C., 1990. Influence of penetrating solar radiation on the heat budget of the equatorial Pacific Ocean. *Nature* 347, 543–545. URL: <http://www.nature.com/articles/347543a0>, doi:10.1038/347543a0.
- Li, C., Yanai, M., 1996. The onset and interannual variability of the Asian summer monsoon in relation to land-sea thermal contrast. *J. Clim.* 9, 358–375. URL: [http://journals.ametsoc.org/doi/abs/10.1175/1520-0442\(1996\)09<0358:TOAIVO>2.0.CO;2](http://journals.ametsoc.org/doi/abs/10.1175/1520-0442(1996)09<0358:TOAIVO>2.0.CO;2), doi:10.1175/1520-0442(1996)09<0358:TOAIVO>2.0.CO;2.
- Lin, J.L., Weickman, K.M., Kiladis, G.N., Mapes, B.E., Schubert, S.D., Suarez, M.J., Bacmeister, J.T., Lee, M.I., 2008. Subseasonal variability associated with Asian summer monsoon simulated by 14 IPCC AR4 coupled GCMs. *J. Clim.* 21, 4541–4567. URL: <http://journals.ametsoc.org/doi/10.1175/2008JCLI1816.1>, doi:10.1175/2008JCLI1816.1.
- Lindzen, R.S., Nigam, S., 1987. On the role of sea surface temperature gradients in forcing low-level winds and convergence in the tropics. *J. Atmos.*

- Sci. 44, 2418–2436. URL: [http://journals.ametsoc.org/doi/abs/10.1175/1520-0469\(2007\)281987\(29044\)3C2418\(3AOTROSS\)3E2.0.CO;2](http://journals.ametsoc.org/doi/abs/10.1175/1520-0469(2007)281987(29044)3C2418(3AOTROSS)3E2.0.CO;2), doi:10.1175/1520-0469(1987)044<2418:OTROSS>2.0.CO;2.
- Little, H., Vichi, M., Thomalla, S., Swart, S., 2018. Spatial and temporal scales of chlorophyll variability using high-resolution glider data. *J. Mar. Syst.* 187, 1–12. URL: <https://linkinghub.elsevier.com/retrieve/pii/S0924796317304530>, doi:10.1016/j.jmarsys.2018.06.011.
- Longhurst, A.R., Harrison, W.G., 1989. The biological pump: Profiles of plankton production and consumption in the upper ocean. *Prog. Oceanogr.* 22, 47–123. URL: <https://linkinghub.elsevier.com/retrieve/pii/0079661189900104>, doi:10.1016/0079-6611(89)90010-4.
- Lotliker, A., Omand, M., Lucas, A., Laney, S., Mahadevan, A., Ravichandran, M., 2016. Penetrative radiative flux in the Bay of Bengal. *Oceanography* 29, 214–221. URL: <https://tos.org/oceanography/article/penetrative-radiative-flux-in-the-bay-of-bengal>, doi:10.5670/oceanog.2016.53.
- Madhu, N.V., Jyothibabu, R., Maheswaran, P.A., John Gerson, V., Gopalakrishnan, T.C., Nair, K.K.C., 2006. Lack of seasonality in phytoplankton standing stock (chlorophyll a) and production in the western Bay of Bengal. *Cont. Shelf Res.* 26, 1868–1883. URL: <https://linkinghub.elsevier.com/retrieve/pii/S0278434306002056>, doi:10.1016/j.csr.2006.06.004.
- Manizza, M., Quéré, C.L., Watson, A.J., Buitenhuis, E.T., 2005. Bio-optical feedbacks among phytoplankton, upper ocean physics and sea-ice in a global model. *Geophys. Res. Lett.* 32, L05603. URL: <http://doi.wiley.com/10.1029/2004GL020778>, doi:10.1029/2004GL020778.
- Marzeion, B., Timmermann, A., Murtugudde, R., Jin, F.F., 2005. Biophysical feedbacks in the tropical Pacific. *J. Clim.* 18, 58–70. URL: <http://journals.ametsoc.org/doi/10.1175/JCLI3261.1>, doi:10.1175/JCLI3261.1.
- McCreary, J.P., Murtugudde, R., Vialard, J., Vinayachandran, P.N., Wiggert, J.D., Hood, R.R., Shankar, D., Shetye, S., 2009. Biophysical processes in the Indian Ocean, in: *Geophys. Monogr. Ser.* volume 185, pp. 9–32. URL: <http://doi.wiley.com/10.1029/2008GM000768>, doi:10.1029/2008GM000768.
- McPhaden, M.J., Meyers, G., Ando, K., Masumoto, Y., Murty, V.S.N., Ravichandran, M., Syamsudin, F., Vialard, J., Yu, L., Yu, W., 2009. RAMA: The Research Moored Array for African-Asian-Australian Monsoon Analysis and Prediction. *Bull. Am. Meteorol. Soc.* 90, 459–480. URL: <http://journals.ametsoc.org/doi/10.1175/2008BAMS2608.1>, doi:10.1175/2008BAMS2608.1.
- Meister, G., Franz, B.A., 2014. Corrections to the MODIS Aqua calibration derived from MODIS Aqua ocean color products. *IEEE Trans. Geosci. Remote Sens.* 52, 6534–6541. URL: <http://ieeexplore.ieee.org/document/6725685/>, doi:10.1109/TGRS.2013.2297233.

- Mignot, A., Claustre, H., Uitz, J., Poteau, A., D'Ortenzio, F., Xing, X., 2014. Understanding the seasonal dynamics of phytoplankton biomass and the deep chlorophyll maximum in oligotrophic environments: A Bio-Argo float investigation. *Global Biogeochem. Cycles* 28, 856–876. URL: <http://doi.wiley.com/10.1002/2013GB004781>, doi:10.1002/2013GB004781.
- Mitchell, B.G., Brody, E.A., Holm-Hansen, O., McClain, C., Bishop, J., 1991. Light limitation of phytoplankton biomass and macronutrient utilization in the Southern Ocean. *Limnol. Oceanogr.* 36, 1662–1677. URL: <http://doi.wiley.com/10.4319/lo.1991.36.8.1662>, doi:10.4319/lo.1991.36.8.1662.
- Morel, A., 1988. Optical modeling of the upper ocean in relation to its biogenous matter content (case I waters). *J. Geophys. Res.* 93, 10749–10768. URL: <http://doi.wiley.com/10.1029/JC093iC09p10749>, doi:10.1029/JC093iC09p10749.
- Morel, A., Antoine, D., 1994. Heating rate within the upper ocean in relation to its bio-optical state. *J. Phys. Oceanogr.* 24, 1652–1665. URL: [http://journals.ametsoc.org/doi/abs/10.1175/1520-0485\(1994\)24<1652:HRWTUO>2.0.CO;2](http://journals.ametsoc.org/doi/abs/10.1175/1520-0485(1994)24<1652:HRWTUO>2.0.CO;2), doi:10.1175/1520-0485(1994)24<1652:HRWTUO>2.0.CO;2.
- Morel, A., Claustre, H., Antoine, D., Gentili, B., 2007. Natural variability of bio-optical properties in Case 1 waters: attenuation and reflectance within the visible and near-UV spectral domains, as observed in South Pacific and Mediterranean waters. *Biogeosciences* 4, 913–925. URL: <http://www.biogeosciences.net/4/913/2007/>, doi:10.5194/bg-4-913-2007.
- Morel, A., Maritorena, S., 2001. Bio-optical properties of oceanic waters: A reappraisal. *J. Geophys. Res. Ocean.* 106, 7163–7180. URL: <http://doi.wiley.com/10.1029/2000JC000319>, doi:10.1029/2000JC000319, arXiv:arXiv:0804.3873v1.
- Morel, A., Prieur, L., 1977. Analysis of variations in ocean color. *Limnol. Oceanogr.* 22, 709–722. URL: <http://doi.wiley.com/10.4319/lo.1977.22.4.0709>, doi:10.4319/lo.1977.22.4.0709.
- Morrison, A.K., Hogg, A.M., Ward, M.L., 2011. Sensitivity of the Southern Ocean overturning circulation to surface buoyancy forcing. *Geophys. Res. Lett.* 38, L14602. URL: <http://doi.wiley.com/10.1029/2011GL048031>, doi:10.1029/2011GL048031.
- Muller, P., 2001. Non-photochemical quenching. A response to excess light energy. *PLANT Physiol.* 125, 1558–1566. URL: <http://www.plantphysiol.org/cgi/doi/10.1104/pp.125.4.1558>, doi:10.1104/pp.125.4.1558.
- Murtugudde, R., Beauchamp, J., McClain, C.R., Lewis, M., Busalacchi, A.J., 2002. Effects of penetrative radiation on the upper tropical ocean circulation. *J. Clim.* 15, 470–486. URL: [http://journals.ametsoc.org/doi/abs/10.1175/1520-0442\(2002\)15<470:EOPROT>2.0.CO;2](http://journals.ametsoc.org/doi/abs/10.1175/1520-0442(2002)15<470:EOPROT>2.0.CO;2), doi:10.1175/1520-0442(2002)15<470:EOPROT>2.0.CO;2.

- Nakamoto, S., Kumar, S.P., Oberhuber, J.M., Ishizaka, J., Muneyama, K., Frouin, R., 2001. Response of the equatorial Pacific to chlorophyll pigment in a mixed layer isopycnal ocean general circulation model. *Geophys. Res. Lett.* 28, 2021–2024. URL: <http://doi.wiley.com/10.1029/2000GL012494>, doi:10.1029/2000GL012494.
- Nakamoto, S., Kumar, S.P., Oberhuber, J.M., Muneyama, K., Frouin, R., 2000. Chlorophyll modulation of sea surface temperature in the Arabian Sea in a mixed-layer isopycnal general circulation model. *Geophys. Res. Lett.* 27, 747–750. URL: <http://doi.wiley.com/10.1029/1999GL002371>, doi:10.1029/1999GL002371.
- Narvekar, J., Prasanna Kumar, S., 2006. Seasonal variability of the mixed layer in the central Bay of Bengal and associated changes in nutrients and chlorophyll. *Deep Sea Res. Part I Oceanogr. Res. Pap.* 53, 820–835. URL: <https://linkinghub.elsevier.com/retrieve/pii/S0967063706000513>, doi:10.1016/j.dsr.2006.01.012.
- Nelson, D.M., Smith, W., 1991. Sverdrup revisited: Critical depths, maximum chlorophyll levels, and the control of Southern Ocean productivity by the irradiance-mixing regime. *Limnol. Oceanogr.* 36, 1650–1661. URL: <http://doi.wiley.com/10.4319/lo.1991.36.8.1650>, doi:10.4319/lo.1991.36.8.1650.
- Nicholson, S.A., Lévy, M., Llort, J., Swart, S., Monteiro, P.M.S., 2016. Investigation into the impact of storms on sustaining summer primary productivity in the Sub-Antarctic Ocean. *Geophys. Res. Lett.* 43, 9192–9199. URL: <http://doi.wiley.com/10.1002/2016GL069973>, doi:10.1002/2016GL069973.
- Ohlmann, J.C., 2003. Ocean radiant heating in climate models. *J. Clim.* 16, 1337–1351. URL: [http://journals.ametsoc.org/doi/abs/10.1175/1520-0442\(2003\)16%3C1337:ORHICM%3E2.0.CO;2](http://journals.ametsoc.org/doi/abs/10.1175/1520-0442(2003)16%3C1337:ORHICM%3E2.0.CO;2), doi:10.1175/1520-0442(2003)16<1337:ORHICM>2.0.CO;2.
- Ohlmann, J.C., Siegel, D.A., 2000. Ocean radiant heating. Part II: Parameterizing solar radiation transmission through the upper ocean. *J. Phys. Oceanogr.* 30, 1849–1865. URL: <http://journals.ametsoc.org/doi/abs/10.1175/1520-0485%282000%29030%3C1849%3AORHPIP%3E2.0.CO%3B2>, doi:10.1175/1520-0485(2000)030<1849:ORHPIP>2.0.CO;2.
- Ohlmann, J.C., Siegel, D.A., Washburn, L., 1998. Radiant heating of the western equatorial Pacific during TOGA-COARE. *J. Geophys. Res. Ocean.* 103, 5379–5395. URL: <http://doi.wiley.com/10.1029/97JC03422>, doi:10.1029/97JC03422.
- O'Reilly, J.E., Maritorena, S., O'Brien, M.C., Siegel, D.A., Toole, D., Menzies, D., Smith, R.C., Mueller, J.L., Mitchell, B.G., Kahru, M., Chavez, F.P., Strutton, P., Cota, G.F., Hooker, S.B., McClain, C.R., Carder, K.L., Muller-Karger, F., Harding, L., Magnuson, A., Phinney, D., Moore, G.F., Aiken, J.,

- Arrigo, K.R., Letelier, R., Culver, M., 2000. SeaWiFS postlaunch calibration and validation analyses, Part 3. Technical Report. NASA Goddard Space Flight Center. URL: <https://oceancolor.gsfc.nasa.gov/docs/technical/seawifs{ }reports/postlaunch/post{ }vol11{ }abs/>.
- Organelli, E., Claustre, H., Bricaud, A., Barbieux, M., Uitz, J., D'Ortenzio, F., Dall'Olmo, G., 2017. Bio-optical anomalies in the world's oceans: An investigation on the diffuse attenuation coefficients for downward irradiance derived from Biogeochemical Argo float measurements. *J. Geophys. Res. Ocean.* 122, 3543–3564. URL: <http://doi.wiley.com/10.1002/2016JC012629>, doi:10.1002/2016JC012629.
- Organelli, E., Claustre, H., Bricaud, A., Schmechtig, C., Poteau, A., Xing, X., Prieur, L., D'Ortenzio, F., Dall'Olmo, G., Vellucci, V., 2016. A novel near-real-time quality-control procedure for radiometric profiles measured by Bio-Argo floats: Protocols and performances. *J. Atmos. Ocean. Technol.* 33, 937–951. URL: <http://journals.ametsoc.org/doi/10.1175/JTECH-D-15-0193.1>, doi:10.1175/JTECH-D-15-0193.1.
- Pandi, S.R., Kiran, R., Sarma, N.S., Srikanth, A.S., Sarma, V.V.S.S., Krishna, M.S., Bandyopadhyay, D., Prasad, V.R., Acharyya, T., Reddy, K.G., 2014. Contrasting phytoplankton community structure and associated light absorption characteristics of the western Bay of Bengal. *Ocean Dyn.* 64, 89–101. URL: <http://link.springer.com/10.1007/s10236-013-0678-1>, doi:10.1007/s10236-013-0678-1.
- Park, J.Y., Kug, J.S., 2014. Marine biological feedback associated with Indian Ocean Dipole in a coupled ocean/biogeochemical model. *Clim. Dyn.* 42, 329–343. URL: <http://link.springer.com/10.1007/s00382-012-1640-5>, doi:10.1007/s00382-012-1640-5.
- Patara, L., Vichi, M., Masina, S., Fogli, P.G., Manzini, E., 2012. Global response to solar radiation absorbed by phytoplankton in a coupled climate model. *Clim. Dyn.* 39, 1951–1968. URL: <http://link.springer.com/10.1007/s00382-012-1300-9>, doi:10.1007/s00382-012-1300-9.
- Patra, P.K., Kumar, M.D., Mahowald, N., Sarma, V.V.S.S., 2007. Atmospheric deposition and surface stratification as controls of contrasting chlorophyll abundance in the North Indian Ocean. *J. Geophys. Res.* 112, C05029. URL: <http://doi.wiley.com/10.1029/2006JC003885>, doi:10.1029/2006JC003885.
- Paulson, C.A., Simpson, J.J., 1977. Irradiance measurements in the upper ocean. *J. Phys. Oceanogr.* 7, 952–956. URL: [http://journals.ametsoc.org/doi/abs/10.1175/1520-0485\(1977\)007<0952:IMITUO>2.0.CO;2](http://journals.ametsoc.org/doi/abs/10.1175/1520-0485(1977)007<0952:IMITUO>2.0.CO;2), doi:10.1175/1520-0485(1977)007<0952:IMITUO>2.0.CO;2.
- Peatman, S.C., Klingaman, N.P., 2018. The Indian summer monsoon in MetUM-GOML2.0: effects of air-sea coupling and resolution. *Geosci. Model Dev.* 11, 4693–4709. URL: <https://www.geosci-model-dev.net/11/4693/2018/>, doi:10.5194/gmd-11-4693-2018.

- Pirro, A., Fernando, H., Wijesekera, H., Jensen, T., Centurioni, L., Jinadasa, S., 2020. Eddies and currents in the Bay of Bengal during summer monsoons. *Deep Sea Res. Part II Top. Stud. Oceanogr.* 172, 104728. URL: <https://linkinghub.elsevier.com/retrieve/pii/S096706451930075X>, doi:10.1016/j.dsr2.2019.104728.
- du Plessis, M., Swart, S., Ansoorge, I.J., Mahadevan, A., 2017. Submesoscale processes promote seasonal restratification in the Subantarctic Ocean. *J. Geophys. Res. Ocean.* 122, 2960–2975. URL: <http://doi.wiley.com/10.1002/2016JC012494>, doi:10.1002/2016JC012494.
- du Plessis, M., Swart, S., Ansoorge, I.J., Mahadevan, A., Thompson, A.F., 2019. Southern Ocean seasonal restratification delayed by submesoscale wind-front interactions. *J. Phys. Oceanogr.* 49, 1035–1053. URL: <http://journals.ametsoc.org/doi/10.1175/JPO-D-18-0136.1>, doi:10.1175/JPO-D-18-0136.1.
- Pope, R.M., Fry, E.S., 1997. Absorption spectrum (380–700 nm) of pure water. II. Integrating cavity measurements. *Appl. Opt.* 36, 8710–8723. URL: <https://www.osapublishing.org/abstract.cfm?URI=ao-36-33-8710>, doi:10.1364/AO.36.008710.
- Prasanna Kumar, S., Nuncio, M., Ramaiah, N., Sardesai, S., Narvekar, J., Fernandes, V., Paul, J.T., 2007. Eddy-mediated biological productivity in the Bay of Bengal during fall and spring intermonsoons. *Deep Sea Res. Part I Oceanogr. Res. Pap.* 54, 1619–1640. URL: <https://linkinghub.elsevier.com/retrieve/pii/S0967063707001501>, doi:10.1016/j.dsr.2007.06.002.
- Rao, R.R., Sivakumar, R., 2003. Seasonal variability of sea surface salinity and salt budget of the mixed layer of the north Indian Ocean. *J. Geophys. Res.* 108, 3009. URL: <http://doi.wiley.com/10.1029/2001JC000907>, doi:10.1029/2001JC000907.
- Revadekar, J.V., Preethi, B., 2012. Statistical analysis of the relationship between summer monsoon precipitation extremes and foodgrain yield over India. *Int. J. Climatol.* 32, 419–429. URL: <http://doi.wiley.com/10.1002/joc.2282>, doi:10.1002/joc.2282.
- Roxy, M., Tanimoto, Y., Preethi, B., Terray, P., Krishnan, R., 2013. Intraseasonal SST-precipitation relationship and its spatial variability over the tropical summer monsoon region. *Clim. Dyn.* 41, 45–61. URL: <http://link.springer.com/10.1007/s00382-012-1547-1>, doi:10.1007/s00382-012-1547-1.
- Roxy, M.K., Ghosh, S., Pathak, A., Athulya, R., Mujumdar, M., Murtugudde, R., Terray, P., Rajeevan, M., 2017. A threefold rise in widespread extreme rain events over central India. *Nat. Commun.* 8, 708. URL: <http://www.nature.com/articles/s41467-017-00744-9>, doi:10.1038/s41467-017-00744-9.
- Roxy, M.K., Ritika, K., Terray, P., Murtugudde, R., Ashok, K., Goswami, B.N., 2015. Drying of Indian subcontinent by rapid Indian Ocean warming and

- a weakening land-sea thermal gradient. *Nat. Commun.* 6, 7423. URL: <http://www.nature.com/articles/ncomms8423>, doi:10.1038/ncomms8423.
- Sallée, J.B., Speer, K.G., Rintoul, S.R., 2010. Zonally asymmetric response of the Southern Ocean mixed-layer depth to the Southern Annular Mode. *Nat. Geosci.* 3, 273–279. URL: <http://www.nature.com/articles/ngeo812>, doi:10.1038/ngeo812.
- Sanchez-Franks, A., Kent, E.C., Matthews, A.J., Webber, B.G.M., Peatman, S.C., Vinayachandran, P.N., 2018. Intraseasonal variability of air-sea fluxes over the Bay of Bengal during the Southwest Monsoon. *J. Clim.* 31, 7087–7109. URL: <http://journals.ametsoc.org/doi/10.1175/JCLI-D-17-0652.1>, doi:10.1175/JCLI-D-17-0652.1.
- Sanchez-Franks, A., Webber, B.G.M., King, B.A., Vinayachandran, P.N., Matthews, A.J., Sheehan, P.M.F., Behara, A., Neema, C.P., 2019. The railroad switch effect of seasonally reversing currents on the Bay of Bengal high-salinity core. *Geophys. Res. Lett.* 46, 6005–6014. URL: <https://onlinelibrary.wiley.com/doi/abs/10.1029/2019GL082208>, doi:10.1029/2019GL082208.
- Sathyendranath, S., Gouveia, A.D., Shetye, S.R., Ravindran, P., Platt, T., 1991. Biological control of surface temperature in the Arabian Sea. *Nature* 349, 54–56. URL: <http://www.nature.com/articles/349054a0>, doi:10.1038/349054a0.
- Schmittner, A., 2005. Decline of the marine ecosystem caused by a reduction in the Atlantic overturning circulation. *Nature* 434, 628–633. URL: <http://www.nature.com/articles/nature03476>, doi:10.1038/nature03476.
- Schott, F.A., McCreary, J.P., 2001. The monsoon circulation of the Indian Ocean. *Prog. Oceanogr.* 51, 1–123. URL: www.elsevier.com/locate/pocean, doi:10.1016/S0079-6611(01)00083-0.
- Schott, F.A., Xie, S.P., McCreary, J.P., 2009. Indian Ocean circulation and climate variability. *Rev. Geophys.* 47, RG1002. URL: <http://doi.wiley.com/10.1029/2007RG000245>, doi:10.1029/2007RG000245.
- Sengupta, D., Bharath Raj, G.N., Ravichandran, M., Sree Lekha, J., Papa, F., 2016. Near-surface salinity and stratification in the north Bay of Bengal from moored observations. *Geophys. Res. Lett.* 43, 4448–4456. URL: <http://doi.wiley.com/10.1002/2016GL068339>, doi:10.1002/2016GL068339.
- Sengupta, D., Goswami, B.N., Senan, R., 2001. Coherent intraseasonal oscillations of ocean and atmosphere during the Asian Summer Monsoon. *Geophys. Res. Lett.* 28, 4127–4130. URL: <http://doi.wiley.com/10.1029/2001GL013587>, doi:10.1029/2001GL013587.
- Shee, A., Sil, S., Gangopadhyay, A., Gawarkiewicz, G., Ravichandran, M., 2019. Seasonal evolution of oceanic upper layer processes in the

- northern Bay of Bengal following a single Argo float. *Geophys. Res. Lett.* 46, 5369–5377. URL: <https://onlinelibrary.wiley.com/doi/abs/10.1029/2019GL082078>, doi:10.1029/2019GL082078.
- Shell, K.M., Frouin, R., Nakamoto, S., Somerville, R.C.J., 2003. Atmospheric response to solar radiation absorbed by phytoplankton. *J. Geophys. Res.* 108, 4445. URL: <http://doi.wiley.com/10.1029/2003JD003440>, doi:10.1029/2003JD003440.
- Shenoi, S.S.C., Shankar, D., Shetye, S.R., 2002. Differences in heat budgets of the near-surface Arabian Sea and Bay of Bengal: Implications for the summer monsoon. *J. Geophys. Res.* 107, 3052. URL: <http://doi.wiley.com/10.1029/2000JC000679>, doi:10.1029/2000JC000679.
- Smetacek, V., Klaas, C., Strass, V.H., Assmy, P., Montresor, M., Cisewski, B., Savoye, N., Webb, A., D'Ovidio, F., Arrieta, J.M., Bathmann, U., Bellerby, R., Berg, G.M., Croot, P., Gonzalez, S., Henjes, J., Herndl, G.J., Hoffmann, L.J., Leach, H., Losch, M., Mills, M.M., Neill, C., Peeken, I., Röttgers, R., Sachs, O., Sauter, E., Schmidt, M.M., Schwarz, J., Terbrüggen, A., Wolf-Gladrow, D., 2012. Deep carbon export from a Southern Ocean iron-fertilized diatom bloom. *Nature* 487, 313–319. URL: <http://www.nature.com/articles/nature11229>, doi:10.1038/nature11229.
- Smetacek, V., Naqvi, S.W.A., 2008. The next generation of iron fertilization experiments in the Southern Ocean. *Philos. Trans. R. Soc. A Math. Phys. Eng. Sci.* 366, 3947–3967. URL: <https://royalsocietypublishing.org/doi/10.1098/rsta.2008.0144>, doi:10.1098/rsta.2008.0144.
- Smith, D.M., Murphy, J.M., 2007. An objective ocean temperature and salinity analysis using covariances from a global climate model. *J. Geophys. Res.* 112, C02022. URL: <http://doi.wiley.com/10.1029/2005JC003172>, doi:10.1029/2005JC003172.
- Smith, R., Jones, P., Briegleb, B., Bryan, F., Danabasoglu, G., Dennis, J., Dukowicz, J., Eden, C., Fox-Kemper, B., Gent, P., Hecht, M., Jayne, S., Jochum, M., Large, W., Lindsay, K., Maltrud, M., Norton, N., Peacock, S., Vertenstein, M., Yeager, S., 2010. The Parallel Ocean Program (POP) reference manual, ocean component of the Community Climate System Model (CCSM). Technical Report. URL: <http://www.cesm.ucar.edu/models/cesm1.0/pop2/doc/sci/POPRefManual.pdf>.
- Smith, R.C., Baker, K.S., 1978. The bio-optical state of ocean waters and remote sensing 1. *Limnol. Oceanogr.* 23, 247–259. URL: <https://aslopubs.onlinelibrary.wiley.com/doi/pdf/10.4319/lo.1978.23.2.0247>, doi:10.4319/lo.1978.23.2.0247.
- Sperber, K.R., Annamalai, H., Kang, I.S., Kitoh, A., Moise, A., Turner, A., Wang, B., Zhou, T., 2013. The Asian summer monsoon: an intercomparison of CMIP5 vs. CMIP3 simulations of the late 20th century. *Clim. Dyn.*

- 41, 2711–2744. URL: <http://link.springer.com/10.1007/s00382-012-1607-6>, doi:10.1007/s00382-012-1607-6.
- Sprintall, J., Tomczak, M., 1992. Evidence of the barrier layer in the surface layer of the tropics. *J. Geophys. Res.* 97, 7305–7316. URL: <http://doi.wiley.com/10.1029/92JC00407>, doi:10.1029/92JC00407.
- Stephan, C.C., Klingaman, N.P., Turner, A.G., 2019. A mechanism for the recently increased interdecadal variability of the Silk Road pattern. *J. Clim.* 32, 717–736. URL: <http://journals.ametsoc.org/doi/10.1175/JCLI-D-18-0405.1>, doi:10.1175/JCLI-D-18-0405.1.
- Stramski, D., Boss, E., Bogucki, D., Voss, K.J., 2004. The role of seawater constituents in light backscattering in the ocean. *Prog. Oceanogr.* 61, 27–56. URL: <https://linkinghub.elsevier.com/retrieve/pii/S0079661104000692>, doi:10.1016/j.pocean.2004.07.001.
- Strutton, P.G., Chavez, F.P., 2004. Biological heating in the equatorial Pacific: Observed variability and potential for real-time calculation. *J. Clim.* 17, 1097–1109. URL: [http://journals.ametsoc.org/doi/abs/10.1175/1520-0442\(2004\)017<1097:BHITEP>2.0.CO;2](http://journals.ametsoc.org/doi/abs/10.1175/1520-0442(2004)017<1097:BHITEP>2.0.CO;2), doi:10.1175/1520-0442(2004)017<1097:BHITEP>2.0.CO;2.
- Sullivan, J.M., Twardowski, M.S., Zaneveld, J.R.V., Moore, C.M., Barnard, A.H., Donaghay, P.L., Rhoades, B., 2006. Hyperspectral temperature and salt dependencies of absorption by water and heavy water in the 400–750 nm spectral range. *Appl. Opt.* 45, 5294–5309. URL: <https://www.osapublishing.org/abstract.cfm?URI=ao-45-21-5294>, doi:10.1364/AO.45.005294.
- Swart, S., Chang, N., Fauchereau, N., Joubert, W., Lucas, M., Mtshali, T., Roychoudhury, A., Tagliabue, A., Thomalla, S., Waldron, H., Monteiro, P.M., 2012. Southern Ocean Seasonal Cycle Experiment 2012: Seasonal scale climate and carbon cycle links. *S. Afr. J. Sci.* 108, 3–5. URL: <http://archive.sajs.co.za/index.php/SAJS/article/view/1089>, doi:10.4102/sajs.v108i3/4.1089.
- Swart, S., Gille, S.T., Delille, B., Josey, S., Mazloff, M., Newman, L., Thompson, A.F., Thomson, J., Ward, B., du Plessis, M.D., Kent, E.C., Girton, J., Gregor, L., Heil, P., Hyder, P., Pezzi, L.P., de Souza, R.B., Tamsitt, V., Weller, R.A., Zappa, C.J., 2019. Constraining Southern Ocean air-sea-ice fluxes through enhanced observations. *Front. Mar. Sci.* 6, 1–10. URL: <https://www.frontiersin.org/article/10.3389/fmars.2019.00421/full>, doi:10.3389/fmars.2019.00421.
- Swart, S., Thomalla, S., Monteiro, P., 2015. The seasonal cycle of mixed layer dynamics and phytoplankton biomass in the Sub-Antarctic Zone: A high-resolution glider experiment. *J. Mar. Syst.* 147, 103–115. URL: <https://linkinghub.elsevier.com/retrieve/pii/S0924796314001535>, doi:10.1016/j.jmarsys.2014.06.002.
- Sweeney, C., Gnanadesikan, A., Griffies, S.M., Harrison, M.J., Rosati, A.J., Samuels, B.L., 2005. Impacts of shortwave penetration depth on large-scale

- ocean circulation and heat transport. *J. Phys. Oceanogr.* 35, 1103–1119. URL: <http://journals.ametsoc.org/doi/abs/10.1175/JPO2740.1>, doi:10.1175/JPO2740.1.
- Talley, L.D., Pickard, G.L., Emery, W.J., Swift, J.H., 2011. Southern Ocean, in: *Descr. Phys. Oceanogr.* Elsevier, pp. 437–471. URL: <https://linkinghub.elsevier.com/retrieve/pii/B9780750645522100137>, doi:10.1016/B978-0-7506-4552-2.10013-7.
- Tamsitt, V., Talley, L.D., Mazloff, M.R., Cerovečki, I., 2016. Zonal variations in the Southern Ocean heat budget. *J. Clim.* 29, 6563–6579. URL: <http://journals.ametsoc.org/doi/10.1175/JCLI-D-15-0630.1>, doi:10.1175/JCLI-D-15-0630.1.
- Terzić, E., Lazzari, P., Organelli, E., Solidoro, C., Salon, S., D’Ortenzio, F., Conan, P., 2019. Merging bio-optical data from Biogeochemical-Argo floats and models in marine biogeochemistry. *Biogeosciences* 16, 2527–2542. URL: <https://www.biogeosciences.net/16/2527/2019/>, doi:10.5194/bg-16-2527-2019.
- Thomalla, S.J., Fauchereau, N., Swart, S., Monteiro, P.M.S., 2011. Regional scale characteristics of the seasonal cycle of chlorophyll in the Southern Ocean. *Biogeosciences* 8, 2849–2866. URL: <https://www.biogeosciences.net/8/2849/2011/>, doi:10.5194/bg-8-2849-2011.
- Thomalla, S.J., Moutier, W., Ryan-Keogh, T.J., Gregor, L., Schütt, J., 2018. An optimized method for correcting fluorescence quenching using optical backscattering on autonomous platforms. *Limnol. Oceanogr. Methods* 16, 132–144. URL: <http://doi.wiley.com/10.1002/lom3.10234>, doi:10.1002/lom3.10234.
- Thomalla, S.J., Racault, M.f., Swart, S., Monteiro, P.M.S., 2015. High-resolution view of the spring bloom initiation and net community production in the Subantarctic Southern Ocean using glider data. *ICES J. Mar. Sci.* 72, 1999–2020. URL: <https://academic.oup.com/icesjms/article/72/6/1999/926541>, doi:10.1093/icesjms/fsv105.
- Thompson, V., Dunstone, N.J., Scaife, A.A., Smith, D.M., Hardiman, S.C., Ren, H.L., Lu, B., Belcher, S.E., 2019. Risk and dynamics of unprecedented hot months in South East China. *Clim. Dyn.* 52, 2585–2596. URL: <http://link.springer.com/10.1007/s00382-018-4281-5>, doi:10.1007/s00382-018-4281-5.
- Thushara, V., Vinayachandran, P.N., 2016. Formation of summer phytoplankton bloom in the northwestern Bay of Bengal in a coupled physical-ecosystem model. *J. Geophys. Res. Ocean.* 121, 8535–8550. URL: <https://onlinelibrary.wiley.com/doi/abs/10.1002/2015JC011516>, doi:10.1002/2015JC011516.
- Thushara, V., Vinayachandran, P.N.M., Matthews, A.J., Webber, B.G.M., Queste, B.Y., 2019. Vertical distribution of chlorophyll in dynamically distinct regions of the southern Bay of Bengal. *Biogeosciences* 16, 1447–1468. URL: <https://www.biogeosciences.net/16/1447/2019/>, doi:10.5194/bg-16-1447-2019.

- Tian, F., Zhang, R.H., Wang, X., 2019. A positive feedback onto ENSO due to tropical instability wave (TIW)-induced chlorophyll effects in the Pacific. *Geophys. Res. Lett.* 46, 889–897. URL: <http://doi.wiley.com/10.1029/2018GL081275>, doi:10.1029/2018GL081275.
- Tilstone, G.H., Angel-Benavides, I.M., Pradhan, Y., Shutler, J.D., Groom, S., Sathyendranath, S., 2011. An assessment of chlorophyll-a algorithms available for SeaWiFS in coastal and open areas of the Bay of Bengal and Arabian Sea. *Remote Sens. Environ.* 115, 2277–2291. URL: <https://linkinghub.elsevier.com/retrieve/pii/S0034425711001568>, doi:10.1016/j.rse.2011.04.028.
- Turner, A.G., Joshi, M., Robertson, E.S., Woolnough, S.J., 2012. The effect of Arabian Sea optical properties on SST biases and the South Asian summer monsoon in a coupled GCM. *Clim. Dyn.* 39, 811–826. URL: <http://link.springer.com/10.1007/s00382-011-1254-3>, doi:10.1007/s00382-011-1254-3.
- Valcke, S., 2013. The OASIS3 coupler: a European climate modelling community software. *Geosci. Model Dev.* 6, 373–388. URL: <https://www.geosci-model-dev.net/6/373/2013/>, doi:10.5194/gmd-6-373-2013.
- Vecchi, G.A., Harrison, D.E., 2002. Monsoon breaks and subseasonal sea surface temperature variability in the Bay of Bengal. *J. Clim.* 15, 1485–1493. URL: [http://journals.ametsoc.org/doi/abs/10.1175/1520-0442\(2002\)15<1485:MBASSS>2.0.CO;2](http://journals.ametsoc.org/doi/abs/10.1175/1520-0442(2002)15<1485:MBASSS>2.0.CO;2), doi:10.1175/1520-0442(2002)15<1485:MBASSS>2.0.CO;2.
- Vinayachandran, P.N., Chauhan, P., Mohan, M., Nayak, S., 2004. Biological response of the sea around Sri Lanka to summer monsoon. *Geophys. Res. Lett.* 31, L01302. URL: <http://doi.wiley.com/10.1029/2003GL018533>, doi:10.1029/2003GL018533.
- Vinayachandran, P.N., Mathew, S., 2003. Phytoplankton bloom in the Bay of Bengal during the northeast monsoon and its intensification by cyclones. *Geophys. Res. Lett.* 30, 1572. URL: <http://doi.wiley.com/10.1029/2002GL016717>, doi:10.1029/2002GL016717.
- Vinayachandran, P.N., Matthews, A.J., Kumar, K.V., Sanchez-Franks, A., Thushara, V., George, J., Vijith, V., Webber, B.G.M., Queste, B.Y., Roy, R., Sarkar, A., Baranowski, D.B., Bhat, G.S., Klingaman, N.P., Peatman, S.C., Parida, C., Heywood, K.J., Hall, R., King, B., Kent, E.C., Nayak, A.A., Neema, C.P., Amol, P., Lotliker, A., Kankonkar, A., Gracias, D.G., Vernekar, S., D'Souza, A.C., Valluvan, G., Pargaonkar, S.M., Dinesh, K., Giddings, J., Joshi, M., 2018. BoBBLE: Ocean-atmosphere interaction and its impact on the South Asian monsoon. *Bull. Am. Meteorol. Soc.* 99, 1569–1587. URL: <http://journals.ametsoc.org/doi/10.1175/BAMS-D-16-0230.1>, doi:10.1175/BAMS-D-16-0230.1.
- Vinayachandran, P.N., Murty, V.S.N., Babu, V.R., 2002. Observations of barrier layer formation in the Bay of Bengal during summer monsoon. *J. Geophys.*

- Res. Ocean. 107, SRF 19–1–SRF 19–9. URL: <http://doi.wiley.com/10.1029/2001JC000831>, doi:10.1029/2001JC000831.
- Vinayachandran, P.N., Neema, C.P., Mathew, S., Remya, R., 2012. Mechanisms of summer intraseasonal sea surface temperature oscillations in the Bay of Bengal. *J. Geophys. Res. Ocean.* 117, C01005. URL: <http://doi.wiley.com/10.1029/2011JC007433>, doi:10.1029/2011JC007433.
- Vinayachandran, P.N., Yamagata, T., 1998. Monsoon response of the sea around Sri Lanka: Generation of thermal domes and anticyclonic vortices. *J. Phys. Oceanogr.* 28, 1946–1960. URL: [http://journals.ametsoc.org/doi/abs/10.1175/1520-0485\(1998\)028<1946:MRO TSA>2.0.CO;2](http://journals.ametsoc.org/doi/abs/10.1175/1520-0485(1998)028<1946:MRO TSA>2.0.CO;2), doi:10.1175/1520-0485(1998)028<1946:MRO TSA>2.0.CO;2.
- Walters, D., Baran, A.J., Boutle, I., Brooks, M., Earnshaw, P., Edwards, J., Furtado, K., Hill, P., Lock, A., Manners, J., Morcrette, C., Mulcahy, J., Sanchez, C., Smith, C., Stratton, R., Tennant, W., Tomassini, L., Van Weverberg, K., Vosper, S., Willett, M., Browse, J., Bushell, A., Carslaw, K., Dalvi, M., Essery, R., Gedney, N., Hardiman, S., Johnson, B., Johnson, C., Jones, A., Jones, C., Mann, G., Milton, S., Rumbold, H., Sellar, A., Ujiie, M., Whitall, M., Williams, K., Zerroukat, M., 2019. The Met Office Unified Model Global Atmosphere 7.0/7.1 and JULES Global Land 7.0 configurations. *Geosci. Model Dev.* 12, 1909–1963. URL: <https://www.geosci-model-dev.net/12/1909/2019/>, doi:10.5194/gmd-12-1909-2019.
- Wang, B., Xie, X., 1997. A model for the boreal summer intraseasonal oscillation. *J. Atmos. Sci.* 54, 72–86. URL: [http://journals.ametsoc.org/doi/abs/10.1175/1520-0469\(1997\)054<0072:AMFTBS>2.0.CO;2](http://journals.ametsoc.org/doi/abs/10.1175/1520-0469(1997)054<0072:AMFTBS>2.0.CO;2), doi:10.1175/1520-0469(1997)054<0072:AMFTBS>2.0.CO;2.
- Wang, M., Knobelspiesse, K.D., McClain, C.R., 2005. Study of the Sea-Viewing Wide Field-of-View Sensor (SeaWiFS) aerosol optical property data over ocean in combination with the ocean color products. *J. Geophys. Res.* 110, D10S06. URL: <http://doi.wiley.com/10.1029/2004JD004950>, doi:10.1029/2004JD004950.
- Wang, M., Son, S., 2016. VIIRS-derived chlorophyll-a using the ocean color index method. *Remote Sens. Environ.* 182, 141–149. URL: <https://linkinghub.elsevier.com/retrieve/pii/S0034425716301948>, doi:10.1016/j.rse.2016.05.001.
- Webber, B.G.M., Matthews, A.J., Vinayachandran, P.N., Neema, C.P., Sanchez-Franks, A., Vijith, V., Amol, P., Baranowski, D.B., 2018. The dynamics of the Southwest Monsoon Current in 2016 from high-resolution in situ observations and models. *J. Phys. Oceanogr.* 48, 2259–2282. URL: <http://journals.ametsoc.org/doi/10.1175/JPO-D-17-0215.1>, doi:10.1175/JPO-D-17-0215.1.
- Webster, P.J., Magaña, V.O., Palmer, T.N., Shukla, J., Tomas, R.A., Yanai, M., Yasunari, T., 1998. Monsoons: Processes, predictability, and the prospects for

- prediction. *J. Geophys. Res. Ocean.* 103, 14451–14510. URL: <http://doi.wiley.com/10.1029/97JC02719>, doi:10.1029/97JC02719.
- Wetzel, P., Maier-Reimer, E., Botzet, M., Jungclaus, J., Keenlyside, N., Latif, M., 2006. Effects of ocean biology on the penetrative radiation in a coupled climate model. *J. Clim.* 19, 3973–3987. URL: <http://journals.ametsoc.org/doi/abs/10.1175/JCLI3828.1>, doi:10.1175/JCLI3828.1.
- Wojtasiewicz, B., Hardman-Mountford, N.J., Antoine, D., Dufois, F., Slawinski, D., Trull, T.W., 2018. Use of bio-optical profiling float data in validation of ocean colour satellite products in a remote ocean region. *Remote Sens. Environ.* 209, 275–290. URL: <https://linkinghub.elsevier.com/retrieve/pii/S0034425718300683>, doi:10.1016/j.rse.2018.02.057.
- Xing, X., Morel, A., Claustre, H., Antoine, D., D’Ortenzio, F., Poteau, A., Mignot, A., 2011. Combined processing and mutual interpretation of radiometry and fluorimetry from autonomous profiling Bio-Argo floats: Chlorophyll a retrieval. *J. Geophys. Res.* 116, C06020. URL: <http://doi.wiley.com/10.1029/2010JC006899>, doi:10.1029/2010JC006899.
- Yuan, X., Martinson, D.G., Liu, W.T., 1999. Effect of air-sea-ice interaction on winter 1996 Southern Ocean subpolar storm distribution. *J. Geophys. Res. Atmos.* 104, 1991–2007. URL: <http://doi.wiley.com/10.1029/98JD02719>, doi:10.1029/98JD02719.
- Yuan, X., Patoux, J., Li, C., 2009. Satellite-based midlatitude cyclone statistics over the Southern Ocean: 2. Tracks and surface fluxes. *J. Geophys. Res.* 114, D04106. URL: <http://doi.wiley.com/10.1029/2008JD010874>, doi:10.1029/2008JD010874.
- Zaneveld, J.R.V., Boss, E., Barnard, A., 2001. Influence of surface waves on measured and modeled irradiance profiles. *Appl. Opt.* 40, 1442–1449. URL: <https://www.osapublishing.org/abstract.cfm?URI=ao-40-9-1442>, doi:10.1364/AO.40.001442.
- Zaneveld, J.R.V., Kitchen, J.C., Pak, H., 1981. The influence of optical water type on the heating rate of a constant depth mixed layer. *J. Geophys. Res.* 86, 6426–6428. URL: <http://doi.wiley.com/10.1029/JC086iC07p06426>, doi:10.1029/JC086iC07p06426.
- Zhang, X., Hu, L., 2009. Scattering by pure seawater at high salinity. *Opt. Express* 17, 12685. URL: <https://www.osapublishing.org/oe/abstract.cfm?uri=oe-17-15-12685>, doi:10.1364/OE.17.012685.
- Zhang, X., Lewis, M., Johnson, B., 1998. Influence of bubbles on scattering of light in the ocean. *Appl. Opt.* 37, 6525–6536. URL: <https://www.osapublishing.org/abstract.cfm?URI=ao-37-27-6525>, doi:10.1364/AO.37.006525.